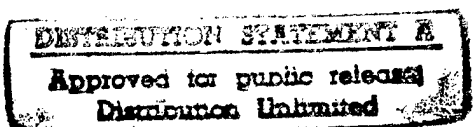


## REPORT DOCUMENTATION PAGE

Form Approved  
OMB No. 0704-0188

Public reporting burden for this collection of information is estimated to average 1 hour per response, including the time for reviewing instructions, searching existing data sources, gathering and maintaining the data needed, and completing and reviewing the collection of information. Send comments regarding this burden estimate or any other aspect of this collection of information, including suggestions for reducing this burden, to Washington Headquarters Services, Directorate for Information Operations and Reports, 1215 Jefferson Davis Highway, Suite 1204, Arlington, VA 22202-4302, and to the Office of Management and Budget, Paperwork Reduction Project (0704-0188), Washington, DC 20503.

1. AGENCY USE ONLY (Leave blank)			2. REPORT DATE 8 Sep 97	3. REPORT TYPE AND DATES COVERED
4. TITLE AND SUBTITLE Tightly Coupled GPS-Gyro Integration for Spacecraft Attitude Determination			5. FUNDING NUMBERS	
6. AUTHOR(S) Varun Puri				
7. PERFORMING ORGANIZATION NAME(S) AND ADDRESS(ES) Massachusetts Institute Of Technology			8. PERFORMING ORGANIZATION REPORT NUMBER 97-118	
9. SPONSORING/MONITORING AGENCY NAME(S) AND ADDRESS(ES) THE DEPARTMENT OF THE AIR FORCE AFIT/CIA 2950 P STREET WPAFB OH 45433			10. SPONSORING/MONITORING AGENCY REPORT NUMBER	
11. SUPPLEMENTARY NOTES				
12a. DISTRIBUTION AVAILABILITY STATEMENT 			12b. DISTRIBUTION CODE	
13. ABSTRACT (Maximum 200 words)				
14. SUBJECT TERMS			15. NUMBER OF PAGES 200	
			16. PRICE CODE	
17. SECURITY CLASSIFICATION OF REPORT	18. SECURITY CLASSIFICATION OF THIS PAGE	19. SECURITY CLASSIFICATION OF ABSTRACT	20. LIMITATION OF ABSTRACT	

# Tightly Coupled GPS-Gyro Integration for Spacecraft Attitude Determination

by

2 Lt Varun Puri

B.S. Astronautical Engineering  
and Mathematical Sciences  
United States Air Force Academy, 1995

SUBMITTED TO THE DEPARTMENT OF AERONAUTICS AND ASTRONAUTICS IN  
PARTIAL FULFILLMENT OF THE REQUIREMENTS FOR THE DEGREE OF

MASTER OF SCIENCE IN AERONAUTICS AND ASTRONAUTICS  
AT THE  
MASSACHUSETTS INSTITUTE OF TECHNOLOGY

JUNE 1997

© 1997 Varun Puri, All Rights Reserved.

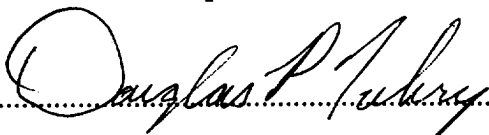
Signature of Author.....



Department of Aeronautics and Astronautics

June 1997

Approved by.....

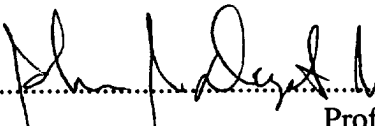


Douglas P. Fuhr

Charles Stark Draper Laboratory, Inc.

Technical Supervisor

Certified by.....



Professor John J. Deyst, Jr.

Department of Aeronautics and Astronautics

Thesis Supervisor

Accepted by.....

Jaime Peraire

Professor of Aeronautics and Astronautics

Chair, Graduate Office



# **Tightly Coupled GPS-Gyro Integration for Spacecraft Attitude Determination**

by

Varun Puri

Submitted to the Department of Aeronautics and Astronautics  
on May 23, 1997 in Partial Fulfillment of the  
Requirements for the Degree of Master of Science in  
Aeronautics and Astronautics

## **ABSTRACT**

A Global Positioning System (GPS) based attitude determination system has never been used as the primary source of attitude information for a spacecraft application. The fundamental reason for this is that a spacecraft attitude determination system must achieve fast attitude acquisition and near perfect solution reliability. Existing GPS based attitude systems cannot meet these requirements, so GPS has only been used as a secondary sensor for spacecraft missions. In this thesis, an attitude determination system is developed which meets spacecraft performance requirements using GPS as the primary source of attitude information. System hardware includes a multiple antenna GPS receiver and a low cost three axis gyro assembly. The attitude determination software consists of an integer ambiguity solution algorithm, an Extended Kalman Filter and an integrity monitoring architecture to improve robustness of the design.

The integer solution algorithm resolves GPS integer ambiguity with no *a priori* attitude knowledge or external aiding. Processing is streamlined by solving the two-dimensional yaw and pitch problem and the one-dimensional roll problem independently.

For performance analysis of the proposed architecture, GPS error sources are modeled using experimental data from an off-the-shelf GPS receiver. The models are also used for design of the Extended Kalman Filter.

Total attitude estimation errors average  $0.25^\circ$  RMS in nominal simulation test cases. Orbit parameters for the nominal tests are based on the Iridium communications system constellation design. Off-nominal test cases prove system reliability for a wide range of initial conditions. Off-nominal test cases also show that tightly coupled gyro aiding significantly improves filter performance in the face of degraded GPS measurement quality.

Thesis Supervisor: Professor John J. Deyst, Jr.  
Title: Professor, Department of Aeronautics and Astronautics

19970912 060

DTIC QUALITY INSPECTED 3

Technical Supervisor: Douglas P. Fuhr

Title: Senior Member Technical Staff, C. S. Draper Laboratory, Inc.

# Acknowledgments

I could not have completed this thesis without the enormous amount of support I have received from my friends, family and co-workers.

I would first like to thank my technical advisor, Doug Fuhr. The enthusiasm he had for my research and his endless patience in waiting for the results are deeply appreciated. Thanks also to my thesis advisor, Professor John Deyst, whose thoughtful questions and suggestions motivated countless improvements to this thesis.

I received valuable assistance from many of the staff and students at the Draper Lab. Thanks to Frank Mullen for teaching me about circular polarization and for tolerating my many attempts to talk a GPS receiver into submission. He is a joy to work with, even if he *is* in the Coast Guard. Thanks to Ramses, Rudy and Chris D'Souza for their company on the late nights and their help in putting the final touches on this thesis. To Tony Giustino, I pass the torch of the VIHIGPS-AIRSJMEF, and I apologize in advance for the mess I'm leaving behind. To Chris Stoll, thanks for the daily warning about my disk quota and for providing the foundation for much of my research.

I couldn't have done this without my roommates, Jeff and Naresh. Thanks for putting up with CMT in the morning. I know I'll never meet a nicer orbital mechanic than Naresh. To Jeff, thanks for the belay. I can only dream to send the gravy like you some day.

To my best friend Chris and to his family, you have given me more than I will ever know how to repay. I owe much of my happiness to you and the rest of my wonderful friends in Minnesota.

And to my family, there are no words to express the debt I feel to you. Mom, Papa, Aarti and Vikas, you know how hard this last year has been for me. Your support has never faltered, and I love you for that.

This thesis was prepared at the Charles Stark Draper Laboratory, Inc., under Independent Research and Development #645.

Publication of this thesis does not constitute approval by the Draper Laboratory or the sponsoring agency of the findings or conclusions contained herein. It is published for the exchange and stimulation of ideas.

I hereby assign my copyright of this thesis to the Charles Stark Draper Laboratory, Inc., Cambridge, Massachusetts.

---

Varun Puri

Permission is hereby granted by the Charles Stark Draper Laboratory to MIT permission to reproduce and to distribute publicly paper and electronic copies of this thesis document in whole or in part.

# Table of Contents

1	Introduction . . . . .	17
1.1	Objectives . . . . .	17
1.2	Mission Concept . . . . .	18
1.3	Background . . . . .	20
1.3.1	GPS Interferometry . . . . .	20
1.3.2	MM Gyro . . . . .	20
1.3.3	Previous Work . . . . .	21
1.4	GPS Interferometry Theory . . . . .	22
1.5	Thesis Overview . . . . .	28
2	Integer Ambiguity Resolution . . . . .	31
2.1	Introduction . . . . .	31
2.2	Solution Methods . . . . .	32
2.2.1	Code Phase Coupling . . . . .	32
2.2.2	Search Methods . . . . .	32
2.3	Decoupled and Constrained Ambiguity Resolution . . . . .	36
2.3.1	De-coupled Roll Search . . . . .	38
2.3.2	Decision Metric . . . . .	42
2.3.3	Roll Solution . . . . .	43
2.4	Performance . . . . .	45
2.4.1	Test Procedure . . . . .	45
2.4.2	Results . . . . .	46
3	Error Characterization . . . . .	49
3.1	Introduction . . . . .	49
3.2	GPS Differential Phase Error . . . . .	49
3.2.1	Overview . . . . .	49

3.3	Error Characterization . . . . .	60
3.3.1	Test Facility . . . . .	60
3.3.2	Calibrated Bias Errors . . . . .	66
3.3.3	Stochastic Errors . . . . .	73
3.3.4	Simulation Parameters . . . . .	83
3.4	Gyro Errors . . . . .	84
3.4.1	Dynamic Models . . . . .	85
3.4.2	Error Parameters for Low Cost Gyros . . . . .	87
4	Filter Design . . . . .	89
4.1	Introduction . . . . .	89
4.2	Filter Equations . . . . .	89
4.3	State Propagation . . . . .	98
4.3.1	Non-Linear Attitude Dynamics . . . . .	98
4.3.2	Linearized Dynamics . . . . .	102
4.4	Measurement Prediction and Update . . . . .	104
4.4.1	Differential Phase . . . . .	104
4.4.2	Gyro Measurement . . . . .	107
4.5	Implementation . . . . .	109
4.5.1	Satellite Selection . . . . .	109
4.5.2	Integrity Monitoring . . . . .	111
5	Linear Covariance Analysis . . . . .	117
5.1	Introduction . . . . .	117
5.2	Sub-Optimal Filter Design . . . . .	117
5.2.1	Implementation . . . . .	119
5.2.2	Error Budget . . . . .	128
5.3	Environment Parameter Variation . . . . .	129
5.4	Sensitivity to Hardware Configuration . . . . .	133

6	Test and Simulation . . . . .	137
6.1	Introduction . . . . .	137
6.2	Simulation . . . . .	137
6.2.1	Environment . . . . .	138
6.2.2	Sensors . . . . .	139
6.2.3	Flight Software . . . . .	141
6.3	Test Cases . . . . .	143
6.3.1	Nominal Test Cases . . . . .	144
6.3.2	Off-Nominal Test Cases . . . . .	147
6.4	Nominal Test Case Results . . . . .	148
6.4.1	Overall Nominal Test Case Results . . . . .	148
6.4.2	Detailed Test Analysis . . . . .	156
6.5	Off-Nominal Test Case Results . . . . .	170
6.5.1	GPS Only Test Case . . . . .	170
6.5.2	High Altitude Test Case . . . . .	171
6.5.3	Multipath Test Cases . . . . .	175
6.5.4	Initial Tumble Test Cases . . . . .	180
6.5.5	Free Drift Test Cases . . . . .	183
6.5.6	Correlated Noise Test Cases . . . . .	188
7	Conclusion . . . . .	193
7.1	Summary of Results . . . . .	193
7.2	Suggestions for Future Work . . . . .	194



# List of Figures

1.1	Iridium Spacecraft . . . . .	19
1.2	GPS Viewing Geometry . . . . .	23
1.3	Delta Range In the Body Frame . . . . .	24
2.1	GPS Measurement Geometry . . . . .	31
2.2	Attitude Search Cost Function . . . . .	35
2.3	Integer Ambiguity Solution Algorithm. . . . .	37
2.4	SNR Constraints for Ambiguity Resolution . . . . .	39
2.5	Measured SNR for 0.6m Array . . . . .	40
2.6	Satellite Geometry Constraint. . . . .	41
3.1	Multipath Geometry . . . . .	52
3.2	Multipath Error on a Single Antenna . . . . .	53
3.3	Multipath Error on Differential Phase. . . . .	53
3.4	Phase Center Variation on a Single Antenna . . . . .	55
3.5	Baseline Error Geometry. . . . .	59
3.6	Test Platform. . . . .	62
3.7	Obstructions. . . . .	63
3.8	Real vs. Expected Phase . . . . .	64
3.9	Measurement Error . . . . .	65
3.10	Distribution of Differential Phase Residuals. . . . .	66
3.11	Total Differential Phase Error (Uncorrected) . . . . .	67
3.12	Phase Error Due to Baseline Expansion . . . . .	68
3.13	Uncorrected Bias Map. . . . .	69
3.14	Uncorrected Bias Model . . . . .	70
3.15	Bias Map After Baseline Correction. . . . .	71
3.16	Total Differential Phase Error (Corrected) . . . . .	71
3.17	Body-Fixed Bias Model . . . . .	72
3.18	Reduction in Differential Phase Error after Calibration . . . . .	73
3.19	Differential Phase Error for Identical GPS Geometry. . . . .	75
3.20	Double Difference Phase Error for Identical GPS Geometry. . . . .	76

3.21	Line Bias RMS Error . . . . .	77
3.22	Line Bias Covariance Contribution . . . . .	77
3.23	PSD of Time Differenced Phase . . . . .	79
3.24	Mean Spectral Density for 40 to 45 ° Elevations . . . . .	79
3.25	Differential Phase White Noise Intensity . . . . .	80
3.26	Standard Deviation of Single Difference Phase . . . . .	80
3.27	Correlated Error Model . . . . .	81
3.28	Receiver Error Contribution . . . . .	82
3.29	Modeled vs. Unmodeled Error Intensity . . . . .	82
3.30	Differential Phase Error Budget . . . . .	83
4.1	LVLH and Body Frames . . . . .	93
4.2	Filter Algorithm . . . . .	97
4.3	Satellite Selection Algorithm . . . . .	111
4.4	Integrity Monitoring . . . . .	115
5.1	Sub-Optimal Filter Analysis . . . . .	119
5.2	1- $\sigma$ Bound for Full Order Filter . . . . .	121
5.3	Nominal $\sigma$ TOT Statistics . . . . .	122
5.4	Simulation: No Gyro Bias State . . . . .	123
5.5	$\sigma$ TOT Statistics: No Gyro Bias State . . . . .	123
5.6	Simulation: No Disturbance Torque State . . . . .	124
5.7	$\sigma$ TOT Statistics: No Disturbance Torque State . . . . .	124
5.8	Simulation: No Correlated Noise State . . . . .	125
5.9	$\sigma$ TOT Statistics: No Correlated Noise State . . . . .	125
5.10	Simulation: No Line Bias State . . . . .	126
5.11	$\sigma$ TOT Statistics: No Line Bias State . . . . .	126
5.12	Simulation: No Baseline Length State . . . . .	127
5.13	$\sigma$ TOT Statistics: No Baseline Length Variation State . . . . .	127
5.14	RSS Attitude Error as a Function of Design Process Noise Intensity . . . . .	128
5.15	Total Attitude Error Budget . . . . .	129
5.16	Satellite Geometry for Linear Analysis . . . . .	130
5.17	Sensitivity to External Torques with Gyros . . . . .	131

5.18	Sensitivity to External Torques without Gyros.....	131
5.19	Sensitivity to Correlated Noise.....	132
5.20	Sensitivity to Line Bias.....	132
5.21	Sensitivity to Baseline Length Error.....	133
5.22	Attitude Error vs. Baseline Length.....	134
5.23	Attitude Error vs. Receiver White Noise Intensity.....	134
5.24	Attitude Error vs. Gyro Random Walk.....	135
5.25	Attitude Error vs. Gyro Bias.....	135
6.1	Simulation Block Diagram.....	138
6.2	Experimental GPS Data Update.....	141
6.3	Control Algorithm.....	143
6.4	Valid GPS Measurements (Experimental Data).....	149
6.5	Valid GPS Measurements (Simulated Data).....	150
6.6	ADOP (Experimental Measurements).....	152
6.7	ADOP (Simulated Measurements).....	152
6.8	RSS Attitude Error Distribution (Experimental Data).....	153
6.9	RSS Attitude Error Distribution (Simulated Data).....	156
6.10	Nominal Case 13E Attitude History.....	159
6.11	Nominal Case 13E.....	160
6.12	Nominal Case 13E True Correlated Noise State.....	161
6.13	Nominal Case 13E Correlated Noise State Error.....	162
6.14	Analysis of Roll Error Using Correlated Noise.....	163
6.15	Nominal Case 05S Attitude History.....	165
6.16	Nominal Case 05S.....	166
6.17	Nominal Case 11E Attitude History.....	168
6.18	Nominal Case 11E.....	169
6.19	Attitude Error with and without Gyros.....	170
6.20	High Altitude Test Case 02S-H.....	173
6.21	High Altitude Performance With and Without Gyros.....	174
6.22	Sensitivity to Multipath Error.....	176
6.23	Effect of Multipath on Attitude Solution.....	177

6.24	Interaction of Multipath and Correlated Noise . . . . .	179
6.25	Tumble Recovery Case 5 . . . . .	182
6.26	Tumble Recovery Case 3 . . . . .	183
6.27	True Attitude for Test 02E-FD . . . . .	184
6.28	Free Drift Test Case 02E-FD . . . . .	185
6.29	Attitude Error for Tests 07E-FD and 07E-FDG . . . . .	187
6.30	Attitude Error with and without Correlated Noise Estimation . . . . .	189
6.31	Attitude Error With No Correlated Noise with and without Correlated Noise Estimation . . . . .	191

# List of Tables

1.1	Iridium Attitude Determination Requirements . . . . .	19
1.2	Evolution of GPS Attitude Determination Filters . . . . .	21
2.1	Integer Solution Performance for the Nominal Configuration . . . . .	46
2.2	Conditions Surrounding Successful and Failed Integer Resolution . . . . .	46
2.3	Ambiguity Solution Computational Time Comparison . . . . .	47
2.4	Off-Nominal Array Size Ambiguity Solution Performance . . . . .	48
2.5	Integer Solution Performance for Orbit Simulation . . . . .	48
3.1	Ground Based and Space Based Error Parameters . . . . .	84
5.1	Covariance Analysis Initial Position	120
5.2	Covariance Analysis Error Parameters . . . . .	120
5.3	Attitude Error Budget . . . . .	129
6.1	Nominal Simulation Parameters . . . . .	145
6.2	Nominal Error Parameters . . . . .	146
6.3	GPS Validity Statistics . . . . .	151
6.4	Nominal Attitude Error Statistics (Experimental Data) . . . . .	153
6.5	Attitude Errors (Simulated Data) . . . . .	155
6.6	RSS Attitude Errors, Test 02S-G . . . . .	171
6.7	High Altitude RSS Attitude Error with and without Gyros . . . . .	174
6.8	Multipath Corrupted RSS Error with and without Gyros . . . . .	180
6.9	Tumble Test Initial Conditions . . . . .	181
6.10	Free Drift RSS Attitude Error with and without Gyros . . . . .	188
6.11	RSS Attitude Error with and without Correlated Noise Estimation . . . . .	190
6.12	RSS Attitude Error with No Correlated Noise . . . . .	191



# Chapter 1

## Introduction

Before the turn of the century, nearly 300 satellites will be launched into low-Earth-orbit (LEO) or medium-Earth-orbit (MEO) [5]. Much of this proliferation is driven by the current boom in commercial satellite telecommunications. The latest entries, including Iridium, Globalstar, Ellipso and Teledesic, are constellations which utilize large numbers of small, low cost satellites to provide global personal communications service (GPCS). With ambitious production schedules and a simultaneous need to cut costs and maintain performance, satellite systems technology must be improved to keep pace with this growth in potential missions.

Attitude determination is one of these critical technologies. Driven by the needs of the payload and support systems, most satellites require pointing knowledge to within at least a few degrees. For a communications satellite, proper orientation of the main antenna array is essential to mission success, and usually requires attitude pointing accuracy on the order of  $0.5^\circ$  [20].

### 1. 1 Objectives

The objective of this thesis is to design an autonomous Global Positioning System (GPS) based attitude determination system (ADS) which meets performance requirements for a variety of low cost satellites including the most recent entries into the multi-satellite telecommunications market.

The design must meet cost, performance and reliability criteria. Hardware costs for the ADS are minimal given the widespread availability of GPS hardware and the selection of a low cost gyro system for the analysis. Attitude estimation performance should meet mission requirements for a typical LEO communications satellite. Reliability is traditionally the main obstacle in the development of a dedicated GPS based attitude determination system [26][17]. Because of this, GPS has never been used as the sole source of attitude information on an operational satellite. To prove

reliability, the ADS must demonstrate consistent attitude acquisition for a wide range of initial conditions. Following acquisition, the attitude error must remain bounded for all expected orbit positions and vehicle attitudes.

The proposed ADS uses a combination of three or more GPS antennas and a three axis gyro assembly (TGA). A tightly coupled filtering approach is used, meaning that GPS and gyro measurement dynamics are incorporated into a single non-linear system. The filter inputs are gyro measurements and raw GPS phase observables. Loosely coupled designs treat GPS and gyro measurements separately. The inputs to a loosely coupled design are independent attitude estimates from the GPS receiver and the TGA.

Initialization of the filter requires solution of the GPS integer ambiguity, a problem which is addressed in Chapter 2. The solution method developed in this thesis uses geometric constraints and a decoupling of the roll Euler angle estimate to speed determination of the integers. Reliability of the algorithm is critical to viability of the ADS, so it is tested independently as well as in the orbital simulation.

## 1. 2 Mission Concept

The Iridium system is relatively mature among GPCS proposals. First launch of an Iridium satellite occurred in May of 1997, and operational capability is targeted for late 1998 [16]. The configuration of Iridium has been finalized, so it is used as a test platform for the ADS design. The Iridium constellation is designed to provide global coverage for ground-based wireless telephone users. Coverage is accomplished using six orbit planes, each with 11 satellites in near-polar orbit at an altitude of 421 nm. The main spacecraft bus is a triangular prism small enough to allow launch of 5 satellites simultaneously on the Delta II rocket. The main mission antennas, which extend outward from the body, are deployed with the solar arrays after separation from the

launcher [12]. Figure 1.1 shows the Iridium spacecraft in its deployed configuration:

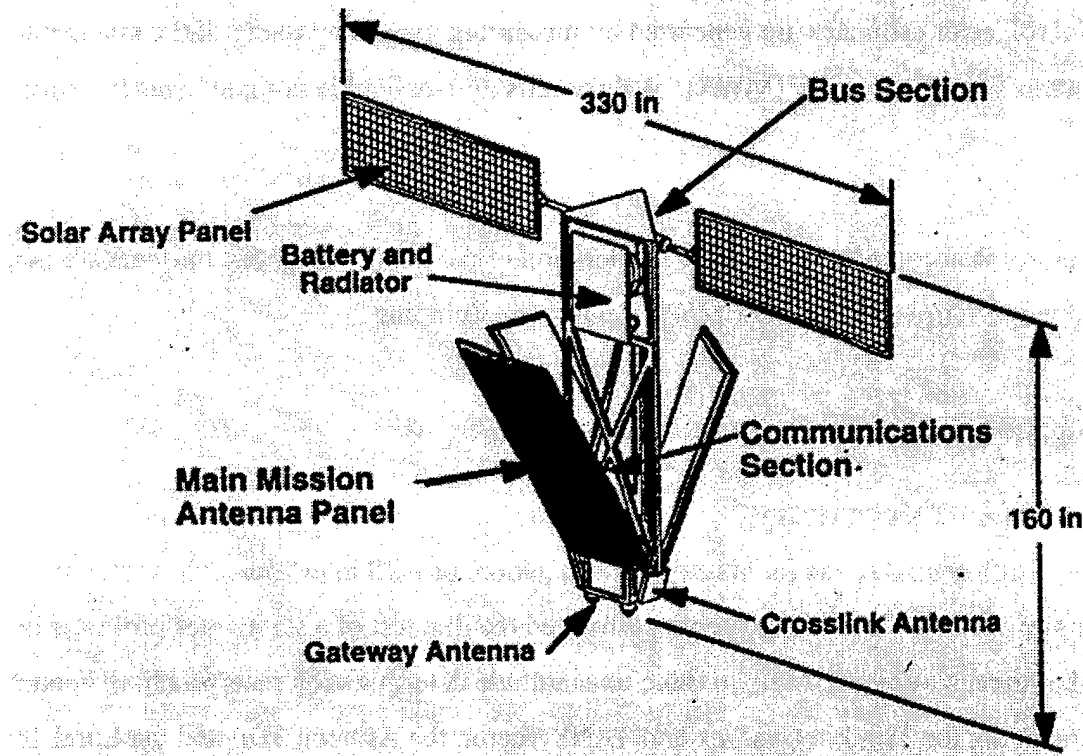


**Figure 1.1: Iridium Spacecraft**

Attitude determination is critical to the mission of Iridium. The solar panels must be sun-oriented to generate power, and the main mission antennas must be nadir-pointing to provide the proper communications footprint. Preliminary attitude determination requirements are shown in table 1.1:

Axis	3- $\sigma$ Pointing Requirement
Yaw	0.4°
Pitch	0.3°
Roll	0.2°

**Table 1.1: Iridium Attitude Determination Requirements**

The definition of 3- $\sigma$  used here is 99.74% probability.

The Iridium satellite uses a traditional attitude determination sensor suite which provides a contrast to the proposed ADS. A coarse horizon sensor is used for earth acquisition immediately after launch. After establishment of a nadir-pointing orientation using seven on-board Reaction Engine

Assemblies, an assembly of fine horizon sensors are used for precise pitch and roll determination. Yaw and roll error estimates are generated by measuring gyrocompassing of the single pitch axis Momentum Wheel Assembly (MWA). A three-axis gyro assembly complements the horizon sensors.

Pitch control is accomplished through acceleration of the MWA; magnetic torquers are used for roll and yaw control as well as for MWA momentum dumping.

## 1. 3 Background

### 1.3.1 GPS Interferometry

The use of differential phase for attitude determination, or GPS interferometry, was first proposed by Spinney in 1976. Texas Instruments performed the first test of a static interferometer in 1981. Since that time, several commercial three-axis attitude determination receivers have been developed, including the Trimble Quadrex and TANS Vector, the Ashtech 3DF and the Loral Tensor. Interferometry has also been demonstrated for ground-based, ship-based and aircraft operation. Recent tests have explored the use of interferometry for space-based attitude determination: the US Air Force RADCAL satellite carries a Trimble Quadrex 4-antenna interferometer [26], and NASA flew a 4-antenna Loral Tensor on a 1996 Space Shuttle mission [17].

All of the commercially available GPS attitude determination systems use a least squares point solution for attitude. This means that each attitude solution is calculated using only the current epoch of measurements - previous attitude knowledge is discarded. The focus of interferometry research in recent years has shifted to filtering of the attitude solution to achieve superior performance over the least squares solution.

### 1.3.2 MM Gyro

The ADS design incorporates measurements from a low quality gyro system to aid the GPS attitude solution. The gyro model used in this investigation is based on performance of a micromachined tuning fork gyro. This micro-mechanical (MM) gyro is the subject of current research at the C. S. Draper Laboratory [19]. MM gyros are well suited for satellite applications because of

their low power consumption, light weight and compact size. Advanced manufacturing techniques also make mass production, and hence low unit cost, a possibility.

### 1.3.3 Previous Work

Table 1.2 outlines the recent evolution of GPS attitude determination filters which are closely related to the proposed ADS:

Year	1994 [11]	1994 [6]	1995 [15]	1995 [26]	1996 [22]
Researcher	Fujikawa	Chesley, Axelrad	Howell, Tang	Stohl	Montgomery
Axes	3	3	1	3	3
Application	Space	Space	Ground	Space	Aircraft
Gyro	No	Yes	Yes	No	Yes
Tightly Coupled	No	No	Yes	No	Yes
Testing	Simulated	Simulated	Simulated	Simulated	Experimental
GPS Error Model	White	White	White	Colored	White

**Table 1.2: Evolution of GPS Attitude Determination Filters**

Fujikawa presents an efficient two-antenna interferometer design for LEO spacecraft in [11]. The design uses a single baseline aligned with the vehicle roll axis. Rotation about a single baseline is unobservable to the GPS differential phase observable, so the filter must estimate roll through dynamic coupling with yaw and pitch. Simulated accuracy is on the order of  $0.1^\circ$  using a white noise error model for GPS.

Chesley and Axelrad have focussed on integration of multiple sensors for the JAWSat small satellite. In [6], least-squares attitude output from the Vector receiver with an associated covariance estimate is used as one input to the Kalman Filter. This is referred to as a loosely coupled design because the GPS and gyro measurement error covariances are treated separately to arrive at two independent estimates of the attitude before integration.

The tightly coupled integration of Howell and Tang uses a single GPS baseline to augment the heading accuracy of an INS for static applications. Montgomery [22] applies the tightly coupled GPS-gyro strategy to a highly dynamic aircraft platform. Through gyro aiding, the filter bandwidth is increased, and the coupled system is flight tested. Attitude propagation through a 20 second loss of GPS visibility is demonstrated.

In [26], Stohl models GPS baseline length error, line bias and multipath using first order exponentially correlated random variables (ECRV). Simulation results for the USAF RADCAL satellite predict an RMS attitude error of 0.3-0.5 degrees on each axis using conservative error models.

This thesis will refine the error models presented in [26], incorporate tightly coupled measurements from a micro-mechanical gyro and test the ADS design using experimental data collected from a TANS Vector receiver.

## 1. 4 GPS Interferometry Theory

The objective of attitude determination is to estimate orientation of a body with respect to a known reference frame. GPS accomplishes this task by precisely determining the relative positions of three or more body-fixed antennas in the reference frame. Although the standard GPS position solution could be differenced to produce relative position, code phase accuracy is limited to about 30 meters, so a 30 meter antenna baseline would be required to attain accuracy on the order of one radian. The solution is to use GPS carrier phase. Carrier phase tracking allows the GPS receiver to measure L1 signal phase with an accuracy better than  $10^\circ$ . Differencing of phase at two antennas produces a measurement of relative range to the GPS satellite with sub-centimeter

accuracy. Figure 1.2 illustrates this principle. Here,  $\Delta r$  is the relative range.

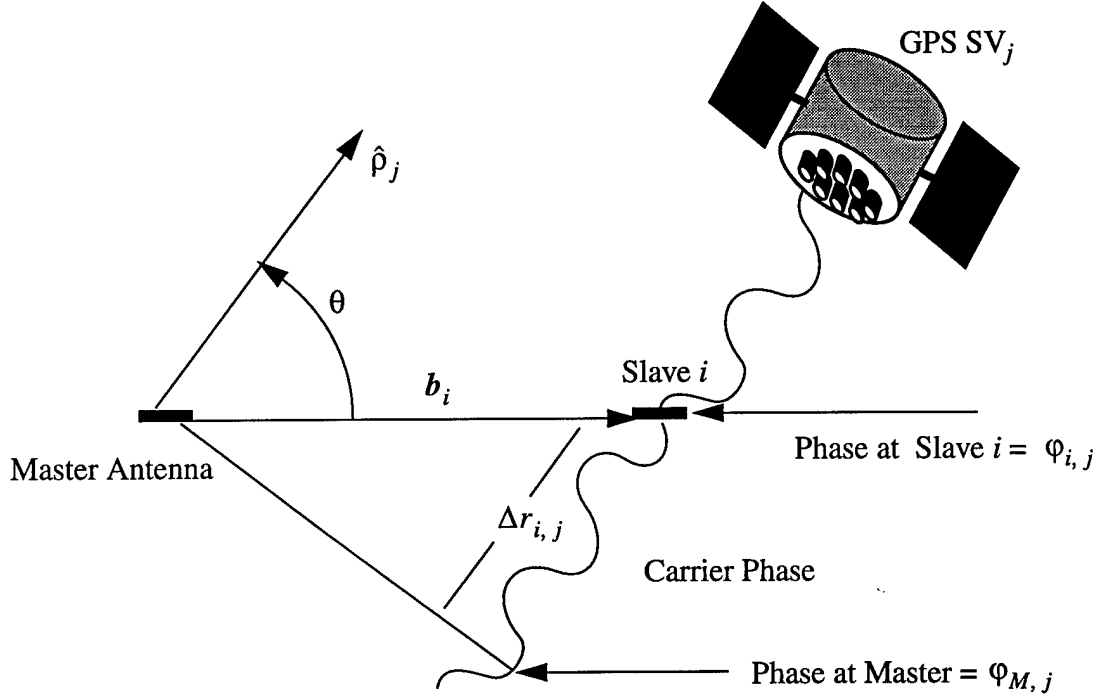


**Figure 1.2: GPS Viewing Geometry**

$\Delta r_{i,j}$  is the projection of the baseline vector  $b_i$  onto the line-of-sight (LOS) vector  $\hat{p}_j$  for the GPS satellite (SV) on channel  $j$ :

$$\Delta r_{i,j} = b_i^T \cdot \hat{p}_j = |b_i| \cdot \cos(\theta) \quad 1.1$$

$\theta$  is the aspect angle between the  $b_i$  and  $\hat{p}_j$ . The baseline  $b$  and delta range  $\Delta r$  are expressed in L1 wavelengths for convenience.

Delta range can be represented graphically as a function of the GPS LOS vector in the body frame. In figure 1.3, the horizontal plane denotes the azimuth and elevation to a GPS SV. For any given SV, the point on the tilted plane immediately above or below the SV body azimuth and ele-

vation represents delta range for the measurement on baseline  $\mathbf{b}$  from that SV.

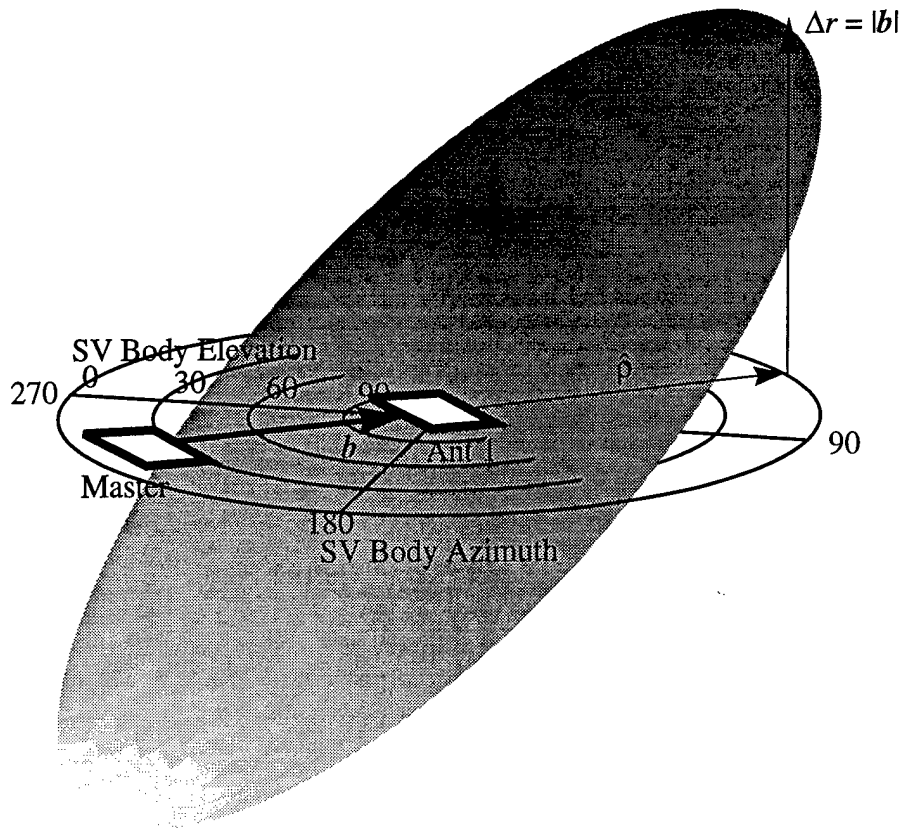


**Figure 1.3: Delta Range In the Body Frame**

Notice that the maximum delta range occurs when the GPS LOS vector is colinear with the baseline vector. In this case, the baseline is aligned at an azimuth of  $45^\circ$  and elevation  $0^\circ$  in the body frame, so an SV on the body frame horizon (the horizon is defined as  $0^\circ$  elevation) and  $45^\circ$  azimuth produces a delta range of  $|\mathbf{b}|$ , the length of the baseline. A satellite directly overhead or orthogonal to the baseline vector produces a delta range of zero.

Differential phase,  $\Delta\phi_{i,j}$ , is the primary observable for GPS interferometry.  $\Delta\phi_{i,j}$  is the difference between slave antenna carrier phase,  $\phi_{i,j}$  and master antenna carrier phase,  $\phi_{M,j}$ . Absolute phase from the GPS satellite is unknown, so each phase measurement  $\phi_{i,j}$  contains an unknown integer number of carrier wavelengths,  $k_{i,j}$ . The resulting relationship between measured phase and differential range is shown in equation 1.2:

$$\Delta r_{i,j} = (\phi_{M,j} + k_{M,j}) - (\phi_{i,j} + k_{i,j}) - \varepsilon_{i,j} \quad 1.2$$

$\Delta\varphi_{i,j}$  differs from delta range by the integer ambiguity  $\Delta k_{i,j}$ . It is also corrupted by various errors in the received signal, which are combined into the common term  $\varepsilon_{i,j}$ . If the integer ambiguity  $\Delta k$  can be solved, we can construct a measurement of  $\Delta r$  according to equation 1.3.

$$\Delta r_{i,j} = \Delta\varphi_{i,j} + \Delta k_{i,j} - \varepsilon_{i,j} \quad 1.3$$

Solving for  $\Delta\varphi_{i,j}$  and substituting for  $\Delta r$  from equation 1.1 yields the measurement equation, which will be used frequently in this text:

$$\Delta\varphi_{i,j} = \mathbf{b}_i^T \cdot \hat{\mathbf{p}}_j - \Delta k_{i,j} + \varepsilon_{i,j} \quad 1.4$$

### Least Squares Solution

The attitude determination problem is solved here by estimating the direction cosine matrix (DCM),  ${}^B\mathbf{C}^N$ , which relates the body frame ( $B$ ) to the navigation frame ( $N$ ). To solve for  ${}^B\mathbf{C}^N$ , equation 1.1 is rewritten with the baseline in the body frame and the GPS LOS vector expressed in the navigation frame:

$$\Delta r_{i,j} = (\mathbf{b}_i^B)^T \cdot {}^B\mathbf{C}^N \cdot \hat{\mathbf{p}}_j^N \quad 1.5$$

The solution is straightforward if equation 1.5 can be restated in vector form. To do this, the DCM is first divided into its component rows  $\mathbf{C}_i$ :

$${}^B\mathbf{C}^N = \begin{bmatrix} \cdots {}^B\mathbf{C}_1^N \cdots \\ \cdots {}^B\mathbf{C}_2^N \cdots \\ \cdots {}^B\mathbf{C}_3^N \cdots \end{bmatrix} \quad 1.6$$

The superscripts on the row vectors  ${}^B\mathbf{C}_i^N$  are dropped for clarity:  $\mathbf{C}_i$  implies  ${}^B\mathbf{C}_i^N$  for the remainder of the text.

Substituting the subdivided DCM into equation 1.5,

$$\Delta r_{i,j} = (\mathbf{b}_i^B)^T \cdot \begin{bmatrix} \cdots {}^B\mathbf{C}_1^N \cdots \\ \cdots {}^B\mathbf{C}_2^N \cdots \\ \cdots {}^B\mathbf{C}_3^N \cdots \end{bmatrix} \cdot \hat{\mathbf{p}}_j^N \quad 1.7$$

This leads to a vector form of the attitude determination problem with nine unknowns:

$$\Delta r_{i,j} = \begin{bmatrix} \mathbf{b}_{i,I}^B(\hat{\mathbf{p}}_j^N)^T & \mathbf{b}_{i,J}^B(\hat{\mathbf{p}}_j^N)^T & \mathbf{b}_{i,K}^B(\hat{\mathbf{p}}_j^N)^T \end{bmatrix} \begin{bmatrix} \mathbf{C}_1^T \\ \mathbf{C}_2^T \\ \mathbf{C}_3^T \end{bmatrix} = \mathbf{H} \begin{bmatrix} \mathbf{C}_1^T \\ \mathbf{C}_2^T \\ \mathbf{C}_3^T \end{bmatrix} \quad 1.8$$

$\mathbf{b}_{i,I}^B$  is the  $\hat{X}$  component of  $\mathbf{b}_i$  in the body frame and  $\mathbf{H}$  is the measurement matrix.

The least squares solution for  ${}^B\mathbf{C}^N$ , shown in equation 1.9, can be solved with a vector of measurements  $\Delta\mathbf{r}$  from a single epoch. This is the solution generated by receivers such as the TANS Vector:

$$\begin{bmatrix} \hat{\mathbf{C}}_1^T \\ \hat{\mathbf{C}}_2^T \\ \hat{\mathbf{C}}_3^T \end{bmatrix} = (\mathbf{H}^T \mathbf{H})^{-1} \mathbf{H}^T \Delta\mathbf{r} \quad 1.9$$

Although attitude is completely determined by three Euler rotations, there are nine unknowns in equation 1.8, so nine measurements are required to compute a linear solution. In practice, this number can be reduced to six if the antennas are coplanar. A body frame is chosen such that the baselines have no  $\hat{Z}$  component, removing measurement dependence on the last three components of the DCM:

$$\Delta r_{i,j} = \begin{bmatrix} \mathbf{b}_{i,I}^B(\hat{\mathbf{p}}_j^N)^T & \mathbf{b}_{i,J}^B(\hat{\mathbf{p}}_j^N)^T & 0(\hat{\mathbf{p}}_j^N)^T \end{bmatrix} \begin{bmatrix} \mathbf{C}_1^T \\ \mathbf{C}_2^T \\ \mathbf{C}_3^T \end{bmatrix} = \begin{bmatrix} \mathbf{b}_{i,I}^B(\hat{\mathbf{p}}_j^N)^T & \mathbf{b}_{i,J}^B(\hat{\mathbf{p}}_j^N)^T \end{bmatrix} \begin{bmatrix} \mathbf{C}_1^T \\ \mathbf{C}_2^T \end{bmatrix} \quad 1.10$$

The constraint of orthogonality on  ${}^B\mathbf{C}^N$  is used to estimate  $\mathbf{C}_3$  based on  $\hat{\mathbf{C}}_1$  and  $\hat{\mathbf{C}}_2$ :

$$\hat{\mathbf{C}}_3^T = \hat{\mathbf{C}}_1^T \times \hat{\mathbf{C}}_2^T \quad 1.11$$

Of course, the first two row estimates must first be normalized and made orthogonal by removing any linear dependence between the estimates.

The least squares solution covariance for unit intensity white sensor noise can be found by manipulation of equation 1.9. This “dilution of precision,” or  $DOP$ , is a function of the measurement sensitivity  $\mathbf{H}$ :

$$DOP_C = \sqrt{diag(\mathbf{H}^T \mathbf{H})^{-1}} \quad 1.12$$

Here,  $diag(\mathbf{x})$  is a vector consisting of the diagonal components of  $\mathbf{x}$ . If the differential phase measurement noise is white, with intensity  $\sigma_v$ ,  $DOP$  can be used to find the variance of the DCM components,

$$\sigma_{^B\mathbf{C}^N(i)} = DOP_C(i) \cdot \sigma_v \quad 1.13$$

where  $^B\mathbf{C}^N(i)$  is the  $i$ th row-wise element of the DCM.

Although the point solution is simple to implement, it is poorly suited to closed loop control applications because of high frequency noise. In addition, a point solution does not allow for estimation of error sources and integration with other sensors. For these reasons, an Extended Kalman Filter (EKF) implementation is chosen for this application. The EKF makes a one-step prediction of attitude based on the current attitude estimate and an *a priori* system model. This prediction is updated using any available sensor measurements. The prediction and update are optimal in the mean-square error sense, and dynamic sensor errors such as gyro biases can be estimated in real time. The result is a better steady state performance than the least squares solution. The least squares solution, however, will still be needed for solution of the integer ambiguity,  $\Delta k_{i,j}$ . This is presented in chapter 2.

### Single Difference Operator

The procedure of subtracting slave antenna phase from master antenna phase is represented by the

single difference operator:

$$\begin{bmatrix} \Delta\varphi_{1,1} \\ \Delta\varphi_{2,1} \\ \Delta\varphi_{1,2} \\ \Delta\varphi_{2,2} \\ \dots \end{bmatrix} = \begin{bmatrix} 1 & -1 & 0 & 0 & 0 & 0 \\ 1 & 0 & -1 & 0 & 0 & 0 \\ 0 & 0 & 0 & 1 & -1 & 0 \\ 0 & 0 & 0 & 1 & 0 & -1 \\ \dots & & & & & \end{bmatrix} \cdot \begin{bmatrix} \varphi_{M,1} \\ \varphi_{1,1} \\ \varphi_{2,1} \\ \varphi_{M,2} \\ \varphi_{1,2} \\ \varphi_{2,2} \\ \dots \end{bmatrix} = SD \cdot \begin{bmatrix} \varphi_{M,1} \\ \varphi_{1,1} \\ \varphi_{2,1} \\ \varphi_{M,2} \\ \varphi_{1,2} \\ \varphi_{2,2} \\ \dots \end{bmatrix} \quad 1.14$$

Equation 1.14 shows the single difference operator for baselines 1 and 2 tracking satellites 1 and 2. The single difference operator is used extensively in chapter 3 to derive the differential phase error characteristics.

Note also that the differential phase vector is listed first by baseline and then by channel, so:

$$\underline{\Delta\varphi} = \left[ \Delta\varphi_{1,1} \ \Delta\varphi_{2,1} \ \dots \ \Delta\varphi_{n_{BL},1} \ \Delta\varphi_{2,1} \ \dots \ \Delta\varphi_{n_{BL},n_{CH}} \right]^T \quad 1.15$$

Here,  $n_{BL}$  is the number of baselines and  $n_{CH}$  is the number of channels.

## 1. 5 Thesis Overview

This chapter presented the objectives of this thesis and a background on GPS interferometry. In Chapter 2, “Integer Ambiguity Resolution” on page 31, an efficient integer solution algorithm is developed for initialization of the attitude filter.

Chapter 3, “Error Characterization” on page 49, present derivation of error models for GPS and gyro measurements and experimental determination of error parameters for a multi-antenna GPS receiver.

Chapter 4, “Filter Design” on page 89, details design of an Extended Kalman Filter based on the error models of chapter 3. The filter uses tightly coupled GPS and gyro measurements to estimate spacecraft attitude, angular rates and gyro biases.

In Chapter 5, “Linear Covariance Analysis” on page 117, a linear covariance analysis is used to choose a reduced order Kalman Filter design and evaluate the sensitivity of the filter to environmental and hardware parameter variations.

Chapter 6, “Test and Simulation” on page 137, presents results of ADS performance using a computer simulation. The system is tested for the nominal Iridium orbit as well as off-nominal test cases using experimental and simulated error data.

Chapter 7, “Conclusion” on page 193, discusses conclusions of this investigation and suggestions for future research.



# Chapter 2

## Integer Ambiguity Resolution

### 2. 1 Introduction

Figure 2.1 illustrates the one-axis attitude determination problem. In this example, the carrier phase at antenna 1 and the carrier phase at the master antenna are separated by two whole carrier wavelengths. This number is referred to as the integer ambiguity. GPS carrier phase tracking provides a measurement of fractional phase at the antenna, so the integer ambiguity is not directly observable. Here, the phase measurement at both antennas is zero degrees, resulting in a differential phase of zero degrees. The true aspect angle,  $\theta_1$ , has a corresponding delta range  $\Delta r = 2.0$  carrier wavelengths and an integer ambiguity of +2. Another possible orientation,  $\theta_2$ , is indicated by the dashed line. Delta range for this orientation is  $\Delta r = 1.0$ , resulting in an integer ambiguity of +1. It is impossible to estimate the attitude until this integer ambiguity is resolved.

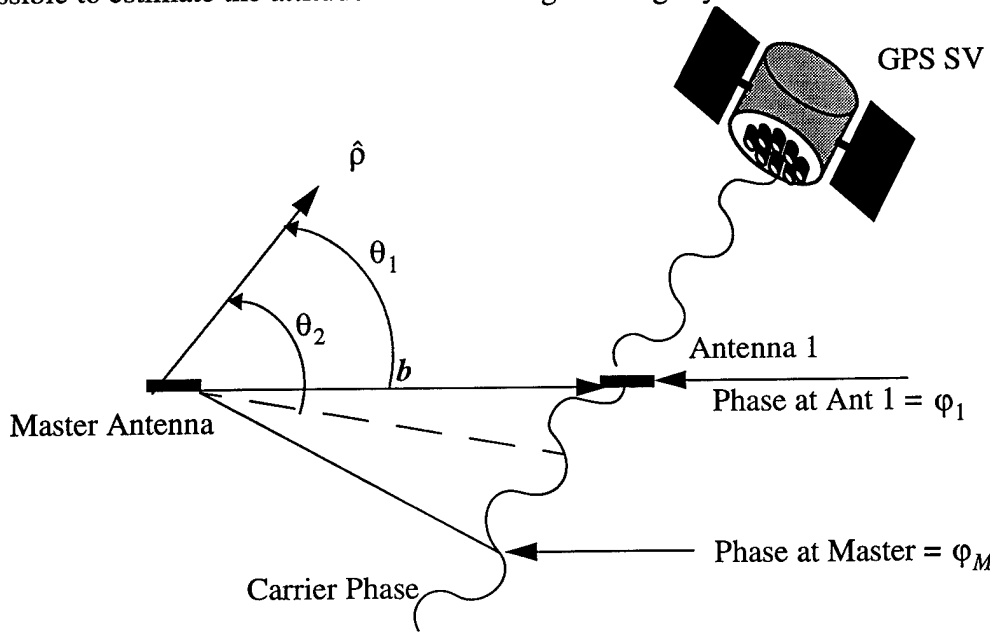


**Figure 2.1: GPS Measurement Geometry**

This chapter addresses the problem of integer ambiguity in the GPS differential phase measurement. After reviewing the measurement geometry, an overview of common ambiguity solution methods is presented in section 2. 2. Section 2. 3 presents the algorithm developed for this application.

cation, which incorporates geometric constraints and decoupling of the roll solution to streamline the ambiguity solution. Performance of the algorithm is evaluated in section 2.4.

## 2. 2 Solution Methods

### 2.2.1 Code Phase Coupling

The integer ambiguity problem is essentially a high precision relative positioning problem. Because GPS code phase is already used in the receiver to generate position estimates, these estimates can be used to aid in the integer solution process. Various filtering algorithms have been developed to accomplish this [8], but aiding requires a long period of solution smoothing to reduce position uncertainty to the 1/2-cycle level. Code phase coupling is best suited to very long baseline applications with limited dynamics such as surveying.

### 2.2.2 Search Methods

For smaller baselines, integer solution is possible using a single epoch of measurements. To do this, some redundancy is required in the measurements. In equation 1.10, we saw that the three-axis attitude equation can be reduced to a sixth order linear problem.

$$\Delta r_{i,j} = \begin{bmatrix} \mathbf{b}_{i,I}^B (\hat{\mathbf{p}}_j^N)^T & \mathbf{b}_{i,J}^B (\hat{\mathbf{p}}_j^N)^T \end{bmatrix} \begin{bmatrix} \mathbf{C}_1^T \\ \mathbf{C}_2^T \end{bmatrix} \quad 1.10$$

This equation is still overdetermined, because the first two rows of the DCM must satisfy the orthonormality constraint:

$$\hat{\mathbf{C}}_i^T \cdot \hat{\mathbf{C}}_j = \delta(i, j) \quad 2.1$$

This constraint provides the information needed to solve the integer ambiguity. The following paragraphs illustrate two of the most common methods for doing this, i.e. the integer search and the attitude search.

#### Integer Search

The integer search method chooses a trial vector of integer ambiguities and adds these to the actual measurement to form a trial vector of measurements  $\Delta\mathbf{r}'$  [10], where the prime indicates that  $\Delta\mathbf{r}'$  may not be the actual delta range. The least squares solution  ${}^B\hat{\mathbf{C}}^N$  is computed for each

possible set of integers. Because equation 1.10 is uniquely determined, the solution will appear to be perfect:

$$\Delta\mathbf{r}' - (\mathbf{b}^B)^T \cdot {}^B\hat{\mathbf{C}}^N \cdot \hat{\mathbf{p}}^N = \mathbf{0} \quad 2.2$$

However, the orthonormality constraint in equation 2.1 may not be satisfied. To select the correct solution, the DCM estimate is first orthonormalized using an algorithm such as the singular value decomposition:

$${}^B\hat{\mathbf{C}}^N = SVD({}^B\hat{\mathbf{C}}^N) \quad 2.3$$

The measurement residual cost function is then calculated to evaluate the merit of this set of integers. This cost function is a scalar parallel to Wahba's cost function for vector observables [8]:

$$J({}^B\hat{\mathbf{C}}^N, \Delta\mathbf{r}') = \sum_{i=1}^m \sum_{j=1}^n [\Delta\mathbf{r}'_{ij} - (\mathbf{b}_i^B)^T \cdot {}^B\hat{\mathbf{C}}^N \cdot \hat{\mathbf{p}}_j^N]^2 \quad 2.4$$

The vector of integers  $\Delta\mathbf{r}'$  and the attitude matrix  ${}^B\hat{\mathbf{C}}^N$  which minimize  $J$  are chosen as the best solution.

The integer search requires resolution of six integers to estimate the attitude matrix in this manner. This leads to  $(2N)^6$  potential integer sets, where  $N$  is the baseline length in GPS wavelengths. Obviously the problem quickly becomes intractable for large baselines, especially since an orthonormalization is required for each integer set. Various algorithms have been proposed to streamline this process [6], but the computational burden is still excessive when a fast solution is required.

### Attitude Search

The attitude search method scans potential attitudes rather than potential phase integers. The idea is to rotate the attitude around a grid of possible roll, pitch and yaw combinations and calculate the expected differential phase at each of these attitudes:

$$\Delta\mathbf{r}'_{i,j} = (\mathbf{b}_i^B)^T \cdot {}^B\mathbf{C}_k^N \cdot \hat{\mathbf{p}}_j^N \quad 2.5$$

Here,  ${}^B\mathbf{C}_k^N$  is a trial attitude. Notice that the normality constraint does not need to be applied in

this case; the trial attitude matrix is orthonormal by construction. For the true attitude and attitudes very close to the truth, the fractional phase prediction will nearly match the actual phase measurement:

$$fractional(\Delta\phi_{i,j} - \Delta\phi'_{i,j}) \approx 0 \quad 2.6$$

The “*fractional*” operation removes the integer part of the difference. All that remains is to choose the best trial attitude using a modification of the cost function in equation 2.4:

$$J(\mathbf{C}_k^N, \Delta\mathbf{r}') = \sum_{i=1}^m \sum_{j=1}^n (fractional[\Delta\phi_{ij} - \Delta\phi'_{i,j}])^2 \quad 2.7$$

For the correct attitude matrix, the fractional error will only contain measurement noise.

The difficulty with an attitude search is that, as baseline length grows, higher resolution is required in choosing trial attitudes to ensure that the true attitude is not passed over.

Consider a one axis example. A test is conducted using the geometry in figure 2.1, with one 3-wavelength (0.57 m) baseline and two satellites in the plane, so the measurements are only dependent on the rotation angle  $\theta$ . White noise with intensity 5 mm is added to both of the measurements, and the cost function of equation 2.7 is calculated using an angle increment of six degrees. Figure 2.2 shows the ability of the cost function to pick out the correct rotation angle, which is  $60^\circ$  in this case. The vertical axis is the figure of merit  $fom = 1/J$ , so the highest peak corresponds to minimum cost. The first two plots show the figure of merit for each of the measurements separately. Obviously, neither satellite alone is sufficient to specify the attitude, but the two measurements together pinpoint the correct solution, as shown in the third plot.

Notice that the second highest peak in the total *fom* graph, at  $320^\circ$ , is nearly equal in magnitude to the true peak. This indicates that any more noise or a search with a larger rotation interval might

cause a false solution.

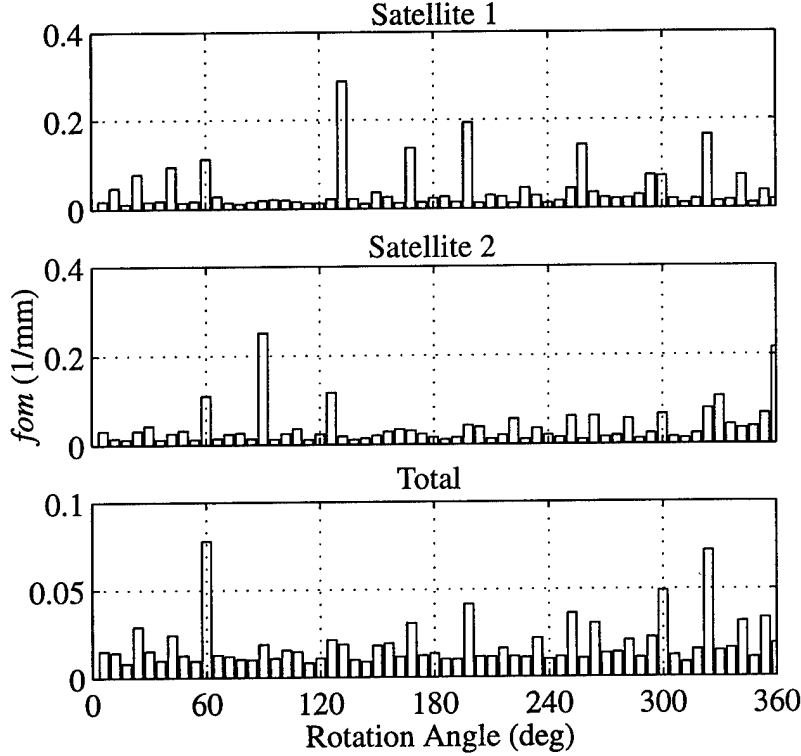


**Figure 2.2: Attitude Search Cost Function**

Solution of the three dimension attitude problem is much more complex than the one dimensional case. Finding an efficient way to grid the three dimensional space of possible orientations without missing the true attitude is a challenge of its own. If a sequence of Euler rotations is used, with 60 steps per axis (as in the example), there are  $60^3 = 216000$  attitudes to check. At each potential attitude, the cost is generated using equation 2.7. In general, the search grid must contain  $(360/\theta_0)^3$  points, where  $\theta_0$  is the angular resolution needed to differentiate the true attitude from other potential solutions. The resolution angle  $\theta_0$  becomes smaller as the length of the baseline grows, so the computation time required to reach a solution becomes excessive for long baselines.

A more recent adaptation of the attitude search method is the maximum likelihood method [29]. Instead of using the cost function in equation 2.7, these methods use a maximum likelihood func-

tion:

$${}^B\hat{C}^N = \frac{\iiint C(\phi, \theta, \psi) \cdot \left( \prod_i \left( \prod_j p(\Delta\phi_{ij} | C(\phi, \theta, \psi)) \right) \right) d\phi \ d\theta \ d\psi}{\iiint \left( \prod_i \left( \prod_j p(\Delta\phi_{ij} | C(\phi, \theta, \psi)) \right) \right) (d\phi \ d\theta \ d\psi)} \quad 2.8$$

Here,  $C(\phi, \theta, \psi)$  is the direction cosine matrix for the Euler angles  $\phi$ ,  $\theta$ , and  $\psi$ .  $p(\bullet)$  is the differential phase residual probability operator:

$$p(\Delta\phi_{ij} | C(\phi, \theta, \psi)) \equiv p(v = \text{fractional}[\Delta\phi_{ij} - (b_i^B)^T (C(\phi, \theta, \psi) \cdot \hat{p}_j^N)]) \quad 2.9$$

$$v \sim N(0, \sigma_\epsilon) \quad 2.10$$

where  $\sigma_\epsilon$  is the standard deviation of the differential phase error,  $\epsilon$ .

Mathematically, this method extracts the most useful data out of the measurements, but in practice it is quite cumbersome. The triple integration of probability is just as computationally intensive as the standard attitude search method. The key benefit of this method is that it is nearly fail-safe. The likelihood function ensures that the integers eventually converge, and it also guarantees graceful degradation of the attitude solution if a number of measurements become invalid.

## 2. 3 Decoupled and Constrained Ambiguity Resolution

The decoupled and constrained ambiguity resolution method (DCAR) developed for this application is based on the integer search technique. Three modifications to the integer search are made to reduce the number of possible integer sets and minimize the computation time required to reach a solution. The most important change is the decoupling of the three dimensional problem into a two axis solution and a one axis solution. Next, geometry constraints are used to eliminate unreasonable integer sets. Finally, orthogonality constraints are imposed to choose the best solution.

Figure 2.3 shows the solution algorithm:

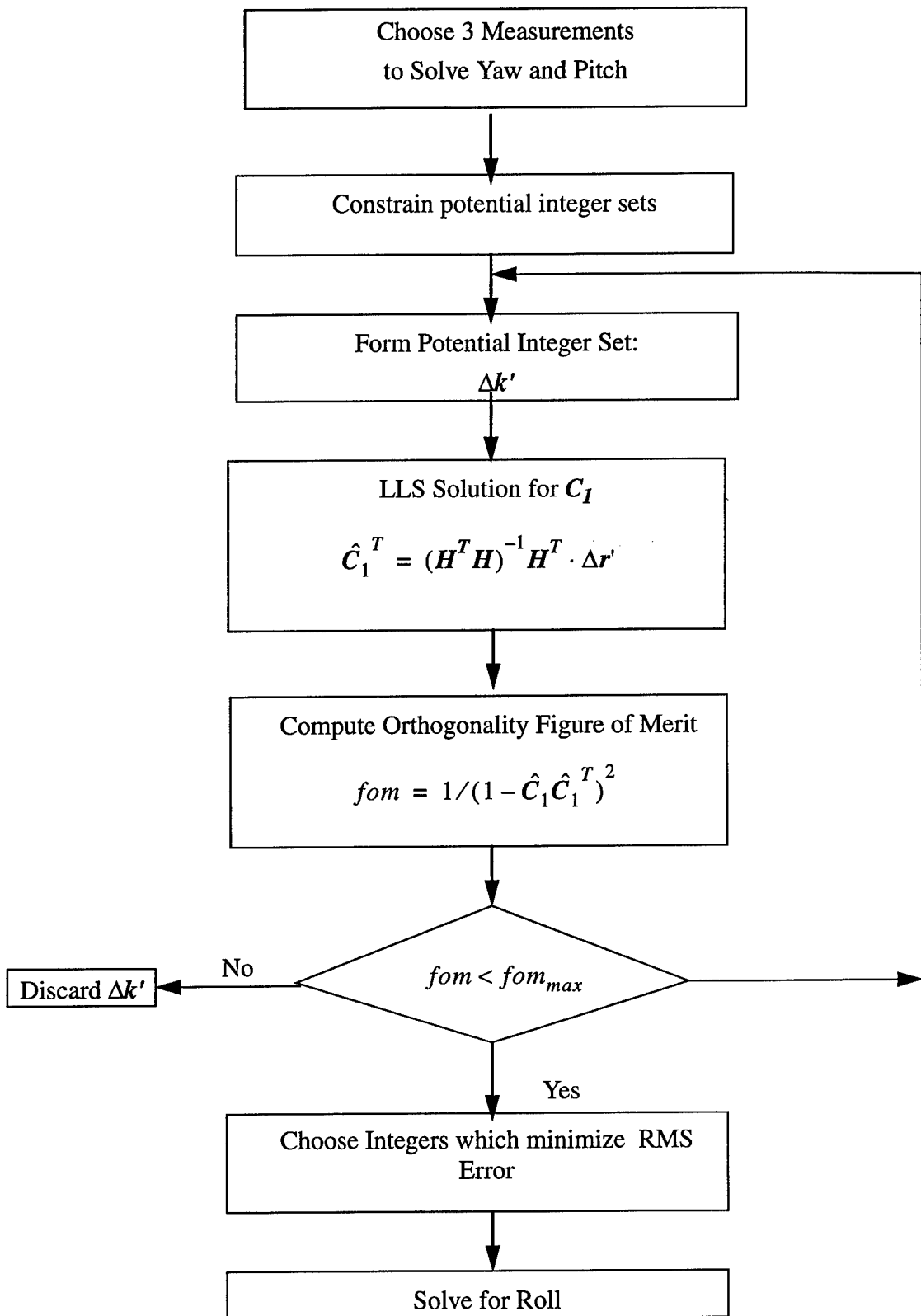


Figure 2.3: Integer Ambiguity Solution Algorithm

### 2.3.1 De-coupled Roll Search

A closer examination of equation 1.5 reveals a simple solution to the complexity of the three axis attitude problem. If the body frame is defined with one baseline ( $\mathbf{b}_1$ , for example) aligned with the first axis,  $\hat{X}$ , measurements from baseline 1 are dependent only on the first row of the DCM ( $\mathbf{C}_1$ ), and an explicit solution for  $\mathbf{C}_1$  is possible with just three measurements.

The measurements on this antenna are *invariant* to roll rotations, decoupling roll from the measurement equation. This relative positioning problem has  $(2N)^3$  possible solutions which can be further constrained by satellite geometry. Once this problem is solved, only the roll angle must be resolved. Solution of roll requires estimation of  $\mathbf{C}_2$ , resulting in a maximum of  $[(2N)^3 + (2N)^3]$  potential solutions, rather than the  $(2N)^6$  possibilities for a traditional three axis solution.

#### Choosing a set of Measurements

To solve the two dimensional problem, all measurements must come from one baseline. If the body frame  $\hat{X}$  axis is aligned with baseline 1, then the measurement matrix has 3 columns:

$$\Delta r_{1,j} = \left[ \mathbf{b}_{1,I}^B (\hat{\rho}_j^N)^T \right] \mathbf{C}_1^T = \mathbf{H}_{1,j} \mathbf{C}_1^T \quad 2.11$$

$\mathbf{H}_{1,j}$  is the measurement matrix for measurement  $\Delta r_{1,j}$ . Three measurements are needed to solve the three degrees of freedom, and there is a single normality constraint:

$$|\hat{\mathbf{C}}_i| = 1 \quad 2.12$$

Three satellites are chosen to produce a well-conditioned measurement matrix  $\mathbf{H}_1$ . To do this, a set of satellites is chosen which minimizes the total of the dot products between satellites according to equation 2.13:

$$J(k) = \sum_{j=1, j \neq k}^{n_{CH}} (\hat{\rho}_k \cdot \hat{\rho}_j^T)^2 \quad 2.13$$

$J(k)$  is the dot product “cost” for the satellite on channel  $k$ . Three channels are chosen with minimum total cost. This picks out satellites which are most nearly orthogonal to each other.

### Constraining Integer Sets

The objective of this step is to produce the minimum set of possible integers which is guaranteed to include the true vector of integers. This step exploits the fact that the baseline and satellite geometries are known *a priori*. For instance, the maximum measurement magnitude on a baseline is produced when the satellite LOS vector is collinear with the baseline vector. This constrains the absolute value of each measurement on baseline number  $i$  to  $b_i$ , where  $b_i$  is the baseline length in wavelengths.

The second constraint on the measurements comes from the SNR. Satellites at high elevations with respect to the body frame and local frame will have stronger SNR than low elevation satellites. Measured SNR is used to bound the possible elevation of a satellite in the body frame, with a confidence interval determined from experimental data:

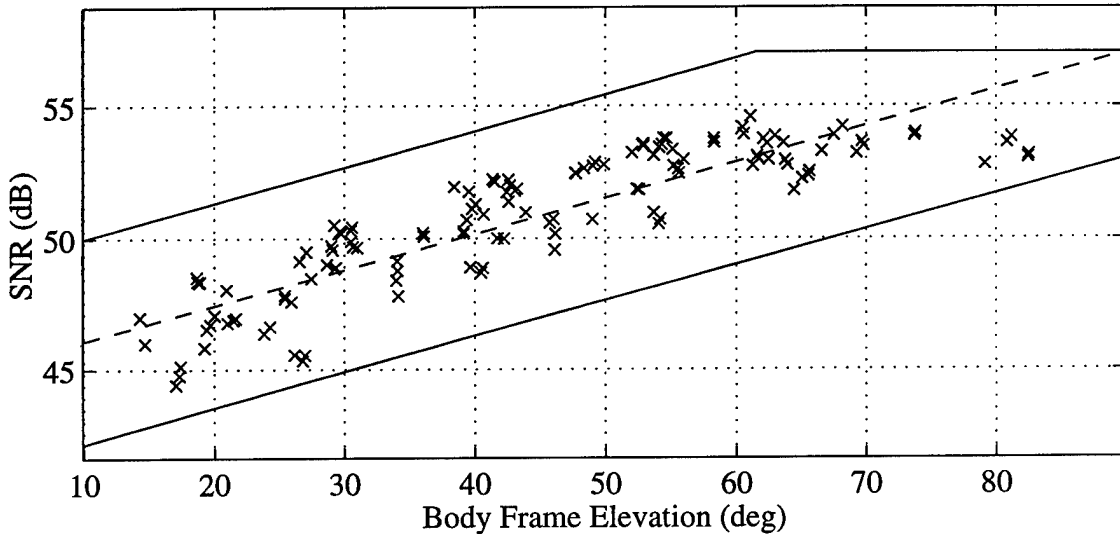


**Figure 2.4: SNR Constraints for Ambiguity Resolution**

The data shown here was collected using a static four antenna Trimble receiver on multiple days. The SNR forms an excellent linear fit to elevation. Unfortunately, the SNR characteristics are dependent on array geometry and the type of ground plane used. Consider the data in figure 2.5, taken at the same location with an array size of 60 cm rather than the 40 cm size used for figure

2.4:

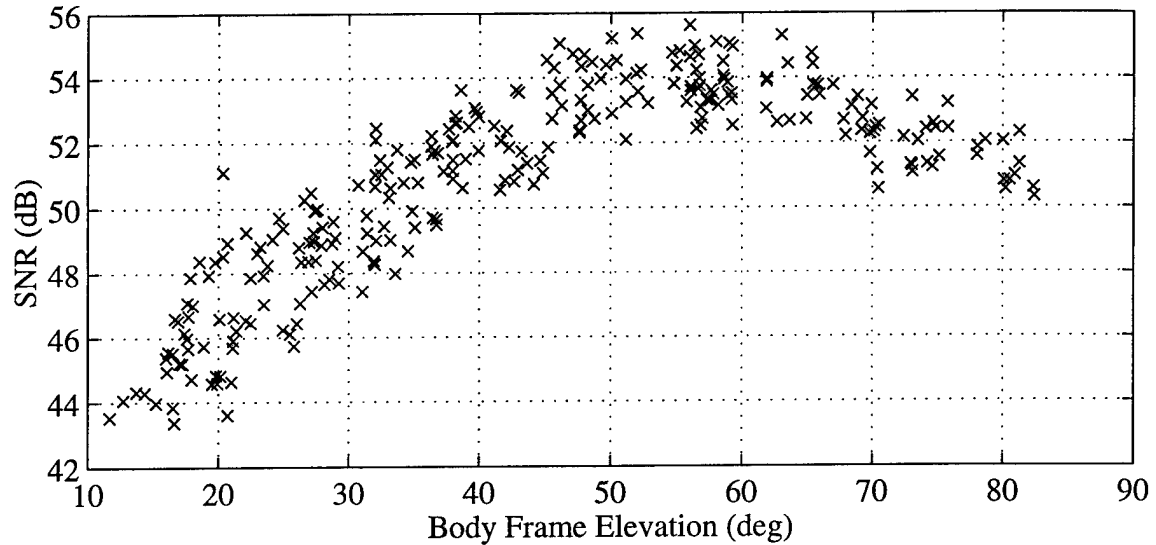


**Figure 2.5: Measured SNR for 0.6m Array**

This data displays a non-linear relationship between elevation and SNR which is not one to one. The SNR can still be used to bound satellite elevation, but the bound is less tight for this configuration.

The SNR constraint imposes a minimum elevation angle of the satellite with respect to the baseline vector. This leads to a maximum direction cosine between the baseline and satellite. The maximum measurement is simply  $(b_i \cdot \max(\cos(\theta)))$ , where  $b_i$  is the length of the baseline and  $\theta$  is the SNR elevation constraint.

All three measurements used to solve for the yaw and pitch share a common baseline. Figure 2.6

shows how this fact can be manipulated to further constrain the measurements.

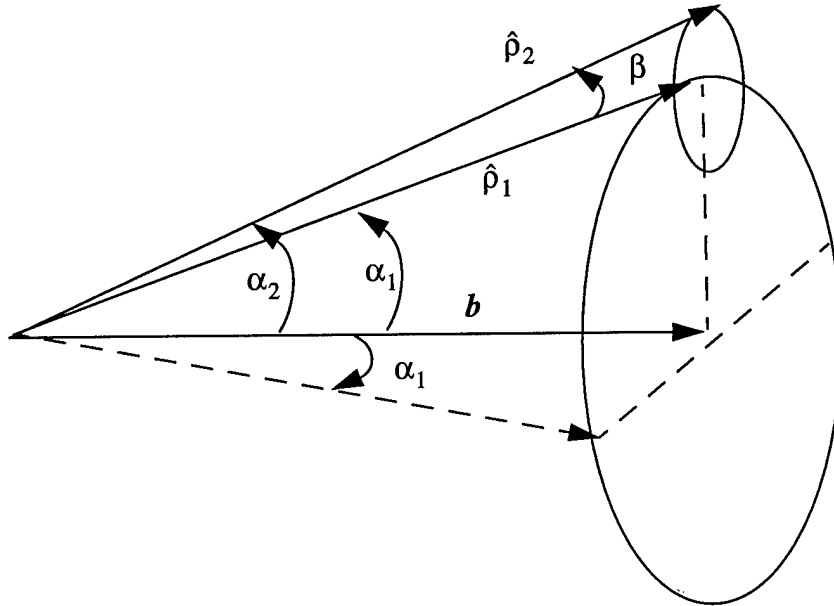


**Figure 2.6: Satellite Geometry Constraint**

$\hat{p}_1$  and  $\hat{p}_2$  are the LOS vectors to satellites 1 and 2, respectively. When forming a vector of possible measurements, the trial measurement from satellite 1,  $\Delta r'_{1,1}$ , determines the aspect angle between the baseline and the LOS vector:

$$\alpha_1 = \arccos((\Delta r'_{1,1})/b_1) \quad 2.14$$

If  $\alpha_2$  is the unknown angle between  $b_1$  and  $\hat{p}_2$  and  $\beta$  is the known angle separating  $\hat{p}_1$  and  $\hat{p}_2$ , then  $\alpha_2$  is geometrically constrained by  $\alpha_1$  and  $\beta$ :

$$(\alpha_1 - \beta) \leq \alpha_2 \leq (\alpha_1 + \beta) \quad 2.15$$

The constraint on  $\alpha_2$  restricts the possible range of measurements from satellite two,  $\Delta r'_{1,2}$ , according to the measurement equation:

$$\Delta r'_{1,2} = b_2 \cdot \cos(\alpha_2) \quad 2.16$$

These bounds are theoretically tight, but there is noise present in the measurements. The noise causes small errors in the estimated angle,  $\alpha_1$ , so equation 2.15 is not “tight”. It is necessary to loosen the bounds slightly to avoid creating bounds on  $\Delta r'_{1,2}$  which disqualify the true measurements.

### Form Integer Set

Once the bounds for measurement  $m$  have been defined given possible measurements  $1, \dots, (m-1)$ , the possible values of the integer  $\Delta k_{1,m}$  can be determined:

$$\min(\Delta r_{1,m}) \leq \Delta \varphi_{1,m} + \Delta k_{1,m} \leq \max(\Delta r_{1,m}) \quad 2.17$$

$$\text{ceil}[\min(\Delta r_{1,m}) - \Delta \varphi_{1,m}] \leq \Delta k_{1,m} \leq \text{floor}[\max(\Delta r_{1,m}) - \Delta \varphi_{1,m}] \quad 2.18$$

The *ceil* operator rounds up to the nearest integer. *floor* rounds down to the nearest integer.

### Least Squares Solution

The LLS estimate of  $\mathbf{C}_1$  is computed for each set of possible measurements according to equation 2.19.

$$\hat{\mathbf{C}}_1^T = (\mathbf{H}_1^T \mathbf{H}_1)^{-1} \mathbf{H}_1^T \Delta \mathbf{r} \quad 2.19$$

Since the measurement matrix  $\mathbf{H}_1$  is independent of the true integers, it is only computed once.

The residuals will be identically 0 since there are three measurements and three unknowns.

#### 2.3.2 Decision Metric

The conventional method of orthonormalizing each solution before calculating residuals is overkill for the problem at hand. Orthonormalization makes all of the possible solutions *look* like real solutions, regardless of whether they are correct. In reality, only the true direction cosine matrix will be orthonormal, so the “degree” of orthonormality can be used as a figure of merit for each potential integer set. For the single row  $\mathbf{C}_1$ , the “degree” of normality is defined by the cost function  $J$ :

$$J(\hat{\mathbf{C}}_1) = (1 - \hat{\mathbf{C}}_1 \hat{\mathbf{C}}_1^T)^2 \quad 2.20$$

The expected covariance of the solution  $\hat{\mathbf{C}}_1$  is calculated using the one axis dilution of precision and the measurement error intensity  $\sigma_\epsilon$ :

$$\sigma_{\mathbf{C}_1(i)} = DOP_{\mathbf{C}_1}(i) \cdot \sigma_\epsilon \quad 2.21$$

The covariance estimate is used to form a cost threshold for  $J$ . This eliminates most of the erroneous potential integers.

If more than one potential integer set remains, each least squares solution of  $\mathbf{C}_1$  is used to construct expected measurements on baseline 1 for the remaining  $n_{CH}-3$  satellites according to equation 2.11:

$$\hat{\Delta r}_{1,j} = \mathbf{b}_1^B \cdot \hat{\mathbf{C}}_1^T \cdot (\hat{\rho}_j^N) \quad 2.11$$

These predicted measurements are compared to the measured differential phase, and an RMS cost is calculated using equation 2.7. Once again, a maximum cost can be calculated using the expected covariance of the solution  $\hat{\mathbf{C}}_1$ , and solutions with RMS error greater than the maximum are discarded. In testing, there is occasionally more than one valid solution at this point. Because the roll solution is very fast, the algorithm solves roll for each of the potential solutions of  $\mathbf{C}_1$  and a best solution is chosen based on which complete solution leads to the smallest RMS errors with the incorporation of all valid satellites.

### 2.3.3 Roll Solution

Solving for the roll angle of the body frame requires estimation of the second row of the DCM. The yaw and pitch solution only needs three measurements to estimate the first row of the DCM because the first baseline is aligned with the body  $\hat{X}$  axis, removing measurement dependence on the rest of the DCM. If the second baseline is aligned with the  $\hat{Y}$  axis, the roll solution is also limited to three ambiguities by using a roll axis parallel to equation 2.11:

$$\Delta r_{2,j} = \left[ \mathbf{b}_{2,j}^B (\hat{\rho}_j^N)^T \right] \mathbf{C}_2^T = \mathbf{H}_{2,j} \mathbf{C}_2^T \quad 2.22$$

However, the requirement of orthogonal baselines is a bit restrictive. To get around this, a “pseudo-orthogonal” baseline is created by using the yaw and pitch estimate of  $\mathbf{C}_1$  to remove dependence of measurements  $\Delta r_{2,j}$  on  $\mathbf{C}_1$ . The starting point is the measurement equation for the measurement on baseline 2:

$$\Delta r_{2,j} = \left[ \mathbf{b}_{2,I}^B (\hat{\rho}_j^N)^T \quad \mathbf{b}_{2,J}^B (\hat{\rho}_j^N)^T \right] \begin{bmatrix} \mathbf{C}_1^T \\ \mathbf{C}_2^T \end{bmatrix} \quad 1.10$$

The component of each measurement which is dependent on the  $\hat{X}$  axis component of baseline 2 is removed using the estimate of  $\mathbf{C}_1$ :

$$\Delta r_{2,j} - \left[ \mathbf{b}_{2,I}^B (\hat{\mathbf{p}}_j^N)^T \right] \left[ \hat{\mathbf{C}}_1^T \right] \approx \left[ \mathbf{b}_{2,J}^B (\hat{\mathbf{p}}_j^N)^T \right] \left[ \mathbf{C}_2^T \right] \quad 2.23$$

A further reduction in the number of ambiguities to be solved is garnered by including the DCM orthogonality requirement explicitly in the measurement equation:

$$0 = \left[ \hat{\mathbf{C}}_1 \right] \left[ \mathbf{C}_2^T \right] \quad 2.24$$

The complete measurement matrix is now:

$$\mathbf{H}_2 = \begin{bmatrix} \hat{\mathbf{C}}_1 \\ \mathbf{b}_{2,J}^B (\hat{\mathbf{p}}_{j_1}^N)^T \\ \mathbf{b}_{2,J}^B (\hat{\mathbf{p}}_{j_2}^N)^T \end{bmatrix} \quad 2.25$$

The first integer, which corresponds to the orthogonality condition, is always 0. The possible integers for measurements 2 and 3 are constructed in a manner identical to the yaw and pitch solution. As a result, less than  $(2N)^2$  integer sets are searched. The least squares solution for  $\mathbf{C}_2$  for each of the possible measurement vectors is always perfect because of the square measurement matrix. Once again, normality of each solution is checked using the figure of merit in equation 2.20. A figure of merit criteria is calculated based on the expected solution covariance, and solutions not meeting this criteria are discarded.

An RMS error test is conducted on the possible integer solutions which remain using methods similar to the yaw and pitch solution.

If more than one solution remains, a subset of the possible solutions is chosen using a quadrant check. The quadrant check eliminates any integer solutions for which valid satellites are below the estimated antenna “horizon”, the plane in which the antennas are mounted. The surviving solution with minimum RMS error is picked as the best solution.

## 2. 4 Performance

The performance of an integer ambiguity solution method is measured by the speed with which a solution is computed and the reliability of the solution.

### 2.4.1 Test Procedure

The receiver for this application is configured with six channels and four antennas in a 1m square planar array mounted on the zenith (top) face of the satellite. In theory, the integer ambiguity solution requires a minimum of two baselines and three channels to operate. However, the key to the success of the RMS check used in section 2.3.2 is the availability of redundant measurements to calculate the merit of solutions which pass the first figure of merit. In practice, a minimum tracking capability of five channels is needed when using this algorithm.

The integer solution performance test aims to mimic the actual conditions under which the algorithm must successfully operate. The test is conducted by attempting a filter “cold start” at random positions at the Iridium orbit altitude of 800 km. It is assumed that the spacecraft will separate from the launch vehicle in an unknown attitude with some slow initial angular velocity due to tip off. At some point after release, the top face of the satellite should pass within about 30° of zenith (this is addressed in more detail in section 6.5.4). To model this, each initialization is attempted with the spacecraft yaw, pitch and roll chosen at random from a uniform distribution spanning -30° to +30°.

For each set of random initial conditions, a single epoch of measurements is fed to the integer solution algorithm. If a successful solution is reached, a new random position is chosen. If not, the orbit and attitude is propagated forward for one second using the simulation framework developed in section 6.2.1 and another solution attempt is made with the next epoch of measurements. The procedure is continued until a correct solution is reached.

The nominal tests use the 1m array for which the algorithm is designed. To display the flexibility of the algorithm, the tests are repeated using smaller and larger arrays.

## 2.4.2 Results

### Nominal Configuration

Nominal results for the 1m array size are summarized in table 2.1. 1000 random initial conditions were used to generate the data:

Attitude	First Attempt Success (%)	Average Epochs Required	Average CPU Time (sec)	3- $\sigma$ Number of Epochs	Maximum Number of Epochs
Local Level	93.00	1.2230	0.6229	13.0000	20.0000
Off-Level (30°)	87.40	1.4510	2.3088	13.0000	81.0000

**Table 2.1: Integer Solution Performance for the Nominal Configuration**

First attempt success is the percentage of solution attempts which resulted in the correct ambiguity solution on the first epoch. Average epochs required is the average number of trials required to solve the ambiguity with a corresponding average CPU time. CPU time is for execution of the algorithm in a Matlab script on a Sun UNIX workstation. The 3- $\sigma$  and maximum number of epochs give an indication of the worst case number of trials required to reach a solution.

The results indicate that an initial fix should occur within 13 epochs with 99.74% certainty in the local level attitude. 3- $\sigma$  performance is identical for attitudes up to 30° from the nominal. However, the off-nominal case requires more average computation time. The maximum number of epochs needed also increases for the off-level case. The reason for this has to do with superior satellite availability and measurement quality in the local level attitude. The first two columns of table 2.2 show a comparison of the average number of satellites available for successful fixes and failed fixes for each of the attitudes:

True Attitude	Average Number of Good Satellites		Maximum Measurement Residual (mm)	
	Good Fix	Bad Fix	Good Fix	Bad Fix
Local Level	5.1470	4.5964	12.5622	11.4196
Off-Level (30°)	5.0840	4.2661	13.5571	15.2948

**Table 2.2: Conditions Surrounding Successful and Failed Integer Resolution**

A satellite is defined as “available” if it is visible and all measurements from the satellite are valid.

Measurement validity is discussed in section 6.4.1. Average availability for the failed fixes is significantly less than the availability for successful solutions. This demonstrates that solution quality is a function of the number of available satellites. Notice that satellite availability is generally lower for the off-level case. This is one cause of the increased computation time.

The last two columns of table 2.2 show the average maximum measurement residual on measurements used to compute the integer solution. The maximum residual for the off-level case is consistently larger than for the nominal. This can also increase computation time, because multiple yaw and pitch solutions may appear valid. According to the algorithm, a roll solution must be computed for each of the valid yaw/pitch solutions to locate the true solution.

### Computation Time

The greatest benefit of the DCAR algorithm is reduced computation time. Table 2.3 compares computation time of a standard integer search algorithm to that of the DCAR algorithm:

	Integer Search	Constrained	Uncoupled	DCAR
Order of Computations	$(2N)^6$	$N^6$	$(2N)^3$	$N^3$
CPU Time (sec)	33067	516.7	4.13	0.52

**Table 2.3: Ambiguity Solution Computational Time Comparison**

The results shown are for one epoch of measurements on a 1m square antenna array. The constrained and uncoupled approaches both show a vast improvement over the standard integer search technique, and combination of the two in the DCAR algorithm reduces computation time to under one second. The order of computations for the constrained search is an approximation, because the ability to constrain integers is dependent on the GPS geometry.

### Off-Nominal Array Size

Performance of the integer ambiguity solution must be satisfactory for a range of array sizes. The off-level ambiguity tests are repeated here for a 0.6m and a 2.0m square array to examine sensitiv-

ity of the solution algorithm to array size.

True Attitude	1st Attempt Success (%)	Average Epochs Required	Average CPU Time	Number Epochs 3- $\sigma$	Maximum Epochs
0.6m Off-Level	94.09	1.0909	0.6045	3	8
1m Off-Level	87.40	1.4510	2.3088	13	81
2m Off-Level	63.82	4.4236	15.6649	102	167

**Table 2.4: Off-Nominal Array Size Ambiguity Solution Performance**

Longer baselines produce more potential integer sets, so the increase in average computation time is expected. The decreased success rate and consequential increase in the maximum number of epochs required to reach a solution is also due to an increase in the number of possible integer sets. The large number of possible attitudes increases the chance that another attitude will look as good as the true solution in terms of the orthogonality of the DCM solution. This can lead to a false solution. The average CPU time is much larger than for the 1m case, but the time required is still a matter of seconds. Re-tuning of validity thresholds in the algorithm might result in performance improvements for the 2m array.

## Simulation Results

Each of the orbital simulation test cases in Chapter 6 uses the DCAR solution algorithm during initialization. The DCAR performance results are shown in table 2.5:

GPS Error Data	Success (%)	Maximum Epochs
Experimental	100.00	1
Simulated	95.00	2

**Table 2.5: Integer Solution Performance for Orbit Simulation**

Performance of the DCAR algorithm meets or exceeds expectations. All of the 40 nominal test cases start in a near local-level attitude; each time, a successful ambiguity resolution is reached within two epochs of the first measurement. As table 2.5 shows, a good solution is reached on the first attempt in 39 of the 40 cases. The single failure occurs when using simulated measurement errors. The filter integrity monitoring algorithm, developed in section 4.5.2, detects this error and another integer search is commanded. The second attempt results in a successful attitude fix.

# Chapter 3

## Error Characterization

### 3. 1 Introduction

The performance of a Kalman Filter is critically dependent on system modeling. Uncertainty in the plant or error model can lead to sub-optimal performance or instability of the filter. This chapter presents models of GPS and gyro measurement errors for use in design of the Kalman filter.

The first section provides an overview of error sources in the GPS differential phase measurement. Dynamic models and measurement sensitivities are presented for each of the primary GPS error sources. In section 3. 3, experimental data is used to determine model parameters which accurately reflect the nature of differential phase error in a GPS receiver. A calibration model is also constructed to mitigate receiver-specific errors which are caused by phase center variation and body-fixed multipath sources.

Section 3. 4 details the primary error sources for a strapdown gyro. Dynamic error models are developed for use in the Kalman filter design, and an overview of low cost gyro systems is presented.

### 3. 2 GPS Differential Phase Error

Most interferometric GPS filter designs use a white noise model for differential phase errors [11][4][18][22]. However, errors in the GPS differential phase measurement are spatially and temporally correlated [9][14], and omission of these characteristics from the measurement model leads to degraded operational performance. The purpose of this section is to develop models for GPS differential phase error sources.

#### 3.2.1 Overview

Error can enter the phase measurement at transmission, during atmospheric propagation, at the

antenna pre-amplifier or within the receiver tracking loop. The various sources of error are listed here in the order that they enter the carrier phase signal:

**Troposphere/Ionosphere errors:** Signal phase shift caused by variations in atmospheric density and conductivity during propagation

**Multipath:** Phase error due to reflected signals reaching the antenna.

**Phase Center Variation:** Error due to movement of the electromagnetic center of the antenna.

**Receiver Noise:** Total of errors caused by thermal noise at the antenna and receiver tracking loop errors (phase jitter).

**Line Bias:** Phase delay due to cable path length from antenna to receiver.

**Clock Bias:** Pseudorange error caused by drift in the receiver clock.

**Baseline Length Error:** *Differential* phase error caused by changes in the relative position of two antennas.

Models are developed here for multipath, phase center variation, receiver noise, line bias and baseline length error. Clock bias is not a factor because carrier phase measurement is not based on time synchronization with the GPS SV. Troposphere/Ionosphere errors are negligible due to the small distance (less than 3 meters) between the antennas considered in this investigation.

Atmospheric effects are a function of the path along which the carrier signal travels; due to the relatively close proximity of the antennas, carrier phase signals arrive on nearly identical paths and encounter similar atmospheric properties. Differencing of two signals eliminates any significant atmospheric errors.

The entry of these errors on the differential phase is shown in equation 3.1, which expands equation 1.4 to include all of the modeled errors:

$$\Delta\phi_{i,j} = \mathbf{b}_{i_0}^T \cdot \hat{\rho}_j - \Delta k_{i,j} + \Delta m_{i,j} + \Delta p_{i,j} + \Delta v_{i,j} + \Delta \xi_{i,j} + \Delta \beta_i + \varepsilon_{b_{i,j}} \quad 3.1$$

$\Delta m$  is multipath error on the differential phase.  $\Delta p$  is phase center variation,  $\Delta \xi$  is the correlated component of receiver noise,  $\Delta v$  is the white noise component, and  $\Delta \beta$  is the line bias. These are all additive errors on the phase. Baseline length error,  $\delta b$ , enters the differential phase as a func-

tion of the measurement geometry, as shown in equation 3.2:

$$\varepsilon_b = f_b(\delta b, \hat{p}^B) \quad 3.2$$

The function  $f_b$  is derived in the baseline length error discussion later in this section.

Ideal differential phase is an error free measurement taken from the nominal baseline:

$$\Delta\varphi_{i, j_{IDEAL}} = \mathbf{b}_{i_0}^T \cdot \hat{p}_j - \Delta k_{i, j} \quad 3.3$$

The resulting total measurement error,  $\Delta\varepsilon_{i,j}$ , is defined in equation 3.4:

$$\Delta\varepsilon_{i, j} \equiv \Delta\varphi_{i, j} - \Delta\varphi_{i, j_{IDEAL}} = \Delta m_{i, j} + \Delta p_{i, j} + \Delta v_{i, j} + \Delta\xi_{i, j} + \Delta\beta_i + \varepsilon_{b_{i, j}} \quad 3.4$$

Multipath, phase center variation, receiver noise and line bias are all errors which affect carrier phase before the single difference operation. Errors on differential phase are produced by single differencing:

$$\underline{\Delta e} = \begin{bmatrix} \Delta e_{1, j} \\ \Delta e_{2, j} \end{bmatrix} = SD \cdot \begin{bmatrix} e_{M, j} \\ e_{1, j} \\ e_{2, j} \end{bmatrix} \quad 3.5$$

Here,  $e$  is an arbitrary error on the carrier phase and  $\Delta e$  is the effect of the error on differential phase. The differential phase error is correlated between baselines according to equation 3.6:

$$\Lambda_{\underline{\Delta e}} = E[\underline{\Delta e}^T \cdot \underline{\Delta e}] = SD^T \cdot \Lambda_e \cdot SD = \begin{bmatrix} 2 & 1 \\ 1 & 2 \end{bmatrix} \cdot \sigma_e \quad 3.6$$

$\Lambda_e$  is the covariance of the error  $e$  on undifferenced carrier phase. The differential phase error covariance,  $\Lambda_{\underline{\Delta e}}$ , has two times the variance of the original error and is correlated across baselines. Note that the covariance matrix is block diagonal, since the correlation does not extend between channels.

## Multipath

Multipath is phase error created when a reflected or diffracted carrier wave reaches the GPS

antenna and interferes with the direct signal. Figure 3.1 shows direct and multipath corrupted signals arriving simultaneously at an antenna. The direct signal is referred to as  $S_d$ , while the reflected energy is  $S_m$ :

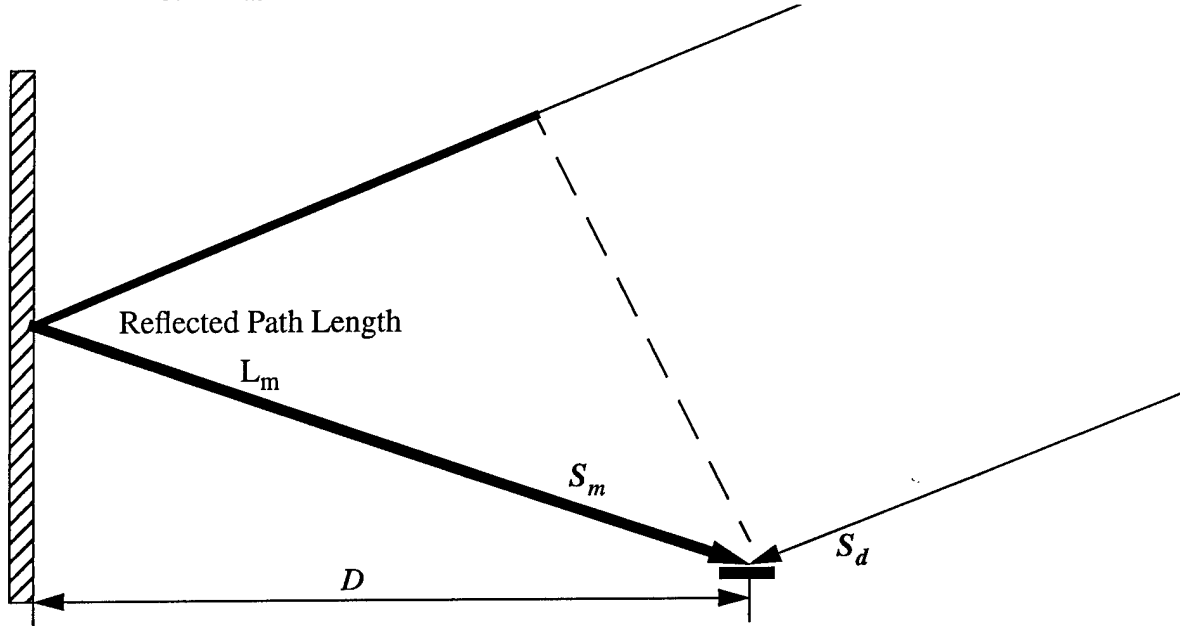


**Figure 3.1: Multipath Geometry**

$D$  is the distance from the antenna to the reflector. The path delay due to reflection,  $L_m$ , is time-varying due to movement of the GPS SV. This causes a frequency shift  $\psi$  in the reflected signal [2]:

$$S_d = A_d \cdot \exp(j\varphi_d) \quad 3.7$$

$$S_m = A_m \cdot \exp(j\varphi_m) = A_m \cdot \exp(j(\varphi_d + \psi)) \quad 3.8$$

$\varphi_d$  and  $\varphi_m$  are the phase of the direct and reflected signals while  $A_d$  and  $A_m$  are their amplitudes. The phase shift  $\psi$  grows as a linear function of time,  $t$ . The rate of growth is dependent on the distance from the antenna to the reflector and the movement of the GPS LOS with respect to the body frame. The growth of  $\psi$  causes a frequency shift in  $S_m$ . When the frequency shifted signal reaches the antenna, interference with the direct phase results in sinusoidal errors in the total phase at the multipath error frequency,  $\omega_m$ . Mullen characterizes this frequency in [23], and finds that the frequency  $\omega_m$  increases with the separation distance  $D$ .

The amplitude of phase errors due to multipath is dependent on strength of the reflected signal and

attenuation of the reflected signal at the antenna. Because the GPS carrier is right hand circularly polarized (RHCP), a single reflection reverses the polarity of multipath radiation. In [23], Mullen demonstrates that a standard dipole GPS antenna attenuates most LHCP radiation at high elevations. The theoretical antenna gain to LHCP signals results in the following profile of multipath phase error as a GPS SV descends from the zenith. The reflector is modeled as a vertical plane 4 meters from the baseline. A baseline length of 1 m is used to generate the error data:

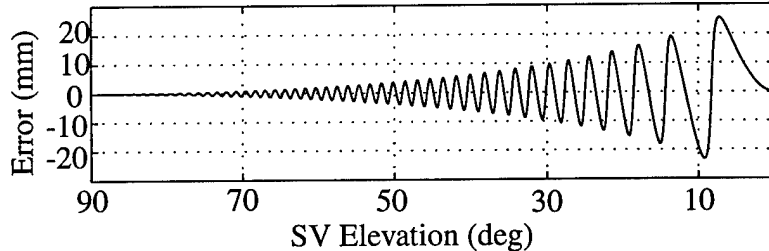


**Figure 3.2: Multipath Error on a Single Antenna**

For the purposes of interferometry, we are interested in the effect of multipath on a second antenna adjacent to the first. The distance to the reflector is unique for each antenna, and the change in distance slightly modifies the multipath error frequency for the second antenna. When phase of the two antennas is differenced, the small frequency offset results in a sinusoidal modulation of the error amplitude:

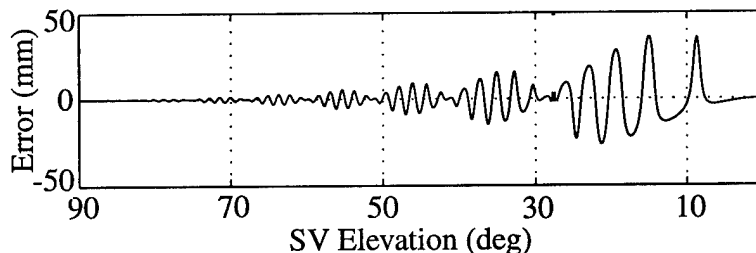


**Figure 3.3: Multipath Error on Differential Phase**

Two sources of multipath are considered in this investigation, environmental sources and body-fixed sources.

Environmental multipath is a greater problem for ground-based receivers than for space-based receivers. Examples of environmental multipath are buildings, ground reflection and other vehicles. The antenna array is not static, so amplitude and frequency of errors caused by environmental multipath are time varying. Environmental multipath sources are usually widely separated from the receiver, resulting in relatively high frequency errors. These characteristics make *a priori*

*ori* modeling of environmental multipath difficult. Axelrad and Comp [3] have had some success modeling environmental multipath through post-processing of SNR data, but a real time multipath mitigation technique has yet to be developed.

In this thesis, a sinusoidal model for environmental multipath is used only to demonstrate the potential effects of multipath on an attitude determination filter. Multipath is modeled as the product of two sinusoids which approximates the behavior shown in figure 3.3. One sinusoid has a period of two minutes and the other has a period of 20 minutes. Maximum error amplitude is 10 mm, and initial phase for each sinusoid,  $\theta_0$ , is chosen from a uniformly distributed random variable.

$$\Delta m_{i,j}(t) = 10 \cdot \sin\left(\frac{2\pi t}{120} + \theta_{0_1}\right) \sin\left(\frac{2\pi t}{1200} + \theta_{0_2}\right) \quad 3.9$$

The parameters for this model are based on a 1 m baseline length, a reflector at a distance of 10 m and a satellite elevation of 30°.

Multipath is an additive error unique to each measurement, so the multipath measurement sensitivity for corrupted measurements is the identity:

$$\frac{\partial \Delta \phi_{i,j}}{\partial \Delta m_{k,l}} = \delta(i, k)\delta(j, l) \quad 3.10$$

Body-fixed multipath is multipath which is caused by nearby reflectors at known locations. The primary sources of body fixed multipath include vehicle appendages and antenna ground planes. In [28], Tranquilla et. al. claim that ground planes can cause phase errors through edge diffraction of the carrier phase. This kind of behavior is characterized as body-fixed multipath. The low frequency and time invariant nature of body-fixed multipath makes it possible to calibrate the resultant differential phase error as a function of the GPS LOS vector in the body frame. Cohen and Parkinson demonstrate virtual cancellation of low frequency multipath errors in [9] using a spherical harmonic error model derived from experimental data. A similar calibration model will be developed for this research and used in the EKF. The calibration cannot capture all of the multipath dynamics, so the receiver noise model will be augmented to account for multipath mismodeling.

### Phase Center Variation

The gain and phase characteristics of a GPS patch antenna are a function of the dielectric substrate which captures the L1 signal [28]. If the substrate is uniform and symmetric, the apparent center of radiation will coincide with the geometric center. Imperfections in the substrate lead to apparent movement of the phase center as a function of the incident angle of the radiated energy. Figure 3.4 depicts the phase error,  $p$ , caused by this movement.

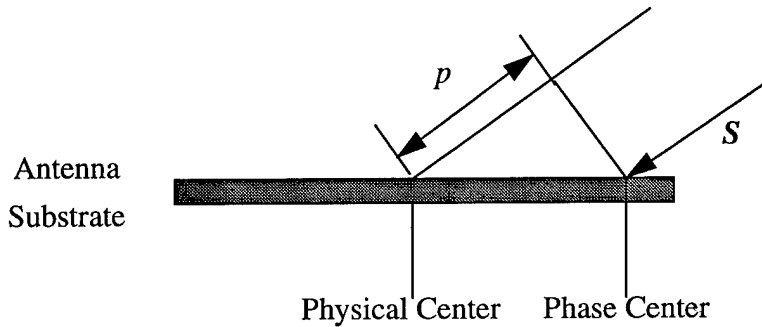


**Figure 3.4: Phase Center Variation on a Single Antenna**

Phase center deviations are always bounded by the size of the antenna patch, and usually produce errors of sub-centimeter magnitude. In [28], Tranquilla et. al. precisely map the phase center variation of several microstrip GPS antennas and find typical RMS variation of 2-4 mm. This level of accuracy is of little concern to code phase users of GPS. For interferometry applications, the magnitude of phase center error is comparable to that of receiver noise, and it should be modeled.

Much like the more common gain pattern, the phase pattern of an antenna can vary from one unit to another, so any modeling must be antenna specific. Phase center variation is body fixed and virtually time invariant, so it is modeled along with low frequency multipath in the calibration model. Any variation or mismodelling of the phase center state is accounted for using adjustment of the receiver correlated noise estimate.

### Receiver White Noise

White noise in the receiver is the sum of all uncorrelated errors, including thermal noise and oscillator noise [24]. It is therefore modeled as white noise with a properly chosen intensity.

Thermal noise in the tracking loop is the dominant source of white noise, and it can be modeled as

a function of the carrier loop noise bandwidth,  $B_n$ , carrier to noise ratio ( $C/N_0$ ) and the predetection integration time  $T$ :

$$\sigma_n = \frac{360}{2\pi} \cdot \sqrt{\frac{B_n}{C/N_0} \left(1 + \frac{1}{2T \cdot C/N_0}\right)} \quad 3.11$$

$\sigma_{tn}$  is the thermal noise intensity.  $B_n$  and  $T$  for a typical GPS receiver are 10 Hz and 20.0 milliseconds, respectively.

In this application, experimental modeling of receiver white noise is used rather than the thermal noise model in equation 3.11. Through experimental modeling, a direct measurement of the *differential* phase noise intensity,  $\sigma_{\Delta\nu}$ , is available.  $\sigma_{\Delta\nu}$  is characterized as a function of GPS body frame elevation and is used by the filter as a GPS measurement noise estimate. Cross correlation of the measurement noise is a function of the single difference operator:

$$\mathbf{R}_{\Delta\nu} = \begin{bmatrix} \sigma_{\Delta\nu}(\theta_{\rho_1}) & 0.5 \cdot \sigma_{\Delta\nu}(\theta_{\rho_1}) & 0 & 0 \\ 0.5 \cdot \sigma_{\Delta\nu}(\theta_{\rho_1}) & \sigma_{\Delta\nu}(\theta_{\rho_1}) & 0 & 0 \\ 0 & 0 & \sigma_{\Delta\nu}(\theta_{\rho_2}) & 0.5 \cdot \sigma_{\Delta\nu}(\theta_{\rho_2}) \\ 0 & 0 & 0.5 \cdot \sigma_{\Delta\nu}(\theta_{\rho_2}) & \sigma_{\Delta\nu}(\theta_{\rho_2}) \end{bmatrix} \quad 3.12$$

$\theta_{\rho_1}$  is the elevation of the SV on channel 1 in the body frame. This example is for two baselines and two satellites, but the extension to additional measurements is straightforward.

Equation 3.13 shows the differential phase sensitivity to receiver white noise. Since  $\Delta\nu$  is an additive error, measurement sensitivity is the identity:

$$\frac{\partial \Delta\varphi_{i,j}}{\partial \Delta\nu_{k,l}} = \delta(i, k)\delta(j, l) \quad 3.13$$

### Receiver Correlated Noise

Receiver correlated noise,  $\Delta\xi$ , models any temporally correlated errors in the receiver. It is also used to absorb mismodelling in the multipath and phase center error calibration. Correlated noise has the same measurement sensitivity as uncorrelated receiver noise, but the dynamics will differ. Assuming that the correlated dynamics are slow with respect to the 1 Hz receiver sampling rate,

they can be modeled as a first order ECRV,

$$\frac{d}{dt} \underline{\Delta\xi}(t) = -\frac{1}{\tau_{\Delta\xi}} \underline{\Delta\xi}(t) + \underline{w}_{\Delta\xi}(t) \quad 3.14$$

where  $\tau_{\Delta\xi}$  is the time constant and  $\underline{w}_{\Delta\xi}$  is white Gaussian process noise. The random process is assumed to be zero mean due to the *a priori* calibration of measurement biases. The time constant and steady state error covariance for  $\underline{\Delta\xi}$  are determined in section 3.3. Note that, because  $\underline{\Delta\xi}$  is a product of the single difference operator, it is correlated between antennas. This is modeled by adding correlations in the process noise  $\underline{w}_{\Delta\xi}$ . This is shown in equation 3.15 for a single channel and two baselines:

$$\mathbf{Q}_{\Delta\xi} = \begin{bmatrix} 1 & 0.5 \\ 0.5 & 1 \end{bmatrix} \cdot \sigma_{w_{\Delta\xi}}^2 \quad 3.15$$

$\mathbf{Q}_{\Delta\xi}$  is the process noise covariance. Variance of the driving noise,  $\sigma_{w_{\Delta\xi}}^2$ , is based on the steady state covariance of  $\underline{\Delta\xi}$ ,  $\sigma_{\Delta\xi}$ :

$$\sigma_{w_{\Delta\xi}}^2 = \frac{2 \cdot \sigma_{\Delta\xi}(\theta_{pj})^2}{\tau_{\Delta\xi}(\theta_{pj})} \quad 3.16$$

$\sigma_{\Delta\xi}$  is also modeled as a function of satellite elevation,  $\theta_{pj}$ . The measurement sensitivity is identical to the white noise component:

$$\frac{\partial \Delta\phi_{i,j}}{\partial \Delta\xi_{k,l}} = \delta(i,k)\delta(j,l) \quad 3.17$$

### Line Bias

The L1 carrier signal travels from each of the patch antennas to the RPU along separate coaxial cables. Each cable has a unique electromagnetic path length known as the line bias. The single difference operator subtracts the line bias of each of the slave antennas from the master antenna

bias to give the differential line bias,  $\Delta\beta$ :

$$\underline{\Delta\beta} = \begin{bmatrix} \Delta\beta_1 \\ \Delta\beta_2 \end{bmatrix} = \begin{bmatrix} 1 & -1 & 0 \\ 1 & 0 & -1 \end{bmatrix} \cdot \begin{bmatrix} \beta_M \\ \beta_1 \\ \beta_2 \end{bmatrix} \quad 3.18$$

Notice that this bias is strictly a function of the baseline; there is no dependence on what channel the measurement comes from. This means that only  $n_{BL}$  line bias parameters are required, with the resulting measurement sensitivity shown in equation 3.19:

$$\frac{\partial \Delta\phi_{i,j}}{\partial \Delta\beta_k} = \delta(i, k) \quad 3.19$$

The dynamics of line bias are relatively slow and primarily dependent on temperature variations. A first order correlated error model is used to model the bias:

$$\frac{d}{dt} \underline{\Delta\beta} = -\frac{1}{\tau_{\Delta\beta}} (\underline{\Delta\beta} - \underline{\Delta\beta}_0) + \underline{w}_{\Delta\beta}(t) \quad 3.20$$

The nominal line bias,  $\underline{\Delta\beta}_0$ , must be loosely calibrated before attempting estimation. The driving noise intensity is a function of the steady state line bias covariance, and the correlation across baselines is identical to that of receiver noise:

$$\sigma_{w_{\Delta\beta}}^2 = \frac{2 \cdot \sigma_{\Delta\beta}^2}{\tau_{\Delta\beta}} \quad 3.21$$

$$\mathbf{Q}_{\Delta\beta} = \begin{bmatrix} 1 & 0.5 \\ 0.5 & 1 \end{bmatrix} \cdot \sigma_{w_{\Delta\beta}}^2 \quad 3.22$$

### Baseline Length Error

The baseline vector separating two antennas,  $\mathbf{b}$ , is subject to mechanical flexure, expansion and contraction. Although this is a physical change rather than an actual measurement error, the measurement equation (equation 1.4) is based on a nominal baseline vector,  $\mathbf{b}_0$ , so these effects lead to apparent errors in the differential phase.

The mathematics of baseline errors are greatly simplified if the errors are strictly limited to con-

traction and expansion. In a spacecraft environment with meter-size baselines, it is possible to construct a platform which provides mm-level flexure rigidity. This would limit any flexure errors to less than the level of receiver noise. The only error of concern then becomes a change in the baseline length,  $b_i$ , due to thermal effects.

If  $\mathbf{u}_b$  is the unit vector for a nominal baseline  $\mathbf{b}_0$ , an error  $\delta b$  in the nominal length  $b_0$  results in the perturbed baseline vector  $\mathbf{b}$ :

$$\mathbf{b} = \mathbf{b}_0 + \delta b \quad 3.23$$

$$\delta \mathbf{b} = \delta b \cdot \mathbf{u}_b \quad 3.24$$

The measurement equation is now:

$$\Delta \phi_{i,j} = (\mathbf{b}_{i_0}^T + \delta \mathbf{b}_i^T) \cdot \hat{\rho}_j + \varepsilon_{other} \quad 3.25$$

Error due to the baseline length error is,

$$\varepsilon_b = \delta \mathbf{b}_i^T \cdot \hat{\rho}_j \quad 3.26$$

and this effect is shown in figure 3.5

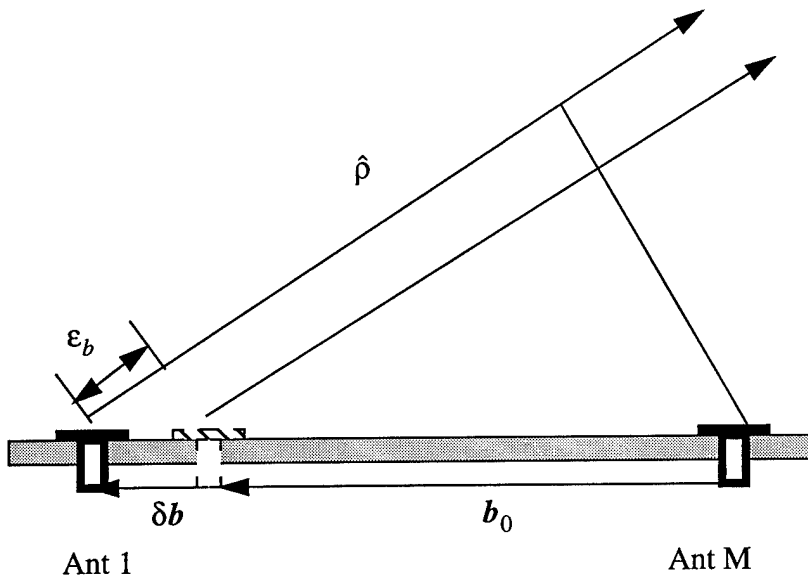


Figure 3.5: Baseline Error Geometry

Substituting from equations 3.24 and 3.26:

$$\varepsilon_{b_{i,j}} = (\mathbf{u}_{b_i}^T \cdot \hat{\rho}_j) \delta b_i \quad 3.27$$

This relationship is linearized about the line of sight geometry,  $\hat{\rho}_j$ , to give differential phase sensitivity to  $\delta b$ :

$$\frac{\partial \Delta \phi_{i,j}}{\partial (\delta b_k)} = \delta(i, k) \cdot (\mathbf{u}_{b_j}^T \cdot \hat{\rho}_j^B) \quad 3.28$$

Baseline error dynamics are dependent on the physical environment of a receiver. The predominant source of expansion for spacecraft applications will be temperature gradients. A first order Markov process is used to model this effect, with the following error dynamics:

$$\frac{d}{dt}(\underline{\delta b}) = -\frac{1}{\tau_b} \underline{\delta b} + \mathbf{w}_b(t) \quad 3.29$$

$$\sigma_{w_b}^2 = \frac{2 \cdot \sigma_b^2}{\tau_b} \quad 3.30$$

Baseline length error does not effect raw carrier phase, so there is no cross correlation due to single differencing. There will likely be some cross coupling of the baseline errors due to simultaneous expansion and contraction of the baselines, but an uncorrelated model is used to allow for baseline-specific variations.

### 3.3 Error Characterization

The purpose of this section is to derive models for each of the components of differential phase error using experimental data. The models developed here are used to design the EKF in Chapter 4 and to test nominal filter performance in Chapters 5 and 6. Two types of models are used. Phase center variation and body-fixed multipath are modeled using a measurement bias calibration. The calibration is a table look-up which the EKF uses to correct incoming phase measurements. The remaining errors are stochastic. These errors are characterized by estimating parameters for the dynamic models of section 3.2.

#### 3.3.1 Test Facility

##### Receiver

The receiver used for this analysis is a Trimble TANS Vector GPS receiver with four micro-strip

patch antennas mounted on a 2 meter maximum length adjustable kinematic frame constructed of reinforced aluminum beams. The frame is designed to limit flexure to less than 2 mm at full extension in moderate winds. Scales mounted to the frame allow antenna placement accuracy to one millimeter. Each antenna is mounted on a Trimble-supplied 8" radius metallic ground plane to improve high elevation gain and reduce susceptibility to reflected signals. The six channel tracking loops are time multiplexed across four antennas with a measurement output rate of 1 Hz. A more detailed discussion of the receiver architecture can be found in [7].

The antennas used on the Vector are standard Trimble L-band patch antennas. The gain and phase patterns are not uniform in azimuth, but the antenna elements are mutually aligned to minimize the effect of these variations when phase measurements are differenced across the antennas. For the error calibration tests, the antennas are arranged in a 60 X 60 cm square, with two 60 cm baselines and one 84 cm baseline across the diagonal.

### **Test Environment**

The receiver frame is mounted on a 2-axis turntable with arc-second readouts for azimuth and elevation. The platform position and attitude are surveyed to provide truth position and orientation. Position uncertainty is less than 0.5 m. Yaw, pitch and roll are accurate to 0.02°. The platform is

mounted on the south-facing edge of an 8-story building.

**Figure 3.6: Test Platform**

Two obstructions to the north of the platform are potential sources of multipath. The approximate

locations of the obstructions, an array of cooling stacks and a slanted sky light, are depicted in figure 3.7:

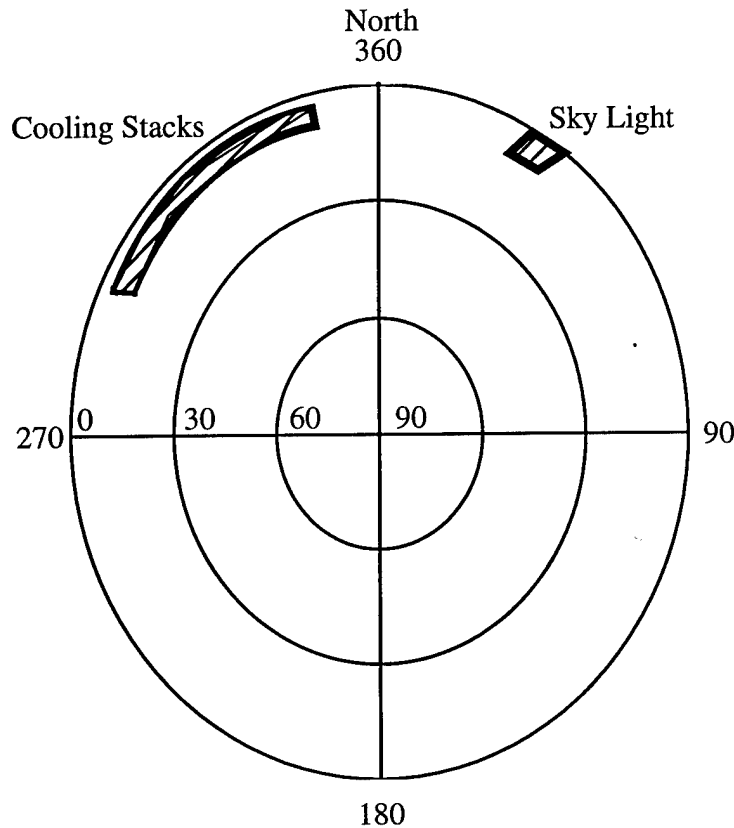


**Figure 3.7: Obstructions**

The obstructions block a very small portion of the sky: the vertical cooling stacks are 15m (80 wavelengths) from the receiver, with a maximum apparent elevation of  $10^\circ$  in the antenna array frame. The sky light is more than 100m from the receiver, with a maximum apparent elevation of  $7^\circ$ .

### Test Procedure

A rigorous procedure was followed during each test period to ensure uniform receiver performance from day to day. This allows comparison of random error sources to those which are repeatable. All receiver parameters, such as elevation and SNR mask settings, were identical during nominal data collection and environmental parameters such as temperature and wind speed were recorded to examine any corresponding change in measurement characteristics.

The platform alignment truth data is used with precise measurement of the antenna positions to

compute expected phase measurements for the receiver using equation 3.3. GPS SV position is calculated using the 15 element precise ephemerides contained in the GPS navigation message. Figure 3.8 shows a typical comparison of real measurements to the truth model differential phase:

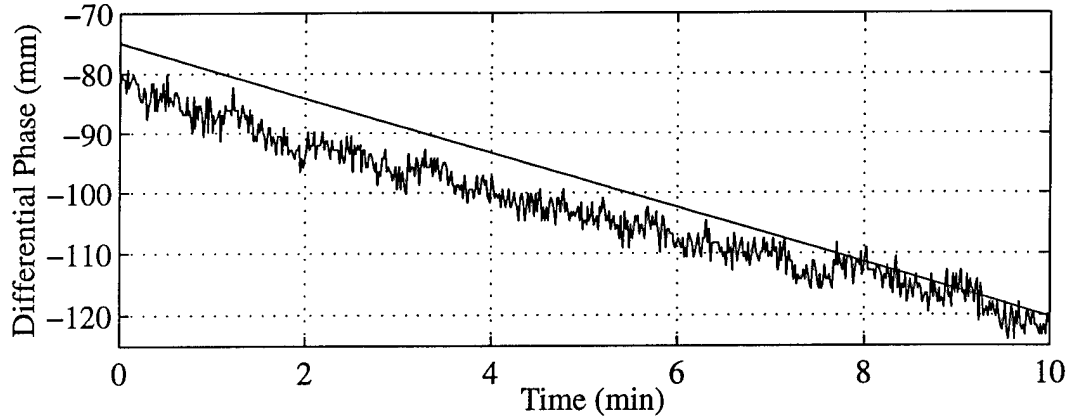


**Figure 3.8: Real vs. Expected Phase**

The difference between predicted and measured phase is total differential phase error. A plot of errors for a half hour period including the above data is shown in figure 3.9 along with the satellite azimuth and elevation in the NED frame. The baseline for this trial was the 84 cm baseline, ori-

ented towards true north:

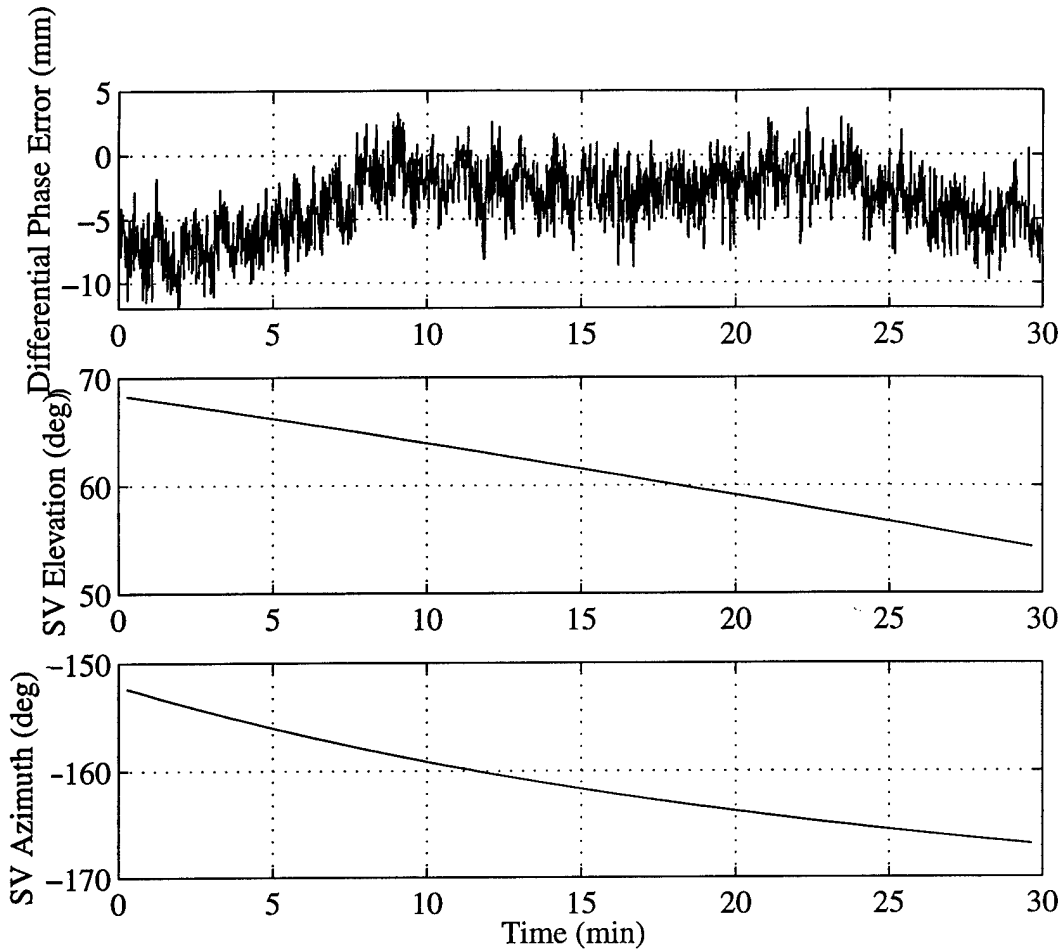


**Figure 3.9: Measurement Error**

### Scope of Analysis

Although this analysis is conducted for a ground-based TANS Vector receiver, the test methods are valid for coplanar configurations with any number of baselines and channels. Slight modifications would allow the error analysis to be performed for non-coplanar arrays as well.

The error models computed in this study are appropriate for use in most ground-based applications. The greatest uncertainty between applications is the reflection environment surrounding the receiver. Models presented here would be dangerously optimistic if applied to an environment with significant obstructions, such as operation near buildings and other planar reflectors. Conversely, a spacecraft application will encounter less geometric interference than a ground based application. As a result, this study presents a conservative GPS error model which can be

adjusted to optimize performance in benign spacecraft environments.

All of the stochastic error sources are assumed to be normally distributed. To verify this qualitatively, error data for a region of the sky is plotted in a histogram as shown in figure 3.10:

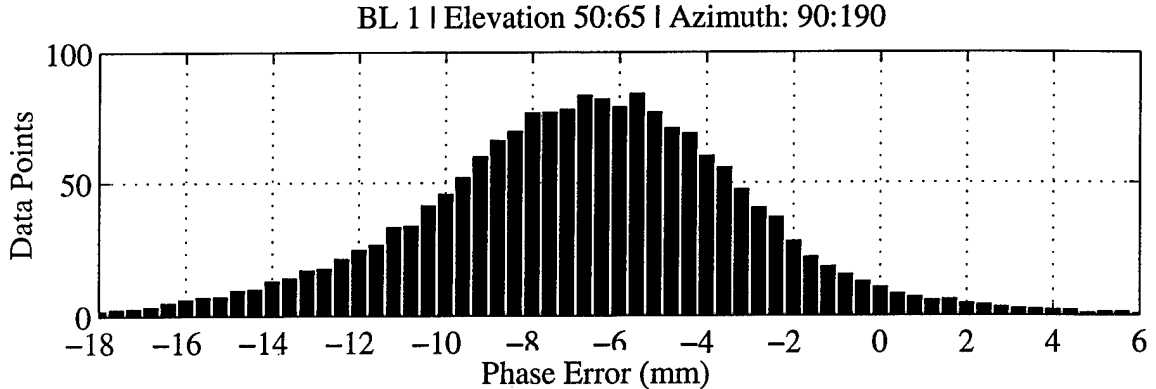


**Figure 3.10: Distribution of Differential Phase Residuals**

This plot includes ten hours of data and is for satellites at high elevations which are not subject to multipath. Satellites at very low elevations do not always have such a uniform distribution. There is a noticeable bias in this sample of data, and a bias of this magnitude is not unusual in the differential phase measurement. The following section addresses these biases.

### 3.3.2 Calibrated Bias Errors

Body fixed multipath sources and phase center variation produce deterministic errors which are a function of the GPS LOS vector in the body frame [9]. By comparing measured phase to predicted phase for a static receiver, these errors can be mapped into the antenna visibility cone and calibrated using numerical best fit methods. This bias map also facilitates initial calibration of two critical receiver parameters, the initial line bias ( $\Delta_{\beta 0}$ ) and the initial baseline lengths ( $b_{i0}$ ).

#### Bias Map

Six test days over a period of four months were used to compile data for the error bias map. The data spans a total of about 30 hours and was taken with the array in four different orientations, including three near-level orientations and one orientation in which the array is pitched up  $30^\circ$ . To construct the bias map, the sky was divided into 18 elevation steps and 72 azimuth steps for a total of 1296 squares, each 5 degrees on a side. For each square, a running count was kept of the num-

ber of data samples created by any satellite within the 5x5 square. In another matrix, a running sum was kept of phase residuals (total phase error) for measurements corresponding to the square. A third matrix was used to store the sum of the squared error for measurements in the square. The error, squared error, and data count allows a rough calculation of mean error and variance for differential phase produced by satellites at specific points in the sky. The total differential phase RMS error can also be calculated, and is shown in figure 3.11. To construct the total error shown in figure 3.11, RMS error was calculated for each of the 5x5° bins. RMS values for bins at the same elevation were averaged across all azimuth steps and all three baselines, producing average error as a function of elevation. Total error encompasses all of the error sources which will be modeled in this section.

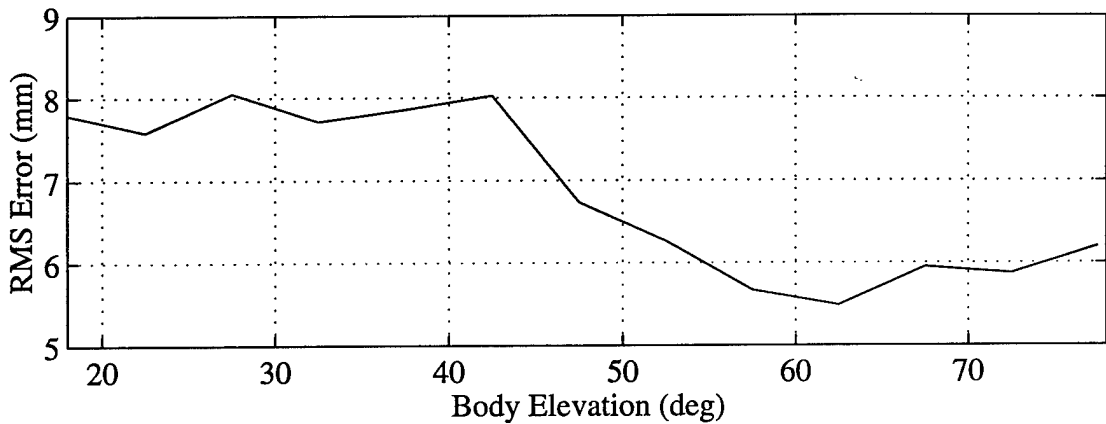


**Figure 3.11: Total Differential Phase Error (Uncorrected)**

The error is referred to as uncorrected because part of the error is caused by errors in the nominal baseline vectors used to calculate the differential phase residuals. Calibration of the baseline vectors is now addressed.

### Baseline Length Calibration

Baseline length calibration is used to estimate the nominal length of the antenna baselines. A difference between the nominal antenna baseline estimate and the true baseline vector causes an apparent error in the measured differential phase. This error can be mapped as a function of the

satellite LOS vector in the body frame:

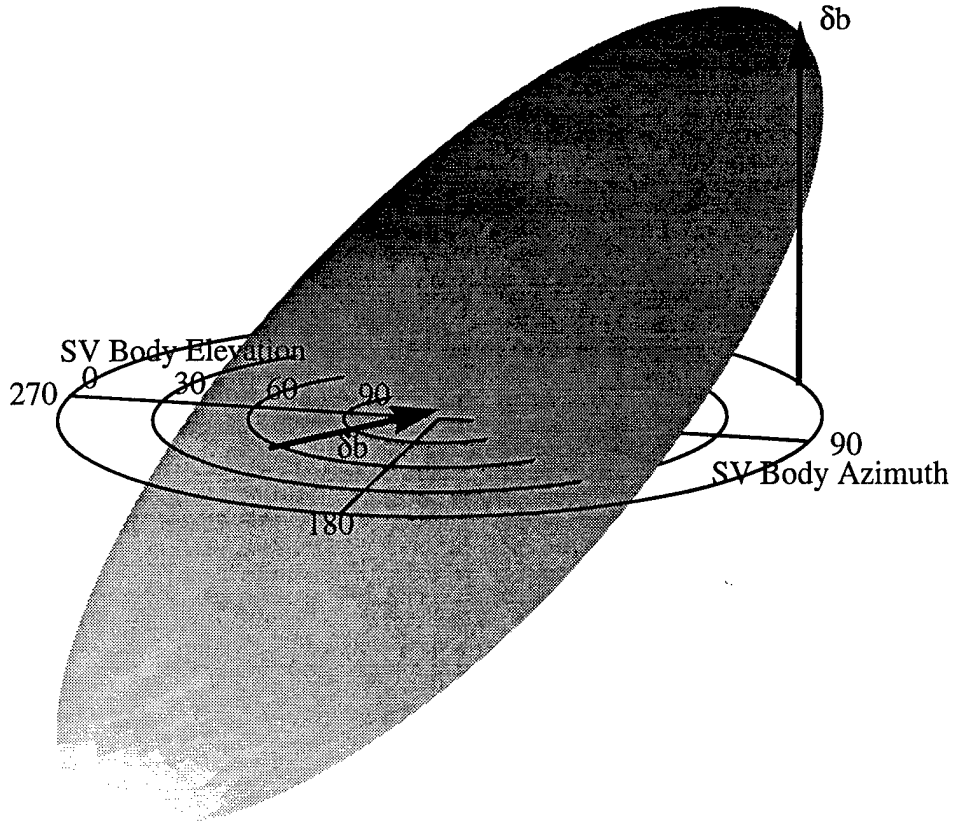


**Figure 3.12: Phase Error Due to Baseline Expansion**

Here, the tilted plane represents differential phase error due to a baseline error  $\delta b$ . The phase error is a function of SV azimuth and elevation, which is depicted in the horizontal plane.  $\delta b$  is the magnitude of the length error. The figure is identical to figure 1.3, which displayed delta range as a function of SV LOS for a nominal baseline. This is expected, because baseline error enters the measurement equation at the same place as the nominal baseline vector. However, the baseline error  $\delta b$  may not be aligned with the nominal baseline  $b_0$ , so the alignment of the plane in figure 3.12 is not known *a priori*. Still, baseline error has a distinct footprint which is significantly different from the other error sources, so it is the first calibration that is attempted using the phase error data. Note that this is *not* an error characterization, nor is it used in the filter. Rather, this is a calibration of the nominal baseline value which is needed to process the experimental data. By correcting the nominal baseline vector and removing the resulting contribution to the total error, characterization of the remaining error sources will be more accurate.

Figure 3.13 shows the map of average error for each bin over all of the data takes with the Vector receiver. The horizontal plane depicts location of a satellite in the sky. The value plotted above or below each square represents the average differential phase error for satellites within the square. There is significant bias on all three of the baselines, and baselines 1 and 2 show a distinct lopsided pattern to the biases.

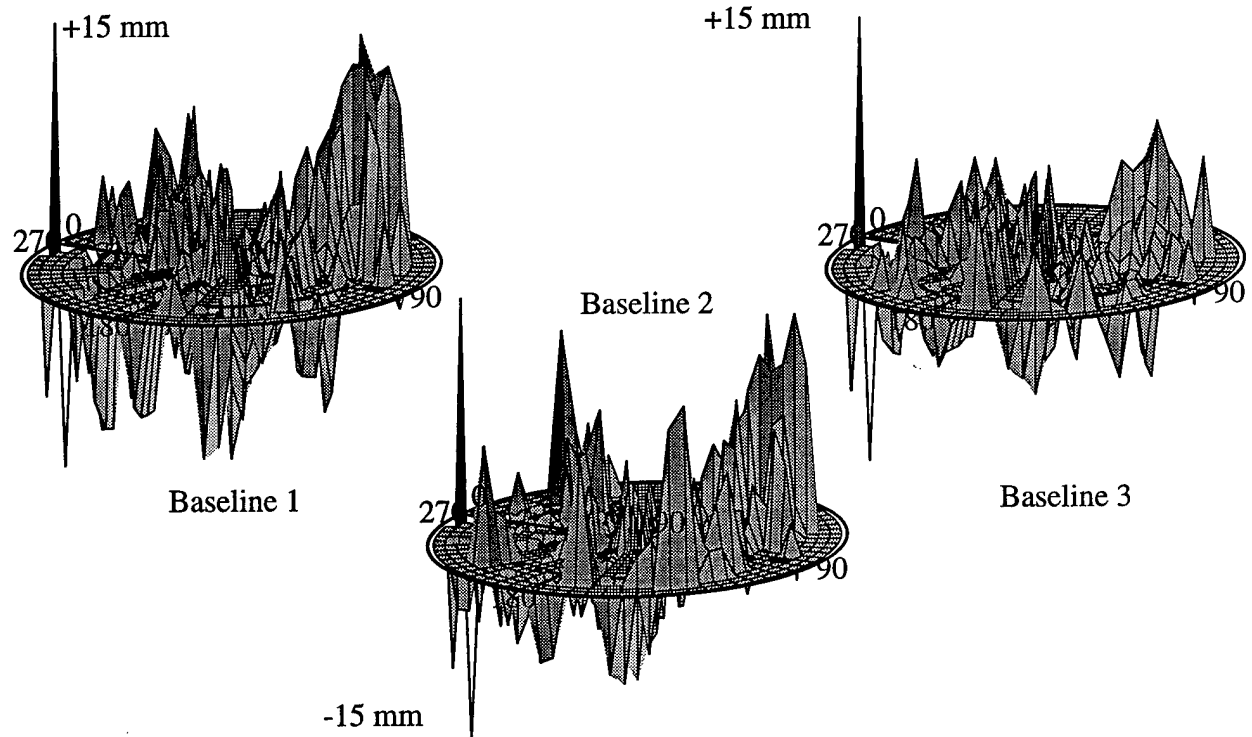


**Figure 3.13: Uncorrected Bias Map**

Gaps in sky coverage give these maps a jagged appearance, so it is useful to examine a least-squares fit to the error data. Figure 3.14 shows a fit of the biases for baseline 1. For each  $5^\circ$  elevation band, a fifth order polynomial model was fit to the bias data around  $360^\circ$  of azimuth. Elevations with insufficient data to produce a useful model are excluded, resulting in a model which

extends from 20° to 80° elevation.

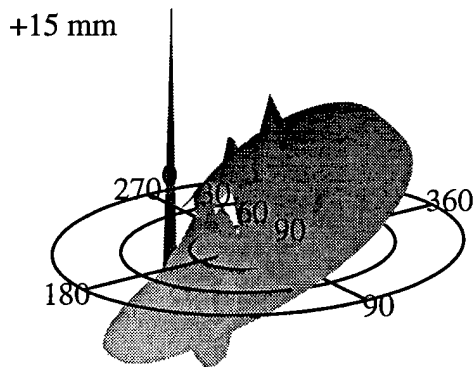


**Figure 3.14: Uncorrected Bias Model**

The model displays a pattern very similar to the predicted error characteristic for a baseline length error. Although the antenna mount used for these tests is marked to millimeter accuracy, there appears to be an error in the calculation of the antenna baselines. The source of the uncertainty remains to be investigated, but through the bias model, it is possible to make a best fit correction to the nominal baseline estimate.

For this application, a trial-and-error method was used to calculate the baseline correction vector, but an automated calibration using the full sky bias map could produce baseline estimates accurate to the millimeter level. The errors for baseline 1, 2 and 3 were 9mm, 7mm and 2mm, respectively. These *corrected* baselines are used to calculate differential phase residuals for the error analysis. After the correction, the biases have smaller magnitude and a less lopsided distribution:

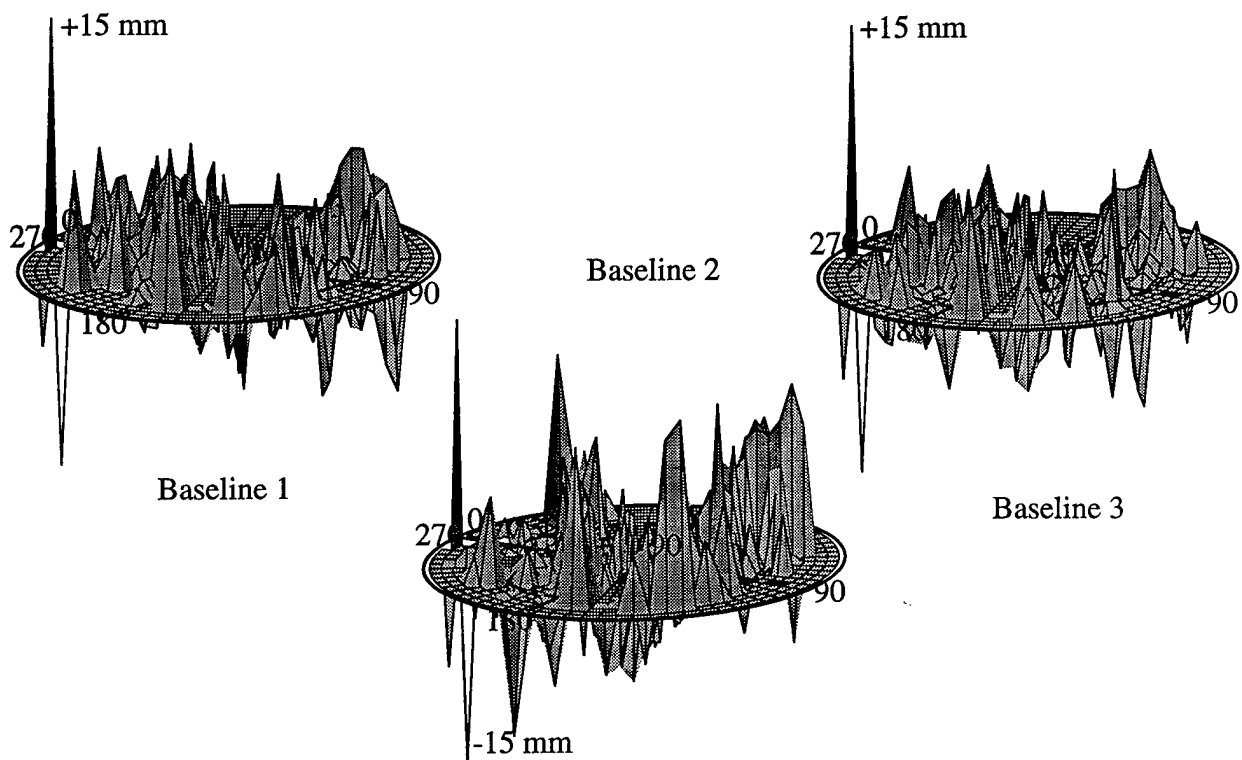


**Figure 3.15: Bias Map After Baseline Correction**

Total error is recalculated after the correction and compared to the original error in figure 3.16:

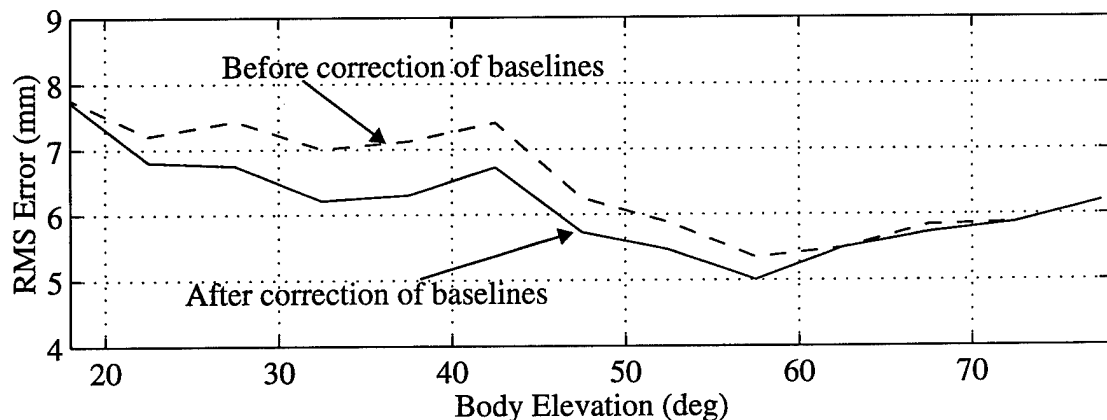


**Figure 3.16: Total Differential Phase Error (Corrected)**

This figure shows that errors in the nominal baseline are responsible for part of the uncorrected error shown in figure 3.11, especially at low elevations. The *corrected* total RMS error is used as a starting point for the remaining analysis.

## Line Bias

Line bias is insensitive to changes in the GPS LOS vector, so it can be calibrated by simply taking the mean error on each baseline. The nominal value,  $\Delta\beta_0$ , is calculated by averaging residuals for a single baseline across all of the channels and all of the days of data. In section 3.3.3, line bias is calculated on each day separately and compared to the nominal value. The day to day variation is used to estimate the stochastic properties of line bias.

## Phase Center and Multipath

The remaining azimuth and elevation dependent biases are due to phase center variation and multipath. This calibration will only attempt to model phase center variation and any multipath due to body-fixed sources, such as diffraction off of the ground planes. Calibration of environmental multipath is not possible, because the location of reflecting surfaces with respect to the array changes as the array is moved. The data used for the calibration model was shown in figure 3.15. In order to cancel the effects of environmental multipath in the model, the data includes measurements from all four test orientations.

The best fit bias model for this data is shown in figure 3.17:

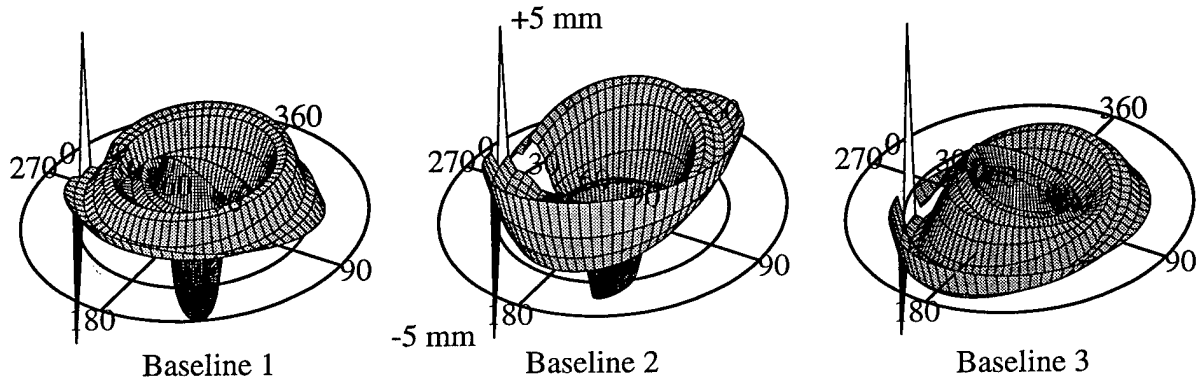


**Figure 3.17: Body-Fixed Bias Model**

This bias model again uses a fifth order polynomial fit for the measurement data at each elevation interval. The biases for each baseline are stored as a function of SV azimuth and elevation in the body frame. The EKF of Chapter 4 removes the modeled bias from each incoming differential phase measurement according to equation 3.31:

$$\Delta\phi'_{i,j} = \Delta\phi_{i,j} - \chi(\hat{\theta}_{\rho_j}, \hat{\Psi}_{\rho_j}, i) \quad 3.31$$

$\Delta\phi'_{i,j}$  is the corrected differential phase measurement.  $\hat{\theta}_{\rho_i}$  and  $\hat{\psi}_{\rho_i}$  are the filter estimates of azimuth and elevation to SV  $j$  in the body frame.  $i$  is the baseline number and  $\chi$  is the calibration value for this baseline, azimuth and elevation.

The reduction in differential phase error realized using the bias model is shown in figure 3.18 as a function of SV elevation. The vertical axis shows the percentage of the total error covariance which is removed by the model:

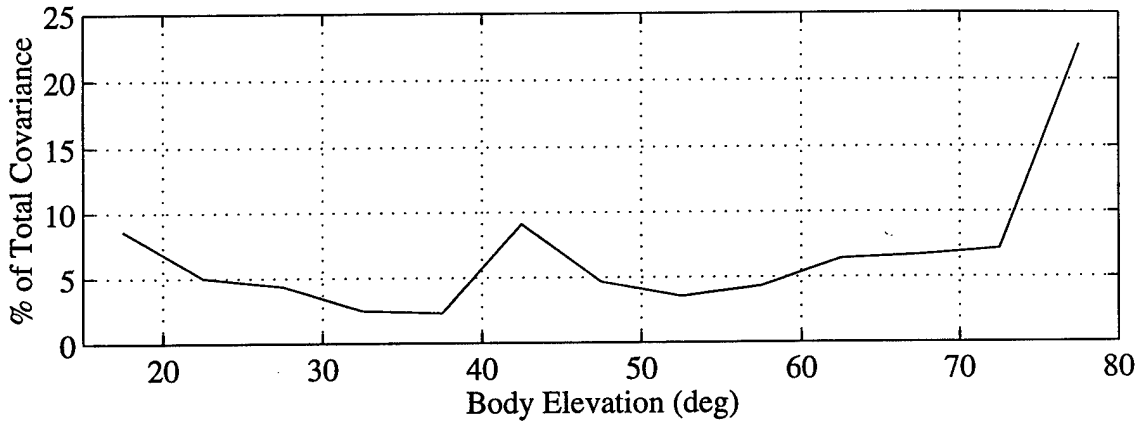


**Figure 3.18: Reduction in Differential Phase Error after Calibration**

The error contribution removed by the calibration only averages about 5%, so it is likely that part of the phase center and multipath errors are not captured in the calibration. The ability of the bias model to map deterministic error sources is limited by the order of the model and the resolution of the 5x5 grid used to map the biases. Errors not accounted for in this model or in the stochastic analysis which follows are caused by uncalibrated biases. Uncalibrated biases are accounted for in the filter design by increasing the intensity of the correlated receiver noise model.

The computational cost of this calibration model is relatively high for the reduction in differential phase errors displayed in figure 3.18. Performance might be improved by including more data in the model or using a different modeling technique. For example, in [9], Cohen achieves a bias fit with 1 mm RMS error using an eighth order spherical harmonic model.

### 3.3.3 Stochastic Errors

Stochastic errors do not repeat from day to day, so they cannot be calibrated out of the estimator.

However, an accurate dynamic model for random errors can be used to estimate the errors in the EKF. Stochastic parameters are developed here for line bias, baseline length and total receiver error.

All of the stochastic errors are analyzed by comparing differential phase data from the same GPS SV at the same position in the sky on different days. The GPS orbit period of approximately twelve hours makes this kind of investigation possible, because the location of a GPS satellite over any point on the earth repeats to within a few arc-minutes after a period of approximately 24 hours.

The position of the GPS satellites in the sky for a particular measurement is referred to as the satellite geometry. Multipath and phase center variation are strictly geometry dependent. If the phase across two days is differenced using a time delay which result in identical geometry, errors in the “double differenced” signal will be solely due to stochastic effects. In equations 3.32 and 3.33, multipath and phase center error on the single difference measurement are shown as functions of the GPS line of sight vector, while receiver error, line bias error and baseline length error are random functions of time.

$$\Delta \varepsilon_{i,j}(t_1) = \Delta m_{i,j}(\hat{p}_{i,j}^B) + \Delta p_{i,j}(\hat{p}_{i,j}^B) + \Delta v_{i,j}(t_1) + \Delta \xi_{i,j}(t_1) + \Delta \beta_i(t_1) + \varepsilon_{b_i}(t_1) \quad 3.32$$

$$\Delta \varepsilon_{i,j}(t_2) = \Delta m_{i,j}(\hat{p}_{i,j}^B) + \Delta p_{i,j}(\hat{p}_{i,j}^B) + \Delta v_{i,j}(t_2) + \Delta \xi_{i,j}(t_2) + \Delta \beta_i(t_2) + \varepsilon_{b_i}(t_2) \quad 3.33$$

Equation 3.34 shows the double difference error which is formed by subtracting errors at  $t_1$  from those at  $t_2$ . For this investigation, the time difference ( $t_2 - t_1$ ) is *always* two GPS orbit periods, referred to here as  $\tau_{\text{GPS}}$ . This way, the geometric phase center and multipath effects cancel, leaving only time differenced error due to baseline length variation ( $\Delta \varepsilon_{b_i}$ ) and double differenced receiver noise ( $\nabla \Delta n_{i,j}$ ,  $\nabla \Delta \xi_{i,j}$ ) and line bias error ( $\nabla \Delta \beta_i$ ):

$$\nabla \Delta \varepsilon_{i,j}(t_1, t_2) = \Delta \varepsilon_{i,j}(t_2) - \Delta \varepsilon_{i,j}(t_1) \quad 3.34$$

$$\nabla \Delta \varepsilon_{i,j}(t_1, t_2) = \nabla \Delta v_{i,j}(t_1, t_2) + \nabla \Delta \xi_{i,j}(t_1, t_2) + \nabla \Delta \beta_i(t_1, t_2) + \Delta \varepsilon_{b_i}(t_1, t_2) \quad 3.35$$

The effect of repeating GPS geometry is apparent in figure 3.19:

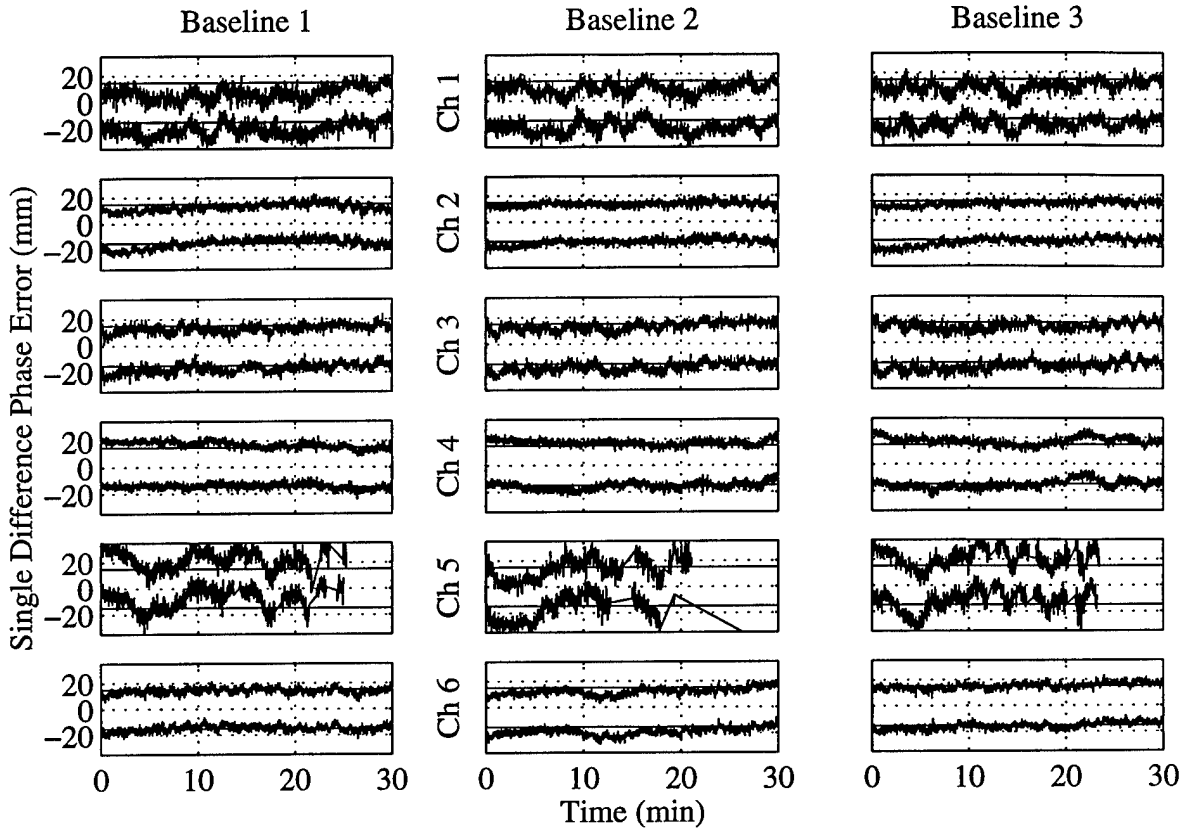


**Figure 3.19: Differential Phase Error for Identical GPS Geometry**

This figure shows differential phase errors for all six channels and three baselines of the receiver on two different days at time separated by  $\tau_{\text{GPS}}$ . Errors for the first day are offset on the vertical axis by -15 mm while those for the second are offset by +15 mm. Clearly, a significant amount of the error energy is deterministic. This is the portion that was mapped by the bias model in section 3.3.2. As equation 3.34 suggests, differencing of the errors between the two days should isolate the stochastic error component. The double difference for channel 6, baseline 2 is shown in figure 3.20. This channel is chosen because the high GPS elevation ( $50^\circ$ ) rules out any multipath. Measurements for the two days are synchronized down to less than one second, and the GPS SV positions match to 10 km. Line of sight to each of the satellites is greater than 20,000 km, resulting in line of sight angular errors less than  $0.03^\circ$  and a phase error contribution under 0.5 mm for a 1

meter baseline.

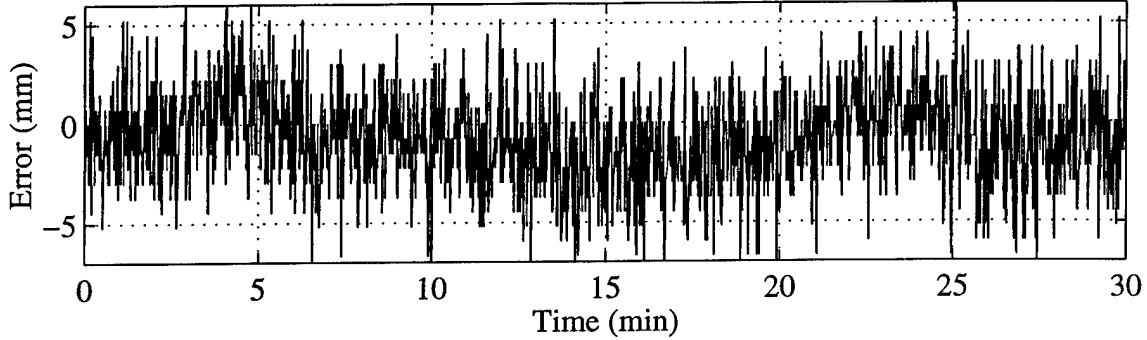


**Figure 3.20: Double Difference Phase Error for Identical GPS Geometry**

Temperature variation across the data takes for this analysis were never greater than 20° F. The thermal coefficient of aluminum is  $22.9 \times 10^{-6}/\text{C}^\circ$ , leading to a maximum expansion on the 84 cm baseline of 0.4mm. This is an order of magnitude smaller than the receiver noise, so baseline expansion and contraction is assumed to be negligible during the tests. Elimination of baseline variation leaves line bias error and receiver noise as the only sources of stochastic error:

$$\nabla \Delta \varepsilon_{i,j}(t_1, t_2) \approx \nabla \Delta v_{i,j}(t_1, t_2) + \nabla \Delta \xi_{i,j}(t_1, t_2) + \nabla \Delta \beta_i(t_1, t_2) \quad 3.36$$

### Line Bias

The line bias time constant is chosen as a function of the receiver environment, so the only parameter which needs to be calculated is the line bias steady state covariance,  $\sigma_{\Delta \beta}$ . Because line bias varies slowly, it can be modeled as a constant, at least over the span of one day:

$$\Delta \beta_i(t) \approx \Delta \beta_i(T_0) \quad 3.37$$

$$(T_0 - 43200) < t < (T_0 + 43200) \quad 3.38$$

This means the line bias contribution to the double differenced phase is approximately a constant:

$$\nabla \Delta \varepsilon_{i,j}(t_1, t_2) \approx \nabla \Delta v_{i,j}(t_1, t_2) + \nabla \Delta \xi_{i,j}(t_1, t_2) + \Delta \beta_i(T_2) - \Delta \beta_i(T_1) \quad 3.39$$

Taking the average across time and  $n_{\text{CH}}$  channels, the double differenced line bias is estimated:

$$\Delta \beta_i(T_2) - \Delta \beta_i(T_1) \approx \sum_{t_1, t_2} \sum_{j=1}^n \frac{[\nabla \Delta \varepsilon_{i,j}(t_1, t_2)]}{n_{\text{meas}}} \quad 3.40$$

Here, the time difference is always  $\tau_{\text{GPS}}$ .  $n_{\text{meas}}$  is the number of measurements. Receiver noise is uncorrelated across the six satellite channels and is modeled as zero mean, so it drops out of the

calculation. The covariance is calculated as one half of the mean squared double difference value:

$$\sigma_{\Delta\beta_i}^2 = \frac{(\Delta\beta_i(T_2) - \Delta\beta_i(T_1))^2}{2} \quad 3.41$$

The steady state line bias RMS error is shown in figure 3.21. The values were calculated using approximately 20 hours of data collection over a 5 day period:

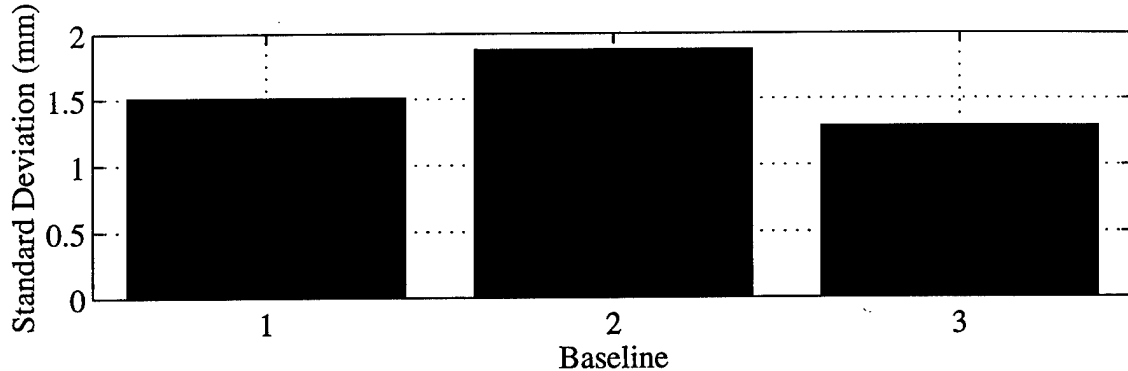


**Figure 3.21: Line Bias RMS Error**

As previously mentioned, the time constant is driven by the environment. Since the principal source of line bias variations is temperature, a twelve hour time constant is appropriate for ground-based applications. For space-based applications, a more suitable time constant is one half the orbital period, to account for solar heating and cooling.

The contribution of line bias error to the total error covariance is shown in figure 3.22:

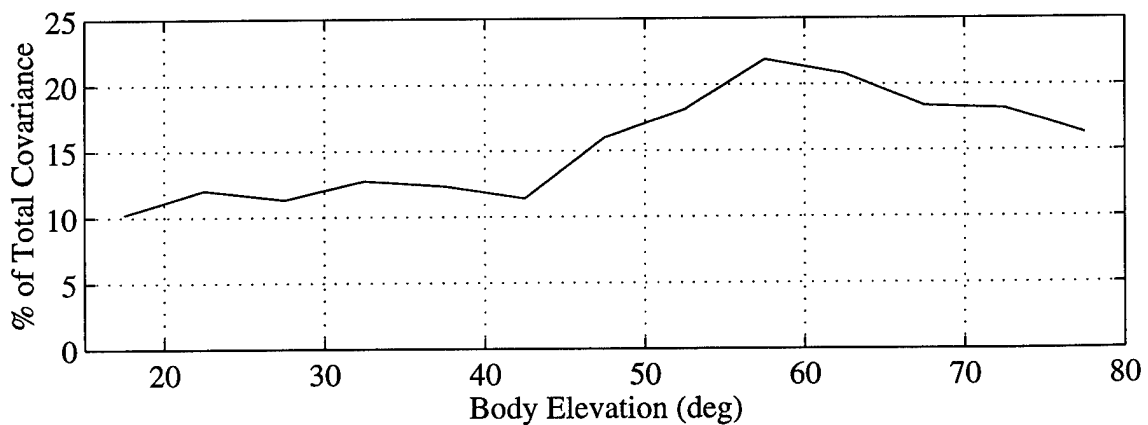


**Figure 3.22: Line Bias Covariance Contribution**

## Receiver Noise

Receiver noise is usually modeled as band-limited white noise [11][4][18], but this error analysis tests the white noise assumption by examining the spectral density of receiver errors. To isolate error due to the receiver, differential phase measurements are again compared for identical GPS geometries. With the line bias contribution removed, the remaining errors are stochastic receiver errors.

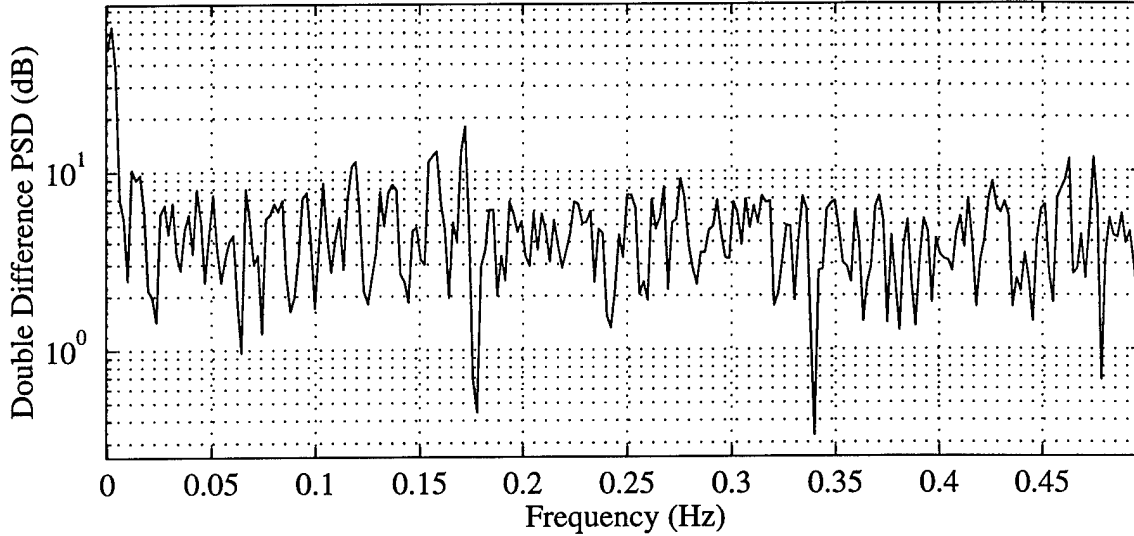
The receiver noise model developed in section 3.2 includes a first order ECRV (equation 3.14) and a white noise component. Spectral density for this model is shown in equation 3.42:

$$S_{\nabla\Delta\phi}(\omega) = 2 \left[ \frac{\left(\frac{2}{\tau_{\Delta\xi}}\right)\sigma_{\Delta\xi}^2}{\left(\omega^2 + \left(\frac{1}{\tau_{\Delta\xi}}\right)^2\right)} + \sigma_{\Delta\nu}^2 \right] \quad 3.42$$

$S_{\nabla\Delta\phi}(\omega)$  is the double differenced phase power spectral density. The single difference spectral density is multiplied by 2 to reflect the effect of double differencing. The doubling of power is valid as long as errors on the two days are not correlated. One day is much longer than the receiver correlated noise time constant, so this is a safe assumption.

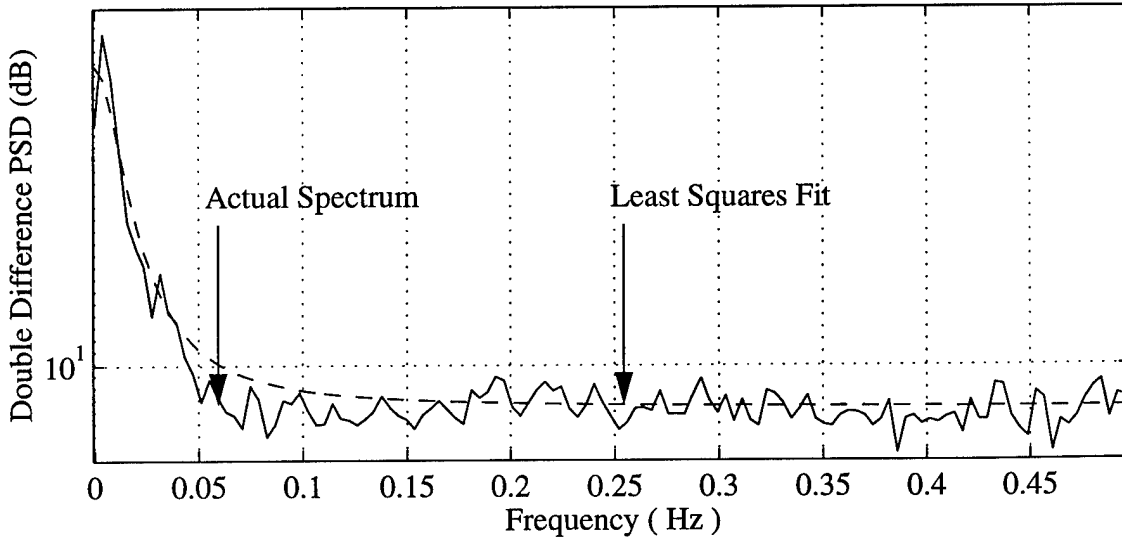
The objective of this section is to determine three parameters: the correlated noise intensity and time constant,  $\sigma_{\Delta\xi}$  and  $\tau_{\Delta\xi}$ , and the white noise intensity,  $\sigma_{\Delta\nu}$ . The parameters are determined using spectral analysis of the double differenced phase errors. As an example, power spectral

density of the double differenced phase from figure 3.20 is shown in figure 3.23.



**Figure 3.23: PSD of Time Differenced Phase**

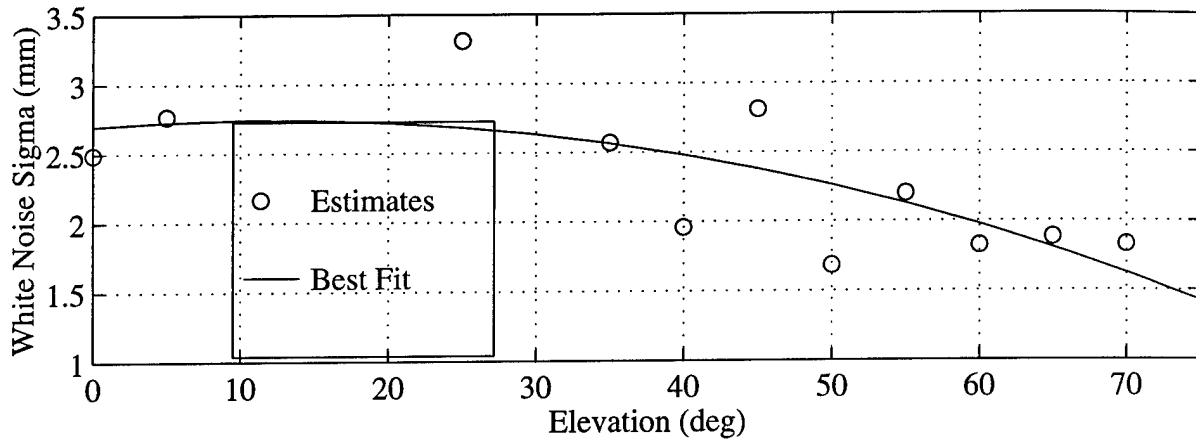
This spectral density was calculated using an average of three 512 point discrete Fourier transforms on the phase error data. To determine model parameters, individual spectral densities are averaged across all azimuths and multiple days by five degree satellite elevation increments to produce elevation-specific spectrum estimates. An example of the averaged spectrum for a five degree elevation increment is shown in figure 3.24:



**Figure 3.24: Mean Spectral Density for 40 to 45 ° Elevations**

The dashed line is a least squares fit to the actual data using the spectral model in equation 3.42. The best fit produces model parameter estimates as a function of elevation.

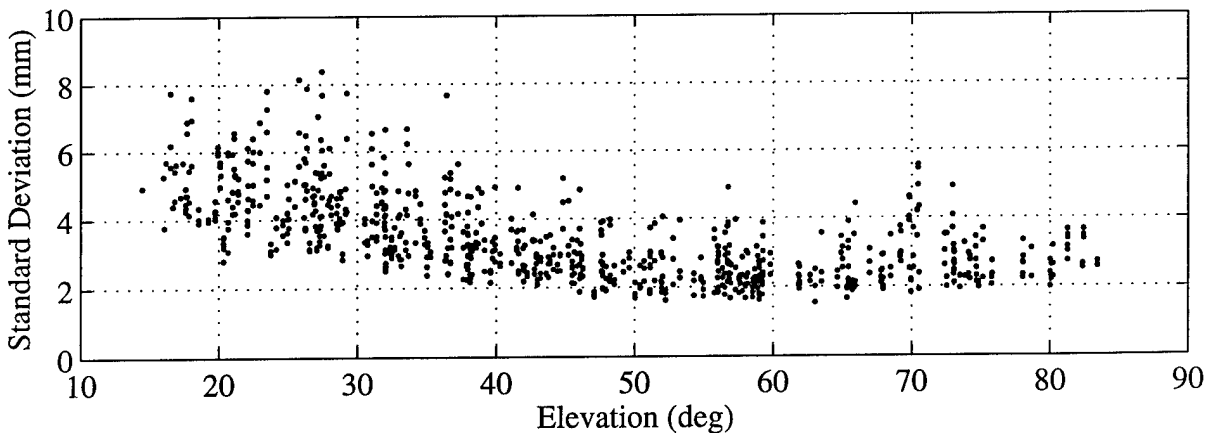
The estimated white noise intensity,  $\hat{\sigma}_{\Delta v}^2$ , is shown in figure 3.25:



**Figure 3.25: Differential Phase White Noise Intensity**

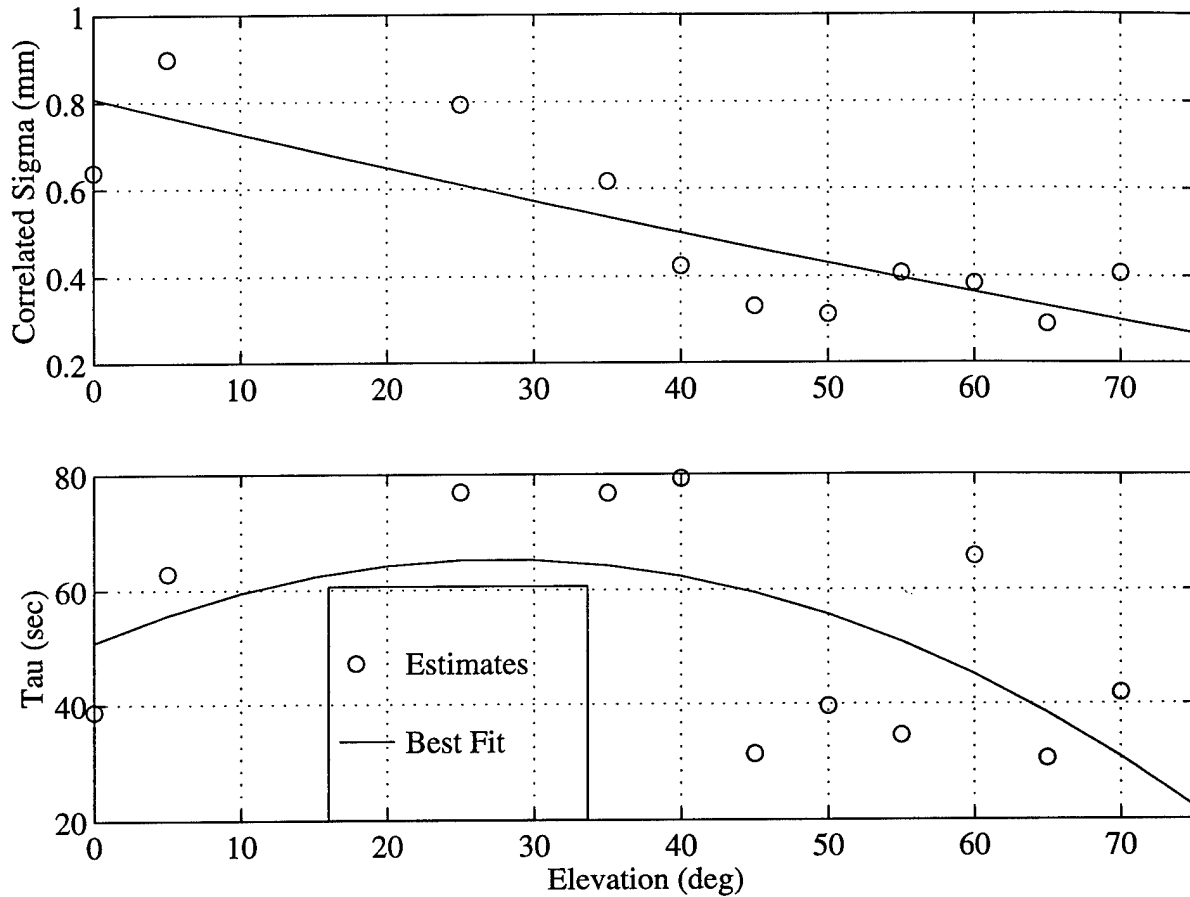
Because data periods for the spectral analysis must have identical GPS geometry, the range of available satellite elevations is limited. Resolution is poorest at low elevations, so single differenced phase error statistics are examined for a number of additional days to fill in the blanks.

Figure 3.26 shows standard deviation of single differenced phase residuals over multiple 30 minute periods, plotted as a function of elevation. The large magnitude of the standard deviation at low elevation warrants an increase in the low elevation white noise intensity model. Incidentally, low elevation measurements are more susceptible to variations in the antenna gain and phase pattern [28]; to add a margin of safety to the filter design, an average of the noise estimates in figures 3.25 and 3.26 is used for the filter design.



**Figure 3.26: Standard Deviation of Single Difference Phase**

Coefficients for the receiver correlated noise model are shown in figure 3.27:



**Figure 3.27: Correlated Error Model**

The low intensity of correlated error in the stochastic model indicates that white noise is a valid model for errors within the receiver. However, the correlated error model is still needed to reflect unmodeled multipath and phase center errors. Figure 3.28 shows the contributions of correlated

error and white noise to the total phase error before modification of the correlated noise intensity:

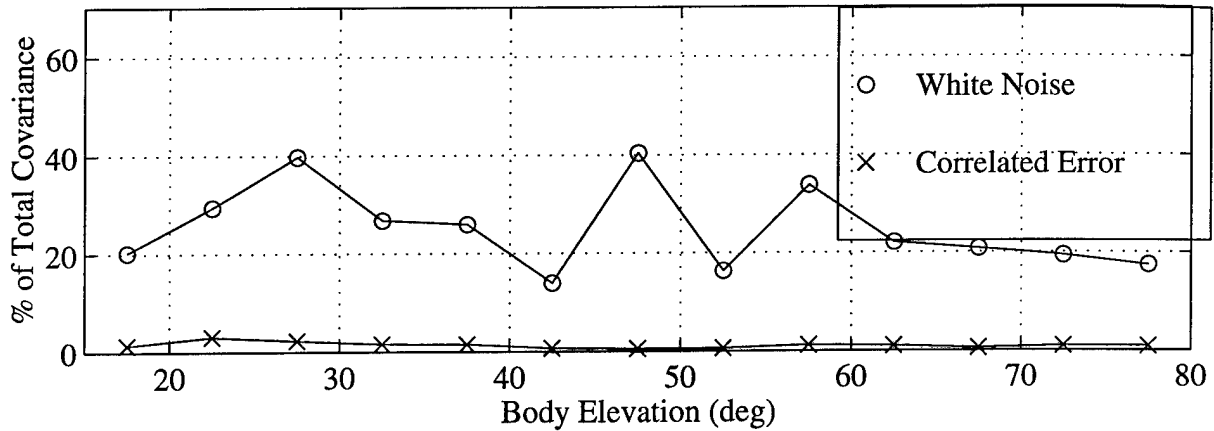


**Figure 3.28: Receiver Error Contribution**

An increase in the correlated noise covariance is used to compensate for unmodeled phase center variation and multipath errors. The magnitude of these unmodeled errors is calculated by subtracting all of the modeled error intensities (i.e. the calibration model, line bias, white noise and correlated noise before augmentation) from the total differential phase RMS error. The resulting correlated noise intensity is shown in figure 3.29:

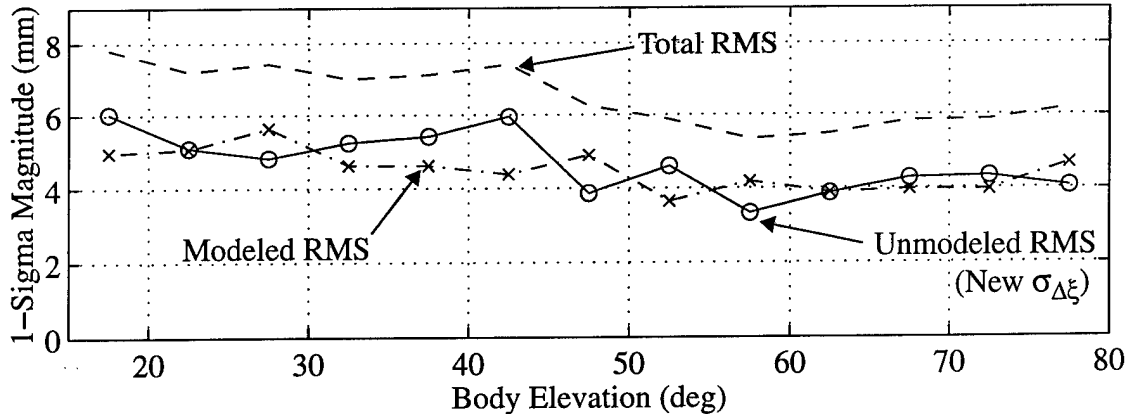


**Figure 3.29: Modeled vs. Unmodeled Error Intensity**

An error budget is now compiled which incorporates all of the error sources, showing the contri-

bution of each error source across the range of SV elevations:

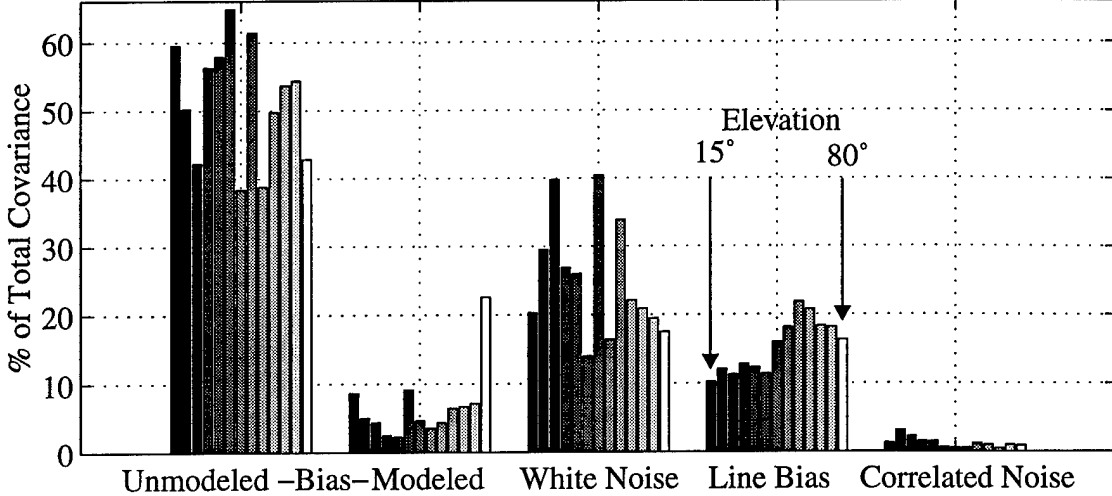


**Figure 3.30: Differential Phase Error Budget**

Figure 3.30 shows a dominant contribution from unmodeled biases. This effect is captured in the filter correlated noise state through the increased steady state covariance. However, the result suggests that a higher order model of deterministic errors may be beneficial.

### 3.3.4 Simulation Parameters

Two adjustments are made for the orbital simulation. The most significant difference between the earth environment and the space environment from a receiver standpoint is much larger temperature variations in orbit. The expected baseline length variation and line bias error covariance must be adjusted to reflect this.

Assuming that the antennas are mounted on an aluminum structure, maximum baseline length variation is the product of the coefficient of thermal expansion for aluminum,  $22.9 \times 10^{-6}/\text{C}^\circ$ , and the maximum expected temperature variation. In [20],  $-45^\circ\text{C}$  to  $+65^\circ\text{C}$  is given as a typical allowable temperature range for spacecraft structural components. This results in a maximum baseline variation of 2.3%. A conservative value of 3% RMS is used in the simulation and filter design.

Temperature change is a primary cause of changes in the line bias,  $\Delta\beta$ . If the receiver cabling is shielded from severe temperature fluctuation, large changes in line bias variation may be avoided. A typical temperature range for spacecraft electronics is 0 to  $40^\circ\text{C}$ . Comparing this temperature

range to the ground based test environment, an approximate doubling of line bias is expected. Average line bias RMS on the ground is about 1.75 mm, so a line bias error RMS value of 3.5 mm is used on all baselines for the orbital tests.

A summary of the parameter changes for space based applications is shown in table 3.1:

	Structure		Cabling	
	Temperature Range	Length Variation Model (RMS)	Temperature Range	Line Bias Model (RMS)
Ground Based	0° to +20°C	0.0%	0° to +20°C	1.75 mm
Space Based	-45° to +65°C	3.0%	0 to 40°C	3.5 mm

Table 3.1: Ground Based and Space Based Error Parameters

### 3. 4 Gyro Errors

The baseline gyro for the EKF design is the Draper Lab micro-mechanical tuning fork gyro [19]. This sensor is used for the primary analysis because of its small size, light weight and potential for low cost mass production. Instead of the traditional spinning mass system, the tuning fork gyro measures the vibration of a suspended mass to estimate angular velocity. The output is therefore an angular rate measurement as opposed to the small angle measurement produced by a rate integrating gyro. A system of three strapdown (body-fixed) gyros is used for this application. One gyro is aligned with each axis of the body frame, forming the three axis rate gyro assembly (TGA).

A generic rate gyro error model is developed here and representative parameter values are given for the Draper gyro and other low cost systems. The purpose is to create a simple model which can be varied to test the sensitivity of the filter to gyro quality. Although the TGA is body-fixed, the gyro is an inertial system, so the dynamics are presented in the inertial frame. Transformation to the body frame is addressed in Chapter 4.

Each gyro rate measurement is corrupted by white noise, gyro bias, misalignment and scale factor

errors:

$$\omega_{M_i} = (1 + k_i) \hat{U}_i \underline{\omega} + b_{g_i} + v_{g_i} \quad 3.43$$

$\omega_{M_i}$  is the measurement from gyro  $i$ .  $k_i$  is the scale factor correction for axis  $i$ ,  $\hat{U}_i$  is the gyro axis unit vector in the body frame,  $b_{g_i}$  is the time varying bias and  $v_{g_i}$  is measurement noise.

### 3.4.1 Dynamic Models

#### Measurement Noise

Measurement noise  $v_{g_i}$  is modeled as white noise with intensity  $\mathbf{R}_g$ . The noise is a function of the gyro output rate and is uncorrelated across the axes. Intensity of gyro noise is usually expressed in terms of the angle random walk (ARW). If the rate measurement is integrated to produce an angle change, the integrated noise produces Brownian motion on the angle measurement. The standard deviation at time  $t$  is  $ARW \cdot t^{1/2}$ . ARW is related to measurement noise by equation 3.44:

$$ARW = \sqrt{\mathbf{R}_g \cdot dt} \quad 3.44$$

$dt$  is integration step size, or the inverse of the output rate. Typical ARW for a low cost gyro is  $1^\circ/\text{hr}^{1/2}$ . This means that if initial attitude knowledge is perfect, estimate uncertainty due to measurement noise is only  $1^\circ$  ( $1-\sigma$ ) after one hour. However, performance is degraded by other error terms as well.

#### Gyro Bias

Slowly varying shifts in the gyro dynamics lead to a measurement drift term commonly referred to as gyro bias. Error due to this drift severely limits the quality of gyro output if the bias is not periodically recalibrated. Integration with GPS measurements provides a source of recalibration of the gyro drift rate.

The gyro bias is modeled as a 1st order ECRV:

$$\frac{d}{dt}(b_{g_i}) = -\frac{1}{\tau_{g_i}}(b_{g_i} - b_{g_{i0}}) + v_{g_i} \quad 3.45$$

$$\sigma_{b_g}^2 = \frac{2 \cdot \sigma_{b_b}^2}{\tau_{b_g}} \quad 3.46$$

The time constant and steady state covariance are determined from experimental data. Typical values for a low cost gyro are a time constant of 8 hours and 10°/hr RMS bias error [19]. The initial bias value can be calibrated on the ground, but some error will be present on start-up.

### Scale Factor

Scale factor is an error in the constant of proportionality relating the angular velocity to the gyro output. For low rotational acceleration applications such as spacecraft, scale factor causes a slowly varying multiplicative error in the measurement. For this analysis, it is assumed that any scale factor error is adequately estimated through the gyro bias term. Typical scale factor for a low cost gyro is 100 ppm.

### Misalignment

The gyro package is strapped down to the body and aligned with the body frame. Small misalignments cause error in the gyro measurement, but the contribution to total attitude error in the filter is negligible. Typical 1-sigma value of initial misalignment for a gyro is 1 milliradian.

Assuming that the scale factor error and misalignments are negligible, the TGA measurement used in the filter is related to the vehicle angular rate by equation 3.47:

$$\underline{\omega}_M = \underline{\omega} + \underline{b}_g + v_g \quad 3.47$$

### 3.4.2 Error Parameters for Low Cost Gyros

Parameters are listed here for three gyro designs with varying levels of performance:

Model	Design	ARW ( $^{\circ}/\text{hr}^{1/2}$ )	Bias ( $^{\circ}/\text{hr}$ )	Size ( $\text{cm}^3$ )
Litton LN200 [25]	Fiber Optic Gyro	0.021	0.47	490
SAGEM GLC8 [13]	Ring Laser Gyro	0.15	0.6	1000
Draper MM Gyro [19]	Tuning Fork Gyro	0.25	5.0	27

The Draper gyro is used in this design to demonstrate the potential benefits of a low cost gyro system. Bias drift performance of  $5^{\circ}/\text{hr}$  RMS for the MM gyro has only been achieved in temperature controlled experiments. The gyro may encounter large temperature variations in space, so the gyro bias statistic is used only as a target value for future on orbit MM gyro performance. All of the simulation tests are conducted using the MM gyro error model. Linear covariance analysis is used in section 5. 4 to examine filter sensitivity to changes in the gyro error parameters.



# Chapter 4

## Filter Design

### 4. 1 Introduction

This chapter details design of an Extended Kalman Filter for attitude determination using measurements from multiple GPS antennas and a three axis gyro assembly. After a review of the Extended Kalman filter and description of the filter state, key elements of the filter algorithm are presented. The algorithm is divided into three components: state propagation, measurement update and integrity monitoring. In the state propagation section, spacecraft attitude dynamics are presented along with an overview of the major environmental disturbance torques acting on the vehicle. Discussion of the measurement update in section 4. 4 includes development of GPS and gyro measurement sensitivities as a function of the filter state.

In section 4. 5, the motivation for an integrity monitoring algorithm is presented. This is followed by a description of the decision making logic used in the filter and potential shortcomings of the design.

### 4. 2 Filter Equations

Spacecraft attitude estimation involves propagation of nonlinear rotational dynamics. An optimal nonlinear solution does not exist to this problem, but an approximate solution is possible using the Extended Kalman Filter. The Kalman filter produces an optimal state estimate for a linear system driven by white process and measurement noise. Extension to nonlinear systems requires linearization of the dynamics about a nominal operating point. Consider the nonlinear dynamics given in equation 4.1:

$$\dot{x}(t) = f(x(t), t) + g(x(t), t)w(t) \quad 4.1$$

$$y_k = h(x_{k-}, t_k) \quad 4.2$$

The subscript  $k$  refers to the measurement at time  $t_k$ .  $w(t)$  is a white Gaussian process noise with

intensity  $\mathbf{Q}(t)$  and  $\nu_k$  is discrete white Gaussian measurement noise with intensity  $\mathbf{R}_k$ :

$$E[\mathbf{w}(t)\mathbf{w}(t-\tau)^T] = \mathbf{Q}(t)\delta(t-\tau) \quad 4.3$$

$$E[\nu_k\nu_k^T] = \mathbf{R}_k\delta(k-j) \quad 4.4$$

Let  $\hat{\mathbf{x}}$  be the state estimate with associated error covariance matrix  $\mathbf{P}$ . The estimate immediately prior to the incorporation of measurement  $\mathbf{y}_k$  is referred to as  $\hat{\mathbf{x}}_{k-}$ .  $\hat{\mathbf{x}}_{k+}$  is the estimate immediately after the measurement update. Dynamics of a small state error vector  $\tilde{\mathbf{x}}$  can be expressed to first order by the linearized system:

$$\dot{\tilde{\mathbf{x}}}(t) = \mathbf{F}(t)\tilde{\mathbf{x}}(t) + \mathbf{G}(t)\mathbf{w}(t) \quad 4.5$$

where the system is linearized about the best estimate of  $\mathbf{x}$  at time  $t$ :

$$\mathbf{F}(t) \equiv \frac{\partial}{\partial \mathbf{x}} f(\mathbf{x}(t), t) \Big|_{\hat{\mathbf{x}}(t_-)} \quad 4.6$$

$$\mathbf{G}(t) \equiv \frac{\partial}{\partial \mathbf{x}} g(\mathbf{x}(t), t) \Big|_{\hat{\mathbf{x}}(t_-)} \quad 4.7$$

If a predicted measurement is formulated at time  $t_k$  using the state estimate and the non-linear measurement equation,

$$\hat{\mathbf{y}}_k = \mathbf{h}(\hat{\mathbf{x}}_{k-}, t_k) \quad 4.8$$

then the measurement residual  $\mathbf{z}_k$  is the difference between the predicted and actual measurement:

$$\mathbf{z}_k = \mathbf{y}_k - \hat{\mathbf{y}}_k \quad 4.9$$

The residual is related to the state error  $\tilde{\mathbf{x}}$  by the linearized sensitivity matrix,  $\mathbf{H}_k$ ,

$$\mathbf{z}_k = \mathbf{H}_k \tilde{\mathbf{x}}_k + \nu_k \quad 4.10$$

$$\mathbf{H}_k \equiv \frac{\partial \mathbf{y}_k}{\partial \mathbf{x}} \Big|_{\hat{\mathbf{x}}_{k-}} \quad 4.11$$

and the optimal state correction is a function of the residual and the Kalman gain,  $K_k$ :

$$\hat{x}_{k+} \equiv \hat{x}_{k-} + K_k z_k \quad 4.12$$

$K_k$  is calculated as:

$$K_k \equiv P_{k-} H_k^T (H_k P_{k-} H_k^T + R_k)^{-1} \quad 4.13$$

The error covariance matrix  $P$  must be updated to reflect incorporation of the measurement. The Joseph form of the covariance update is used to preserve symmetry of the covariance matrix:

$$P_{k+} = (1 - K_k H_k) P_{k-} (1 - K_k H_k)^T + K_k R_k K_k^T \quad 4.14$$

After the measurement update, the state estimate  $\hat{x}_{k+}$  is propagated to time  $t_{k+1}$  using the noise-free nonlinear dynamics:

$$\dot{\hat{x}}(t) = f(\hat{x}(t), t) \quad 4.15$$

The dynamics of the linearized error covariance  $P$  over this interval are given by the matrix Riccati equation:

$$\dot{P} = FP + FP^T + GQG^T \quad 4.16$$

Discrete propagation of the covariance matrix is possible using the linearized state transition matrix  $\Phi$  and the process noise dynamics  $\tilde{Q}$ :

$$P_{(k+1)-} = \Phi_{k+1, k} P_k \Phi_{k+1, k}^T + \tilde{Q}(t_{k+1, k}) \quad 4.17$$

The state transition matrix is equivalent to linear propagation of a small state perturbation.  $\Phi$  and

$\tilde{\mathbf{Q}}$  are calculated using integration of the linearized state dynamics:

$$\Phi_{k+1, k} = \int_{t_k}^{t_{k+1}} \mathbf{F}(\tau) \Phi_\tau d\tau \quad 4.18$$

$$\Phi_{k, k} = \mathbf{1} \quad 4.19$$

$$\tilde{\mathbf{Q}}(t_{k+1, k}) = \int_{t_k}^{t_{k+1}} \Phi_\tau \mathbf{G}(\tau) \mathbf{Q}(\tau) \mathbf{G}(\tau)^T \Phi_\tau d\tau \quad 4.20$$

Over small time steps computation of  $\Phi$  and  $\tilde{\mathbf{Q}}$  is streamlined by use of the first order Taylor series approximations:

$$\Phi_{k, k} = (\mathbf{1} + \mathbf{F}\Delta t) \quad 4.21$$

$$\tilde{\mathbf{Q}}(t_{k+1, k}) = \mathbf{G}[\mathbf{Q}\Delta t]\mathbf{G}^T \quad 4.22$$

### Filter State

The state of interest for this application is spacecraft orientation with respect to the Local Vertical Local Horizontal (LVLH) frame. The LVLH frame is constructed with the X axis in the orbit velocity direction, the Z axis toward the center of the Earth and the Y axis out of plane. Figure 4.1 depicts the coordinate frame geometry. The body frame, referred to with the subscript B, is shown in an attitude with zero yaw and roll and a positive pitch angle  $\theta$ . The LVLH frame is also

referred to as the navigation frame, and is denoted by the subscript N.

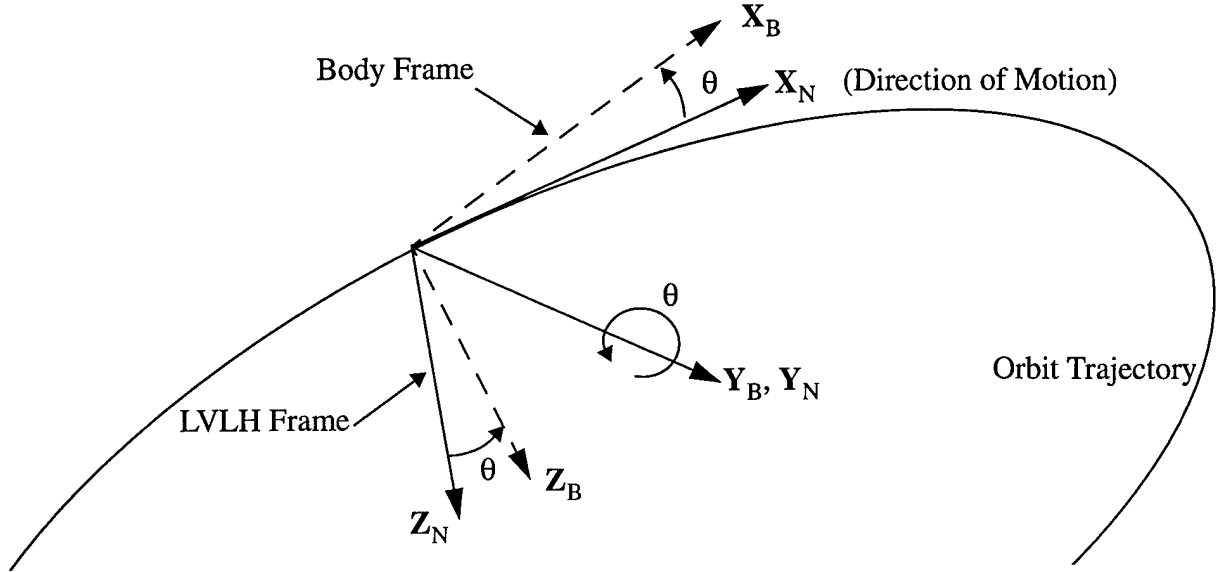


**Figure 4.1: LVLH and Body Frames**

Various parameterizations can be used to represent the transformation from the navigation frame to the body frame. Euler angles are commonly used as an intuitive method of representing rotations, but they suffer from trigonometric terms and a singularity at 90° pitch which make implementation difficult. A direction cosine matrix parameterization eliminates these problems, but the nine matrix elements lead to redundancy in the attitude state [30]. A quaternion attitude representation is chosen to avoid the singularities of Euler angles and the redundancy of a direction cosine representation.

Any coordinate transformation can be expressed in terms of an axis of rotation,  $\hat{e}$  and a rotation angle  $\Phi$ . The quaternion,  $\underline{q}$ , is defined as a function of these two quantities:

$$\underline{q} \equiv \begin{bmatrix} \hat{e} \cdot \sin(\Phi) \\ \cos(\Phi) \end{bmatrix} = \begin{bmatrix} q_1 \\ q_2 \\ q_3 \\ q \end{bmatrix} = \begin{bmatrix} \underline{q} \\ q \end{bmatrix} \quad 4.23$$

$\underline{q}$  is defined as the vector part of the quaternion, while  $q$  is the scalar part. The quaternion from the LVLH to body frame is  ${}^B_N \underline{q}$ . In the remainder of the text, the quaternion  $\underline{q}$  refers to the

LVLH to body transformation,  ${}^B\tilde{\mathbf{q}}^N$ . The superscripts are dropped for clarity.

With each sensor measurement, the filter makes a correction to the estimated quaternion  $\hat{\mathbf{q}}$ .

Quaternion corrections use the quaternion composition operator:

$$\hat{\mathbf{q}}_+ = \mathbf{q}' \otimes \hat{\mathbf{q}}_- = \begin{bmatrix} q' & q_3' & -q_2' & q_1' \\ -q_3' & q' & q_1' & q_2' \\ q_2' & -q_1' & q' & q_3' \\ -q_1' & -q_2' & -q_3' & q' \end{bmatrix} \begin{bmatrix} \hat{q}_{1-} \\ \hat{q}_{2-} \\ \hat{q}_{3-} \\ \hat{q}_- \end{bmatrix} \quad 4.24$$

Here,  $\mathbf{q}'$  is some arbitrary correction to the estimated state. The error quaternion,  $\tilde{\mathbf{q}}$ , is defined as the quaternion rotation from the estimated state  $\hat{\mathbf{q}}$  to the true state  $\mathbf{q}$ :

$$\tilde{\mathbf{q}} = \mathbf{q} \otimes \hat{\mathbf{q}}^* \quad 4.25$$

$\mathbf{q}^*$  is the quaternion inverse operator:

$$\mathbf{q}^* = \begin{bmatrix} -\mathbf{q} \\ q \end{bmatrix} \quad 4.26$$

If the update step is chosen small enough, the quaternion state correction at the update time will be sufficiently small to ensure that the scalar component is close to unity [21], and all of the correction knowledge can be captured in the vector part  $\mathbf{q}$ .

When deriving the differential phase measurement sensitivity, it is useful to relate the error quaternion,  $\tilde{\mathbf{q}}$ , to the DCM error,  ${}^B\tilde{\mathbf{C}}^N$ , defined in equation 4.27:

$${}^B\tilde{\mathbf{C}}^N = {}^B\mathbf{C}^N ({}^B\hat{\mathbf{C}}^N)^T \quad 4.27$$

For small rotation magnitudes, the DCM error can be expressed as a function of the small angle

roll, pitch and yaw Euler angles,  $\phi$ ,  $\theta$ , and  $\psi$ :

$${}^B\tilde{\mathbf{C}}^N \approx \left[ \mathbf{1} + \begin{bmatrix} \phi \\ \theta \\ \psi \end{bmatrix}_x \right] \quad 4.28$$

Here,  $[ ]_x$  is the skew matrix:

$$\begin{bmatrix} \phi \\ \theta \\ \psi \end{bmatrix}_x = \begin{bmatrix} 0 & \psi & -\theta \\ -\psi & 0 & \phi \\ \theta & -\phi & 0 \end{bmatrix} \quad 4.29$$

By definition, the error  $\tilde{\mathbf{q}}$  is just one half of the small Euler angle rotations,

$$\tilde{\mathbf{q}} = \begin{bmatrix} \frac{\phi}{2} & \frac{\theta}{2} & \frac{\psi}{2} \end{bmatrix}^T \quad 4.30$$

resulting in a quaternion representation of the DCM error:

$${}^B\tilde{\mathbf{C}}^N \approx (\mathbf{1} + [2\tilde{\mathbf{q}}]_x) \quad 4.31$$

Because of this convenient property, the filter attitude state is defined as  $2\tilde{\mathbf{q}}$ , making it interchangeable with the small angle rotations.

The filter state also includes  $\underline{\omega}_{BN}^B$ , the angular rate vector in the *body-fixed* frame.  $\underline{\omega}_{BN}^B$  expresses motion of the body with respect to the navigation frame. A body fixed representation simplifies propagation of the attitude quaternion [21]. The rest of the state vector is composed of a disturbance torque estimate,  $N_o$ , the gyro bias estimate,  $\mathbf{b}_g$ , and the GPS error states

$$[\underline{\Delta\beta} \ \underline{\Delta\xi} \ \underline{\delta b}] :$$

$$\mathbf{x} = [2\tilde{\mathbf{q}} \ \underline{\omega}_{BN}^B \ N_o \ \mathbf{b}_g \ \underline{\Delta\beta} \ \underline{\Delta\xi} \ \underline{\delta b}] \quad 4.32$$

### Algorithm

The filter algorithm is shown in figure 4.2. The attitude and gyro portion of the filter are con-

structed using a standard EKF design. GPS measurement integration requires some additional steps. GPS “housekeeping” involves satellite selection and calculation of the GPS spacecraft states. The selection algorithm is discussed in section 4. 5 along with the integrity monitoring algorithm. Integrity monitoring is necessary due to the non-linear nature of integer ambiguities and the differential phase measurement equation.

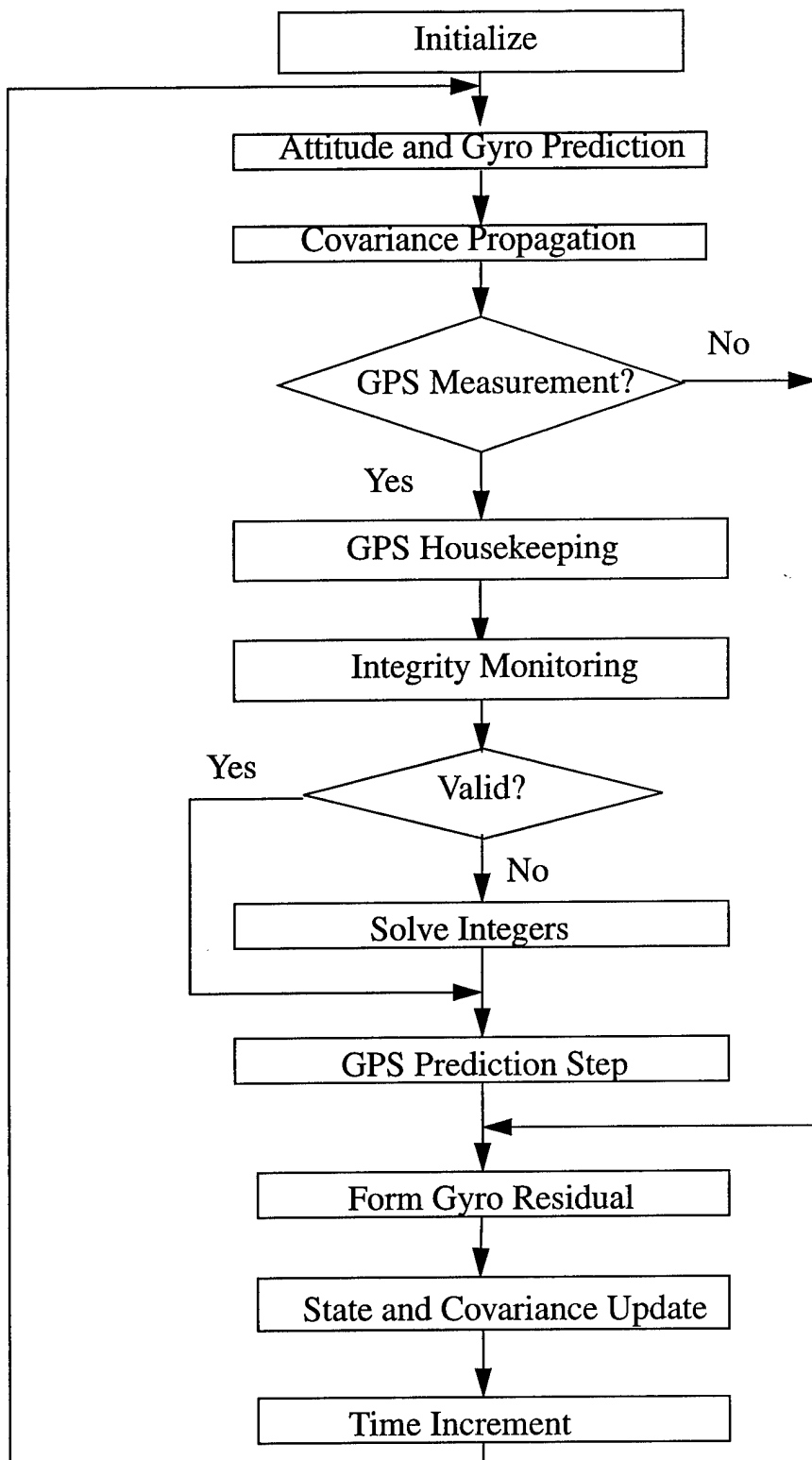


Figure 4.2: Filter Algorithm

## 4.3 State Propagation

The propagation section is divided into two sections. Section 4.3.1 discusses the non-linear attitude dynamics required to predict the filter state. Section 4.3.2 presents the linearized attitude dynamics needed for propagation of the error covariance matrix. Linearized dynamics for the gyro and GPS error states are also presented here. The error states are all modeled as linear systems, so these dynamics are used for both the state prediction and covariance propagation.

### 4.3.1 Non-Linear Attitude Dynamics

The quaternion attitude is propagated using the quaternion kinematic equation:

$$\dot{\underline{q}} = \frac{1}{2} \cdot \begin{bmatrix} \underline{\omega}_{BN}^B \\ 0 \end{bmatrix} \otimes \underline{q} \quad 4.33$$

As stated previously,  $\underline{\omega}_{BN}^B$  is the angular rate of the body frame with respect to the navigation frame expressed in the body frame.  $\underline{\omega}_{BN}^B$  can be measured directly from the gyros or propagated analytically using the rate dynamics. The former method, referred to as “gyro replacement mode,” does not exploit *a priori* modeling of dynamic forces such as the gravity gradient torque. In order to take advantage of dynamic modeling, this filter uses the latter method, treating the gyro rate output as a measurement rather than truth. The required rate dynamics are now derived using conservation of angular momentum.

Total angular momentum for a rigid body is given by equation 4.34:

$$\mathbf{h} = \mathbf{I} \underline{\omega}_{BI} \quad 4.34$$

The inertia tensor,  $\mathbf{I}$ , and the inertial frame to body frame angular rates,  $\underline{\omega}_{BI}$ , must be expressed in a common frame. All of the following equations are formulated in the *body* frame if not otherwise specified. If internal momentum storage devices such as momentum wheels are used, the additional momentum must be included on the right hand side of equation 4.34.

Conservation of angular momentum dictates that the derivative of  $\mathbf{h}$  with respect to the inertial

frame equals the sum of the applied torques [11]:

$$\frac{d\mathbf{h}}{dt} \Big|_I = N \quad 4.35$$

Here,  $N$  is the sum of external disturbance torques expressed in the body frame. Substituting for  $\mathbf{h}$  according to 4.34 results in Euler's vector equation of motion:

$$\frac{d}{dt}(\mathbf{I}\underline{\omega}_{BI}) \Big|_I = N \quad 4.36$$

Equation 4.36 is formulated in inertial space, but the desired dynamics must be derived in the body frame. The two representations are related according to equation 4.37:

$$\frac{d}{dt}(\mathbf{A}) \Big|_I = \frac{d}{dt}(\mathbf{A}) \Big|_B + \underline{\omega}_{BI} \times (\mathbf{A}) \quad 4.37$$

Applying this identity to equation 4.36,

$$\frac{d}{dt}(\mathbf{I}\underline{\omega}_{BI}) \Big|_B + \underline{\omega}_{BI} \times (\mathbf{I}\underline{\omega}_{BI}) = N \quad 4.38$$

Total angular velocity is the sum of the filter state,  $\underline{\omega}_{BN}$ , and the orbit rate,  $\underline{\omega}_{NI}$ :

$$\underline{\omega}_{BI} = \underline{\omega}_{BN} + \underline{\omega}_{NI} \quad 4.39$$

This substitution is used along with the assumption that the inertia tensor,  $\mathbf{I}$ , is fixed in the body frame to isolate the derivative of  $\underline{\omega}_{BN}$ :

$$\frac{d\underline{\omega}_{BN}}{dt} \Big|_B + \frac{d\underline{\omega}_{NI}}{dt} \Big|_B = \mathbf{I}^{-1} [N - \underline{\omega}_{BI} \times (\mathbf{I}\underline{\omega}_{BI})] \quad 4.40$$

Applying equation 4.37 again,

$$\frac{d\underline{\omega}_{NI}}{dt} \Big|_B = \frac{d\underline{\omega}_{NI}}{dt} \Big|_N + \underline{\omega}_{BN} \times \underline{\omega}_{NI} \quad 4.41$$

For a circular orbit,  $\underline{\omega}_{NI}$ , the angular velocity of the navigation frame with respect to the inertial

frame, is constant in the navigation frame:

$$\underline{\omega}_{NI}^N = \begin{bmatrix} 0 \\ -\omega_{NI} \\ 0 \end{bmatrix} \quad 4.42$$

Applying equation 4.41 and 4.42 to equation 4.40, the angular rate dynamics are expressed as a function of the current state:

$$\frac{d\underline{\omega}_{BN}}{dt} \Big|_B = \mathbf{I}^{-1} [\mathbf{N} - \underline{\omega}_{BI} \times (\mathbf{I} \underline{\omega}_{BI})] - \underline{\omega}_{BN} \times \underline{\omega}_{NI} \quad 4.43$$

Equation 4.43 is applied to the state estimate to predict  $\underline{\omega}_{BN}$  in the filter:

$$\frac{d\hat{\underline{\omega}}_{BN}}{dt} \Big|_B = \mathbf{I}^{-1} [\hat{\mathbf{N}}_o + \hat{\mathbf{N}}_{gg} - \hat{\underline{\omega}}_{BI} \times \mathbf{I}(\hat{\underline{\omega}}_{BI})] - \hat{\underline{\omega}}_{BN} \times \hat{\underline{\omega}}_{NI} \quad 4.44$$

$\mathbf{N}_{gg}$  is the gravity gradient torque. The orbit rate is an estimate because the estimated attitude matrix is used to transform the rate to the body frame:

$$\hat{\underline{\omega}}_{NI}^B = {}^B\hat{\mathbf{C}}^N \underline{\omega}_{NI}^N \quad 4.45$$

A first order linearized approximation of equation 4.44 is used to propagate  $\hat{\underline{\omega}}_{BN}$  in the filter at the integration rate of 2 Hz. At each integration step, the quaternion state estimate is propagated using the new rate estimate and equation 4.33. Any commanded control is added as an impulsive correction to the angular rate.

### Disturbance Torque

The primary disturbance torques acting on a spacecraft in low earth orbit are the gravity gradient torque, solar pressure, magnetic dipole and aerodynamic forces [20]. Gravity gradient torque is computed analytically using the spacecraft inertia tensor and the estimated body attitude. Solar pressure, magnetic torque and other disturbances are lumped into a first order exponentially correlated stochastic term with a time constant of one half the orbit period.

The gravity gradient torque is conveniently expressed in body coordinates [26]:

$$N_{gg} = \frac{3\mu}{|r|^5} [r \times (Ir)] \quad 4.46$$

Here,  $\mu$  is the earth gravitational constant and  $r$  is the position of the vehicle in the ECEF frame expressed in body coordinates. The dependence of the gravity gradient torque (and hence angular acceleration) on spacecraft attitude will be factored into the linearized dynamics.

The gravity gradient torque is a function of the spacecraft inertia tensor,  $I$ . The Iridium inertia tensor is estimated for this analysis by assuming a cylindrical body, two dimensional solar arrays and an even mass distribution. The resulting inertia tensor is shown in equation 4.47:

$$I = \begin{bmatrix} 1538 & 0 & 0 \\ 0 & 1006 & 0 \\ 0 & 0 & 622 \end{bmatrix} \quad 4.47$$

The remaining disturbance torques,  $N_o$ , are modeled as a first order Markov process. The steady state covariance of this process is estimated using worst case equations from [20].

Solar radiation pressure torque,  $N_{sp}$ , is related to the spacecraft physical characteristics through equation 4.48:

$$N_{sp} = F_{sp}(c_{ps} - c_g) \quad 4.48$$

$(c_{ps} - c_g)$  is the distance between the spacecraft center of solar pressure and center of gravity. A value of 1/6 of the total height, or 0.7 m, is used. Maximum solar pressure force,  $F_{sp}$ , is approximately  $7.3 \times 10^{-5}$  N in an 800 km orbit, so the maximum solar pressure is  $5.0 \times 10^{-5}$  N-m.

Magnetic dipole is the product of the vehicle residual dipole,  $D$ , and the strength of the Earth's magnetic field,  $B$ . Typical value of  $D$  for a small spacecraft is  $1 \text{ A} \cdot \text{m}^2$  [20], resulting in a maximum magnetic torque of  $4.3 \times 10^{-5}$  N-m.

Aerodynamic forces are multiplied by the distance from the spacecraft center of pressure,  $c_{sp}$ , to

the center of gravity,  $c_g$ , to give the aerodynamic torque:

$$N_a = F_a(c_{pa} - c_g) \quad 4.49$$

The maximum expected aerodynamic force at 800 km is  $5.6 \times 10^{-5}$  N. Because of the large offset of the Iridium solar panels from the center of gravity of the spacecraft, an aerodynamic offset of 1 m is used to calculate the maximum aerodynamic torque.

The total maximum disturbance torque from all three of these sources is  $1.5 \times 10^{-4}$  N-m. As a conservative approximation, this value is used as the steady state standard deviation of the disturbance torque model on each axis,  $\sigma_{N_o}^2$ . A time constant of one half the orbit period is used to model dependence of the torques, primarily magnetic dipole and solar pressure, on the location of the satellite within its orbit. The resulting disturbance torque dynamics are shown in equations 4.50 and 4.51:

$$\frac{d}{dt} N_o = -\frac{1}{\tau_N} N_o + w_N(t) \quad 4.50$$

$$\sigma_{w_N}^2 = \frac{2 \cdot \sigma_{N_o}^2}{\tau_{N_o}} \quad 4.51$$

### 4.3.2 Linearized Dynamics

The linearized dynamics are divided into an attitude partition and an error partition based on the following division of the state:

$$\begin{aligned} x_1 &= \left[ 2\tilde{\mathbf{q}} \ \underline{\omega}_{BN} \ N_o \right]^T \\ x_2 &= \left[ \underline{b}_g \ \underline{\Delta\beta} \ \underline{\Delta\xi} \ \underline{\delta b} \right]^T \end{aligned} \quad 4.52$$

The process noise is divided into two blocks which correspond to this partition. Notice that there is process noise on the angular rate but not on the attitude state:

$$\begin{aligned} w_1 &= \left[ \mathbf{0}_{1 \times 3} \ w_\omega \ w_N \right]^T \\ w_2 &= \left[ w_{b_g} \ w_{\Delta\beta} \ w_{\Delta\xi} \ w_{\delta b} \right]^T \end{aligned} \quad 4.53$$

The resulting dynamics are given in equations 4.54 and 4.55:

$$\ddot{\tilde{x}}_1 = \mathbf{F}_1 \tilde{x} + \mathbf{G}_1 w_1 \quad 4.54$$

$$\ddot{\tilde{x}}_2 = \mathbf{F}_2 \tilde{x} + \mathbf{G}_2 w_2 \quad 4.55$$

The linearized attitude dynamics are computed by partial differentiation of equations 4.33, 4.44 and 4.50:

$$\mathbf{F}_1 = \begin{bmatrix} \mathbf{A} \mathbf{1}_{3 \times 3} & \mathbf{0} \\ \mathbf{B} \mathbf{I}^{-1} \mathbf{C} & \mathbf{I}^{-1} \\ \mathbf{0} & -\frac{1}{\tau_N} \mathbf{1}_{3 \times 3} \end{bmatrix} \quad 4.56$$

$$\mathbf{A} = [\hat{\omega}_{BN}^B]_x \quad 4.57$$

$$\mathbf{B} = \mathbf{I}^{-1} \left( \frac{\partial N_{gg}}{\partial (2\tilde{\mathbf{q}})} \right) = 3\omega_{NI}^2 ([\hat{r}]_x \mathbf{I} - [\mathbf{I} \hat{r}]_x) [\hat{r}]_x \quad 4.58$$

$$\mathbf{C} = \mathbf{I}^{-1} ([\mathbf{I} \hat{\omega}_{BI}^B]_x - [\hat{\omega}_{BI}^B]_x \mathbf{I}) - [\hat{\omega}_{NI}^B]_x \quad 4.59$$

$$\mathbf{G}_1 = \begin{bmatrix} \mathbf{0} & \mathbf{0} \\ \mathbf{I}^{-1} & \mathbf{0} \\ \mathbf{0} & \mathbf{1}_{3 \times 3} \end{bmatrix} \quad 4.60$$

Dynamics of the error states were derived in section 3. 2. The results are summarized here:

$$F_2 = \begin{bmatrix} \left(-\frac{1}{\tau_{b_s}}\right)I_{3 \times 3} & 0 & 0 & 0 \\ 0 & \left(-\frac{1}{\tau_{\Delta\beta}}\right)I_{n_{BL} \times n_{BL}} & 0 & 0 \\ 0 & 0 & \begin{bmatrix} \left(-\frac{1}{\tau_{\Delta\xi_1}}\right)I_{n_{BL} \times n_{BL}} & 0 \\ \dots & \left(-\frac{1}{\tau_{\Delta\xi_{n_{CH}}}}\right)I_{n_{BL} \times n_{BL}} \end{bmatrix} & 0 \\ 0 & 0 & 0 & \left(-\frac{1}{\tau_{\delta b}}\right)I_{n_{BL} \times n_{BL}} \end{bmatrix} \quad 4.61$$

$$G_2 = \begin{bmatrix} I_{3 \times 3} & 0 & 0 & 0 \\ 0 & I_{n_{BL} \times n_{BL}} & 0 & 0 \\ 0 & 0 & I_{(n_{BL}n_{CH}) \times (n_{BL}n_{CH})} & 0 \\ 0 & 0 & 0 & I_{n_{BL} \times n_{BL}} \end{bmatrix} \quad 4.62$$

As mentioned earlier, these linearized dynamics are used for the error state prediction as well as for covariance propagation.

## 4. 4 Measurement Prediction and Update

The measurement update incorporates all available sensor measurements to correct errors in the state estimate. The filter compares the actual measurement to the measurement prediction and applies an optimal gain to the difference based on the measurement sensitivity,  $H_k$ . This section presents calculation of the predicted measurements along with derivation of the associated measurement sensitivity for both GPS and gyro measurements.

### 4.4.1 Differential Phase

#### Predicted Phase

The predicted phase at time  $t_k$  is calculated by substituting the appropriate state estimates into

equation 1.4. All of the estimates come from the state  $\mathbf{x}_{k-}$ :

$$\Delta\hat{\phi}_{i,j} = (\mathbf{b}_{i_0}^B)^T [\hat{\rho}_{j,est}^B] - \Delta\hat{k}_{ij} + \hat{\epsilon}_{ij} \quad 4.63$$

The estimated LOS vector,  $\hat{\rho}_{j,est}^B$ , is constructed by transforming the true LOS in the navigation frame using the estimated attitude matrix:

$$[\hat{\rho}_{j,est}^B] = {}^B\hat{C}^N \cdot \hat{\rho}_j^N \quad 4.64$$

The predicted GPS error is composed of the bias calibration value and the line bias, correlated noise and baseline length error estimates at time  $t_{k-}$ .

$$\Delta\hat{\epsilon}_{ij} = \chi([\hat{\rho}_{j,est}^B], i) + \Delta\hat{\beta}_i + \Delta\hat{\xi}_{i,j} + (\mathbf{u}_{b_i}^T \cdot [\hat{\rho}_{j,est}^B])\delta\hat{b}_i \quad 4.65$$

Implementation of the bias calibration model,  $\chi$ , is discussed in section 3.3.2. The differential phase error due to baseline length variation ( $\delta\hat{b}_i$ ) is formulated according to equation 3.27:

$$\epsilon_{b_{i,j}} = (\mathbf{u}_{b_i}^T \cdot \hat{\rho}_j)\delta b_i \quad 3.27$$

Predicted phase is subtracted from measured differential phase to produce the differential phase residual,

$$z_{k_{GPS}} = \underline{\Delta\phi}(t_k) - \hat{\Delta\phi}(t_{k-}) \quad 4.66$$

### Differential Phase Sensitivity

The differential phase measurement sensitivity is derived from the measurement equation:

$$\Delta\phi_{i,j} = (\mathbf{b}_{i_0}^B)^T \cdot \hat{\rho}_j^B - \Delta k_{ij} + \Delta\epsilon_{ij} \quad 1.4$$

The error term was defined in section 3.2,

$$\Delta\epsilon_{i,j} = \Delta m_{i,j} + \Delta p_{i,j} + \Delta\beta_i + \Delta\xi_{i,j} + (\mathbf{u}_{b_i}^T \cdot \hat{\rho}_j^B)\delta b_i + \Delta v_{i,j} \quad 3.4$$

and sensitivity of differential phase to each of the GPS differential phase errors was derived in section 3.2. Sensitivity to the attitude state,  $2\tilde{\mathbf{q}}$ , is shown in equation 4.67:

$$\mathbf{H}_{2\tilde{\mathbf{q}}} = \frac{\partial \Delta\phi_{i,j}}{\partial 2\tilde{\mathbf{q}}} \quad 4.67$$

The sensitivity is easier to calculate if the differential phase prediction is first subtracted from the measurement:

$$\mathbf{H}_{2\tilde{\mathbf{q}}} = \frac{\partial}{\partial 2\tilde{\mathbf{q}}} (\underline{\Delta\varphi} - \hat{\underline{\Delta\varphi}}) = \frac{\partial z_{k_{GPS}}}{\partial 2\tilde{\mathbf{q}}} \quad 4.68$$

This is possible because the measurement prediction at time  $t_{k-}$  is not a function of the attitude state at time  $t_k$ :

$$\frac{\partial}{\partial 2\tilde{\mathbf{q}}_k} \underline{\Delta\varphi}(t_{k-}) = \mathbf{0} \quad 4.69$$

Assuming that the integer solution is correct, residual  $z_k$  is calculated by substituting equations 1.4 and 4.63 into equation 4.66:

$$z_{k_{i,j}} = (\mathbf{b}_{i_0}^B)^T \cdot [\hat{\mathbf{p}}_j^B - \hat{\mathbf{p}}_{j,est}^B] + \Delta\varepsilon_{i,j} - \Delta\hat{\varepsilon}_{ij} \quad 4.70$$

An expression is needed for the error in the LOS vector. According to equation 4.31, the attitude error matrix can be formulated as a function of the error quaternion. This substitution is used with equation 4.64 to calculate error in the LOS vector as a function of the attitude error state:

$$\hat{\mathbf{p}}_j^B \approx (\mathbf{1} + [2\tilde{\mathbf{q}}]_x)^B \hat{\mathbf{C}}^N \cdot \hat{\mathbf{p}}_j^N \quad 4.71$$

$$\hat{\mathbf{p}}_j^B = (\mathbf{1} + [2\tilde{\mathbf{q}}]_x) [\hat{\mathbf{p}}_{j,est}^B] \quad 4.72$$

$$\hat{\mathbf{p}}_j^B - [\hat{\mathbf{p}}_{j,est}^B] \approx [2\tilde{\mathbf{q}}]_x \cdot [\hat{\mathbf{p}}_{j,est}^B] \quad 4.73$$

Incorporating this expression into equation 4.70, the measurement residual to first order is:

$$z_{i,j} = \mathbf{b}_{i_0}^T \cdot [2\tilde{\mathbf{q}}]_x \cdot [\hat{\mathbf{p}}_{j,est}^B] + \Delta\tilde{\varepsilon}_{ij} \quad 4.74$$

The left hand side of equation 4.74 is the component of the residual due to attitude error, while the term  $\Delta\tilde{\varepsilon}_{ij}$  is the difference between the true and predicted GPS measurement errors, calculated using equations 3.4 and 4.65:

$$\Delta\tilde{\varepsilon}_{ij} = \Delta m_{i,j} + \Delta p_{i,j} - \chi([\hat{\mathbf{p}}_{j,est}^B], i) + \Delta\tilde{\beta}_i + \Delta\tilde{\xi}_{i,j} + (\mathbf{u}_{b_i}^T \cdot [\hat{\mathbf{p}}_{j,est}^B]) \delta\tilde{b}_i + \Delta v_{i,j} \quad 4.75$$

Taking the partial derivative of equation 4.75 with respect to the quaternion error state  $2\tilde{\mathbf{q}}$ ,

$$\frac{\partial z_{i,j}}{\partial 2\tilde{\mathbf{q}}} = [\hat{\mathbf{p}}_{j,est}^B]_x \cdot \mathbf{b}_{i_0} \quad 4.76$$

The GPS differential phase measurement has no sensitivity to the angular rate, disturbance torque or gyro bias.

The remaining GPS error sensitivities are summarized here. Derivation of the error sensitivities can be found in section 3.2.

Correlated noise sensitivity is the identity for the channel and baseline corresponding to the correlated error state:

$$\frac{\partial \Delta \varphi_{i,j}}{\partial \Delta \xi_{k,l}} = \delta(i, k) \delta(j, l) \quad 3.17$$

Line bias sensitivity is the identity for each measurement on the appropriate baseline:

$$\frac{\partial \Delta \varphi_{i,j}}{\partial \Delta \beta_k} = \delta(i, k) \quad 3.19$$

Sensitivity to a baseline length variation  $\delta b_k$  is a function of the geometric relationship between the LOS vector and the baseline unit vector:

$$\frac{\partial \Delta \varphi_{i,j}}{\partial (\delta b_k)} = \delta(i, k) \cdot (\mathbf{u}_{b_j}^T \cdot \hat{\mathbf{p}}_{j,est}^B) \quad 3.28$$

### White Noise

White noise on the GPS measurement is modeled according to equations 3.12 and 3.13 using the intensity model from section 3.3.3.

## 4.4.2 Gyro Measurement

Assuming that the gyro assembly is mounted at the center of gravity of the vehicle, the gyro measurement  $\omega_M$  is a direct measurement of the spacecraft inertial rates in the body frame corrupted

only by a bias term and white noise:

$$\underline{\omega}_M = \underline{\omega}_{BI}^B + \mathbf{b}_g + \mathbf{v}_g \quad 4.77$$

Substituting from equation 4.39,

$$\underline{\omega}_M = \underline{\omega}_{BN}^B + \underline{\omega}_{NI}^B + \mathbf{b}_g + \mathbf{v}_g \quad 4.78$$

### Prediction

A measurement prediction is formulated based on the non-linear attitude propagation and linear gyro bias dynamics:

$$\hat{\underline{\omega}}_M = \hat{\underline{\omega}}_{BN}^B + {}^B\hat{\mathbf{C}}^N \underline{\omega}_{NI}^N + \hat{\mathbf{b}}_g \quad 4.79$$

### Update

The measurement residual,  $z_g$ , includes angular rate error, bias error, white noise and an orbit rate transformation error,  $[2\tilde{\mathbf{q}}]_x \cdot \hat{\underline{\omega}}_{NI}^B$ . This term represents error in the orbit rate produced when the rate is transformed to the body frame using an estimate of the attitude matrix,  ${}^B\hat{\mathbf{C}}^N$ .

$$z_g = \tilde{\underline{\omega}}_{BN}^B + [2\tilde{\mathbf{q}}]_x \cdot \hat{\underline{\omega}}_{NI}^B + \tilde{\mathbf{b}}_g + \mathbf{v}_g \quad 4.80$$

Taking the partial derivative of equation 4.80 with respect to the quaternion error state  $[2\tilde{\mathbf{q}}]$ ,

$$\frac{\partial z_g}{\partial [2\tilde{\mathbf{q}}]} = -[\hat{\underline{\omega}}_{NI}^B]_x \quad 4.81$$

The sensitivity to angular rate and gyro bias are both the identity:

$$\frac{\partial z_g}{\partial \underline{\omega}_{BN}^B} = \mathbf{1}_{3 \times 3} \quad 4.82$$

$$\frac{\partial z_g}{\partial \mathbf{b}_g} = \mathbf{1}_{3 \times 3} \quad 4.83$$

## 4.5 Implementation

### 4.5.1 Satellite Selection

Ideally, a receiver would track every visible GPS satellite and all of the measurements could be processed to reach an optimal state estimate in the filter. In most applications, however, the number of measurements must be limited by receiver capability or computational limitations. A simple satellite selection algorithm is presented here which quickly selects a subset of satellites which produces minimal estimation error.

A metric is needed for measuring the quality of a potential set of satellites. The most useful metric of GPS constellation quality for attitude determination is *ADOP*, or attitude dilution of precision. As explained in section 1.4, a dilution of precision gives the ratio between measurement error covariance and solution covariance for the case of normally distributed uncorrelated measurement noise [26]:

$$\sigma_x = DOP \cdot \sigma_\epsilon \quad 4.84$$

The measurement error covariance used here,  $\sigma_\epsilon$ , is the sum total of all differential phase error sources. The least squares solution is not sensitive to the dynamics of each of the individual error sources.

In section 1.4,  $DOP_C$ , the dilution of precision for the attitude matrix, was presented. The objective here is to develop  $DOP_{2\tilde{q}}$ , or *ADOP*, the dilution of precision for the small angle correction in the filter. This *DOP* provides a measure of the theoretical attitude solution accuracy possible with a given set of satellites.

*ADOP* is derived by formulating the least squares solution for attitude at the filter update step. Measurement sensitivity to the small angle state is given in equation 4.76:

$$\mathbf{H}_{2\tilde{q}_{i,j}}^T = [\hat{\rho}_{j,est}^B]_x \cdot \mathbf{b}_{i_0} \quad 4.76$$

If at least three measurements are available, the least squares solution for the small angles can be

computed as shown in equation 4.85:

$$\hat{2\tilde{\mathbf{q}}} = (\mathbf{H}_{2\tilde{\mathbf{q}}}^T \cdot \mathbf{H}_{2\tilde{\mathbf{q}}_{i,j}})^{-1} \mathbf{H}_{2\tilde{\mathbf{q}}_{i,j}}^T \cdot \mathbf{z}_{k_{GPS}} \quad 4.85$$

If the measurement noise is uncorrelated, covariance of the solution is a function of the measurement sensitivity and the measurement noise covariance:

$$\sigma_{2\tilde{\mathbf{q}}}^2 = (\mathbf{H}_{2\tilde{\mathbf{q}}}^T \cdot \mathbf{H}_{2\tilde{\mathbf{q}}})^{-1} \sigma_{\Delta\phi}^2 \quad 4.86$$

Solving for  $ADOP$ ,

$$ADOP_{2\tilde{\mathbf{q}}} = \sqrt{diag(\mathbf{H}_{2\tilde{\mathbf{q}}}^T \cdot \mathbf{H}_{2\tilde{\mathbf{q}}})^{-1}} \quad 4.87$$

Total  $ADOP$ , or  $ADOP_{TOT}$ , is the RSS total of the components of  $ADOP_{2\tilde{\mathbf{q}}}$ :

$$ADOP_{TOT} = \sqrt{tr(\mathbf{H}_{2\tilde{\mathbf{q}}}^T \cdot \mathbf{H}_{2\tilde{\mathbf{q}}})^{-1}} \quad 4.88$$

$tr$  is the trace operator. Because  $2\tilde{\mathbf{q}}$  is the vector of small angle attitude errors,  $ADOP_{TOT}$  is an estimate of total attitude solution accuracy, as shown in equation 4.89:

$$\sqrt{\sigma_\phi^2 + \sigma_\theta^2 + \sigma_\psi^2} = ADOP_{TOT} \cdot \sigma_\epsilon \quad 4.89$$

The various forms of  $ADOP$  are derived in units of rad/rad. In the sequel,  $ADOP$  is converted to units of degrees of attitude error per millimeter of measurement noise ( $^{\circ}/\text{mm}$ ).

A small  $ADOP$  is desirable, as this leads to small estimation errors. Sullivan demonstrates in [27] that  $ADOP_{TOT}$  is minimized for the two baseline, one satellite case by choosing a satellite which is orthogonal to the antenna plane. The satellite selection algorithm developed here extends this logic to the multiple satellite case by choosing the subset of visible satellites which are most nearly orthogonal. In this context, two vectors are defined as “nearly orthogonal” if their dot product is small. For channel  $m$ , the selection algorithm chooses the visible SV with a line of sight vector which minimizes the cost function  $J$ :

$$J(SV_i) = \sum_{j=1}^{m-1} (\hat{\mathbf{p}}_{SV_i}^T \cdot \hat{\mathbf{p}}_j)^2 \quad 4.90$$

Here,  $\hat{\beta}_j$  is the LOS vector for the satellite already chosen for channel  $j$ .  $J(SV_i)$  is the sum of the squared dot products of a candidate satellite,  $i$ , with the  $m-1$  satellites on channels 1 through  $m-1$ . As shown in figure 4.3, the cost function is minimized for the selection of every satellite besides the first. The highest satellite is selected first to guarantee that at least one of the satellites will remain valid until the next satellite selection step:

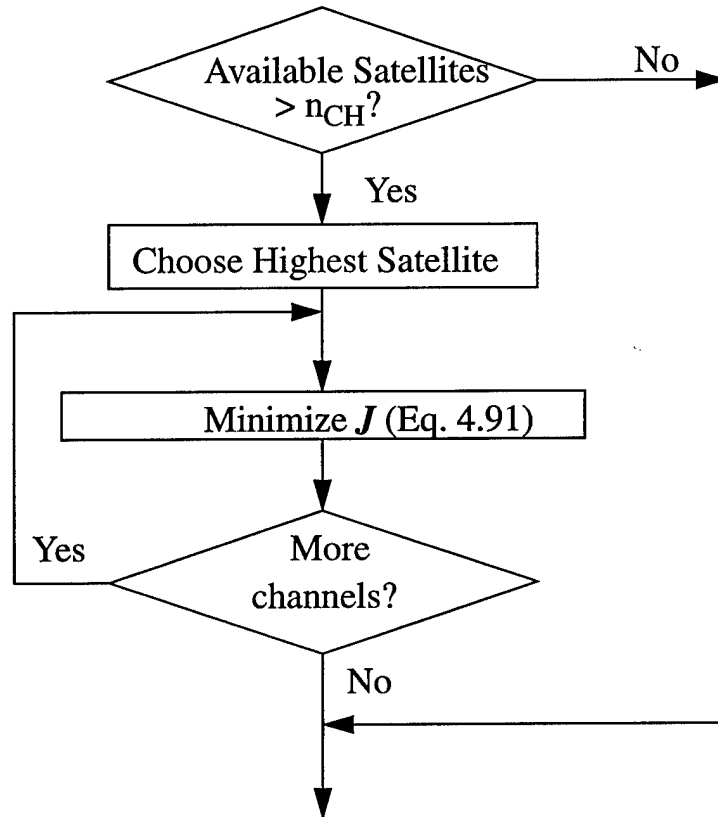


**Figure 4.3: Satellite Selection Algorithm**

The algorithm continues adding satellites until all of the channels are filled or all available satellites are selected.

### 4.5.2 Integrity Monitoring

There are two primary failure modes of this filter algorithm. One is violation of the small angle approximation and the other is an incorrect integer solution.

#### Failure of Linearization

The assumption of small error magnitudes is used to linearize the filter about a nominal operating

point. If the true errors violate these small magnitude constraints, the assumption fails and non-linear terms can de-stabilize the filter. For example, the sensitivity of differential phase to the attitude correction is based on the small angle DCM rule in equation 4.31:

$${}^B\tilde{\mathbf{C}}^N \approx (\mathbf{1} + [2\tilde{\mathbf{q}}]_x) \quad 4.31$$

If the angular correction is large, this identity develops significant errors, and filter gains based on the linearization become invalid.

The filter error covariance  $\mathbf{P}$  can be used to measure uncertainty in the linearization. The linearization is based on the attitude estimate, so uncertainty in the linearization is measured using  $\sigma_{TOT}$ , the total RSS attitude estimation covariance:

$$\sigma_{TOT} = \sqrt{tr(\mathbf{P}_{2\tilde{\mathbf{q}}})} \quad 4.91$$

If  $\sigma_{TOT}$  is greater than a pre-determined threshold, a filter reset is triggered. In practice, this occurs during periods of poor satellite visibility. If no GPS satellites are in sight for an extended period of time, process noise and disturbance torques will cause the attitude covariance to grow. When the uncertainty reaches the linearity threshold, a reset is commanded. As soon as enough satellites are available, the search algorithm resets the filter. In a filter without the linearity constraint, GPS measurements are incorporated into the state estimate as soon as they become available, even if attitude uncertainty is very large. This can lead to divergent state errors, because the filter gains are based on a linearization which may differ significantly from the truth.

### False Integers

The second failure mode is selection of incorrect integers. An incorrect integer solution occurs when the ideal phase for a false attitude matches the measured fractional phase better than ideal measurements for the true attitude. At first, the measurement residuals will remain small, but any motion of the vehicle or the GPS constellation should change the viewing geometry enough to reveal that the integer solution is in error. Unfortunately, the filter has no way of knowing this, and it continues to compute an “optimal” correction with every measurement update.

The integer validity algorithm solves this problem by identifying incorrect integers. Keep in mind

that this algorithm is independent of the integer solution algorithm; while that algorithm solves for possible integers, this algorithm evaluates validity of the integers based on the size of the measurement residuals.

The integrity algorithm could reject any attitude solution which produces large measurement residuals, but some precautions are necessary to avoid invalidating the true solution. Before entering the integer validity loop, the algorithm determines whether the filter is in transient or steady state mode. Transient mode is defined as the time during which the combined attitude and angular rate uncertainty may result in large corrections to the attitude estimate. While this is occurring, large fluctuations in the measurement residuals might be falsely interpreted as invalid integers. Equation 4.92 defines the mode of the filter:

$$SS = [(\sqrt{tr(\mathbf{P}_{2\tilde{q}})} + \Delta t \cdot tr(\mathbf{P}_\omega)) < 10^\circ] \quad 4.92$$

Here,  $SS = 1$  during steady state operation and  $SS = 0$  during transient mode.

The most common source of a transient mode is initialization of the filter after an integer reset. If the filter is not given time to settle transients before the integer validity subroutine is called, the filter may become stuck in endless loops of calling the integer solution and integer validity algorithms.

If the filter is indeed in steady state mode, the integer validity subroutine is called. Only good measurements are used in the validity routine. Bad measurements include measurements from satellites flagged below the elevation mask and measurements reported as invalid by the receiver. Residuals are calculated by comparing the good measurements to predicted differential phase for the current attitude estimate. The residuals are compared to a threshold which is measurement-specific. The threshold is calculated by combining residual uncertainty from the state covariance with residual uncertainty from the measurement noise:

$$\sigma_{\Delta\phi(2\tilde{q}, \omega)}^2 = ((\mathbf{H}_{2\tilde{q}}^T \mathbf{H}_{2\tilde{q}}) \sigma_{2\tilde{q}}^2 + (\mathbf{H}_\omega^T \mathbf{H}_\omega) (\Delta t \cdot \sigma_\omega)^2) \quad 4.93$$

$$\sigma_{\Delta\phi(v)}^2 = \mathbf{R} \quad 4.94$$

$$z_{Thresh} = 3\sqrt{\sigma_{\Delta\phi(2\tilde{q}, \omega)}^2 + \sigma_{\Delta\phi(v)}^2} \quad 4.95$$

$\sigma_{\Delta\varphi(2\tilde{q}, \underline{\omega})}^2$  is the differential phase uncertainty due to attitude and angular rate errors.  $\sigma_{\Delta\varphi(v)}^2$  is the uncertainty due to the measurement noise. As shown in equation 4.95, the threshold  $z_{Thresh}$  is three times the total uncertainty expected from the attitude, attitude rate and measurement noise. A more robust design could incorporate the uncertainty due to line bias, baseline length and correlated noise errors as well.

Figure 4.4 shows the integrity monitoring algorithm:

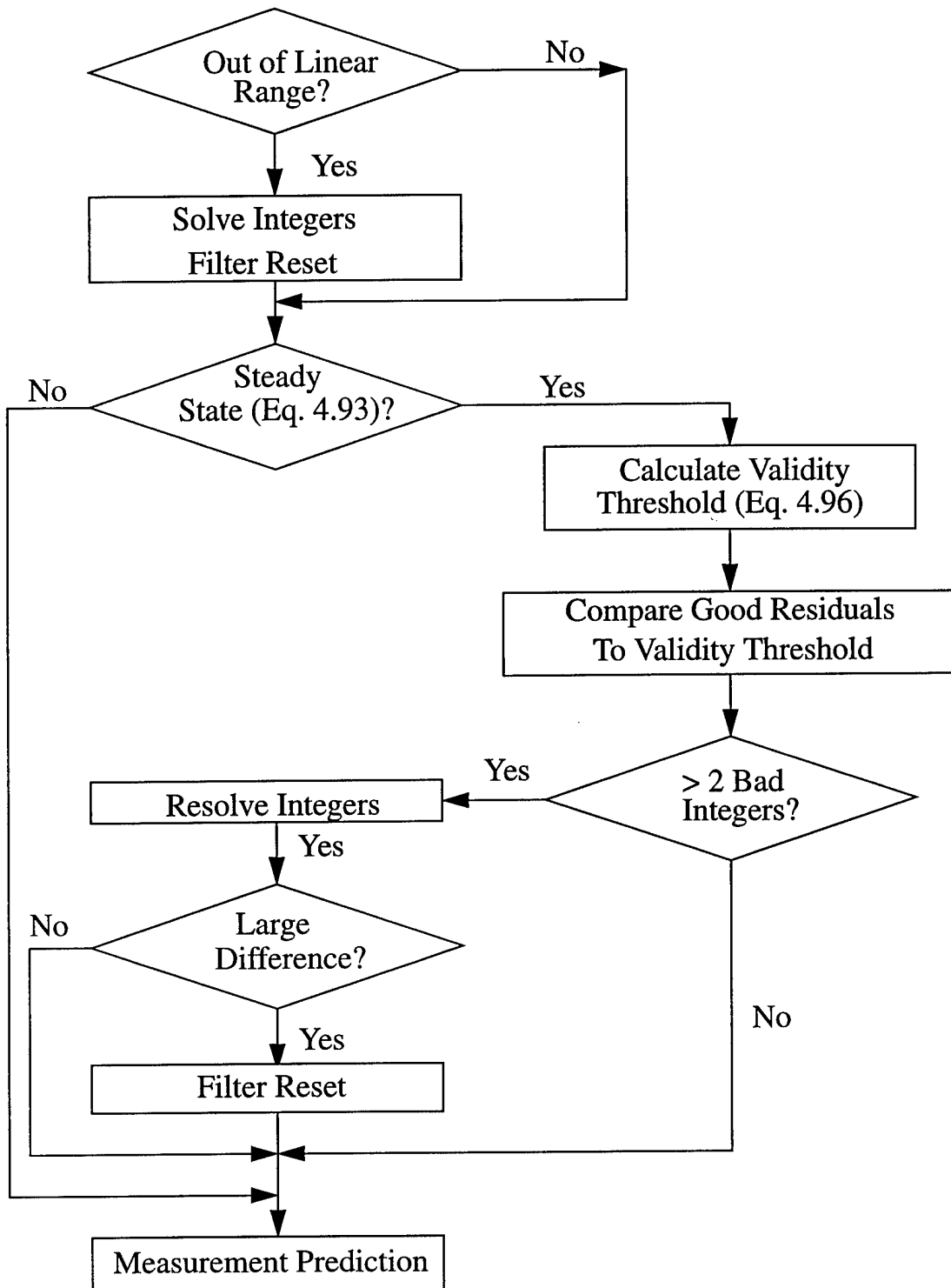


**Figure 4.4: Integrity Monitoring**

A filter reset consists of returning the state estimates to their nominal values and returning the covariance of each state to the steady state model  $1-\sigma$  value. The exception to this is the attitude

error covariance, which is calculated in the integer solution algorithm.

As a final safeguard, two out of bound residuals are required to trigger a new integer solution. This is because otherwise a single large random noise value might invalidate a good attitude solution. After the new integer solution is commanded, the attitude solution from the integer ambiguity solution is compared to the attitude before the reset. If the two attitudes are close, the rest of the state vector and covariance matrix is *not* reset. This kind of “nearby” solution indicates that the reset was triggered by noise rather than the wrong integer solution, and all of the estimated states will still be valid. If the integer solution differs significantly from the previous attitude solution, the entire state will be in error because of filter corrections based on a linearization which was nowhere near the true nominal. This triggers a complete reset of the filter states.

Demonstration of performance of the integrity monitoring algorithm is found in sections 6.5.4 and 6.5.5.

# Chapter 5

## Linear Covariance Analysis

### 5. 1 Introduction

The purpose of this chapter is to examine the theoretical error covariance of the integrated Kalman filter. Three specific objectives are covered. In section 5. 2, performance of various reduced order filter designs is compared to the full order design using time domain covariance analysis. A single reduced order design is chosen, and an error budget is calculated for this final design. Section 5. 3 examines sensitivity of the reduced order filter to environmental uncertainty and changes in GPS error intensity using a steady state linear covariance solution. In section 5. 4, the same steady state solution is used to look at the effects of hardware parameters such as array size and gyro quality on filter performance.

The nominal model used here is a Kalman filter with 18 GPS measurements and a three gyro MMIMU package. The full order filter includes states which model a correlated disturbance torque (3), gyro bias (3), correlated noise (18), line bias (3), and baseline length error (3). The full order filter has a total of 36 states.

### 5. 2 Sub-Optimal Filter Design

Optimal Kalman filter performance is obtained when every system dynamic is included in the design model. However, performance of a Kalman filter can be hindered by too many error states, especially if the number of available measurements is significantly less than the number of states. A high order filter may also cause excessive computational burden, so filter design is a compromise between obtaining good performance and choosing a reasonable set of states. A reduced order filter is chosen here after comparing the performance of various sub-optimal designs.

The most simple method of predicting estimation error is to solve the closed loop Lyapunov equa-

tion for the linearized system:

$$\mathbf{0} = (\mathbf{F} - \mathbf{KH})\mathbf{P}_\infty + \mathbf{P}_\infty(\mathbf{F} - \mathbf{KH})^T + \mathbf{GQG}^T + \mathbf{RK}^T \quad 5.1$$

Here,  $\mathbf{F}$ ,  $\mathbf{G}$ ,  $\mathbf{H}$ ,  $\mathbf{K}$ ,  $\mathbf{Q}$ , and  $\mathbf{R}$  are calculated at the linearized point and iteration is used to solve for  $\mathbf{P}_\infty$ , the steady state covariance. But interferometry is a time-varying problem: GPS satellite geometry is constantly changing, so the filter never reaches steady state at a single point. Instead of steady state analysis, performance is compared using time domain propagation of the error covariance matrix with the matrix Riccati equation and the measurement update equation:

$$\dot{\mathbf{P}}(t) = \mathbf{F}(t)\mathbf{P}(t) + \mathbf{P}(t)\mathbf{F}(t)^T + \mathbf{G}(t)\mathbf{Q}(t)\mathbf{G}(t)^T \quad 5.2$$

$$\mathbf{P}_{k+} = (\mathbf{1} - \mathbf{K}_k \mathbf{H}_k) \mathbf{P}_{k-} (\mathbf{1} - \mathbf{K}_k \mathbf{H}_k)^T + \mathbf{K}_k \mathbf{R}_k \mathbf{K}_k \quad 5.3$$

$\mathbf{P}(t)$  is the estimate covariance, but it is not the covariance which is reported by the filter. The reduced order filters examined here are sub-optimal in the sense that they are designed with incomplete system models. This means that the covariance estimate *within* the filter is propagated using the reduced order system model:

$$\dot{\underline{\mathbf{P}}}(t) = \underline{\mathbf{F}}(t)\underline{\mathbf{P}}(t) + \underline{\mathbf{P}}(t)\underline{\mathbf{F}}(t)^T + \underline{\mathbf{G}}(t)\underline{\mathbf{Q}}(t)\underline{\mathbf{G}}(t)^T \quad 5.4$$

$$\underline{\mathbf{P}}_{k+} = (\mathbf{1} - \underline{\mathbf{K}}_k \underline{\mathbf{H}}_k) \underline{\mathbf{P}}_{k-} (\mathbf{1} - \underline{\mathbf{K}}_k \underline{\mathbf{H}}_k)^T + \underline{\mathbf{K}}_k \underline{\mathbf{R}}_k \underline{\mathbf{K}}_k \quad 5.5$$

Here,  $\underline{\mathbf{F}}$ ,  $\underline{\mathbf{G}}$ ,  $\underline{\mathbf{Q}}$  and  $\underline{\mathbf{R}}$  are the system matrices used for the suboptimal design,  $\underline{\mathbf{P}}$  is the estimated covariance and  $\underline{\mathbf{K}}$  is the suboptimal filter gain, calculated using  $\underline{\mathbf{P}}$  in equation 4.13. To calculate the true error covariance,  $\mathbf{P}$ , the full order dynamics are propagated using equation 5.2 and updated with the suboptimal gain from the filter. If the order of the sub-optimal filter is  $n_x$ , the gain matrix  $\underline{\mathbf{K}}$  must be padded with  $(36-n_x)$  columns of zeros in order calculate the full order update. The augmented matrix is referred to as  $\underline{\mathbf{K}}'$ .

Figure 5.1 shows this simultaneous propagation of the filter covariance and truth covariance. The output,  $\mathbf{P}(t)$ , is used to calculate statistical filter performance. A more elaborate description of this reduced order analysis technique is found in [26]:

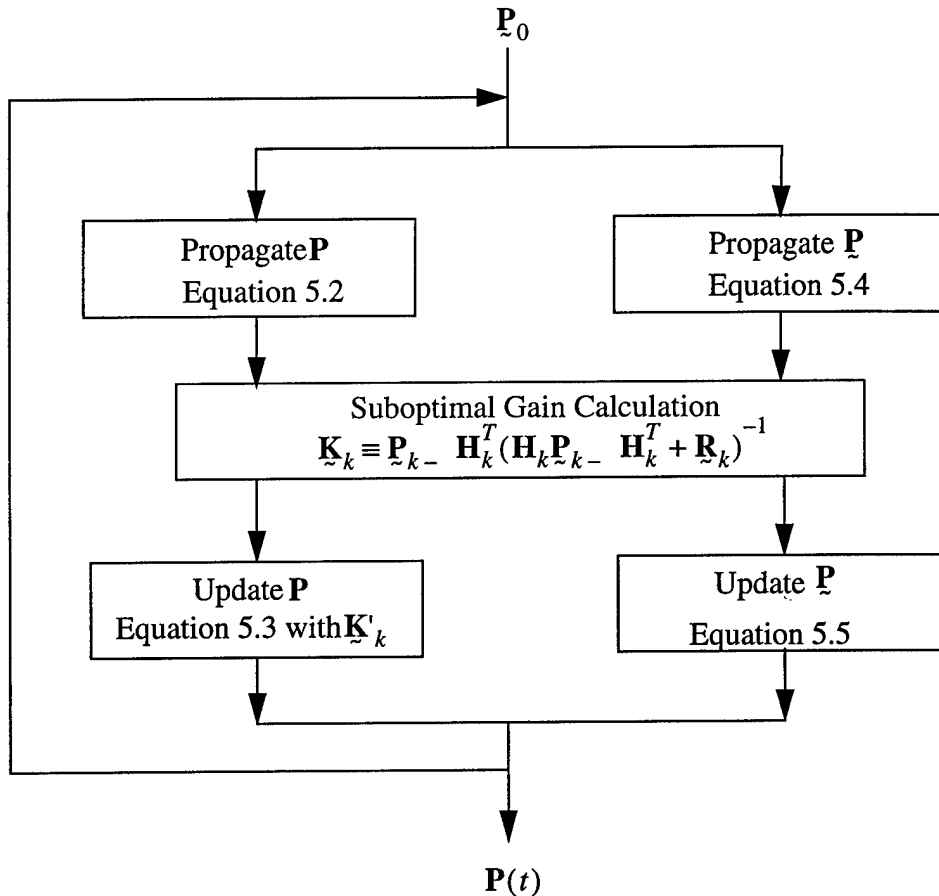


Figure 5.1: Sub-Optimal Filter Analysis

### 5.2.1 Implementation

Performance is compared on a nominal trajectory. Each linearized point consists of a nominal state vector and nominal satellite geometry. Filter performance is not sensitive to nominal angular rate, so initial rates are identically zero. The state vector and satellite geometry history for the time domain simulation are produced by running the environment portion of the non-linear simulation developed in section 6.2.1 for two orbits with initial conditions taken from test case 02 (test

cases are developed in section 6. 3):

Parameter	Value
Longitude of the Ascending Node ( $\Omega_0$ )	135.0570°
True Anomaly ( $\Omega_0$ )	114.4437°
Attitude	+5° yaw, pitch, roll
Angular Rate	+0.01°/s yaw, pitch, roll
Control Target	LVLH Hold

**Table 5.1: Covariance Analysis Initial Position**

The disturbance torque model and differential phase error intensities used for the covariance analysis are shown in table 5.2:

Parameter	Model (Simulated Data)
Differential Phase White Noise	Intensity in section 3.3.3
Correlated Noise	1st order model (section 3.3.3)
Line Bias	$\tau_{\Delta\beta} = TP/2$ $\sigma_{\Delta\beta} = 3 \text{ mm}$
Baseline Error	$\tau_b = TP/2$ $\sigma_b = 0.3\%$
Disturbance Torque	Gravity gradient + 1st order (section 4.3.1) $\tau_{N_o} = TP/2$ $\sigma_{N_o} = 1e-4 \text{ N-m}$

**Table 5.2: Covariance Analysis Error Parameters**

TP is the orbit period of 100 minutes. For each sub-optimal filter, the history of the total attitude 1- $\sigma$  error,  $\sigma_{TOT}$ , is presented, where:

$$\sigma_{TOT} = \sqrt{tr(\mathbf{P}_{2\tilde{q}})} \quad 5.6$$

In addition, the maximum value and 95% confidence interval of  $\sigma_{TOT}$  for each design is compared to the same values for the nominal design.

All of the test cases use a 4-antenna, 1 m square antenna array as the baseline.

## Full Order Filter

The full order filter is presented first. Figure 5.2 shows the  $1-\sigma$  error bound ( $\pm\sigma_{TOT}$ ) along with total  $ADOP$  and the number of valid measurements over the trial. Total  $ADOP$  is an indicator of the quality of the GPS viewing geometry, as described in section 4.5.1:

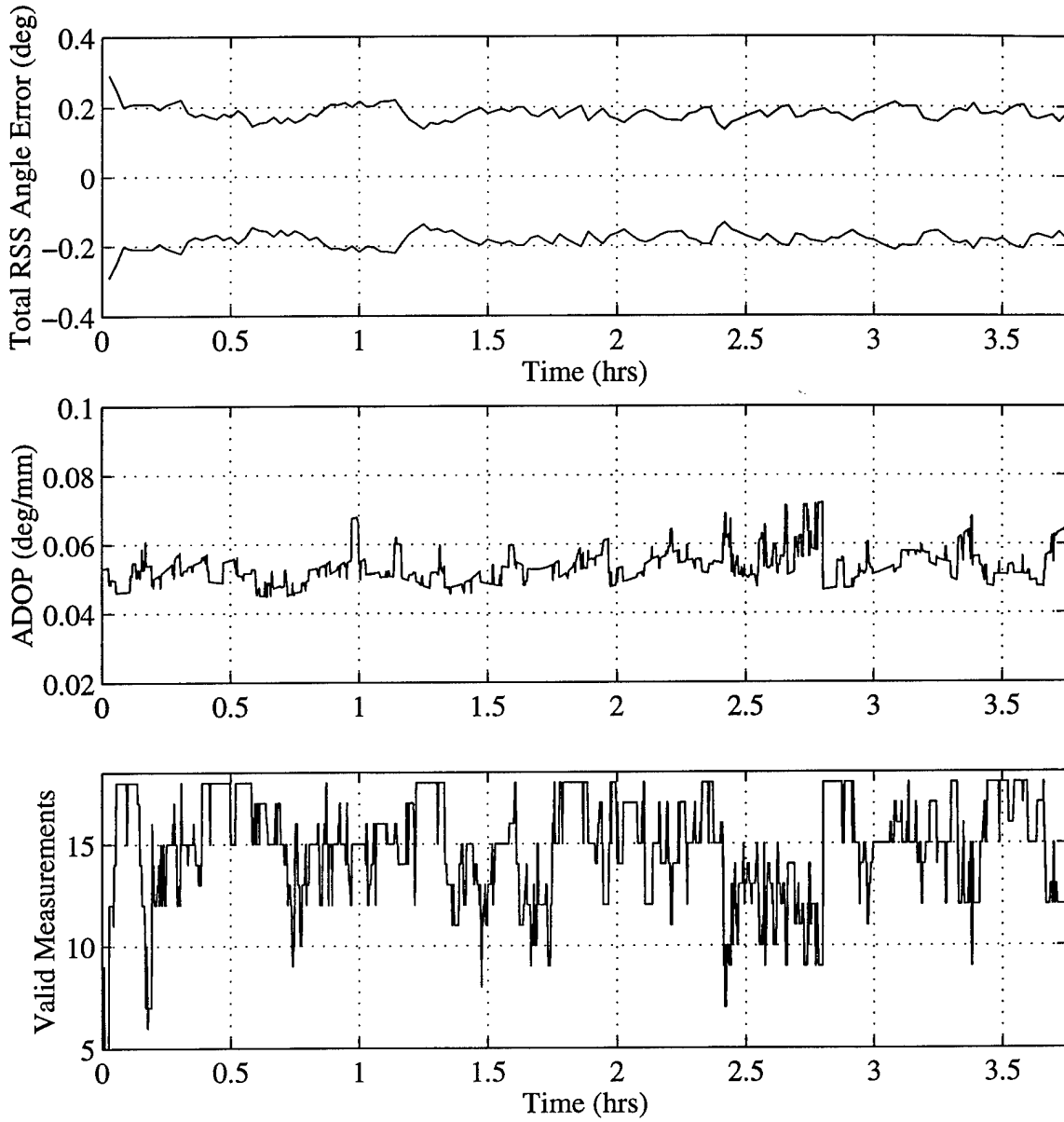


**Figure 5.2:  $1-\sigma$  Bound for Full Order Filter**

The scalloped appearance of the covariance bounds is the result of the satellite update rate. Satellite positions for the covariance analysis are sampled every 100 seconds during the simulation to reduce the size of the database. Notice that the covariance bounds do not change significantly over the time span of two orbits despite changes in the number of valid measurements and total

*ADOP*. The reason for this is that spacecraft disturbance torques cause very small angular accelerations. In turn, the attitude covariance grows slowly in the open loop, and just a few measurements at the 1 Hz GPS output rate are enough to maintain tight covariance bounds.

Figure 5.3 shows a bar chart of the total angle uncertainty statistics for the nominal run. The initial transients are not included in the figure. Note that a 95% confidence interval for  $\sigma_{TOT}$  does *not* imply 95% estimation confidence. The chart is simply used as a comparison tool to measure sensitivity of the filter in its suboptimal configurations.

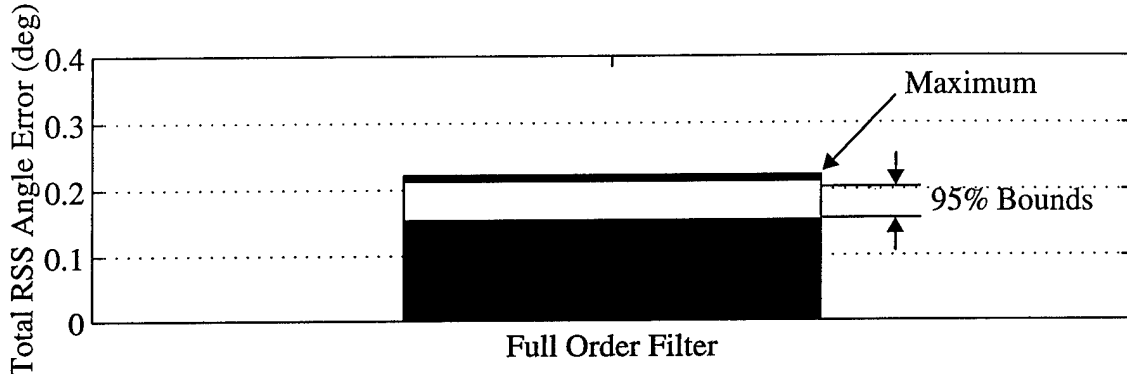


**Figure 5.3: Nominal  $\sigma_{TOT}$  Statistics**

Sub-optimal filters are now formulated which remove the states one at a time.

### Gyro Bias

Estimation of the gyro bias is included in most integrated filters for good reason. Figure 5.4 shows the attitude covariance bound for a filter which does not include a gyro bias state. The attitude error is only limited by the ability of the GPS measurements to contradict the gyro bias term.

If GPS visibility was poor, attitude error would grow without bound.

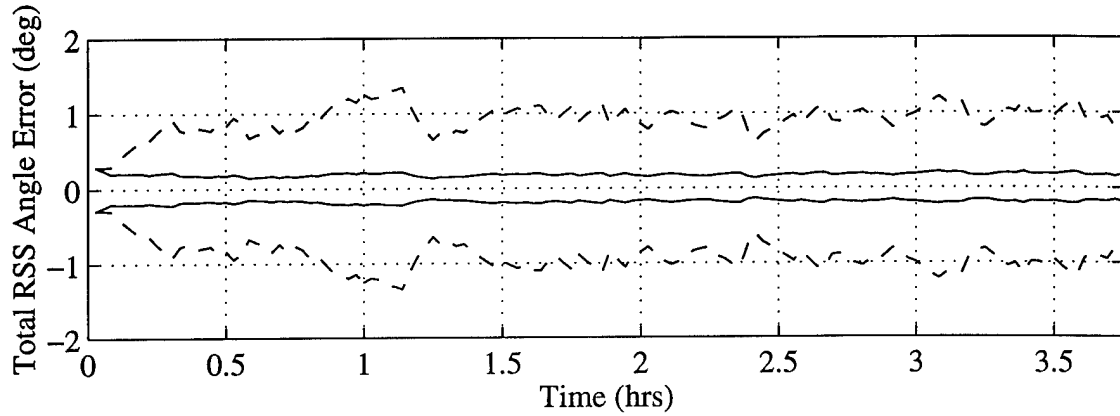


**Figure 5.4: Simulation: No Gyro Bias State**

Figure 5.5 summarizes the change in RMS error. Obviously, elimination of the gyro bias state is not an option.

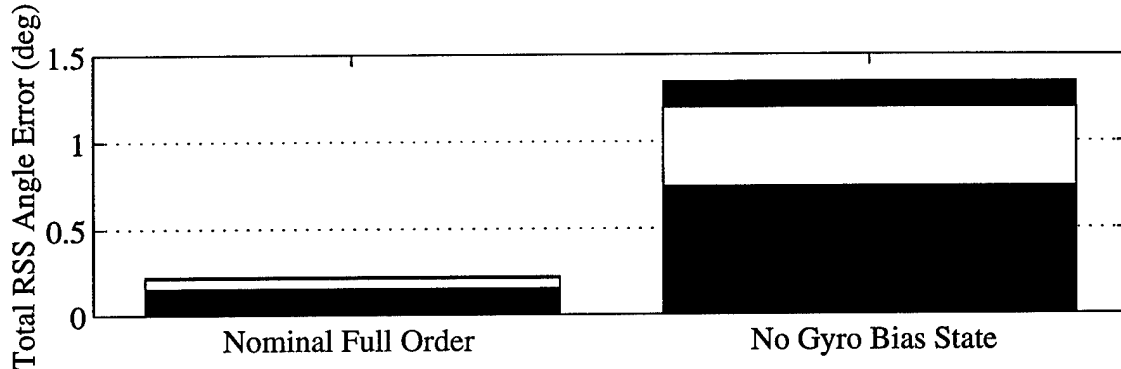


**Figure 5.5:  $\sigma_{TOT}$  Statistics: No Gyro Bias State**

### Disturbance Torque

Removal of the disturbance torque results in a singularity in the Kalman filter design, because the steady state attitude covariance is 0. To evaluate a design without correlated disturbance torques, attitude rate process noise is added to the filter design. Figure 5.6 shows the covariance bounds using process noise equal in intensity to the disturbance torque and no disturbance torque estimation. There is virtually no difference in the performance, indicating that estimation of the disturbance torque is an unnecessary computational burden. The reason for this is that the gyros provide a measurement of external disturbance torques. Filter designs which use only GPS are

more sensitive to external disturbances.

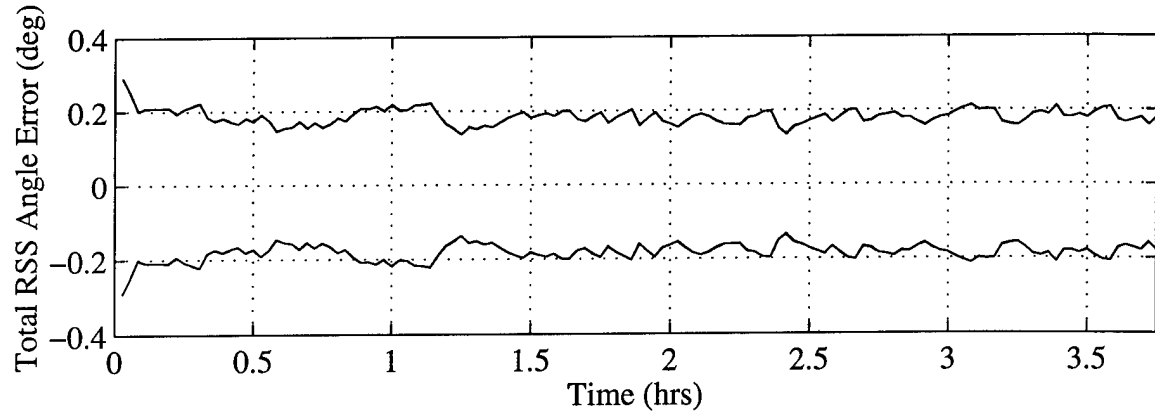


**Figure 5.6: Simulation: No Disturbance Torque State**

The uncertainty statistics show a negligible change in performance for the reduced order filter:

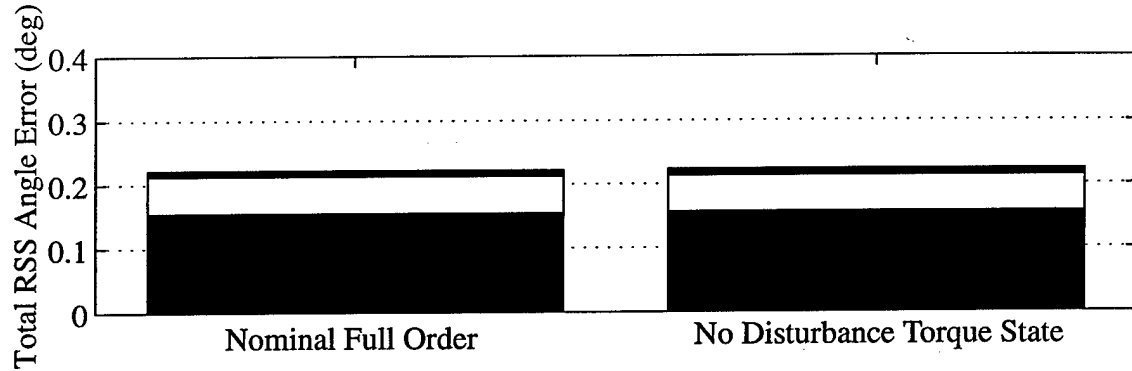


**Figure 5.7:  $\sigma_{TOT}$  Statistics: No Disturbance Torque State**

### Correlated Noise

In the presence of correlated noise, a white noise error model produces excessive RSS attitude error. Figure 5.8 shows simulation results for a filter designed without correlated noise states. The average  $1-\sigma$  bound is nearly doubled throughout most of this trajectory. Even worse, the bounds are much more sensitive to variations in satellite geometry than for the nominal filter. Note the large increase in the covariance bounds 1.7 hours into the simulation. This increase corresponds to a period of time when only 9-10 measurements are valid. Covariance of the full order

filter does not change significantly in this time.

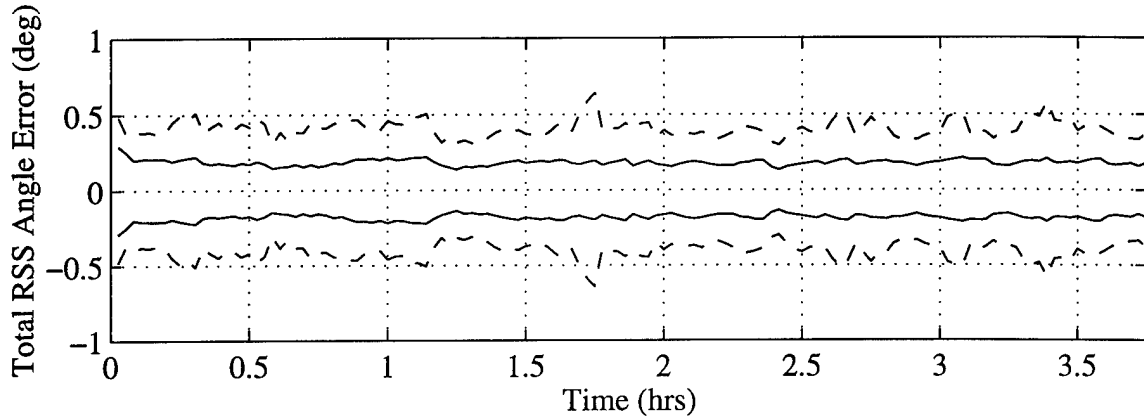


**Figure 5.8: Simulation: No Correlated Noise State**

For the error characteristics modeled in this thesis, the 18 correlated noise states recover a critical portion of the attitude errors. The benefit is summarized in figure 5.9

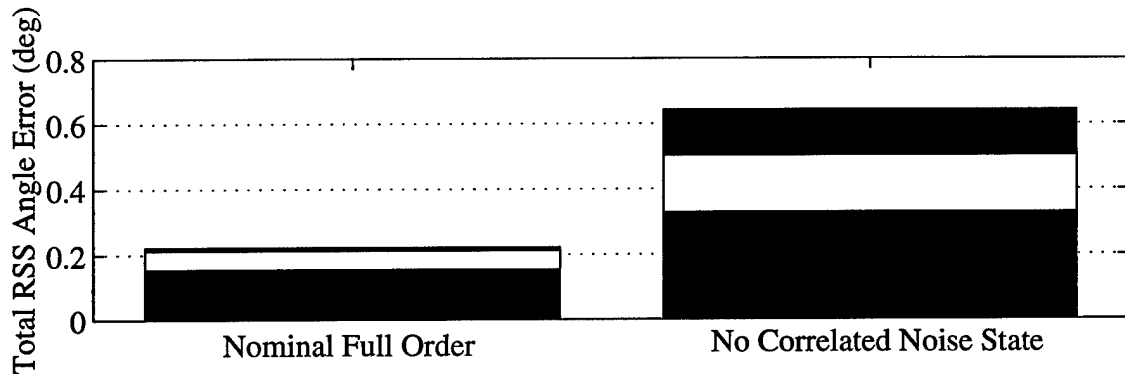


**Figure 5.9:  $\sigma_{TOT}$  Statistics: No Correlated Noise State**

### Line Bias

There are only three line bias states, so estimation of line bias does not impose a heavy computational burden. At the same time, linear covariance analysis shows that the impact of line bias

error on the attitude error covariance is significant:

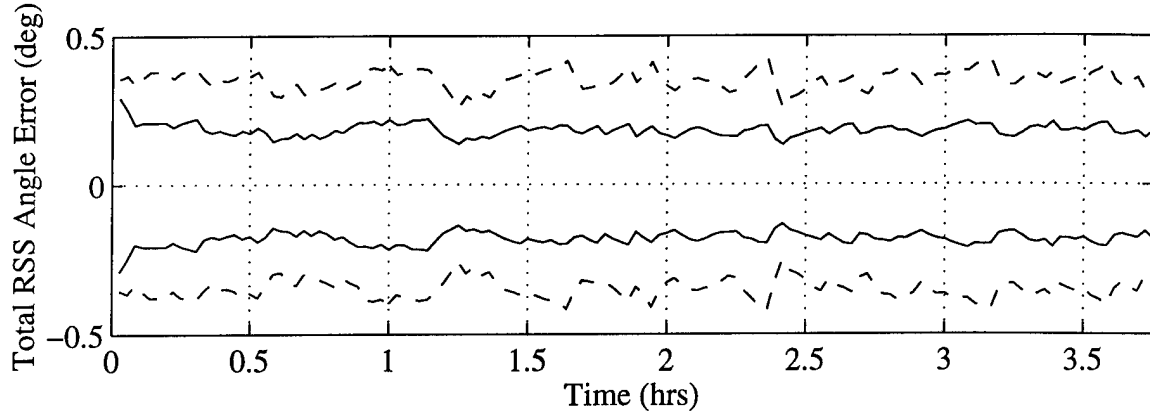


**Figure 5.10: Simulation: No Line Bias State**

Because line bias is independent of GPS constellation geometry, the increase in total RSS error is fairly constant during the simulation.

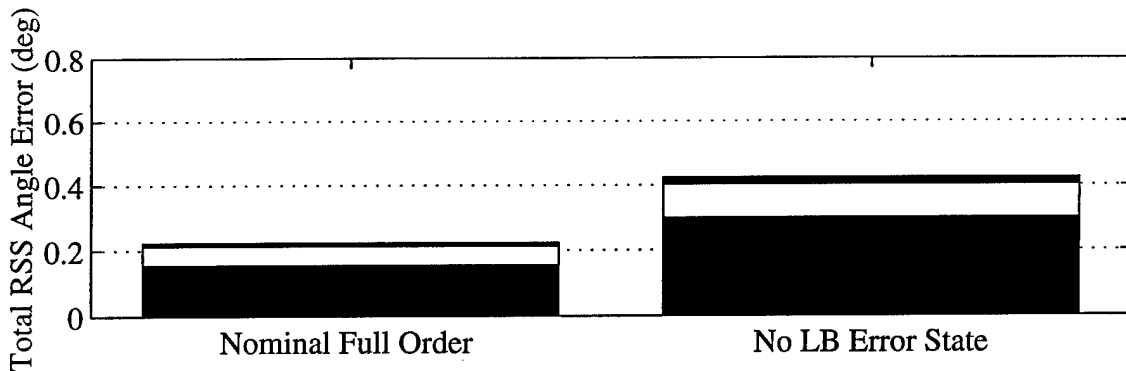


**Figure 5.11:  $\sigma_{TOT}$  Statistics: No Line Bias State**

The increase in total error of about  $0.15^\circ$  justifies retention of the line bias estimation state.

### Baseline Length Error

The behavior of the filter with no baseline length error modeling is very interesting. The covariance increases significantly only in a very distinct set of GPS geometries. The reason for this characteristic is not clear, but it may correspond to the elevation of GPS satellites in the body frame. Baseline length variation causes a multiplicative error on differential phase, so phase from

low elevation satellites with high delta range incur the largest errors.

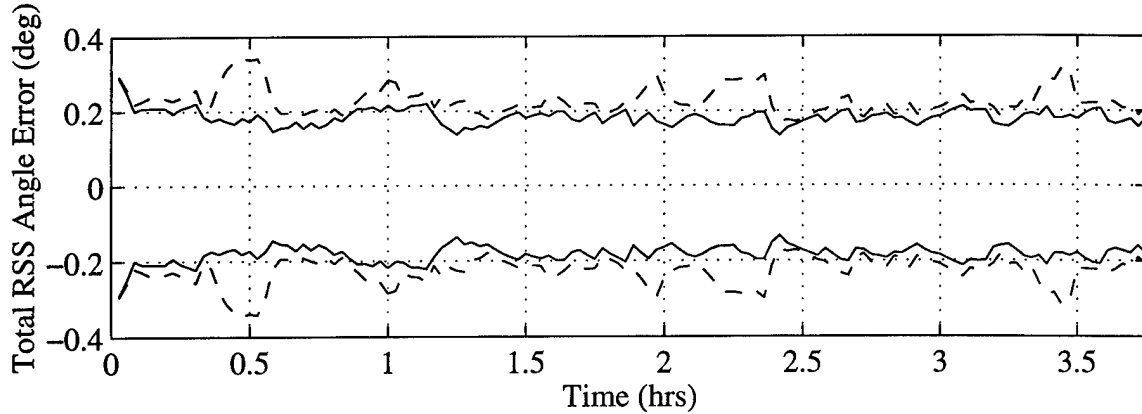


**Figure 5.12: Simulation: No Baseline Length State**

Once again, the overall performance change is significant, so the three baseline length states will be kept in the reduced order filter.

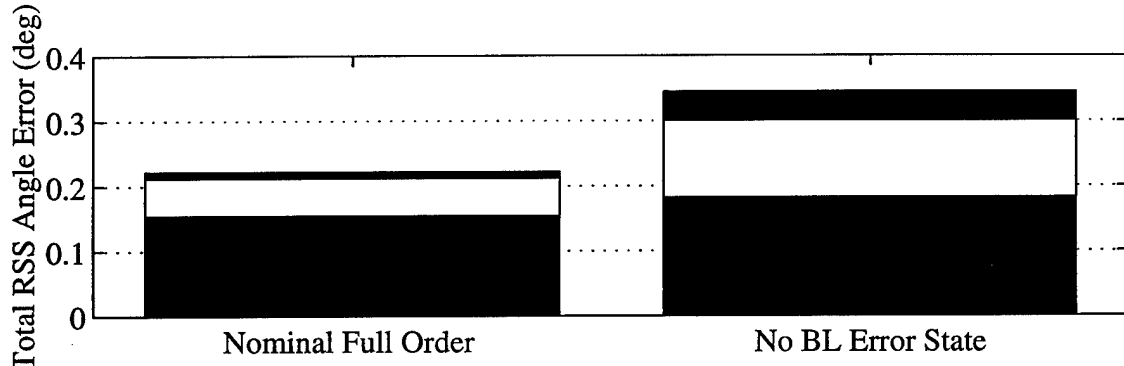


**Figure 5.13:  $\sigma_{TOT}$  Statistics: No Baseline Length Variation State**

### Reduced Order Design

The performance of the full order filter did not degrade appreciably after removal of the disturbance torque state. Estimation of all of the other states is necessary to maintain filter 1- $\sigma$  total attitude error near the 0.2° level achieved with the full order filter. With the elimination of the disturbance torque model, it is necessary to add process noise to the angular rate dynamics to compensate for the mismodeling. To choose a process noise intensity, theoretical RMS error is calculated for the reduced order filter with a range of values for angular rate process noise inten-

sity,  $\sigma_{w_\omega}$ :

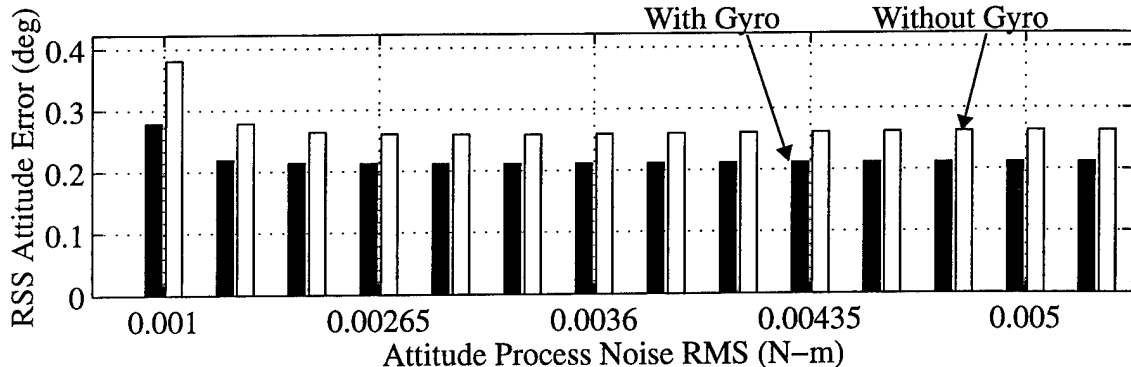


**Figure 5.14: RSS Attitude Error as a Function of Design Process Noise Intensity**

The attitude covariance reaches a minimum for a design process noise RMS value of  $3.6 \times 10^{-3}$  N-m. This process noise intensity is used in the final filter design to offset the elimination of the correlated disturbance state.

### 5.2.2 Error Budget

An error budget is calculated for the reduced order in order to see the contribution of each error source to the final filter attitude uncertainty. The errors are separated by propagating and updating one covariance contribution matrix for each of the error sources. The matrices are propagated using the full order system dynamics, but each one is driven solely by the process noise for the error source of interest. All of the covariance matrices are updated using the full order feedback gain, but the measurement noise intensity  $\mathbf{R}$  is only included in updating the measurement noise covariance contribution. The resulting final error contributions are shown by axis in figure

5.15:

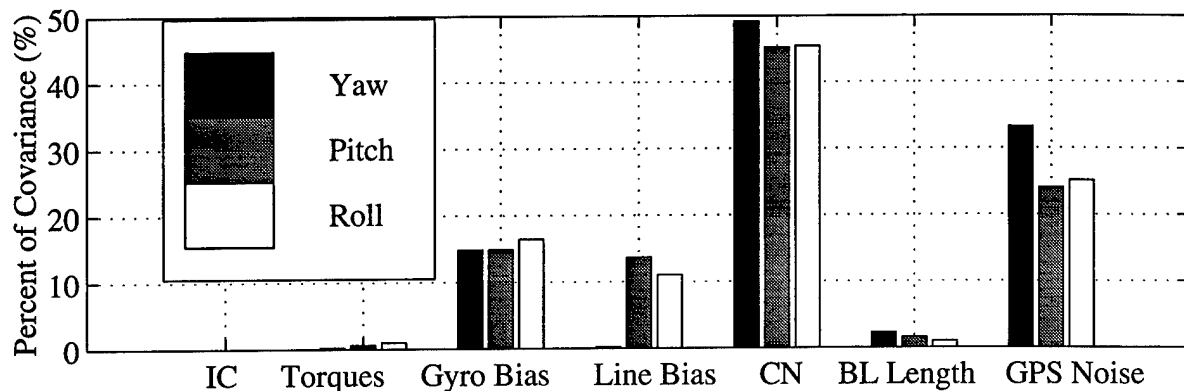


**Figure 5.15: Total Attitude Error Budget**

“IC” denotes the contribution of the initial covariance and “CN” is the correlated noise error contribution. As expected, correlated noise makes a large contribution to the attitude uncertainty. Notice the distribution of line bias errors. Sensitivity of differential phase to line bias variation has a similar structure to the roll and pitch angle sensitivities, so line bias primarily effects these two axes. The total error contributions are broken down in table 5.3:

Source	Percent of Total Error (%)	RMS Error Contribution (deg)
Initial Conditions	0.0000	0.0000
Disturbance Torque	0.7561	0.0014
Gyro Bias	15.5825	0.0282
Line Bias	10.4384	0.0189
Correlated Noise	45.9074	0.0832
Baseline Length	1.4127	0.0026
GPS Noise	25.9029	0.0469

**Table 5.3: Attitude Error Budget**

## 5. 3 Environment Parameter Variation

The sensitivity of the reduced order design to environmental parameter variation is now evaluated. The sensitivity is measured by calculating filter gains at a linearized nominal point with the nominal error intensities and solving the Lyapunov equation with the nominal gains and perturbed dis-

turbance intensities. Using this analysis, insight can be gained into which error sources the filter is most sensitive to as well as how important accurate modeling of the errors is.

The linearized system for this analysis uses the set of six satellites shown in figure 5.16, which produces a total *ADOP* of 0.055, typical for the Iridium orbit. One of the satellites is invalid:

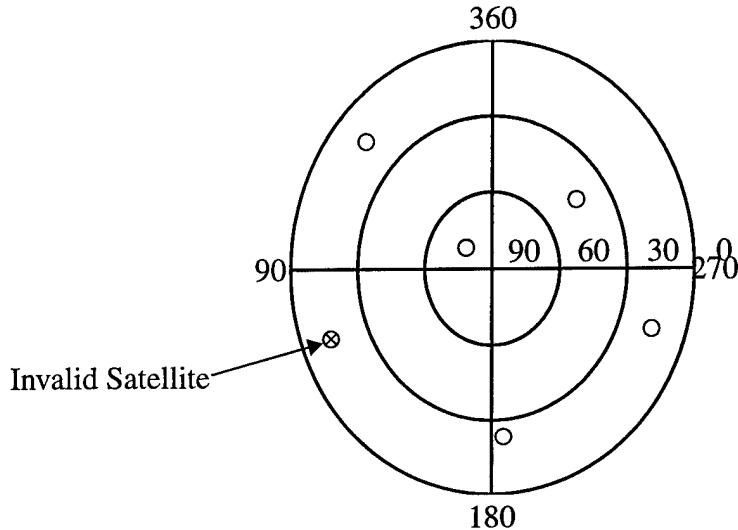


**Figure 5.16: Satellite Geometry for Linear Analysis**

In the following plots, the vertical axis represents total RMS attitude error and the horizontal axis is intensity of the environment parameter. The nominal parameter intensity value, used in the Iridium design, is at the center of the horizontal axis. The left set of bars (black) indicates RMS attitude error of a filter designed for the perturbed parameter intensity (optimal design). The right (white) bar is performance of the nominal filter in an environment with the perturbed parameter intensity (nominal design). Each parameter is tested from approximately 0.1 to 10 times the nominal value. All of the plots are shown with uniform limits on the vertical axis to allow for comparison between the various error sources. As a result, some of the larger RMS values are truncated at the limit of 0.4°.

### Disturbance Torque

Variation of the disturbance torque has virtually no effect on the attitude solution, even if the nom-

inal design is not changed.

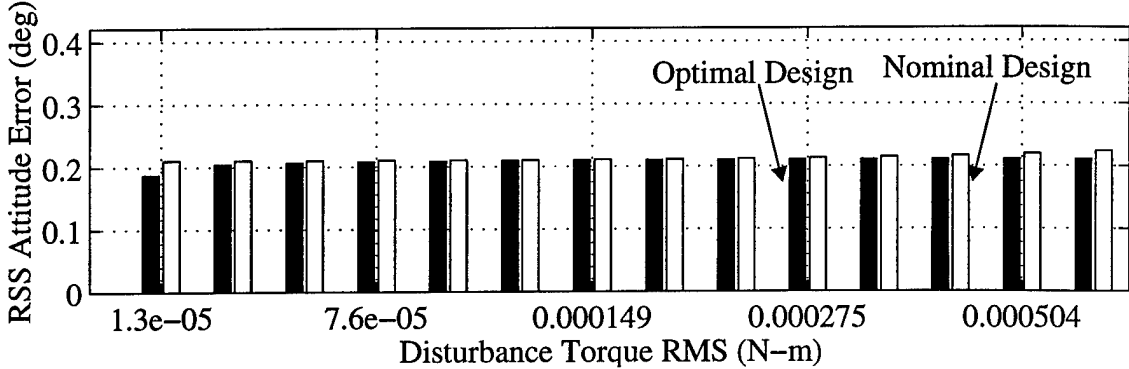


**Figure 5.17: Sensitivity to External Torques with Gyros**

The lack of sensitivity to disturbance torque magnitude is a function of gyro augmentation. Without the gyros, sensitivity to disturbance torque is more apparent, as shown in figure 5.18:

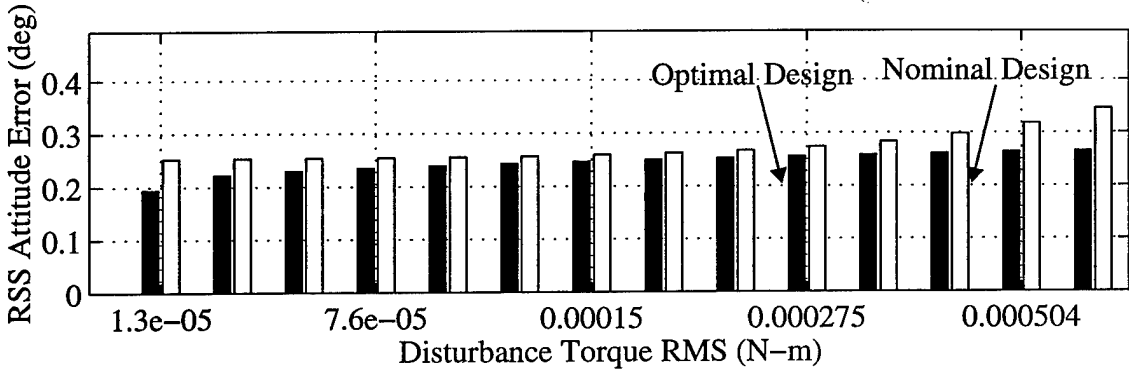


**Figure 5.18: Sensitivity to External Torques without Gyros**

Without gyro aiding, the nominal design suffers from large errors as the disturbance torque grows larger than the nominal value. Much of this deterioration can be avoided if the larger disturbance magnitude is modeled in the filter.

### Correlated Noise

The filter design is very sensitive to correlated noise magnitude regardless of whether the noise is modeled or not. Figure 5.19 shows a range of correlated noise intensities from less than half of a millimeter to over 1 cm. First, notice that the attitude error does not reach an equilibrium for large noise magnitudes. This makes sense, because a separate correlated noise state corrupts each of the GPS measurements; without any redundant measurements, the filter cannot attenuate large correlated noise magnitude. Fortunately, the measured correlated noise intensity is quite manageable. In addition, performance of the nominal design is comparable to the optimal design for

intensities ranging from 1.5 to 5 mm. This means that the filter has some flexibility to deal with correlated noise intensity. At very small (less than 1 mm) correlated noise intensities, nominal design performance does break away from the optimal performance. The optimal design for a correlated noise intensity of 0.25 mm achieves a total RMS error of nearly  $0.05^\circ$ , but the nominal design performance remains at about  $0.12^\circ$  in this scenario.

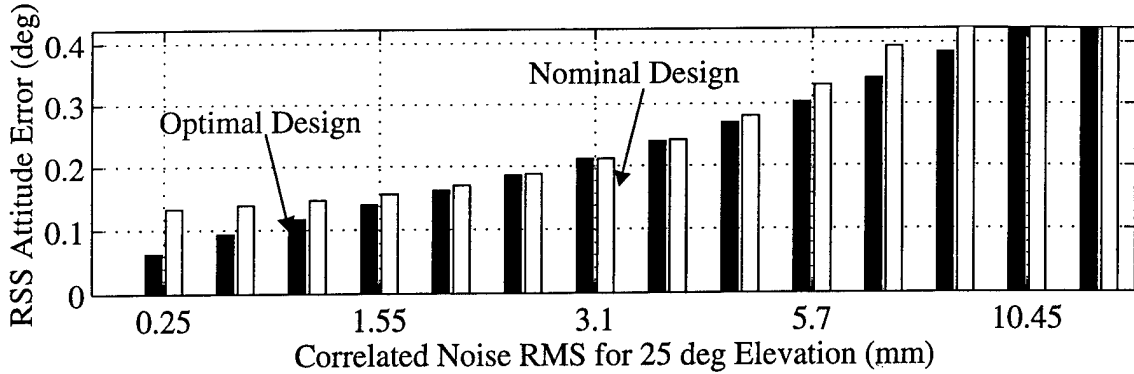


**Figure 5.19: Sensitivity to Correlated Noise**

Correlated noise intensity for this test was scaled for all of the measurements simultaneously. The horizontal axis is the scaled value for a satellite at  $25^\circ$  elevation to provide a point of reference.

### Line Bias

Line bias shares the low frequency properties of correlated receiver noise, but estimation of line bias is more flexible because one line bias measurement is available from each of the  $n_{ch}$  receiver channels. Line bias sensitivity is shown below for the case when five satellites are available.

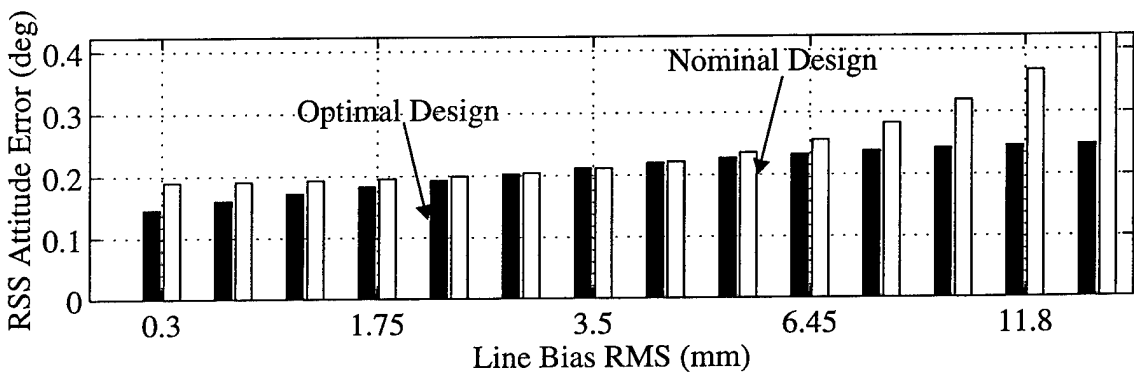


**Figure 5.20: Sensitivity to Line Bias**

The first few millimeters of line bias error have a significant effect on the attitude solution, but beyond about 5mm of RMS error, the attitude error contribution levels off for the optimal filter. The slow dynamics and redundant measurements of line bias allow the filter to effectively track

large line bias excursions. Error for the nominal design increases significantly above about 7 mm RMS line bias intensity.

Even with an optimal filter, large line bias variations can be dangerous when visibility degrades to two or three satellites. In poor visibility situations, line bias changes are indistinguishable from attitude movements. In applications with large temperature variations (such as this one), proper modeling of line bias dynamics is essential.

### Baseline Length Error

The filter shows very little sensitivity to the baseline length error intensity.

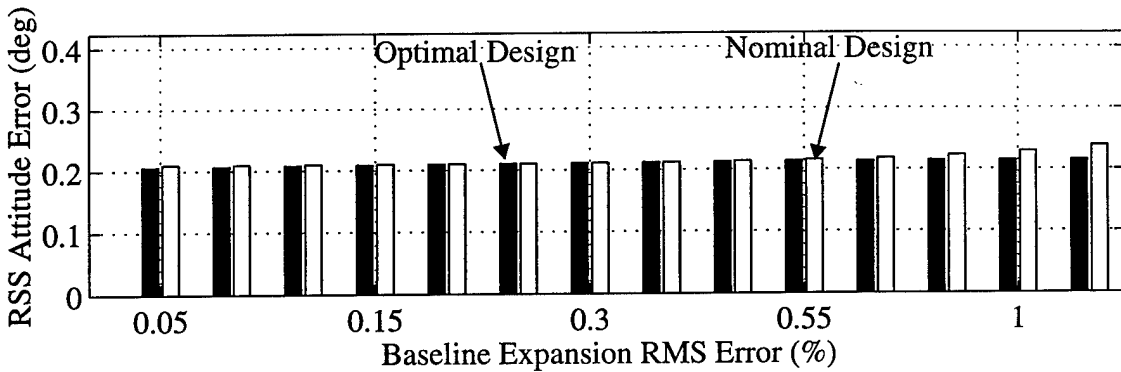


**Figure 5.21: Sensitivity to Baseline Length Error**

As with line bias,  $n_{CH}$  measurements of each baseline length error state are available, making the baseline error very observable. The only significant increase in error occurs as the baseline expansion error RMS approaches 1%. However, this correspond to a 1 cm change in the length of a 1 m baseline. Baseline errors this large are not likely to occur.

## 5.4 Sensitivity to Hardware Configuration

This section investigates the effect of hardware changes on the capabilities of the EKF. The results are by no means exhaustive; the results are meant to aid in configuring an attitude determination system by providing some hardware trade-offs.

### Array Size

The first parameter examined is size of the array. Using four antennas arranged in a square array,

figure 5.22 shows the total steady state RSS attitude error as a function of array.

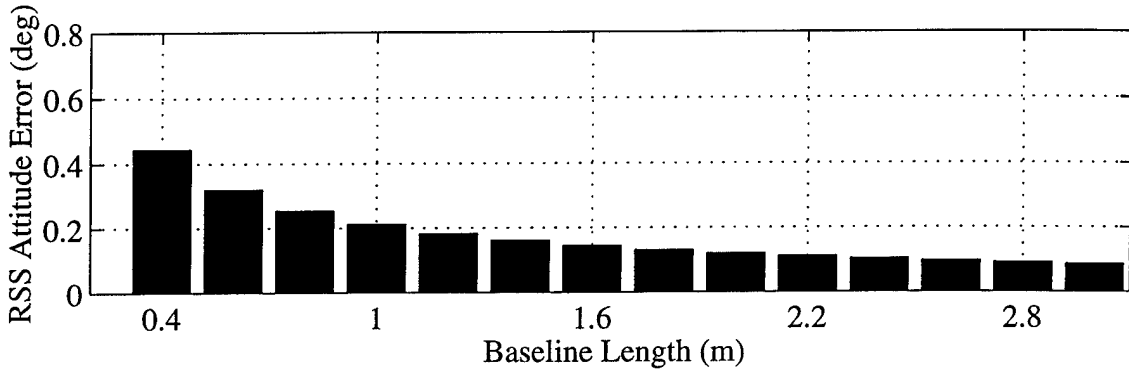


**Figure 5.22: Attitude Error vs. Baseline Length**

The horizontal axis is the length in meters of one side of the array. Total RMS error is inversely proportional to the size of the array, and increases sharply for baselines shorter than about 1 meter. On the other hand, shorter arrays do simplify initialization, because the number of possible integers for a differential phase measurement is proportional to baseline length. This is the primary trade-off required for designing an array.

### Receiver White Noise

If the intensity of receiver noise is modeled correctly, the filter shows very little sensitivity to the true intensity. Figure 5.23 show RSS error as a function of  $1-\sigma$  white noise intensity. The intensity shown on the horizontal axis is actually a scaling used on all of the measurements. The numbers shown here are for a satellite at  $25^\circ$  elevation with respect to the body frame:

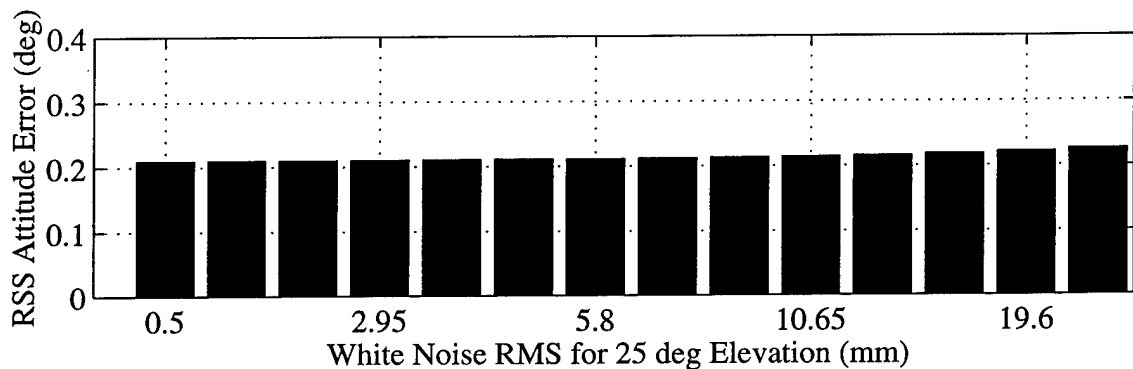


**Figure 5.23: Attitude Error vs. Receiver White Noise Intensity**

### Gyro Angle Random Walk

For the nominal array and error parameters, steady state covariance is calculated for a range of

gyro angle random walk values.

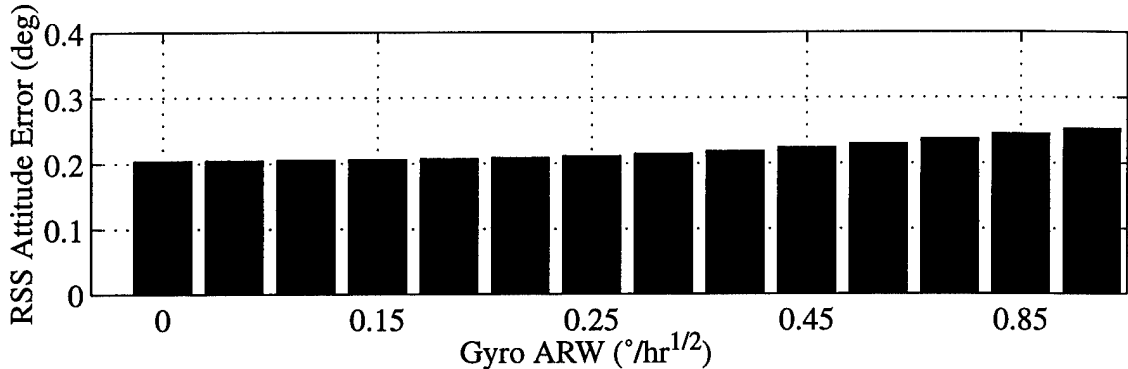


**Figure 5.24: Attitude Error vs. Gyro Random Walk**

The nominal gyro bias RMS value of  $5^{\circ}/\text{hr}$  is used for these trials. The filter shows very little sensitivity to angle random walk for values below the nominal value of  $0.25^{\circ}/\text{hr}^{1/2}$ . There are two reasons for this. First, the gyro is only an angular rate measurement; GPS is needed to fix absolute attitude, so rate aiding has a limited impact on attitude accuracy, especially with good satellite visibility. Also, gyro performance is still limited by the bias term. No matter how good the measurement is, the bias must still be separated from the actual angular rate. As the angle random walk grows, attitude error increases, and at  $0.85^{\circ}/\text{hr}^{1/2}$ , attitude error is approaching the GPS-only total error of  $0.26^{\circ}$ .

### Gyro Bias

With nominal angle random walk performance, the attitude determination performance sensitivity to gyro bias is also examined:

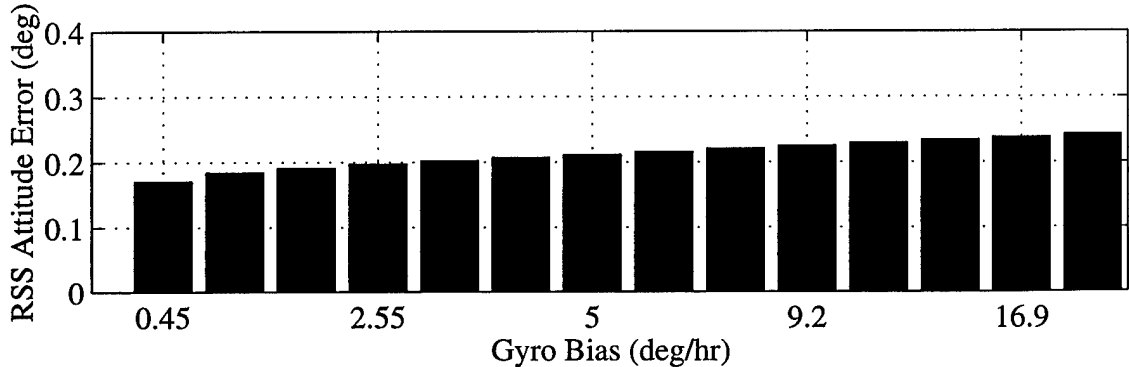


**Figure 5.25: Attitude Error vs. Gyro Bias**

The gyro bias sensitivity looks quite different from the ARW sensitivity. In this case, the greatest sensitivity is at low values of the intensity. This means that reduction of the gyro bias term is a

paramount obstacle to improving performance of the integrated system.

# Chapter 6

## Test and Simulation

### 6. 1 Introduction

This chapter presents the computer simulation used to test the integrated attitude determination system. Section 6. 2 covers design of the simulation environment and generation of test measurements and disturbances. The remaining sections present the test results. Performance analysis is divided into nominal and off-nominal test cases. In section 6. 3, parameters are reviewed for each of the test cases. Section 6.4.1 includes overall performance results for the nominal test case for both experimental and simulated GPS measurement data. Detailed analysis is presented in section 6.4.2 for test cases which illustrate the unique capabilities of the ADS.

After analysis of the nominal data, off-nominal test cases are used to demonstrate robustness of the software design. Several off-nominal test cases are used to examine the benefits of gyro aiding and correlated noise estimation in the EKF. The remaining cases test the limits of the algorithms used for filter initialization and solution integrity monitoring.

### 6. 2 Simulation

The simulation code is divided into three modules. Figure 6.1 shows a flow chart of the construc-

tion:

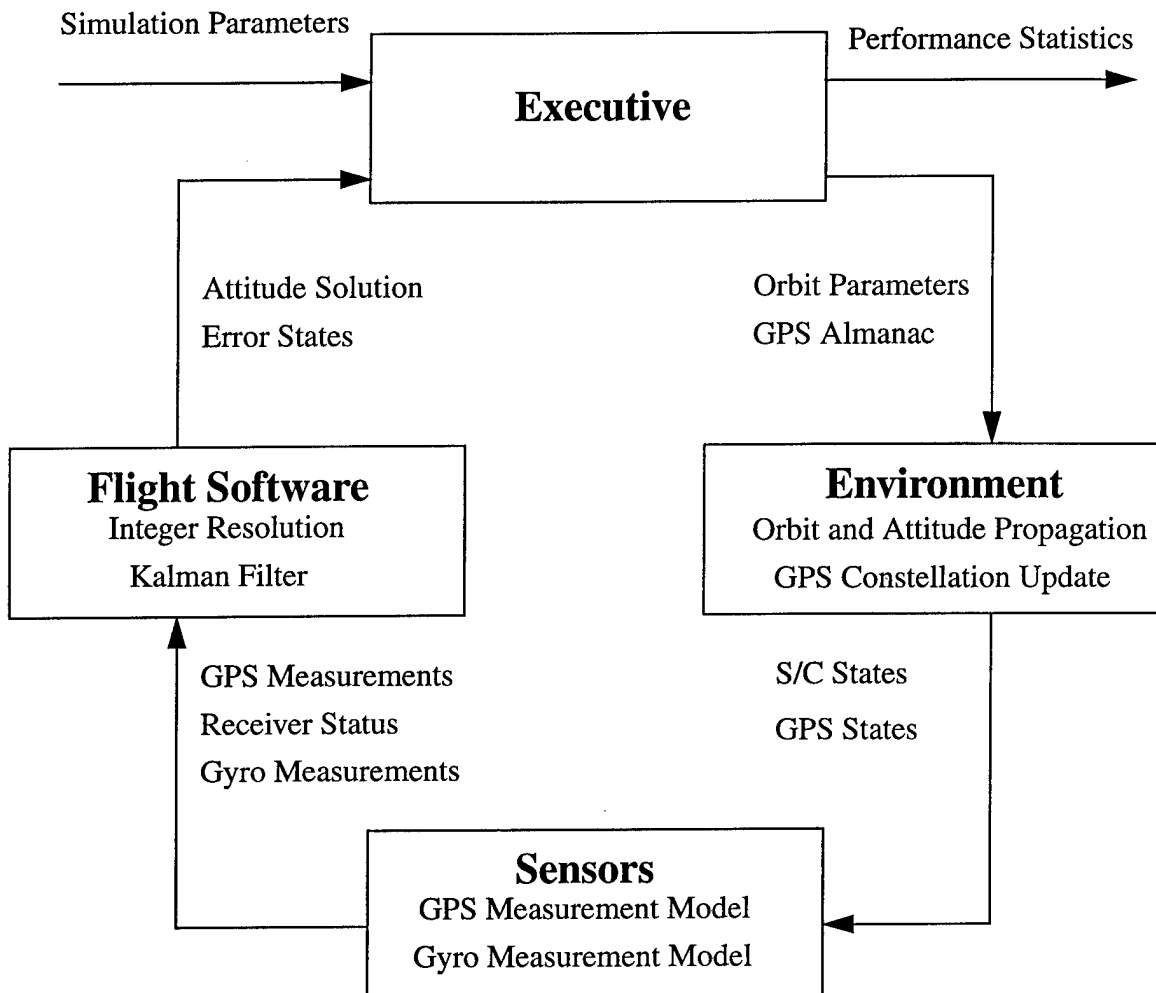


**Figure 6.1: Simulation Block Diagram**

### 6.2.1 Environment

The environment calculates truth states for the vehicle and GPS constellation.

#### Orbit

Vehicle position is computed using a circular orbit model with variable inclination, semi-major axis and longitude of the ascending node. Velocity is orthogonal to position with magnitude defined by the semi-major axis. No modeling of orbit perturbations is attempted.

#### Attitude

Computation of the truth attitude incorporates the disturbance torque models defined in section

4.3.1. The angular rates and quaternion are updated using the dynamics defined in equations 4.33 and 4.44. A first order Taylor series approximation is used with a 0.5 second integration time step. Control inputs generated using the control law in section 6.2.3 are added to the angular rate update with perfect following of the commanded rate and no lag. The control law maintains a 3-axis stabilized attitude aligned with the LVLH frame.

### **GPS Constellation**

The GPS constellation is propagated using the ICD-GPS-200 almanac equations [1]. Input to the propagation routine is the GPS Yuma almanac data for week 900 (April 9, 1997). State vectors for all operational satellites are transformed to the LVLH frame and passed to the sensor block.

### **6.2.2 Sensors**

The sensor block simulates on-orbit function of the gyro and GPS hardware.

#### **Gyro**

Gyro measurements are simulated using the gyro model developed in section 3.4. Simulated bias and noise terms are added to the true angular rate calculated in the environment. The orbital rate  $\omega_0$  is removed from the measurements before output to the filter.

#### **GPS Receiver**

The receiver is modeled with six-channels, four antennas and a nominal half-cone angle of  $80^\circ$ . If more than six GPS satellites are visible to the receiver, the satellite selection algorithm from section 4.5.1 is used to select a subset of six satellites for the attitude solution.

#### **GPS Measurement Errors**

GPS differential phase measurement errors can be generated through simulation or from experimental test data. Simulation is accomplished using the dynamic error models developed in section 3.3.

Experimental data comes from multiple data collection periods with the TANS Vector receiver. Measurements from the receiver are post-processed to extract the measurement error according to

equation 3.4:

$$\Delta\epsilon_{i,j} = \Delta\phi_{i,j} - \Delta\phi_{i,j_{IDEAL}} \quad 3.4$$

Here, the ideal phase is defined as the fractional part of true delta range based on knowledge of true body attitude ( ${}^B C^N$ ) during the test:

$$\Delta\phi_{i,j_{IDEAL}} = [b_{i_0}^B]^T \cdot \hat{\rho}_j^B - \Delta k_{i,j} \quad 3.3$$

The resulting total measurement error,  $\Delta\epsilon_{i,j}$ , is calculated for an entire experiment and then stored in 5 minute intervals. Errors on each channel for each interval are labeled with the average SV azimuth and elevation with respect to the antenna frame during the interval. The errors are also indexed with elapsed time from the beginning of the interval,  $t_\epsilon$ .

During the simulation, true SV azimuth and elevation in the antenna frame are calculated for each SV using the environment output. Every 100 seconds, this azimuth and elevation is compared to values in the experimental data base. A best match is located in the error database by minimizing the sum of the squared azimuth and elevation differences between the simulated SV and an SV contained in the database. GPS measurements for the next 100 seconds are constructed by adding error data from the data base to delta range measurements predicted by the environment. The error data is added sequentially:  $t_\epsilon$  is matched to  $mod(t, 300)$ , where  $t$  is the simulation time step in seconds.

Construction of the GPS measurement is outlined in figure 6.2:

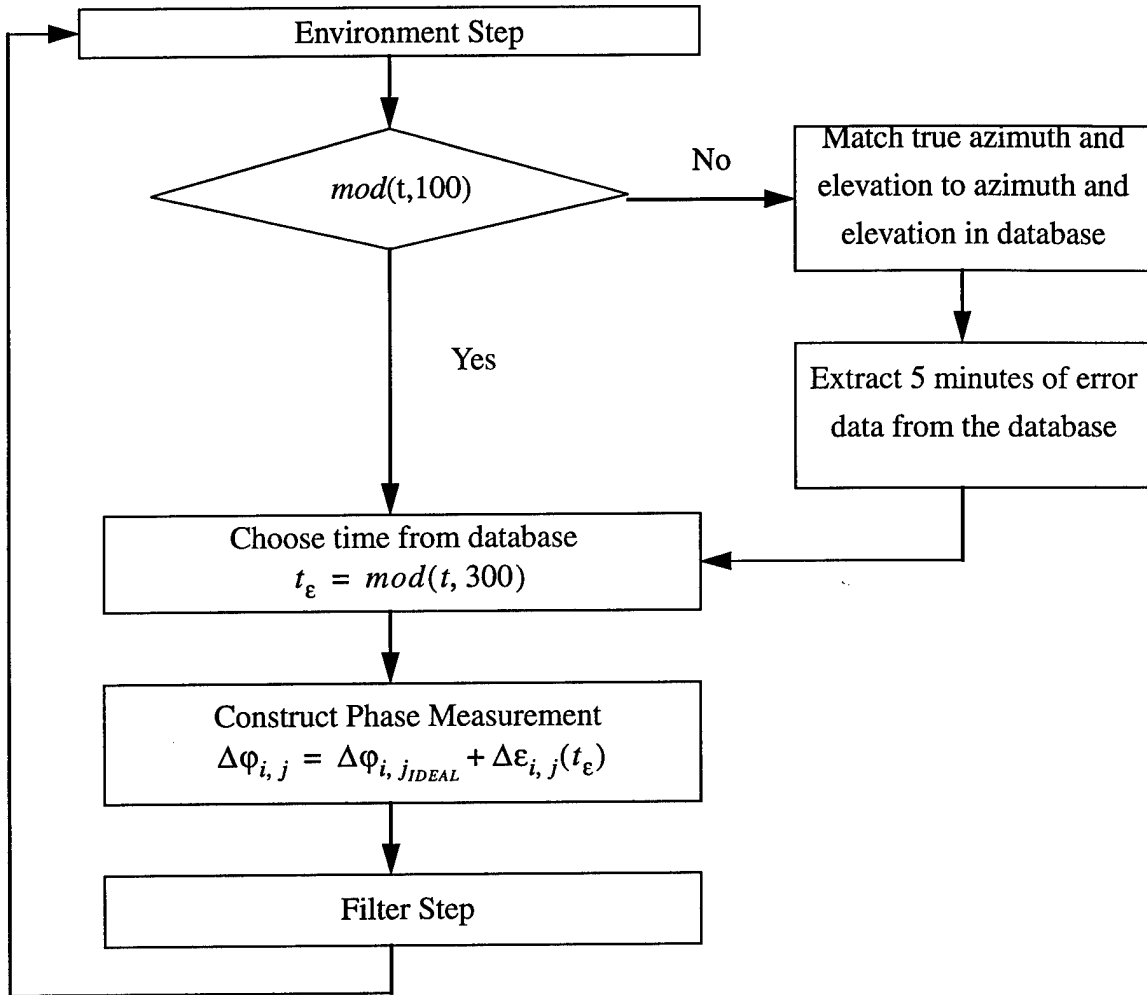


**Figure 6.2: Experimental GPS Data Update**

Only the fractional part of the measurement is passed to the flight software. The sensor block also passes a vehicle position estimate from the receiver to the flight software. Errors on the GPS position fix are modeled as white noise with a standard deviation of 75 meters. These errors are added to the true vehicle position and the corrupted fix is passed to the software.

### 6.2.3 Flight Software

Flight software consists of the integer ambiguity algorithm developed in chapter 2, the EKF from chapter 4 and a simple feedback control law. The filter is parameterized to allow enabling and disabling of all of the error states.

A quaternion feedback law is used to align spacecraft attitude with the LVLH frame. Control action is taken if magnitude of the sum of the angle error and rate error falls outside of a pre-defined dead band threshold,  $\theta_{DB}$ . Angle error is defined as  $2\dot{\underline{\epsilon}}_q$ , two times the vector part of the quaternion error, where quaternion error is the rotation from the desired quaternion to the estimated quaternion:

$$\begin{bmatrix} \dot{\underline{\epsilon}}_q \\ \dot{\underline{\epsilon}}_q \end{bmatrix} = \underline{q}_0^* \otimes {}^B \hat{\underline{q}}^N \quad 6.1$$

The desired quaternion is simply:

$$\underline{q}_0 = \begin{bmatrix} 1 \\ 0 \\ 0 \\ 0 \\ 1 \end{bmatrix} \quad 6.2$$

The rate error,  $\dot{\underline{\epsilon}}_\omega$ , is the difference between the estimated rate,  $\hat{\omega}_{BN}^B$ , and the desired rate,  $\underline{\omega}_0$ , which is **0** in this case.

Outside of this threshold, the commanded control is a linear combination of the vector part of the error quaternion and the rate error which is designed to give a closed loop natural frequency of 0.05 Hz and a 0.707 damping ratio. To avoid excessive slew rates, the control system is rate limited to  $\omega_{max}$ . Above this rate, the control law is strictly rate feedback. Implementation of this

control law is shown in figure 6.3

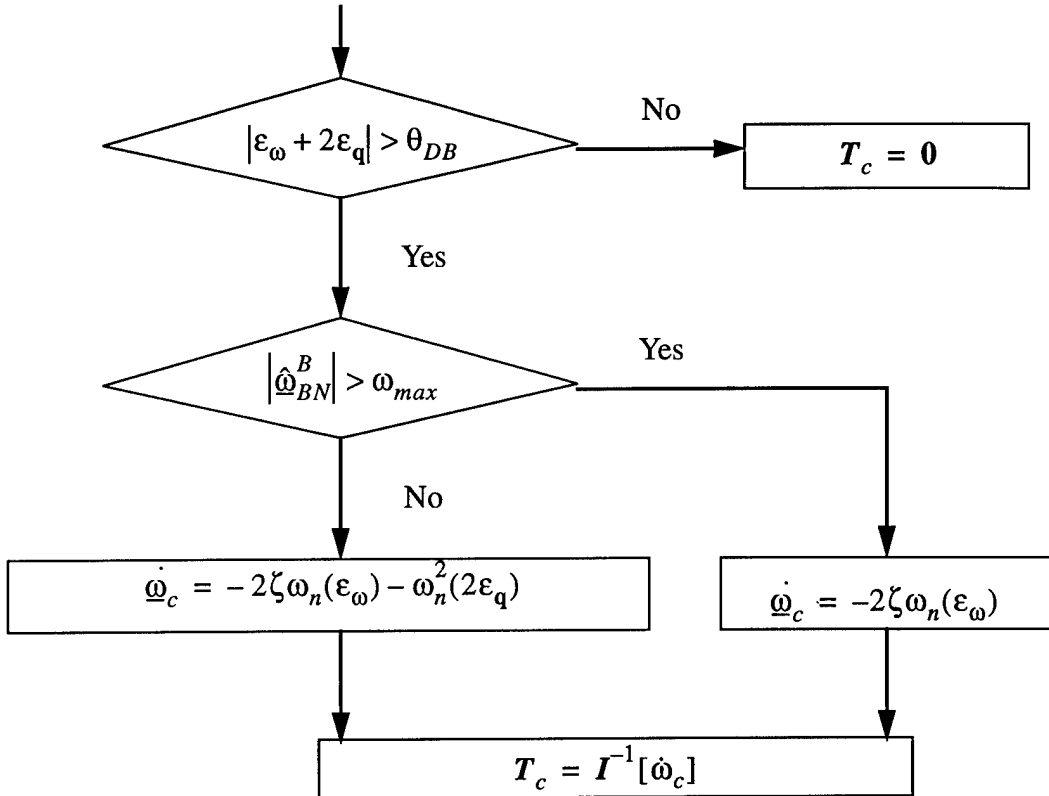


**Figure 6.3: Control Algorithm**

$\omega_n$  and  $\zeta$  are the desired natural frequency and damping ratio, respectively.  $\dot{\omega}_c$  is the commanded angular acceleration, which leads to a torque command  $T_c$ .

### 6. 3 Test Cases

The flight software is tested in nominal and off-nominal configurations. The nominal test phase, which consists of 40 trajectories, is designed to determine expected performance of the system. The off-nominal test cases test the sensitivity of the filter to parameter variation and changes in the environment. Off-nominal test cases include tumble tests, free drift tests, high altitude and multipath tests and testing with no gyro aiding.

Each test case is identified by two numbers followed by one or more letters. The numbers indicate the seed that was used to generate initial conditions and to initialize random process noise and measurement noise for the test case. The first letter indicates the source of differential phase error for the test case. “E” indicates experimental data while “S” indicates simulated data. Any

additional letters refer to off nominal test conditions.

Initial conditions are generated at random to test filter performance across a representative sample of trajectories. Longitude of the ascending node,  $\Omega_0$ , and mean anomaly,  $v_0$ , are unique to each test case, resulting in a unique GPS viewing geometry for each case. Initial conditions for each of the error parameters are selected at random from a normal distribution with standard deviation equal to the modeled intensity ( $\sigma$ ).

The process noise is also unique to each test case. The purpose is to create random, repeatable GPS and gyro error histories to be used in the performance analysis. This also creates a different disturbance torque environment for each test.

### **6.3.1 Nominal Test Cases**

Each nominal trajectory lasts 7000 seconds, slightly longer than the 6000 second Iridium orbit. Twenty nominal trajectories are run using simulated GPS measurement data for the sensor output, each with unique initial conditions. The remaining 20 trajectories test filter performance on experimental GPS measurement data collected with the Vector receiver. These 20 trajectories use the same initial conditions as the 20 simulated data trials.

Simulation parameters for the nominal runs are shown in table 6.1:

Item	Parameter	Value
Orbit	Altitude	421 nm
	Inclination	89°
	$\Omega_0$	Random
	$v_0$	Random
Initial Conditions	Attitude	+5° yaw, pitch, roll
	Angular Rate	+0.01°/s yaw, pitch, roll
Attitude Control	Control Method	3-Axis Stabilized
	Target Attitude	LVLH Aligned
Receiver	Number of Antennas	4
	Number of Channels	6
	Array Size	1m x 1m square
	Output Rate	1 Hz
Gyro	Model	MMIMU (Chapter 3)
	Output Rate	2 Hz

**Table 6.1: Nominal Simulation Parameters**

The orbit parameters are based on the Iridium constellation specifications. The receiver output rate is based on the Trimble Vector. The micro-mechanical gyro is capable of generating measurements faster than the 2 Hz update rate used in the simulation, but the slower output rate allows for pre-filtering of the gyro measurement. The 5° initial offset in yaw, pitch and roll simulates initialization of the software near the nominal nadir-pointing attitude. Larger initial attitude and attitude rate offsets are considered in the off-nominal test phase.

Nominal error parameters for the sensors and environment are shown in table 6.2:

Parameter	Sensor Model (Simulated Data)	Sensor Model (Experimental Data)	Filter Model
Position Error	White, 75m RMS	White, 75m RMS	No Model
Differential Phase White Noise	Intensity in section 3.3.3	Experimental	Intensity in section 3.3.3
Phase Center/Body Fixed Multipath	Calibrated bias (sec- tion 3.3.2)	Experimental	Calibrated bias (sec- tion 3.3.2)
Correlated Noise	1st order model (sec- tion 3.3.3)	Experimental	1st order model (sec- tion 3.3.3)
Line Bias	$\tau_{\Delta\beta} = \text{TP}/2$ $\sigma_{\Delta\beta} = 3 \text{ mm}$	Experimental	$\tau_{\Delta\beta} = \text{TP}/2$ $\sigma_{\Delta\beta} = 3 \text{ mm}$
Baseline Error	$\tau_b = \text{TP}/2$ $\sigma_b = 0.3\%$	$\tau_b = \text{TP}/2$ $\sigma_b = 0.3\%$	$\tau_b = \text{TP}/2$ $\sigma_b = 0.3\%$
Multipath	No model	Experimental	No model
Disturbance Torque	Gravity gradient + 1st order (section 4.3.1) $\tau_{N_o} = \text{TP}/2$ $\sigma_{N_o} = 1\text{e-}4 \text{ N}\cdot\text{m}$	Gravity gradient + 1st order (section 4.3.1) $\tau_{N_o} = \text{TP}/2$ $\sigma_{N_o} = 1\text{e-}4 \text{ N}\cdot\text{m}$	Gravity gradient (sec- tion 4.3.1) White noise (section 5. 2) $\sigma_{w_o} = 1.2\text{e-}5 \text{ N}\cdot\text{m}$

Table 6.2: Nominal Error Parameters

TP is the orbit period. The only artificial error injected into the experimental data is a baseline length error designed to mimic potential expansion and contraction of the antenna array in space. As discussed in section 3.3.4, baseline expansion was not experienced on the ground due to minimal temperature variation. The intensity of line bias in the experimental measurements is about one half of the intensity used in the simulated data, so this difference must be considered when examining the test results.

Performance of the software for the nominal test cases is indicative of on-orbit performance. However, the results cannot be considered a guarantee of on-orbit performance, as the test cases do not simulate every possible combination of gyro errors, GPS errors and visibility conditions. To ensure performance robustness and to test the operational limits of the filter, off-nominal test cases are considered.

## 6.3.2 Off-Nominal Test Cases

### No Gyro

The benefit of gyro augmentation under nominal conditions is tested by conducting a test without measurements from the gyro. The results of this test are compared to predicted results using linear covariance analysis.

### High Altitude

GPS satellite visibility is generally very good for a LEO satellite. In order to test the filter in more sparse visibility conditions, high altitude simulations are conducted to define the upper altitude limit for unaided filter operation. Tests are conducted with and without gyro measurements to examine the role of gyros as GPS visibility degrades.

### Multipath

The purpose of the multipath test is to examine the response of the filter to measurements that are artificially corrupted with multipath. No attempt is made in the software to model environmental sources of multipath, but it must remain stable in the presence of multipath. Ideally, the performance of the filter should not degrade significantly due to a typical multipath signal. Multipath error for the test is generated using the sinusoidal model developed in chapter 3.

### Tumble Initialization

The nominal tests all use an initial 5° yaw, pitch and roll offset with a slow (0.01°/s) drift on each axis. The tumble initialization tests examine the ability of the attitude software to successfully initialize when the initial attitude and attitude rate are chosen at random. Ten tests are conducted, with some of the initial attitudes nearly inverted from the nominal.

### Free Drift

The free drift test measures the ability of the filter to maintain attitude tracking during a loss of control authority. The worst case initial conditions from the tumble initialization are used as a starting point for this one orbit test. Results are compared with and without the availability of gyro measurements.

## Correlated Noise

The correlated noise tests demonstrate the impact of correlated noise on the attitude solution and examine the costs and benefits of removing correlated noise estimation.

## 6.4 Nominal Test Case Results

Overall results for a single nominal test case are presented in section 6.4.1. In section 6.4.2, detailed analysis is presented for individual runs chosen to highlight the ability of the filter to reject disturbances in the presence of significant measurement uncertainty.

The attitude solution and gyro bias estimate are of primary importance in the spacecraft guidance and control system. The attitude solution is needed for control system feedback as well as by all of the pointing equipment on the spacecraft. Gyro bias estimation is used to harness the full capability of the gyro assembly; without knowledge of the gyro bias, gyro measurements are virtually useless. These two outputs will be at the focus of the nominal and off-nominal results discussion.

The filter angular rate estimate is also used in the control system, but rate error performance can be gleaned directly from the gyro bias estimate. This is because the gyro assembly is the filter's only source of direct rate measurements.

### 6.4.1 Overall Nominal Test Case Results

#### Initialization

Initialization of the filter includes solution of the integer ambiguity and the transient response of the filter to initial conditions. The transient response is defined as the initial 10 minutes of filter operation for each test case. Performance of the integer solution algorithm is addressed in section 2.4. Discussion of the transient response is found in the individual test case analyses, in section 6.4.2. The portion of each test following initialization is defined as steady state operation. The attitude statistics presented here are calculated for filter steady state operation.

#### Visibility Conditions

The quality of a GPS based attitude solution is dependent on the geometry of GPS satellites visible to the receiver and the validity of the measurements from those satellites. Two metrics of con-

stellations quality are examined here. The most simple measure of quality is the number of good measurements available to the receiver. The receiver is capable of handling 18 differential phase measurements per 1 second epoch, but 18 measurements will only be available when six satellites are within the  $80^\circ$  antenna half cone angle. In addition, each of the six satellites must be valid. A *visible* satellite will be *invalid* if the receiver cannot achieve a lock on the carrier phase from the satellite or if for any reason the receiver determines that measurements from the satellite are not reliable.

With a low orbit altitude and a nadir-pointing vehicle attitude, the nominal configuration encounters visibility similar to that expected on the earth. Figure 6.4 shows the number of valid GPS measurements available to the filter over all 20 of the test orbits for the experimental GPS measurement error tests:

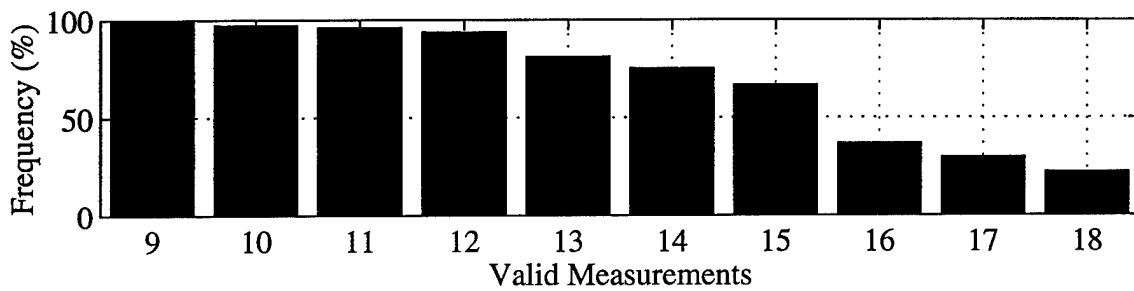


**Figure 6.4: Valid GPS Measurements (Experimental Data)**

The horizontal axis is the number of valid measurements. The height of each bar is the percentage of time at least that many valid measurements are available. Nine valid measurements is virtually a guarantee, but the frequency drops off sharply above 15 measurements.

The fluctuations in validity are caused by characteristics of the Vector receiver used for ground based testing. Recall that the experimental data is stored in 5 minute intervals for use during the simulation. The receiver reports a validity flag with each measurement, and this flag is stored in the database as well. During the simulation, six satellites were *visible* to the receiver almost 80% of the time, but a measurement was only used if the corresponding ground based data was tagged with a good validity flag.

Inspection of the experimental data reveals that two primary instances which lead to invalid mea-

surements. The receiver usually tags the measurements from a channel as invalid for a short period following each satellite change on the channel. Another frequent occurrence is intermittent invalidation of satellites at approximately  $15^{\circ}$  to  $30^{\circ}$  elevation in the body frame. This behavior could be caused by signal blockage, but as shown in the sky map in figure 3.7, the highest obstruction in the vicinity of the receiver is below  $10^{\circ}$  in the body frame. In fact, a mask setting of  $10^{\circ}$  elevation was used during testing to prevent selection of satellites below this elevation. It is possible that the validity behavior is caused by gain pattern characteristics of the patch antennas at low elevation or by fault detection algorithms in the Vector software.

This hardware characteristic is not modeled in the simulated data. As a result, measurement validity is much better for the simulated error cases:

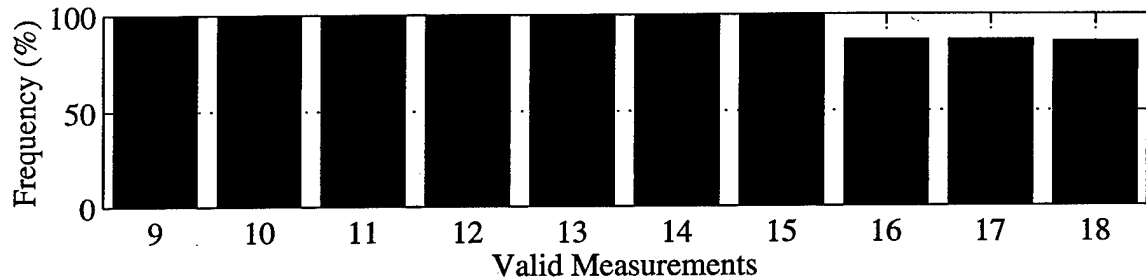


**Figure 6.5: Valid GPS Measurements (Simulated Data)**

In fact, the validity data for simulated measurement is only a function of satellite geometry and the attitude estimate, not receiver characteristics. Validity is a function of the attitude estimate because a  $10^{\circ}$  body frame elevation mask angle is used to invalidate low-lying satellites. If the attitude estimate is in error, the software may erroneously label a valid measurement as invalid or vice-versa. Otherwise, every visible measurement is considered valid. The key validity statistics

are compared in table 6.3:

	Number Valid Measurements (Experimental Data)	Number Valid Measurements (Simulated Data)
Mean	14.9772	17.5721
Standard Deviation	2.3847	1.1202
1- $\sigma$ (Lower Bound)	15	18
2- $\sigma$	11	15
3- $\sigma$	6	12

**Table 6.3: GPS Validity Statistics**

The simulated data clearly has better average validity than the experimental data, but, as the *ADOP* discussion will show, the benefit of 18 measurements versus 15 measurements is marginal.

The number of valid measurements is always 6 or greater. Six measurements are sufficient to determine the attitude of the spacecraft even without previous attitude knowledge (provided that the integers are resolved), so measurement validity never reaches a critical level.

Another metric which measures the quality of the GPS geometry is *ADOP*. As explained in section 4.5.1, *ADOP* is an instantaneous measure of estimation accuracy which is dependent on the linearized differential phase measurement sensitivity. Total *ADOP* is used to estimate the total RSS attitude uncertainty as a function of total differential phase error:

$$\sqrt{\sigma_\phi^2 + \sigma_\theta^2 + \sigma_\psi^2} = ADOP_{TOT} \cdot \sigma_\epsilon \quad 4.89$$

The distribution of total *ADOP* for the nominal test cases is presented in figures 6.6 and 6.7:

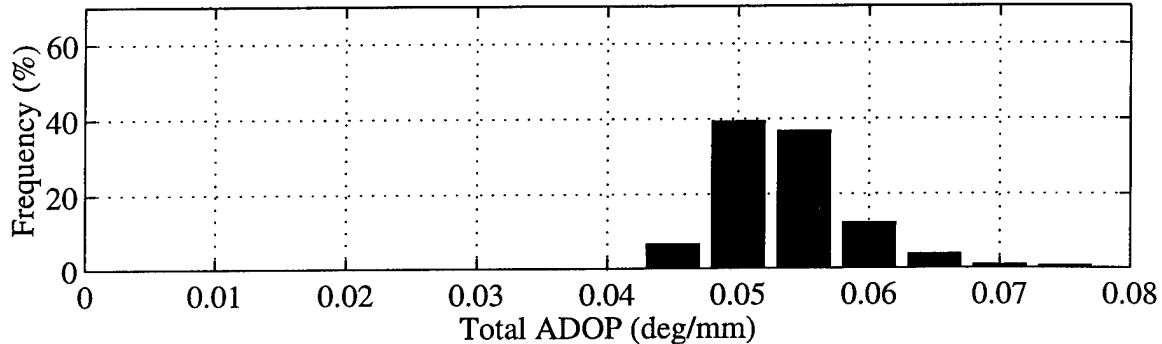


**Figure 6.6: ADOP (Experimental Measurements)**

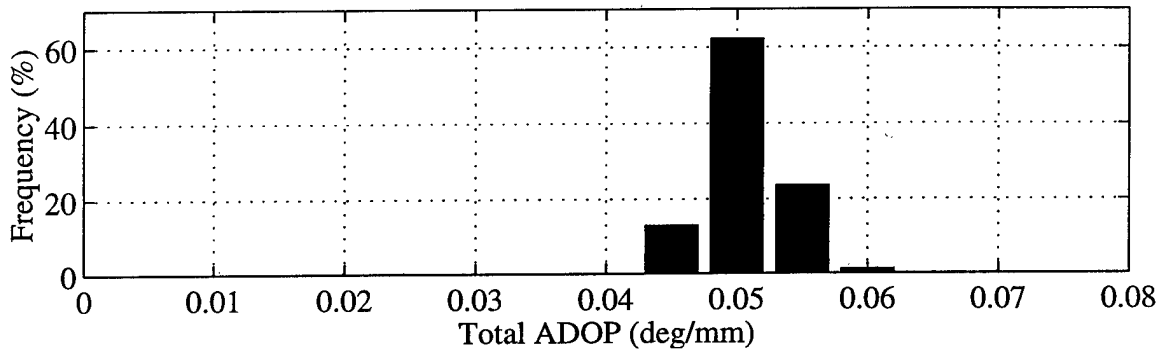


**Figure 6.7: ADOP (Simulated Measurements)**

Here, the height of each bar denotes probability density. For example, the middle bar in figure 6.7 shows that *ADOP* was greater than 0.0475 and less than 0.0525 about 60% of the time across all of the nominal test cases. Notice that, although the simulated data produces an average of three more valid measurements than the experimental data, the average *ADOP* only differs by about 10%. This proves that the marginal benefit an added satellite when three or four are already available is relatively small when calculating an attitude point solution. However, additional satellites do increase the resolution of the filter in estimating the gyro drift and combatting correlated noise and biases, so the difference in visibility could result in superior performance when using the simulated GPS errors.

## Attitude

The distribution of total attitude error (RSS) over the 20 nominal runs with experimental data is

shown in figure 6.8:

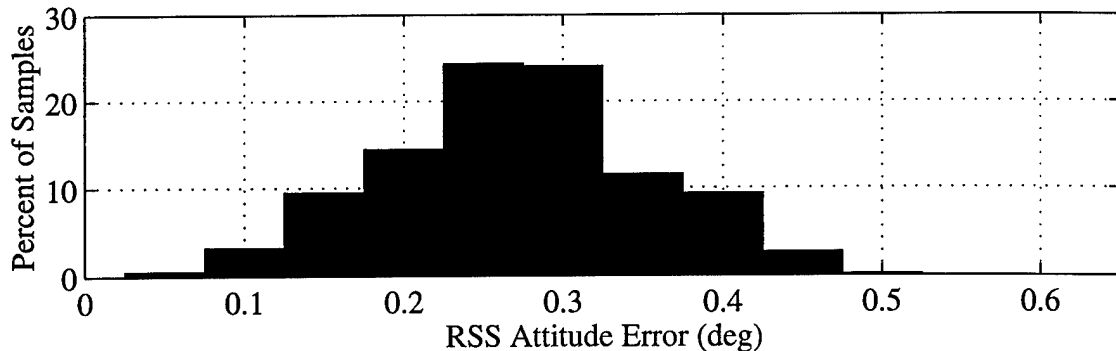


**Figure 6.8: RSS Attitude Error Distribution (Experimental Data)**

The distribution shows that total RSS attitude error is typically  $0.2$  to  $0.3^\circ$ . Attitude error statistics for each axis are summarized in table 6.4:

	Yaw (deg)	Pitch (deg)	Roll (deg)	Total (deg)
RMS	0.1250	0.1548	0.1578	0.2540
$2\sigma$	0.2357	0.2934	0.2996	0.3875
$3\sigma$	0.3412	0.4029	0.4320	0.4836
Maximum	0.4150	0.4537	0.4943	0.5706

**Table 6.4: Nominal Attitude Error Statistics (Experimental Data)**

Yaw performance is generally superior to pitch and roll. The difference is a result of the antenna array configuration. Yaw *DOP* for the planar antenna array is generally smaller than the *DOP* for pitch and roll because the baselines are orthogonal to the yaw axis. The geometry results in better conditioning of the yaw angle measurement sensitivity than pitch and roll.

Recall that the Iridium design requires roll estimation performance superior to that of yaw and pitch:

Axis	3- $\sigma$ Pointing Requirement
Yaw	$0.4^\circ$
Pitch	$0.3^\circ$
Roll	$0.2^\circ$

**Table 1.1: Iridium Attitude Determination Requirements**

Nominal filter performance meets the yaw requirement, but the results fall slightly short of the roll and pitch specifications. If reduction of roll and pitch errors is mission critical, three methods may be used to improve performance. One is to incorporate additional sensors into the ADS suite. Another is to increase the size of the antenna array. The linear covariance analysis in section 5.4 showed that doubling of the array size to a 2 m square reduces attitude errors by approximately one half. The third solution is to change the geometry of the existing array. Recall that yaw performance is better than roll and pitch because the array is orthogonal to the yaw axis. Tilting the array forward into the plane orthogonal to the roll axis would decrease the roll *ADOP*. However, this would also result in less available measurements, so a better option would be to tilt the array slightly forward. Finally, a simple rotation of the square array would also improve roll performance. In the nominal configuration, the diagonal baseline is aligned with the roll axis. Rotation of the array to align the long baseline with the pitch axis would decrease the roll *ADOP*. Of course, this would come at the expense of pitch performance.

Although the Iridium requirements are not satisfied, performance of the ADS should satisfy estimation requirements for many LEO spacecraft missions. Total 3- $\sigma$  pointing error over the nominal test cases is only 0.48°. Another favorable characteristic is that maximum estimation errors on each axis are very well behaved.

As mentioned previously, these are the steady state attitude performance statistics. Filter initialization for each of the test cases was excellent, with the results presented in section 2.4.

The attitude solution using simulated GPS data behaves much like the solution with experimental data. Recall that the average number of valid measurements with experimental data is lower than the number with simulated measurements, so improved performance might be expected with the simulated error data. The RMS errors are indeed smaller, but maximum roll and pitch errors for the simulated data case are significantly larger than the corresponding values for the experimental

data case.

	Yaw (deg)	Pitch (deg)	Roll (deg)	Total (deg)
RMS	0.0735	0.1390	0.1438	0.2131
2- $\sigma$	0.1383	0.2683	0.2692	0.3573
3- $\sigma$	0.3041	0.4737	0.4840	0.5610
Maximum	0.3995	0.6388	0.5910	0.6648

**Table 6.5: Attitude Errors (Simulated Data)**

One cause of the difference in performance is the nature of stochastic errors. If the assumption of normally distributed experimental errors is not entirely accurate, the random noise sequences used to generate simulated GPS data will contain more (or less) outliers than typical samples of experimental data. If the stochastic error data *does* contain more outliers than the experimental data, the result would be large 3- $\sigma$  and maximum attitude error statistics.

Another cause of the degradation of roll and pitch performance for the simulated data case might be a discrepancy in the line bias model. In section 3.3.4, measured line bias intensity from ground based tests was *doubled* to calculate line bias intensity for the simulated data. This modification adjusts for the harsh temperature extremes encountered in space. However, additional line bias was not added to the experimental data. Line bias intensity for the experimental tests is therefore smaller than for the simulated tests. Since roll and pitch are more sensitive to line bias than yaw, the difference leads to an increase in roll and pitch estimation errors for simulated measurement data.

Figure 6.9 shows that the distribution of errors for the simulated data tests is slightly different

from the experimental data results:

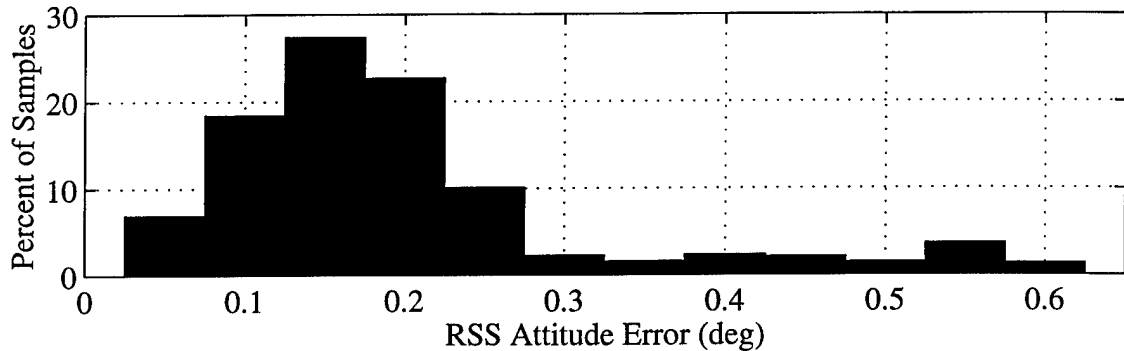


**Figure 6.9: RSS Attitude Error Distribution (Simulated Data)**

The median error is about  $0.15^\circ$ , as opposed to  $0.25^\circ$  for experimental data. However, large magnitude ( $>0.5^\circ$ ) RSS errors occur more often in the experimental data. As mentioned previously, this may be the result of a non-Gaussian experimental error distribution.

#### 6.4.2 Detailed Test Analysis

Four nominal test runs are presented here in detail. Test case 13E represents typical performance of the filter for nominal test conditions. Each of the three remaining tests target a specific error source. Test 5S illustrates response of the filter to a particularly ill-behaved correlated noise trajectory. Test 11E shows the response to a line bias deviation, test 7S focuses on gyro bias disturbance rejection, and test 16S is an example of a large baseline length variation.

Some remarks on the formatting of output data are necessary before proceeding.

Correlated noise errors are smoothed before plotting to clarify the low frequency dynamics of the error. True line bias is available for simulated measurement data, but it cannot be directly computed for the experimental measurements. Recall that the experimental measurement is formed by superimposing total error from real tests on top of ideal phase for the simulated attitude. To extract true line bias from these measurements, the average differential phase error is calculated across all six channels and across time for measurements on a single baseline. The average is then smoothed in a low pass filter to remove the high frequency component of the total error. This is the line bias truth used to compute errors for the experimental data runs.

### Nominal Case 13E

This test run exhibits performance which is typical for filter operation on experimental data. Attitude error, attitude rate error, gyro bias and gyro bias error and *ADOP* information are shown in figure 6.10. Figure 6.11 gives the line bias and line bias error, baseline length variation and length estimation error and satellite visibility data. Figure 6.12 and 6.13 show true correlated noise and correlated noise estimation error for all 18 measurements.

Line bias and correlated noise are the main factors driving the attitude estimation error. To see this, notice the large negative roll deviation at  $t = 100$  min. The roll axis is aligned with baseline 2, so the source of the deviation must be an error on baselines 1 or 3 or a gyro bias error on the roll axis. Figure 6.10 shows that the roll gyro bias is relatively flat at the end of the run, so gyro bias is not a factor. True line biases on baselines 1 and 3 are fluctuating throughout the run with a 2-3 mm amplitude, but there is no distinct trend in these biases.

Examination of the correlated noise states reveals that the source of the roll error is the measurement on channel 2, baseline 3. Figure 6.14 provides a close-up view of the correlated noise behavior on this measurement along with the roll axis attitude error. At  $t = 96$  min, a satellite change takes place on this channel. Examination of the correlated noise state reveals that the measurement from the new satellite has a large positive bias. The bias calibration model does not completely model the bias, so the correlated noise estimate is slightly low and the estimation error starts at about -2mm.

The response of the filter to this measurement bias is a function of sensitivity of the measurement to each of the filter states. The two states of interest here are the correlated noise state and the small angle roll correction. Figure 6.14 shows the location of the satellite on channel 2 relative to baseline 3. The satellite is nearly overhead, so a positive roll angle  $\phi$  moves slave antenna 3 “away” from the satellite. This decreases the delta range  $b \bullet s$ , so the measurement has a *negative* sensitivity to roll. The correlated noise state is an additive error, so the measurement has a *positive* sensitivity to the correlated noise state.

Thus the positive measurement bias results in a combination of a negative roll correction and a

positive correction to the correlated noise state. The sudden change in the correlated noise state due to the satellite change occurs faster than the expected correlated noise dynamics, so the initial filter reaction is a negative roll correction. The other measurements cannot overrule this correction, so the filter remains in error until the correlated noise state reaches a smaller value.

Notice that the filter can estimate roll rate as the slope of the roll angle, so the negative roll correction creates a negative roll rate bias. The gyro reports no change in the roll rate, so a positive gyro bias error develops as the filter attempts to reconcile the gyro measurement with the GPS correction.

Examination of the attitude error statistics reveals that this large of an attitude error deviation is unusual. In most instances, the abundance of GPS measurements is enough to counteract the drift due to correlated noise.

As an aside, the detailed view of the noise in figure 6.14 reveals that there is a repeating pattern in the correlated noise state. This is not a physical phenomenon but a result of the experimental data test methodology. Recall that in the sensor model, GPS errors are extracted from a data base according to azimuth and elevation every 100 seconds. In this instance, the satellite on channel 2 matched the same ground-based data set for three consecutive updates. A possible remedy for this would be to choose error data at random from the matching data set rather than extracting the data sequentially.

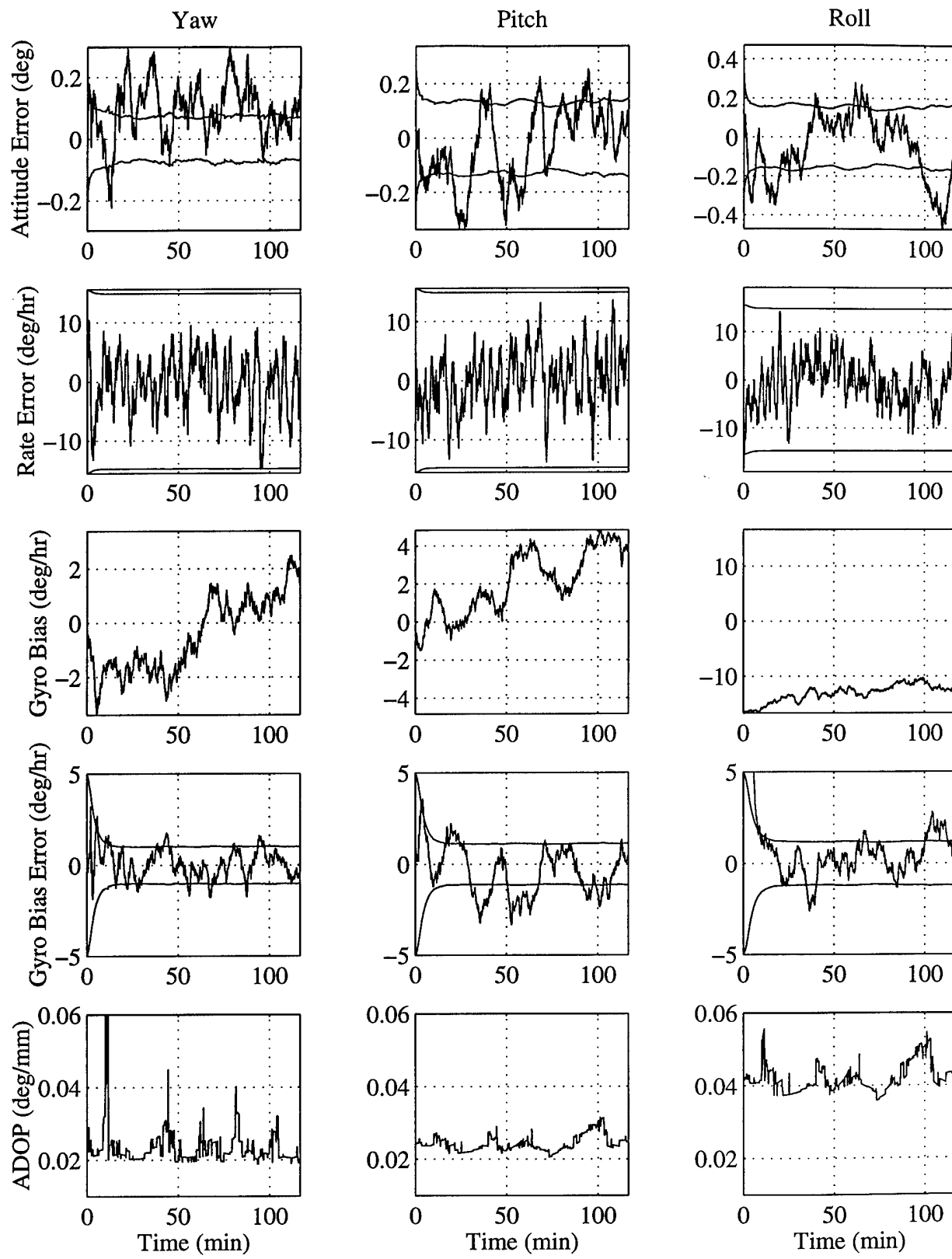


**Figure 6.10: Nominal Case 13E Attitude History**

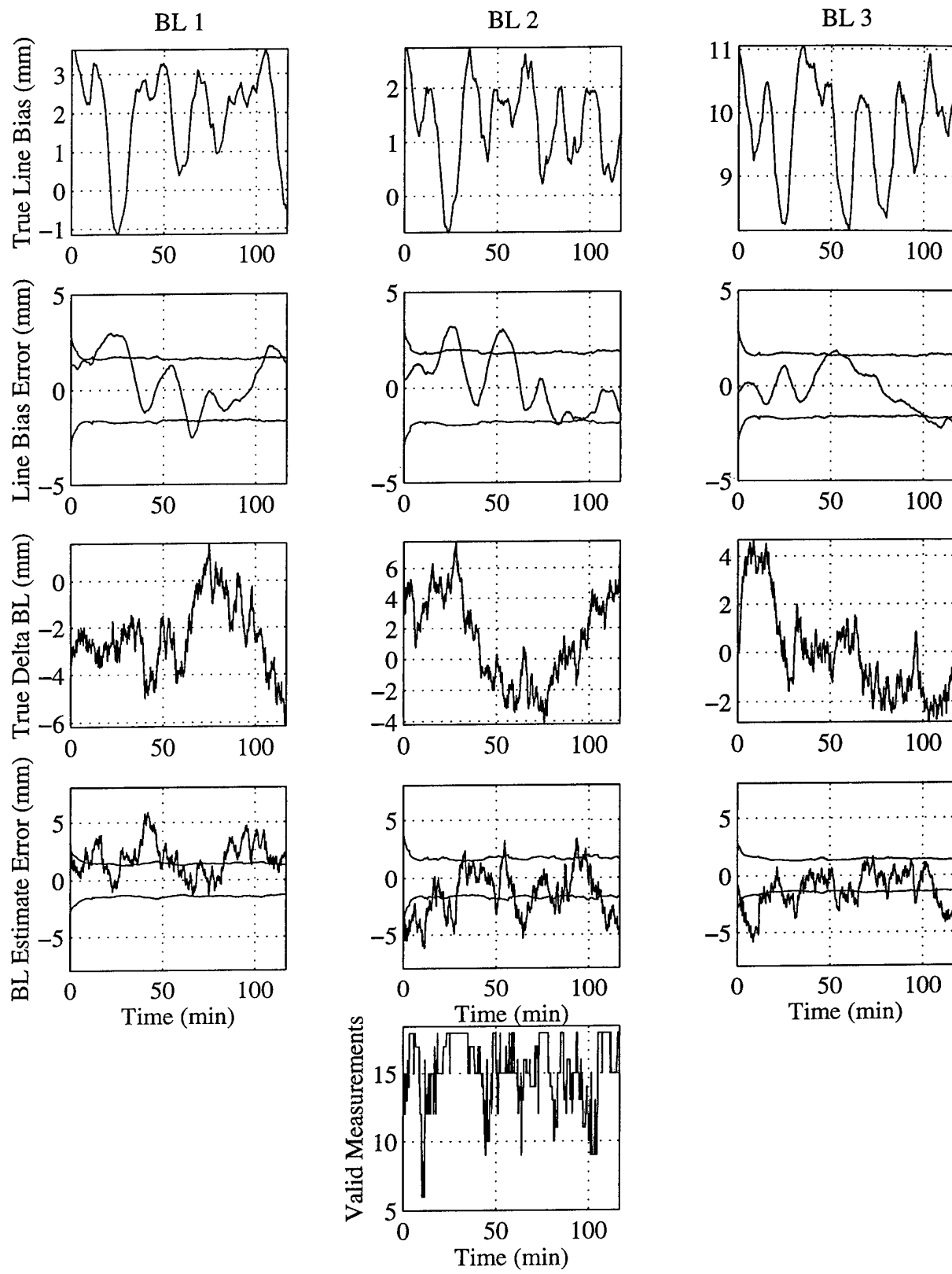
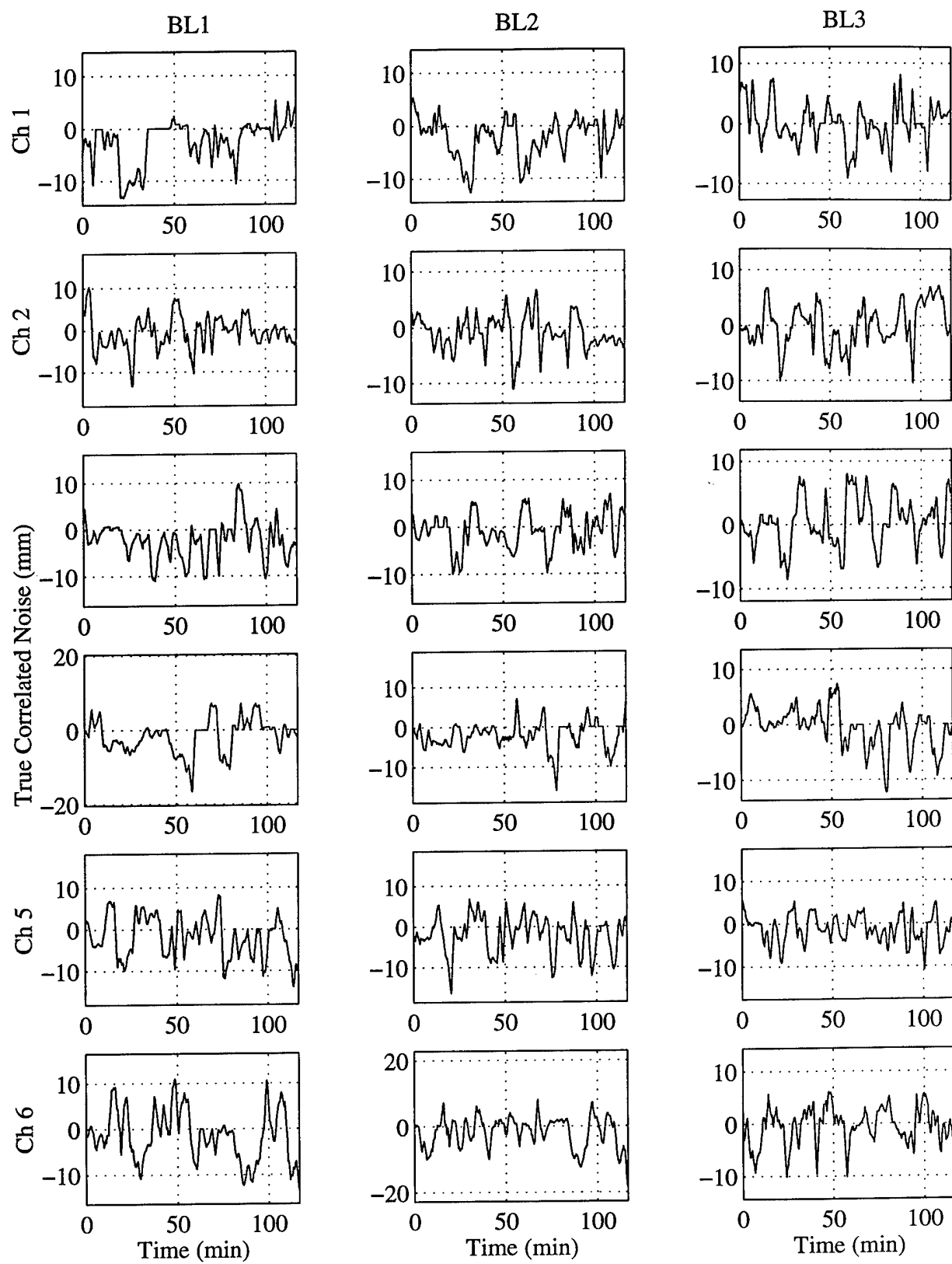
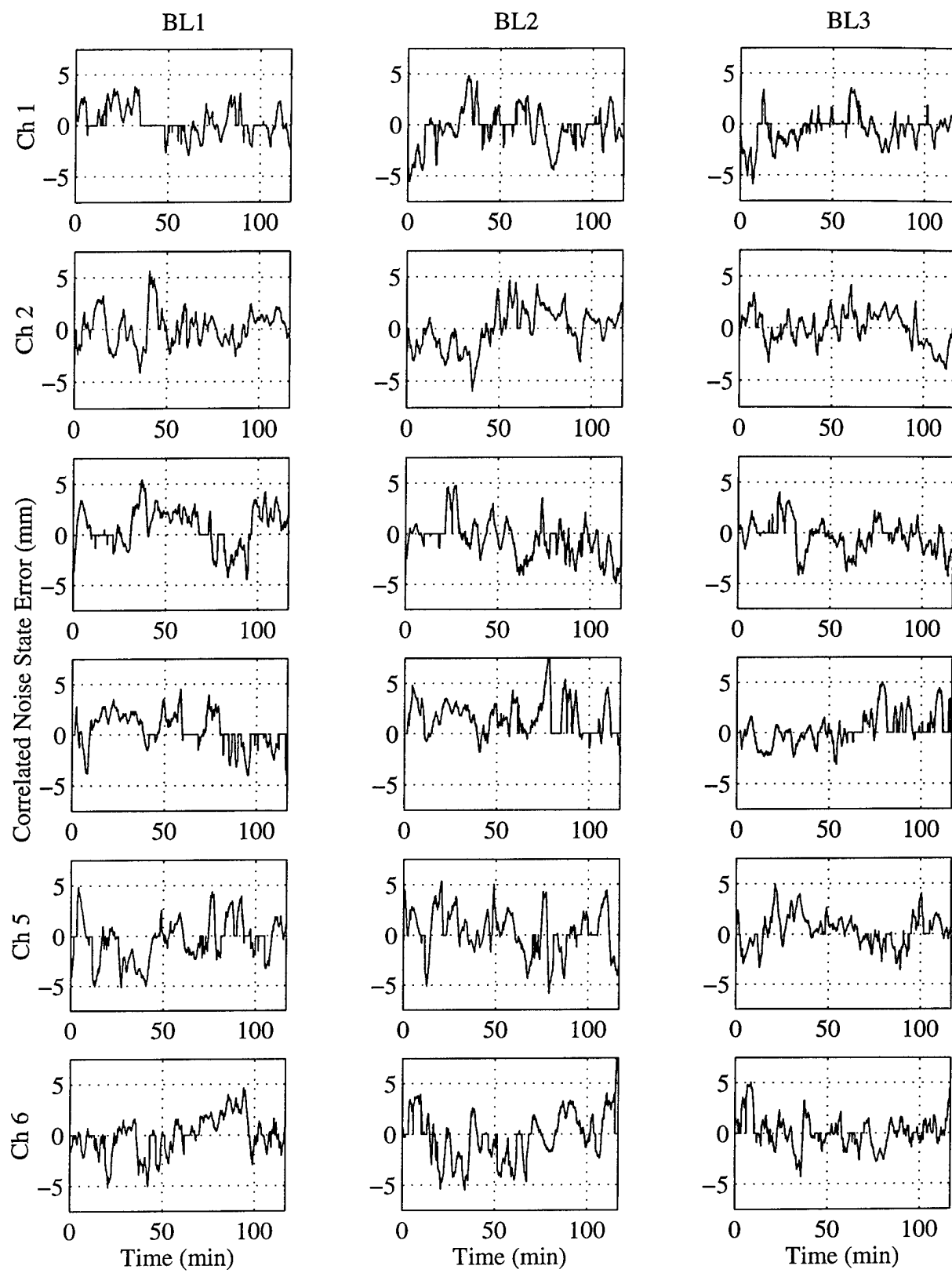


Figure 6.11: Nominal Case 13E



**Figure 6.12: Nominal Case 13E True Correlated Noise State**



**Figure 6.13: Nominal Case 13E Correlated Noise State Error**

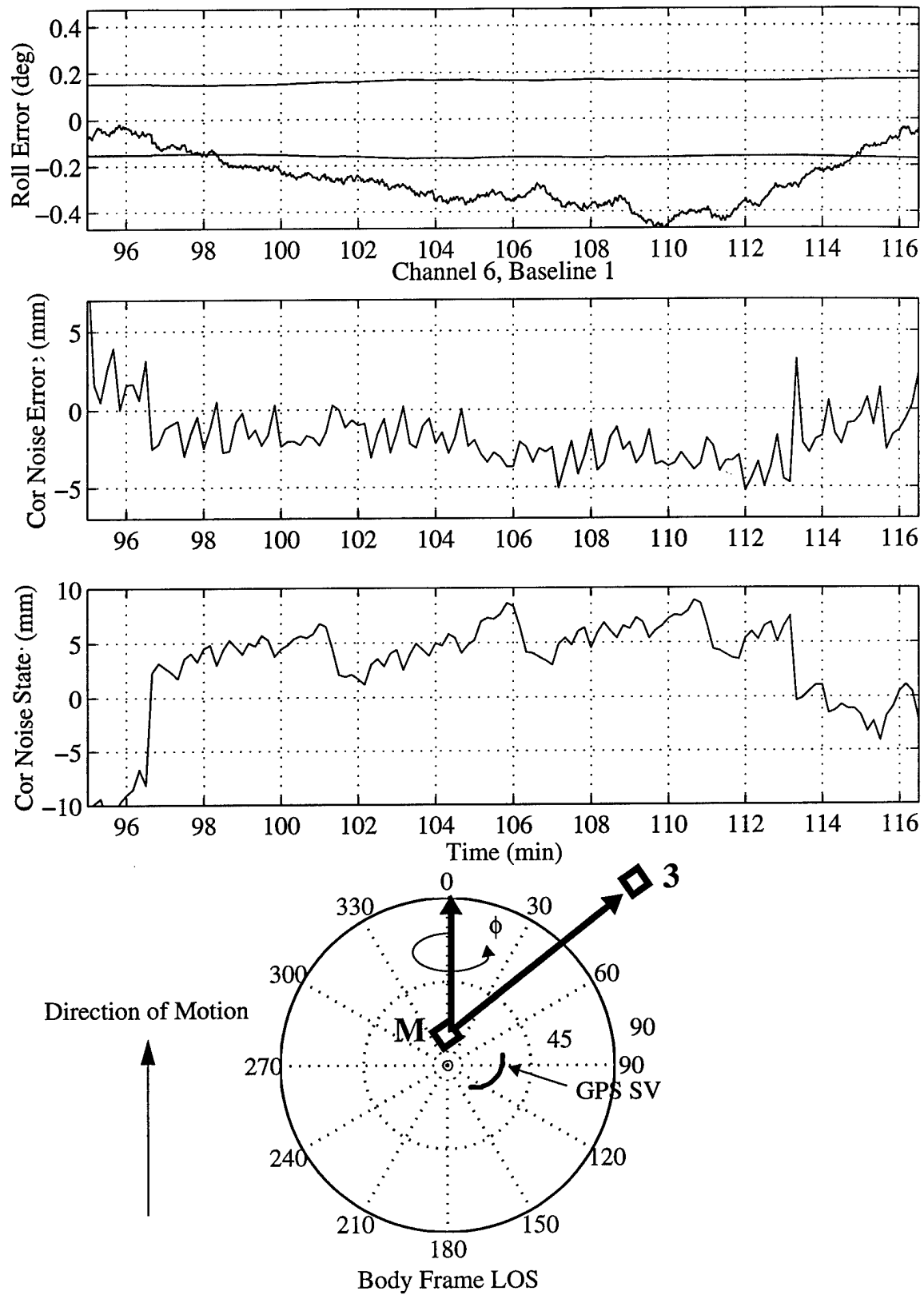


Figure 6.14: Analysis of Roll Error Using Correlated Noise

### Nominal Case 05S

This test case exhibits a worst case combination of gyro bias and line bias errors. The discussion will again focus on the roll estimation error around  $t = 100$  min. Attitude error, attitude rate error, gyro bias and gyro bias error and *ADOP* information are shown in figure 6.15. Figure 6.16 gives the line bias and line bias error, baseline length variation and length estimation error and satellite visibility data.

No significant trends are present in the correlated noise states or the baseline length error throughout this test, but figure 6.16 shows that the line bias on baseline 3 changes by nearly 1.5 cm beginning at  $t = 50$  min. The filter closely tracks the line bias until  $t = 100$  min, and no large attitude errors develop before this point.

In the mean time, the roll axis gyro bias begins a sharp decrease beginning at  $t = 90$  min. As this happens, the filter bias estimate lags behind and a negative offset develops in the estimated roll rate.

At 100 minutes, the line bias estimate has just reached equilibrium when the true line bias reverses direction and increases. The small angle roll state has a negative sensitivity to line bias on antenna 3. A negative error has already developed in the roll rate due to the gyro bias dynamics, so this compounds the negative roll tendency caused by an increase in line bias 3. The result is a sharp negative roll correction which peaks at a magnitude of  $-0.5^\circ$ . This is the largest roll error over all 40 of the simulated and real nominal test cases.

The results show that in the face of a worst case combination of a 1 cm line bias deviation and a  $4^\circ/\text{hr}$  change in the gyro bias over a 50 minute period, the filter is able maintains pointing accuracy to  $0.5^\circ$ , which is about  $2\sigma$  using the attitude uncertainty estimate within the filter.

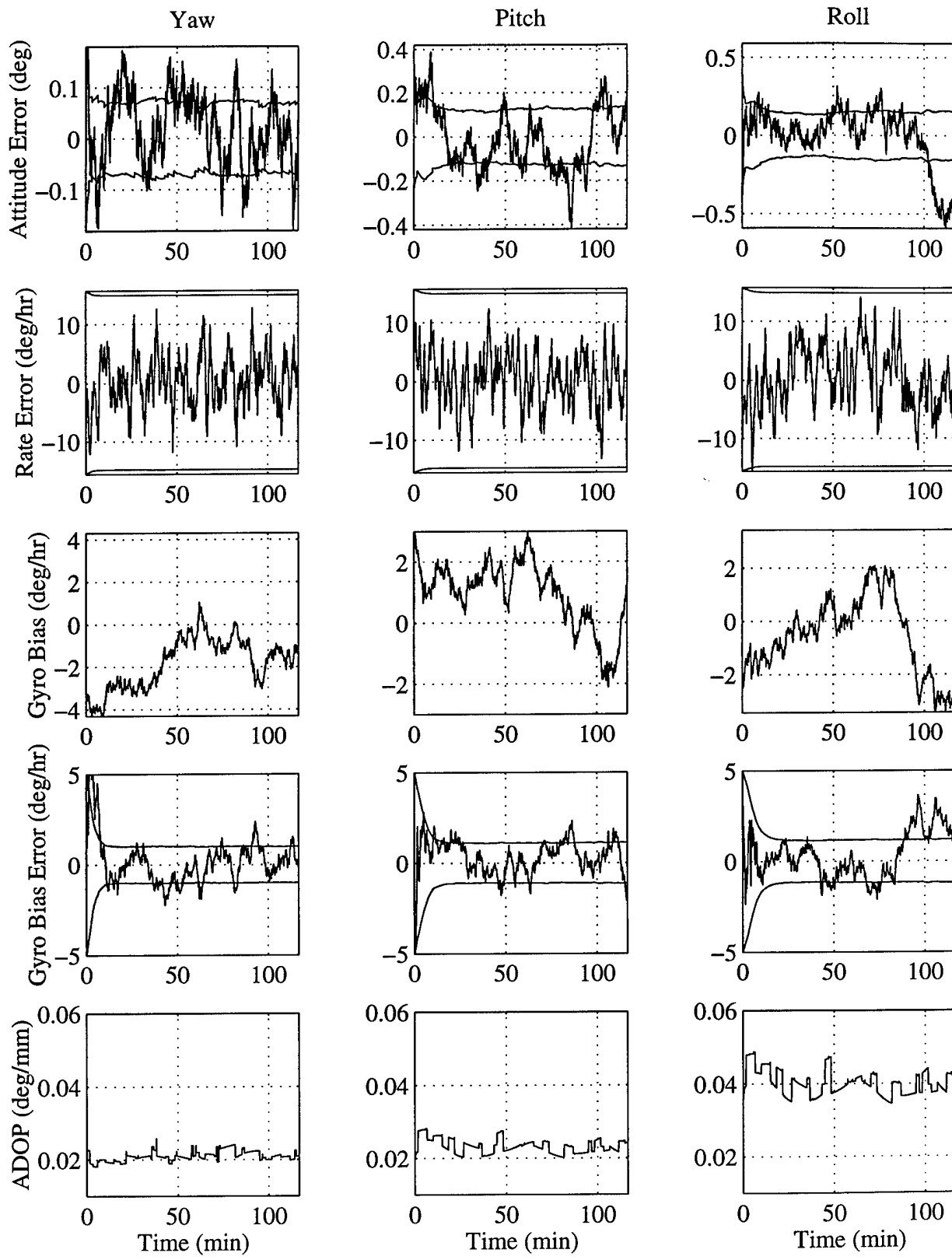


**Figure 6.15: Nominal Case 05S Attitude History**

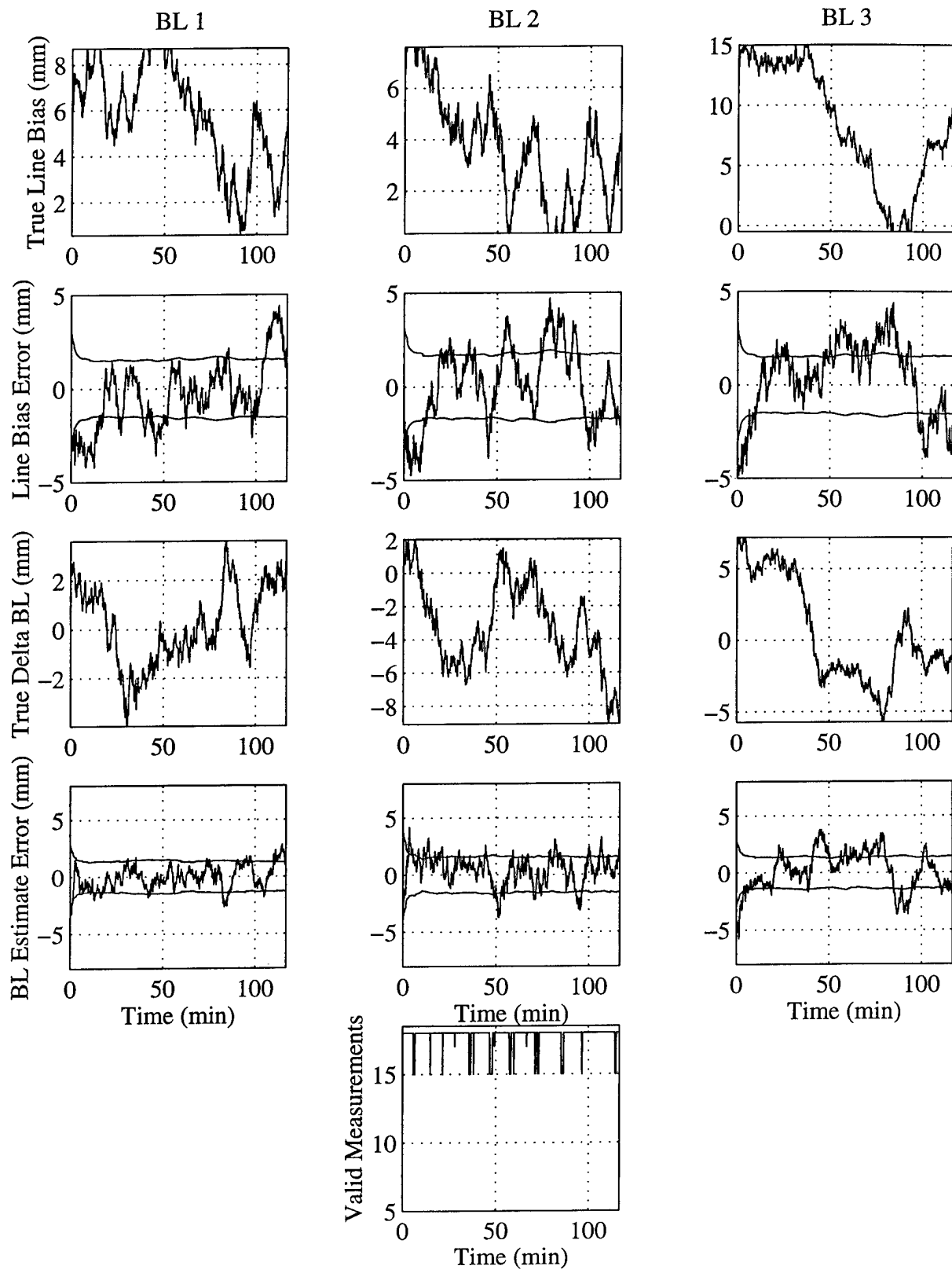


**Figure 6.16: Nominal Case 05S**

### Nominal Case 11E

This test case demonstrates the capacity of the filter to reject large, relatively fast changes in the baseline length. Figure 6.17 includes the standard attitude, gyro bias and ADOP plots. In figure 6.18, notice the variation in the length of baseline 2. At  $t = 40$  min, the length of baseline 2 rises from -5 mm to +4 mm and back down to nearly 1 cm shorter than the nominal in a matter of one hour. The maximum baseline length estimate error during this time is only about 4 mm.

Baseline 2 is orthogonal to the pitch axis, so any effects of the length error should be seen in the pitch attitude estimate. At  $t = 40$  min, the pitch error does reach slightly more than  $-0.3^\circ$ , but this is reasonable given the magnitude of baseline length variation. Pitch peaks again at  $+0.4^\circ$  around  $t = 80$  min, but this error does not appear to be associated directly with the baseline length error.

The peak-to-peak variation in baseline length through this test is over 1 cm, nearly 1% of the nominal baseline length, but attitude errors remain well bounded through the trajectory. The test suggests that the baseline length variation states make a valuable contribution to filter performance, especially considering the low order required to model baseline length variations.

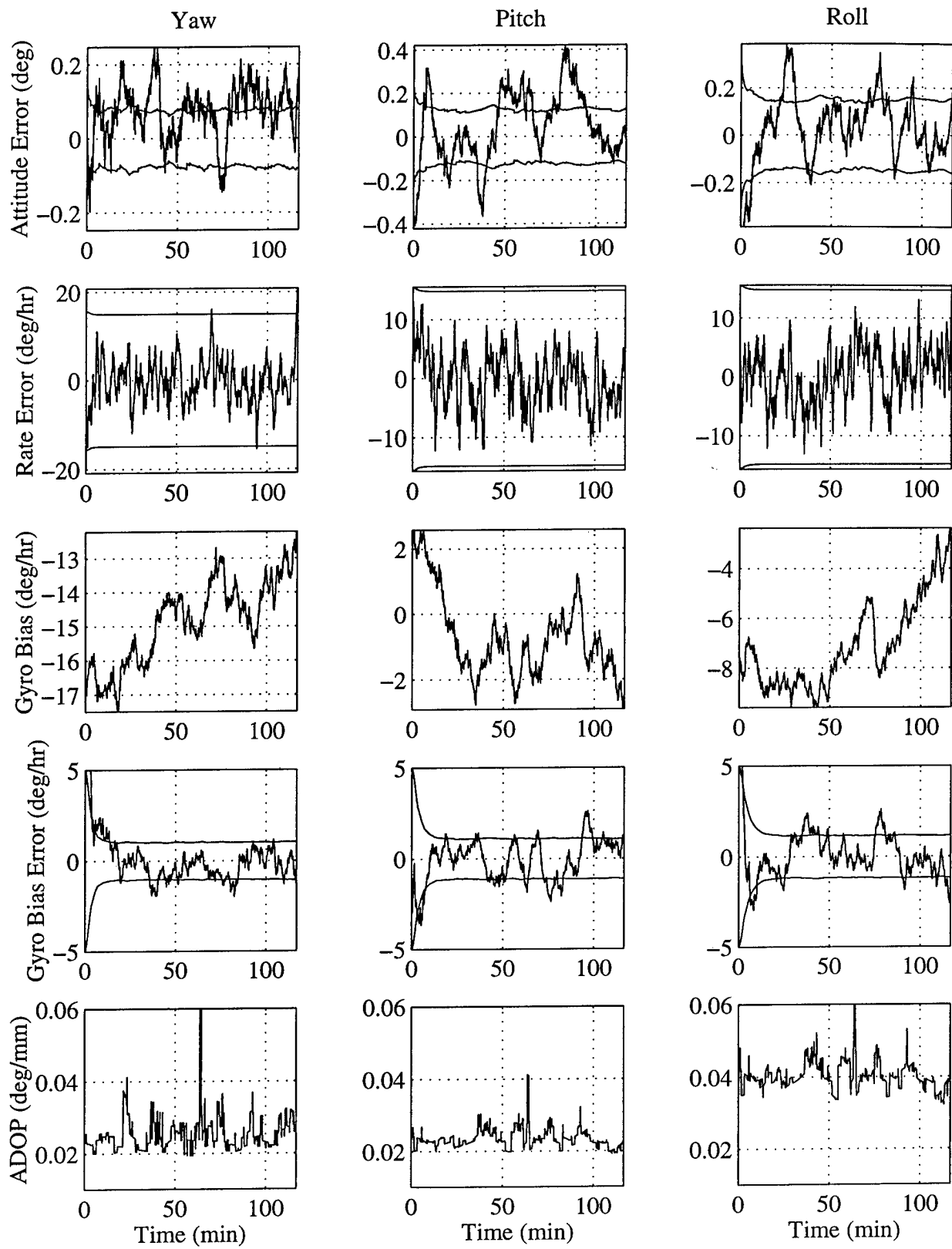


**Figure 6.17: Nominal Case 11E Attitude History**

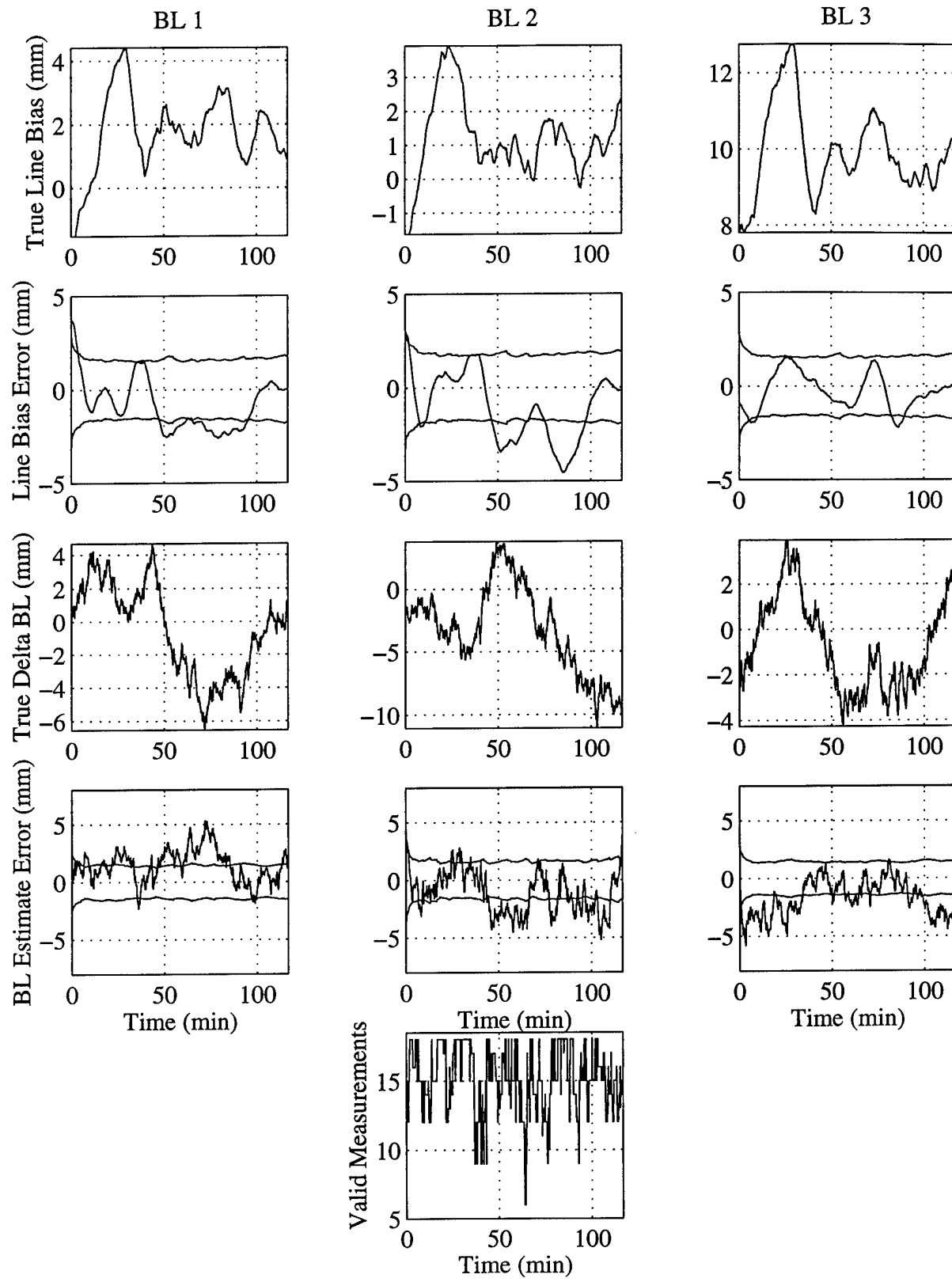


**Figure 6.18: Nominal Case 11E**

## 6.5 Off-Nominal Test Case Results

### 6.5.1 GPS Only Test Case

This test case, 02S-G, analyzes the effect of gyro augmentation on the filter performance under nominal conditions. Conditions during the test are identical to those of the nominal test, 02S; the only difference is that the filter does not use gyro measurements in case 02S-G. GPS visibility during the test is excellent and the spacecraft is stabilized in a nadir pointing attitude, so nominal estimation errors are predominantly caused by GPS differential phase errors.

Figure 6.19 shows attitude error for the two cases:

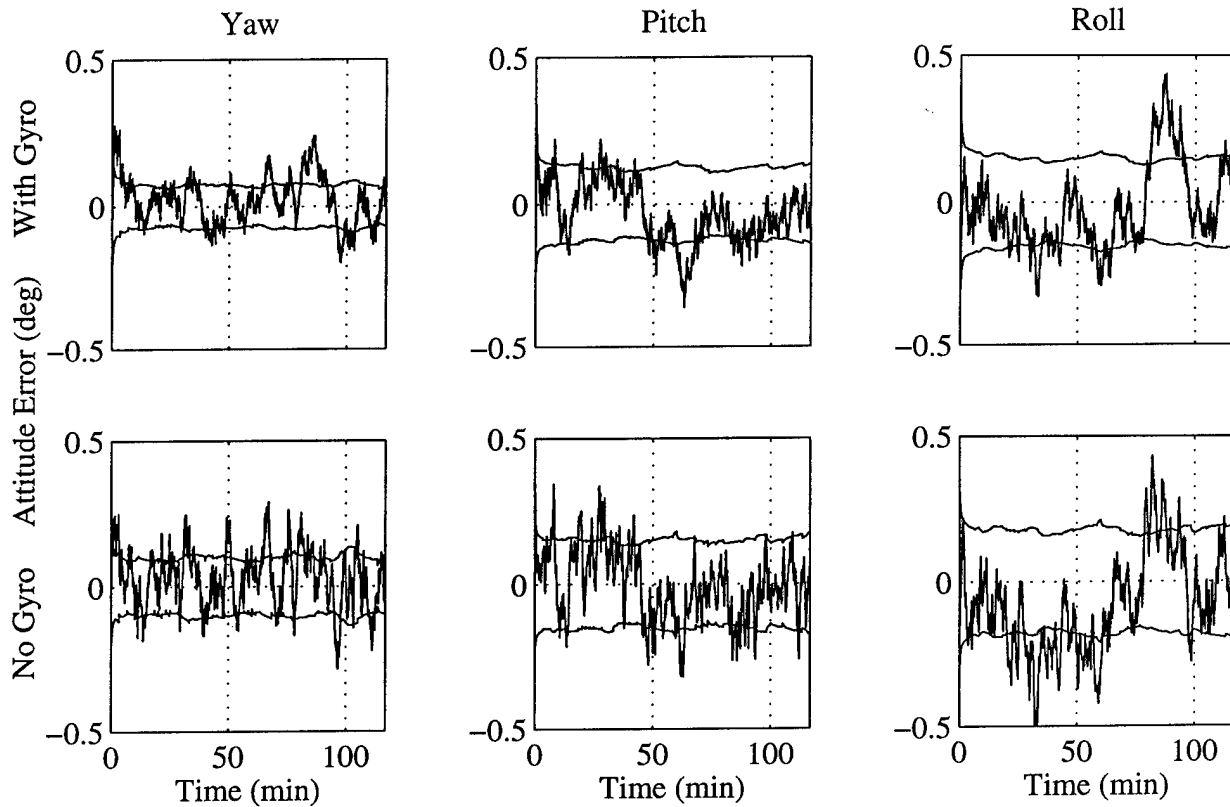


**Figure 6.19: Attitude Error with and without Gyros**

The most striking difference is in the character of the two solutions. The GPS only solution exhibits more high frequency noise than the gyro aided design. This is a result of the angular rate knowledge provided by the gyro assembly. A large process noise intensity on the angular rate is necessary to optimize the reduced order filter in the presence of a correlated disturbance torque (see section 5.2). The process noise increases the bandwidth of the gyroless EKF, resulting in higher gains on the GPS measurements and less noise rejection. With angular rate knowledge

from the gyro, the gyro aided filter is able to reduce gains on the GPS measurement and hence GPS noise.

The total RSS errors are shown in table 6.6:

	RSS Attitude Error (deg)		
Case	Mean	3- $\sigma$	Max
With Gyro	0.2021	0.5091	0.5285
Without Gyro	0.2496	0.5532	0.5945

**Table 6.6: RSS Attitude Errors, Test 02S-G**

The average RSS attitude penalty of  $0.04^\circ$  without gyro aiding is an increase of almost 25% over the nominal performance. The gyro assembly also limits the size of attitude error peaks. A clear example of this is the negative roll error at  $t = 40$  min. Without gyros, GPS errors force the roll error to a peak of  $-0.5^\circ$ . With rate information from the gyros, the integrated design successfully limits the roll error to about  $-0.3^\circ$ . The results show that gyro integration improves the quality of the filter attitude solution for two filters with an equivalent design bandwidth even with good GPS visibility.

### 6.5.2 High Altitude Test Case

The high altitude test case is a demonstration of the effects of high orbit altitude on the filter design and GPS interferometry in general. Reduced GPS availability also highlights the benefit of gyro augmentation at high orbit altitude.

A number of possible altitudes were examined and one example is chosen which illustrates the key effects of a high altitude application. Altitude for this test is 10,000 km, with an orbit period of 5.6 hours. Incidentally, this is slightly less than one half the GPS orbit altitude. Initial conditions and error trajectories are taken from trial 02S, because the initial position results in a particularly poor initial viewing geometry. Only three satellites are visible, and the integer solution cannot initialize the filter until about one minute into the test, when two more satellites come into view.

Attitude solution, gyro bias and *ADOP* outputs are shown in figure 6.20. Notice that the attitude covariance bound is significantly larger than for the nominal case. Also, the ADOP is consistently 50 to 100% larger than the low orbit configuration.

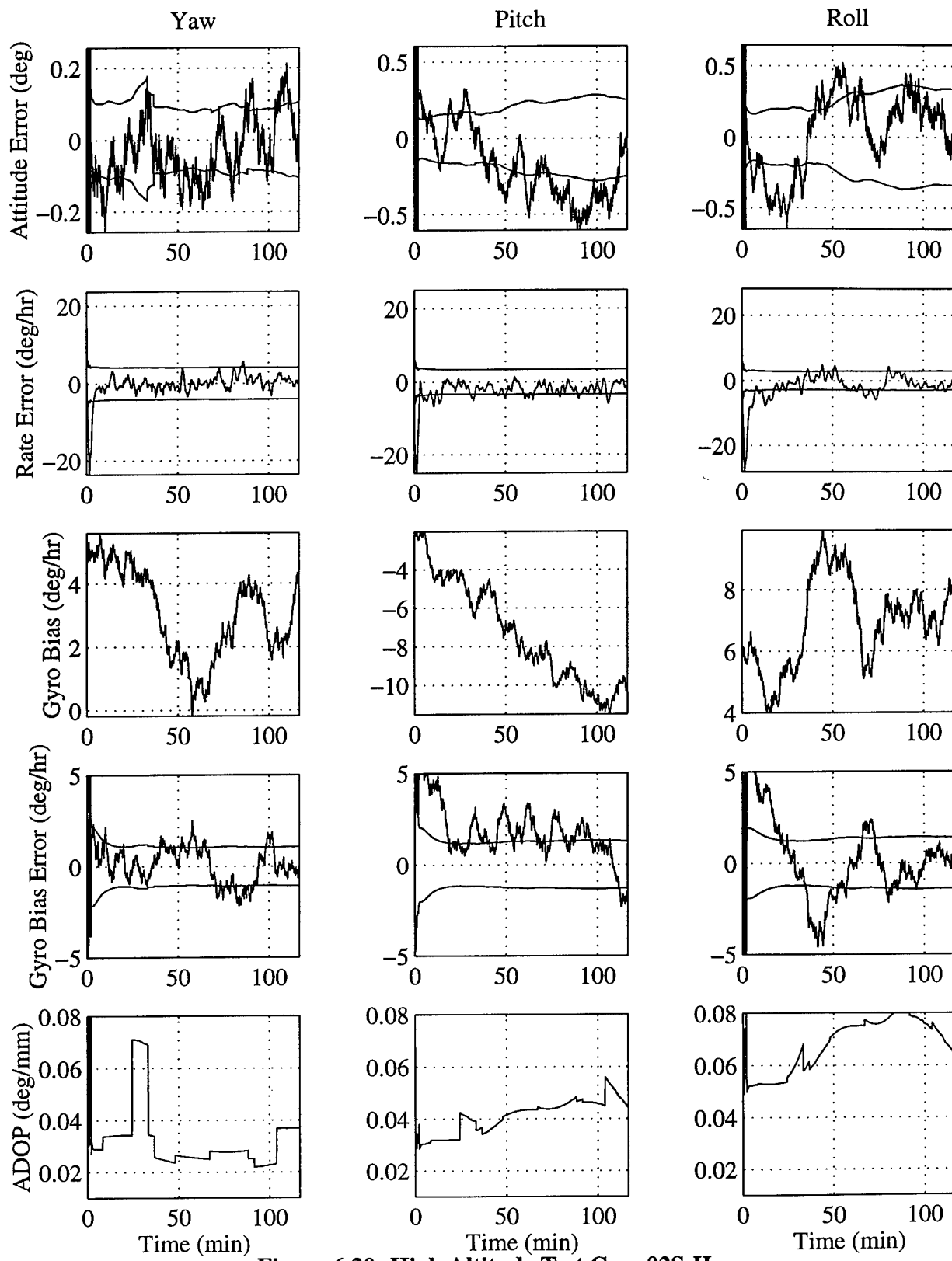
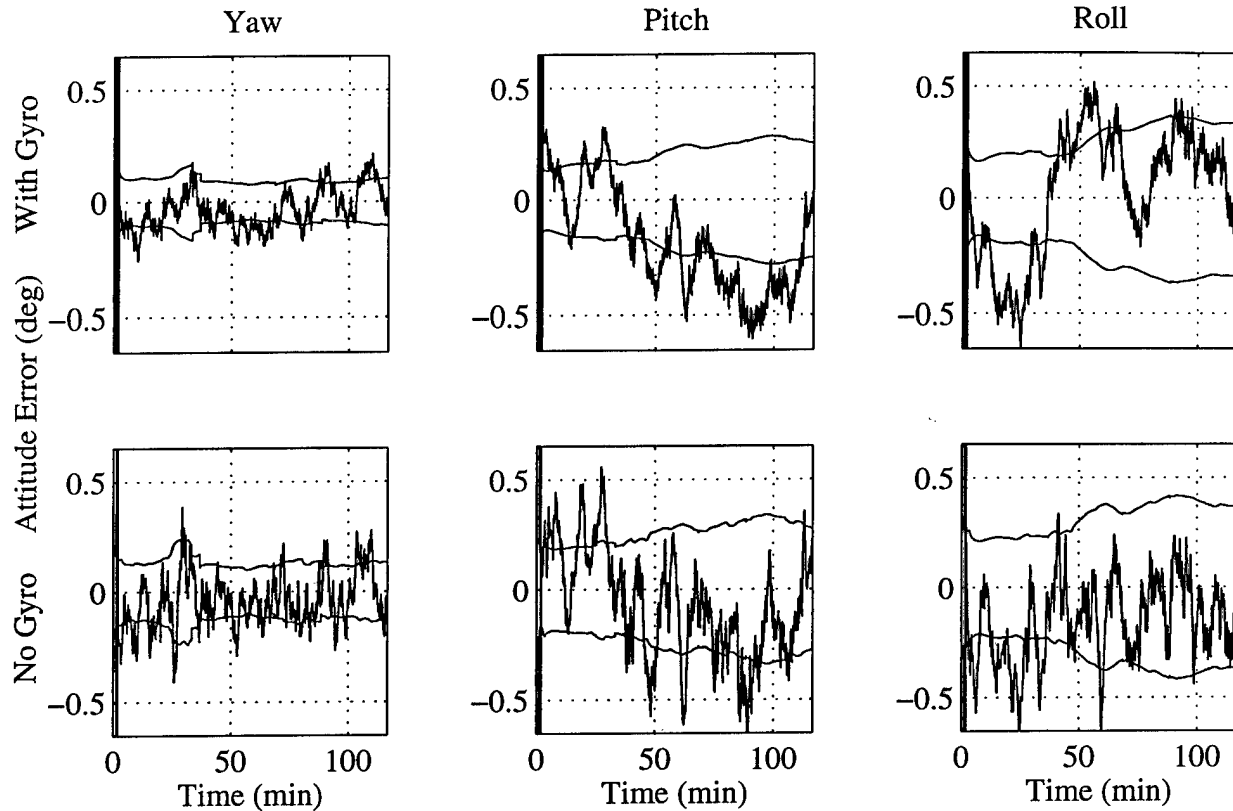


Figure 6.20: High Altitude Test Case 02S-H

Despite the high altitude and very large values of *ADOP*, especially in roll, the solution remains stable, and growth of the covariance bounds is relatively slow. A second test run, 02S-HG, tests performance of the filter without gyro measurements at this high altitude. Figure 6.21 compares the attitude solution for the two cases.



**Figure 6.21: High Altitude Performance With and Without Gyros**

The covariance bounds for test 02S-HG are larger than the bounds for 02S-H. The difference can be attributed to angular rate knowledge provided by the gyros. In addition, high frequency noise in the GPS-only solution is even more pronounced now due to degradation of the GPS viewing geometry. The result is a penalty on the GPS-only 3- $\sigma$  and maximum RSS attitude error statistics.

However, mean RSS error is actually larger with gyros:

Case	RSS Attitude Error (deg)		
	Mean	3- $\sigma$	Max
02S	0.2021	0.5091	0.5285
02S-H	0.4141	0.6940	0.7173
02S-HG	0.3805	0.7462	0.7889

**Table 6.7: High Altitude RSS Attitude Error with and without Gyros**

The large mean RSS error for the gyro aided design is caused primarily by a significant roll bias through most of the test. The gyro only measures relative position, not absolute position, so if GPS errors cause an attitude bias, the gyro will sometimes “sustain” the bias by keeping the angular velocity estimate steady. Still, peak to peak error is much larger without the gyros. This is highlighted at  $t = 60$  min, when both the pitch and roll attitude errors are large and negative for the no gyro case. The gyro is able to counteract this change in the attitude estimate, and very little effect is observed in performance of the nominal design.

### 6.5.3 Multipath Test Cases

The greatest challenge to attitude determination in an environment with reflecting surfaces is multipath. These test cases examine the effect of environmental multipath on filter performance. A sinusoidal model of environmental multipath was presented in equation 3.9:

$$\Delta m_{i,j}(t) = 10 \cdot \sin\left(\frac{2\pi t}{120} + \theta_{0_1}\right) \sin\left(\frac{2\pi t}{1200} + \theta_{0_2}\right) \quad 3.9$$

This sinusoidal model is used to corrupt differential phase measurements for the multipath test cases. The test cases are executed at high orbit altitude in order to magnify the effects of multipath. Multipath is most damaging when the number of available measurements is limited; a high orbit altitude furnishes the desired deterioration of GPS visibility. Results from the multipath test are compared to the nominal high altitude test case.

Before conducting the time domain simulation, a linearized analysis is used to examine the potential benefits of multipath estimation. Recall from section 3.2 that environmental multipath is difficult to model. The sources of environmental multipath are not fixed in the body frame, so the

frequency and amplitude of the resulting differential phase errors are time varying. Modeling multipath in a Kalman filter would require knowledge of this frequency and amplitude and the addition of two filter states for each multipath corrupted measurement. Two states are required because of the oscillatory nature of multipath. An example of a stochastic model for multipath is shown in equation 6.3:

$$\begin{bmatrix} \dot{\Delta m}_{i,j} \\ \ddot{\Delta m}_{i,j} \end{bmatrix} = \begin{bmatrix} 0 & 1 \\ -\omega_n^2 & -2\zeta\omega_n \end{bmatrix} \begin{bmatrix} \Delta m_{i,j} \\ \dot{\Delta m}_{i,j} \end{bmatrix} + \begin{bmatrix} 0 \\ 1 \end{bmatrix} w_m \quad 6.3$$

$\omega_n$  is the modeled natural frequency and  $\zeta$  is the damping ratio.  $w_m$  is white noise with an intensity  $\sigma_{w_m}$  chosen as a function of the expected multipath amplitude.

Performance of an augmented filter which includes this multipath model is evaluated by solving for steady state attitude covariance at a linearized point. The environment for the analysis includes the usual GPS error models and the multipath model of equation 6.3. Results are shown in figure 6.22. For the nominal ADS design, multipath performance does not improve dramatically when multipath estimation is added to the filter. However, in the absence of gyro measurements, attitude error increases dramatically without multipath estimation:

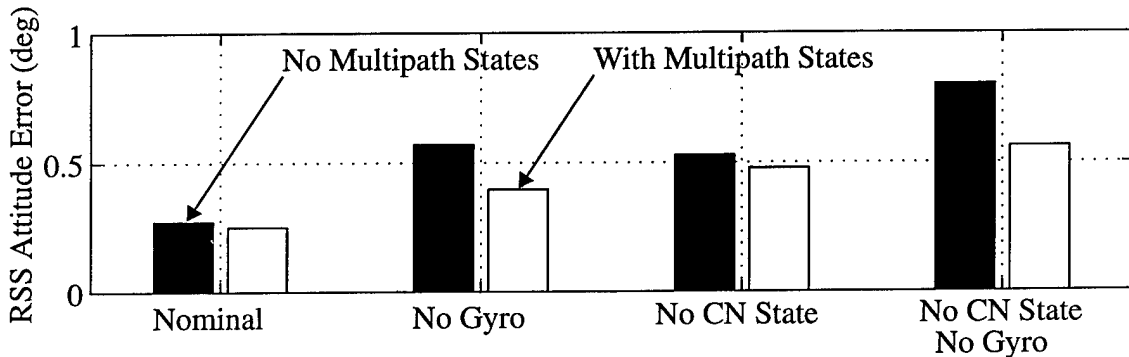


**Figure 6.22: Sensitivity to Multipath Error**

“No CN State” indicates a design with no correlated noise estimation. Notice that performance of the fourth design deteriorates by about  $0.3^\circ$  RMS without a multipath model. This design does not incorporate correlated noise estimation or gyro aiding.

The contrasts shown in figure 6.22 highlight the ability of the gyro and GPS error states to absorb multipath errors. A time domain simulation using initial condition 02S is conducted for gyro aug-

mented and GPS-only test cases.

Figure 6.23 compares results for the two tests over a period of 15 minutes. The first row shows attitude errors for the augmented system, while the second row is the GPS-only filter. The third row shows the actual multipath error history used to corrupt the differential phase measurements.

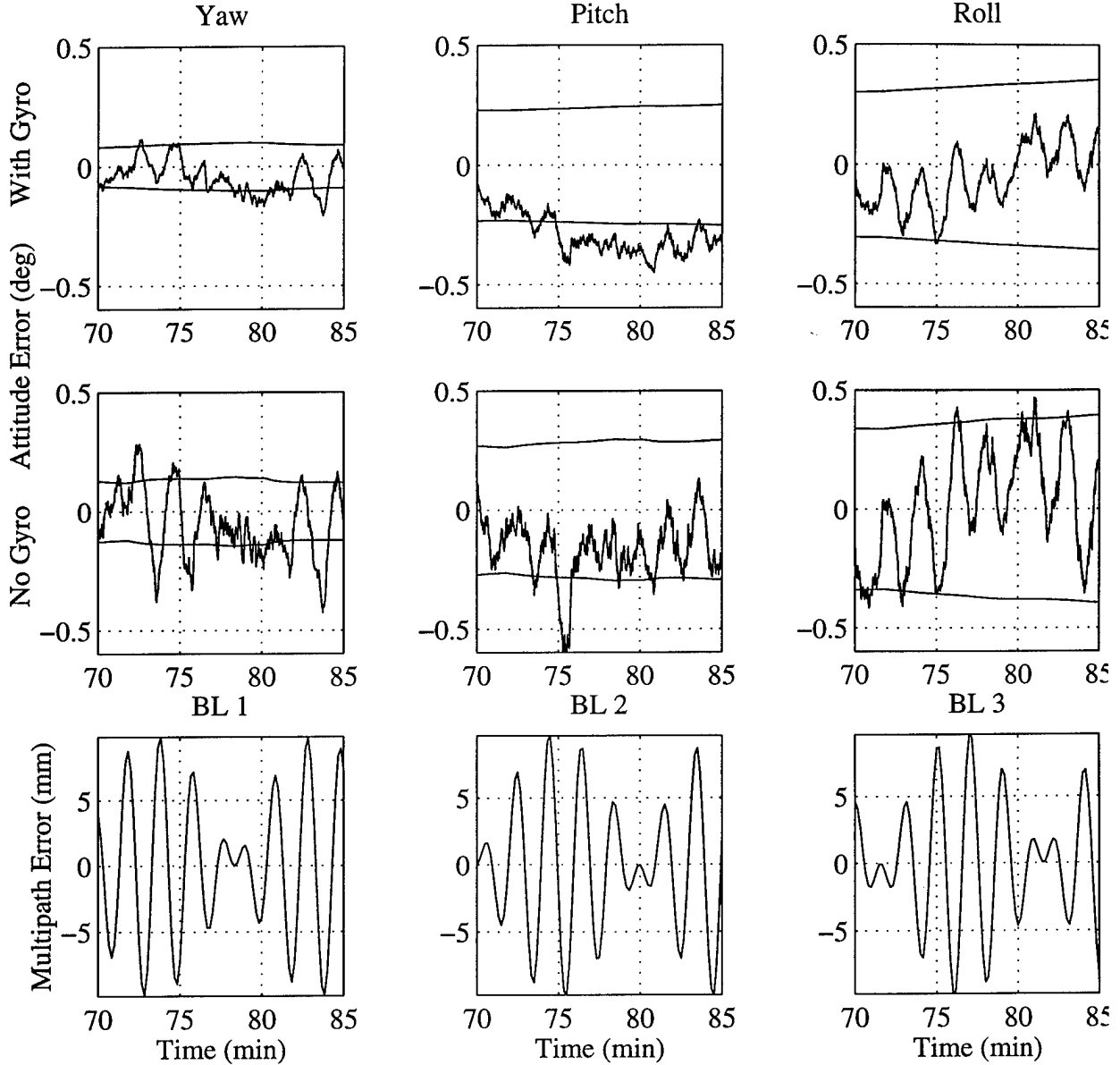


**Figure 6.23: Effect of Multipath on Attitude Solution**

There is a clear correlation between the multipath errors and the attitude errors on all three axes. Notice that the solution with gyro measurements has a smaller oscillation magnitude, but at least one axis, pitch, exhibits a larger bias than the GPS-only solution. The bias is triggered by the

large magnitude of multipath errors on baseline 2 around  $t = 75$  min. The errors cause large negative pitch corrections for both configurations at  $t = 75$  min. The gyro assembly recognizes that no motion is taking place and limits the error magnitude. However, the same stabilizing effect preserves the pitch bias even after the error for the GPS-only design dissipates.

The time period of  $t = 70$  min to  $t = 85$  min is chosen to highlight the contribution of the correlated noise states in mitigating multipath. Although the states are designed to combat low frequency bias mismodeling, they absorb some of the energy of the multipath signal. Figure 6.24 demonstrates this using test case 02S-HM. At  $t = 76$  min, the SV channel which is corrupted by multipath changes. The switch of multipath from one SV to another is an artificial phenomenon inserted into the simulation, but it illustrates a key point. In the first five minutes, while channel 2 is corrupted by multipath, the correlated noise states on channel 2 clearly absorb some of the multipath energy. After the multipath switches to channel 1, the channel 2 noise state returns to more

typical dynamics, while the noise states for channel 1 pick up tracking of the multipath error.

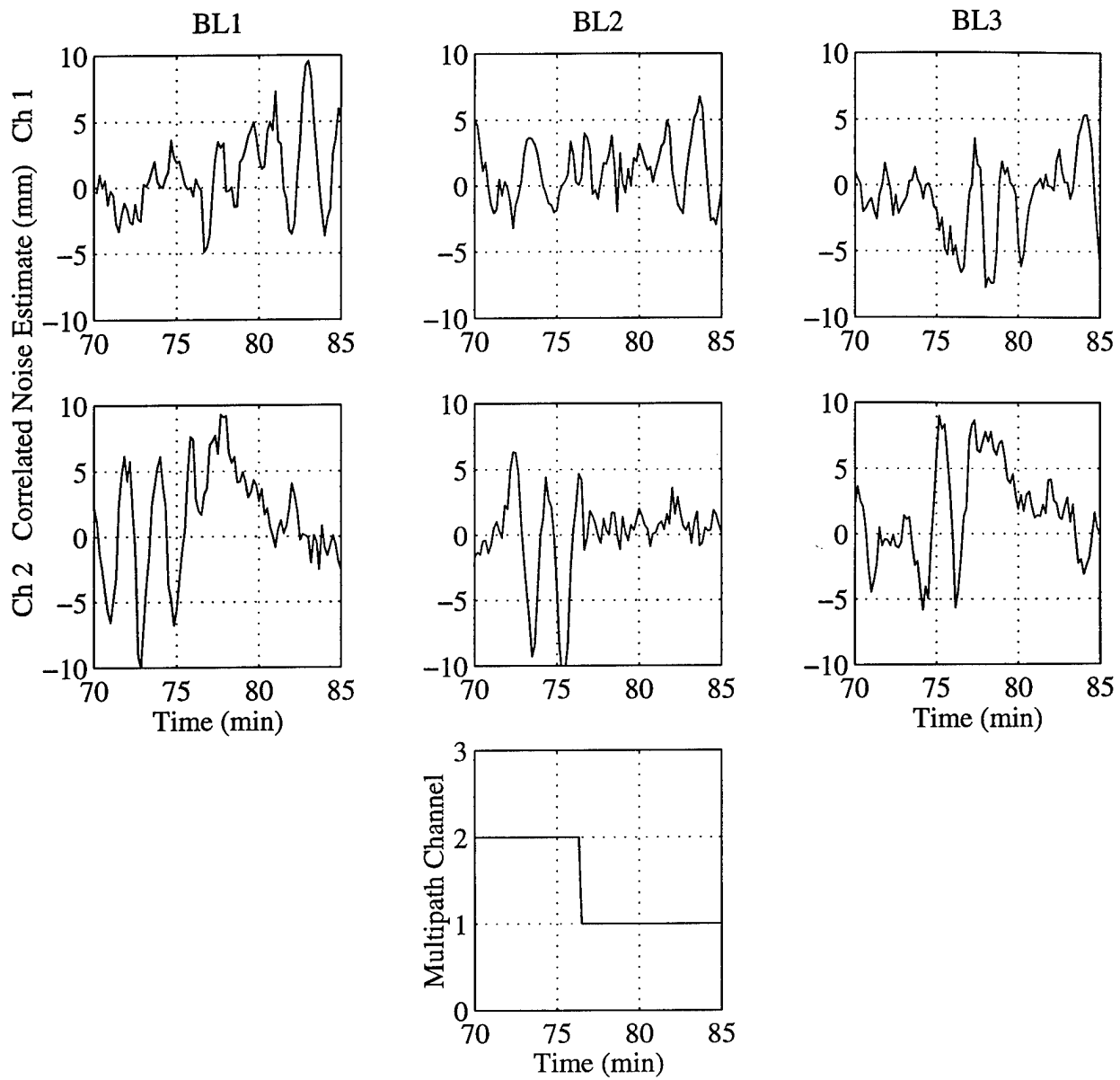


**Figure 6.24: Interaction of Multipath and Correlated Noise**

Table 6.8 shows the attitude error statistics for these test cases.

Case	RSS Attitude Error (deg)		
	Mean	3- $\sigma$	Max
02S-H	0.4141	0.6940	0.7173
02-HM	0.4251	0.6820	0.7194
02-HMG	0.4145	0.9480	1.0326

**Table 6.8: Multipath Corrupted RSS Error with and without Gyros**

As expected, mean RSS error in the presence of multipath is greater than in the nominal high altitude test case, but the differences are quite small. In fact, performance of the nominal filter design across the two tests is virtually unchanged. The multipath corrupted measurements *do* have an impact on the no gyro filter design, producing a maximum RSS attitude error  $0.3^\circ$  larger than the nominal design. Notice that mean RSS error for test case 02S-HM is actually larger than the mean for 02S-HMG. This is due to the pitch bias discussed earlier.

#### 6.5.4 Initial Tumble Test Cases

All of the nominal runs were conducted with  $5^\circ$  initial yaw, pitch and roll offsets from the LVLH frame and rates of  $0.01^\circ/\text{s}$  on each axis. The purpose of the initial tumble tests is to demonstrate capability of the flight software to initialize in an unknown attitude at an arbitrary angular rate. This scenario is designed to simulate satellite motion after orbit insertion or following a loss of attitude control. As a coincidental benefit, these tests validate the design of the quaternion feedback control law. Large initial attitude offsets result in sustained slew commands from the controller.

Ten test cases were executed. In each case, the initial condition attitude is a combination of randomly chosen yaw, pitch and roll. The initial angular rates for all three of the axes are chosen from an uncorrelated normally distributed random variable with standard deviation of  $1^\circ/\text{s}$ . Table

6.9 shows the attitude initial conditions:

Case	Yaw (deg)	Pitch (deg)	Roll (deg)
01E-T	4.6472	14.2258	-53.8577
02E-T	9.2944	-28.4517	-107.7153
03E-T	13.9416	42.6775	-161.5729
04E-T	18.5889	-56.9034	144.5693
05E-T	23.2361	71.1292	90.7117
06E-T	27.8833	-85.3551	36.8540
07E-T	-147.4695	80.4191	162.9963
08E-T	-142.8223	-66.1932	109.1387
09E-T	-138.1750	51.9674	55.2810
10E-T	-133.5278	-37.7415	1.4233

**Table 6.9: Tumble Test Initial Conditions**

The integer ambiguity algorithm is automatically activated at every GPS measurement until a valid solution is found. The control system is only activated once this valid solution is reached.

A successful attitude recovery was accomplished in each case. In fact, 9 of the attitudes achieved

a solution within five seconds. Figure 6.25 shows the results for test case 05E-T as an example:

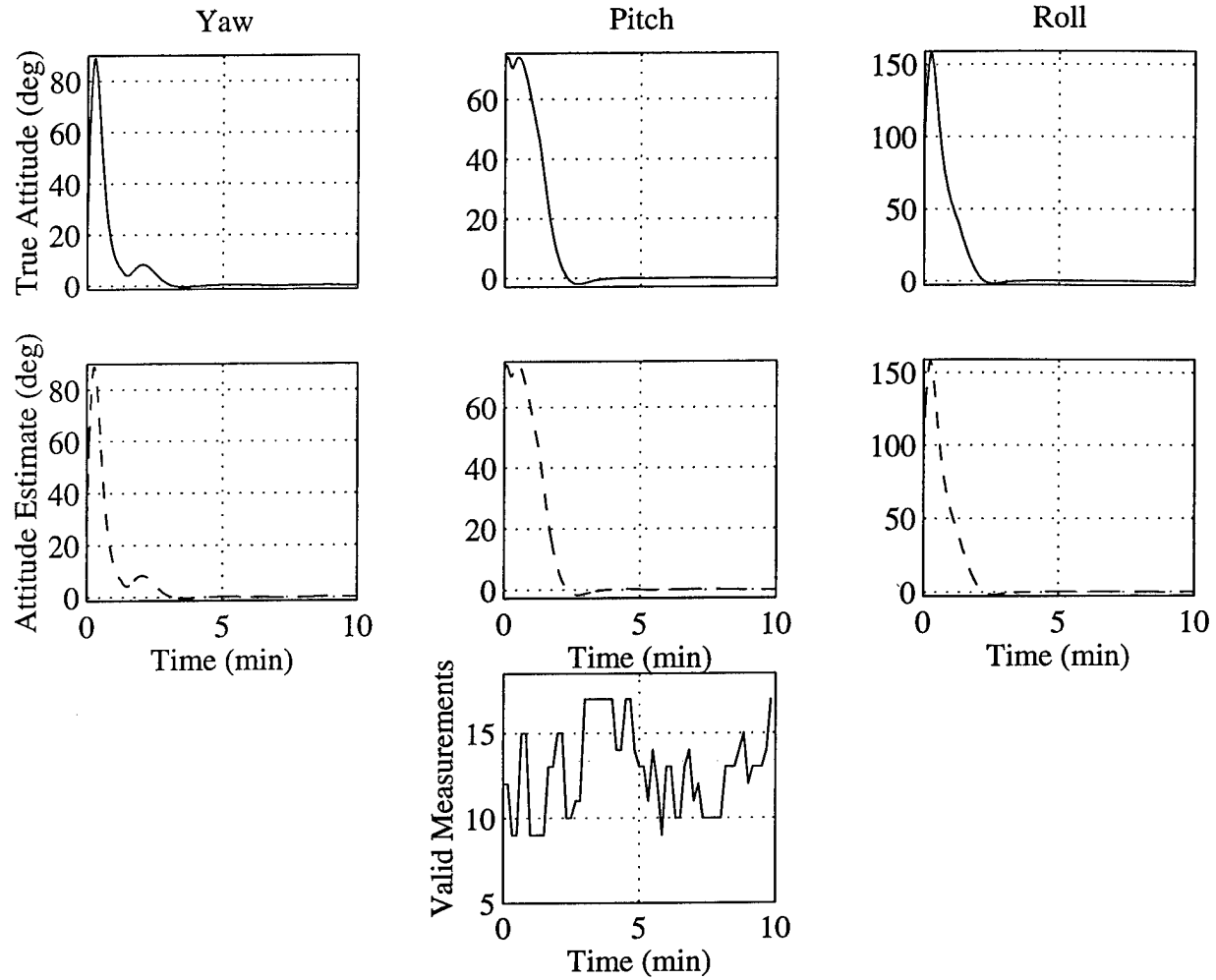


**Figure 6.25: Tumble Recovery Case 5**

Successful initialization occurred with the first measurement set, so the estimated trajectory looks identical to the truth. The trajectory dynamics are a function of the commanded correction from the control system.

Case 3 was the only test case which did not allow immediate ambiguity resolution. Figure 6.26 shows the attitude and attitude estimate for this case along with the number of good measure-

ments.

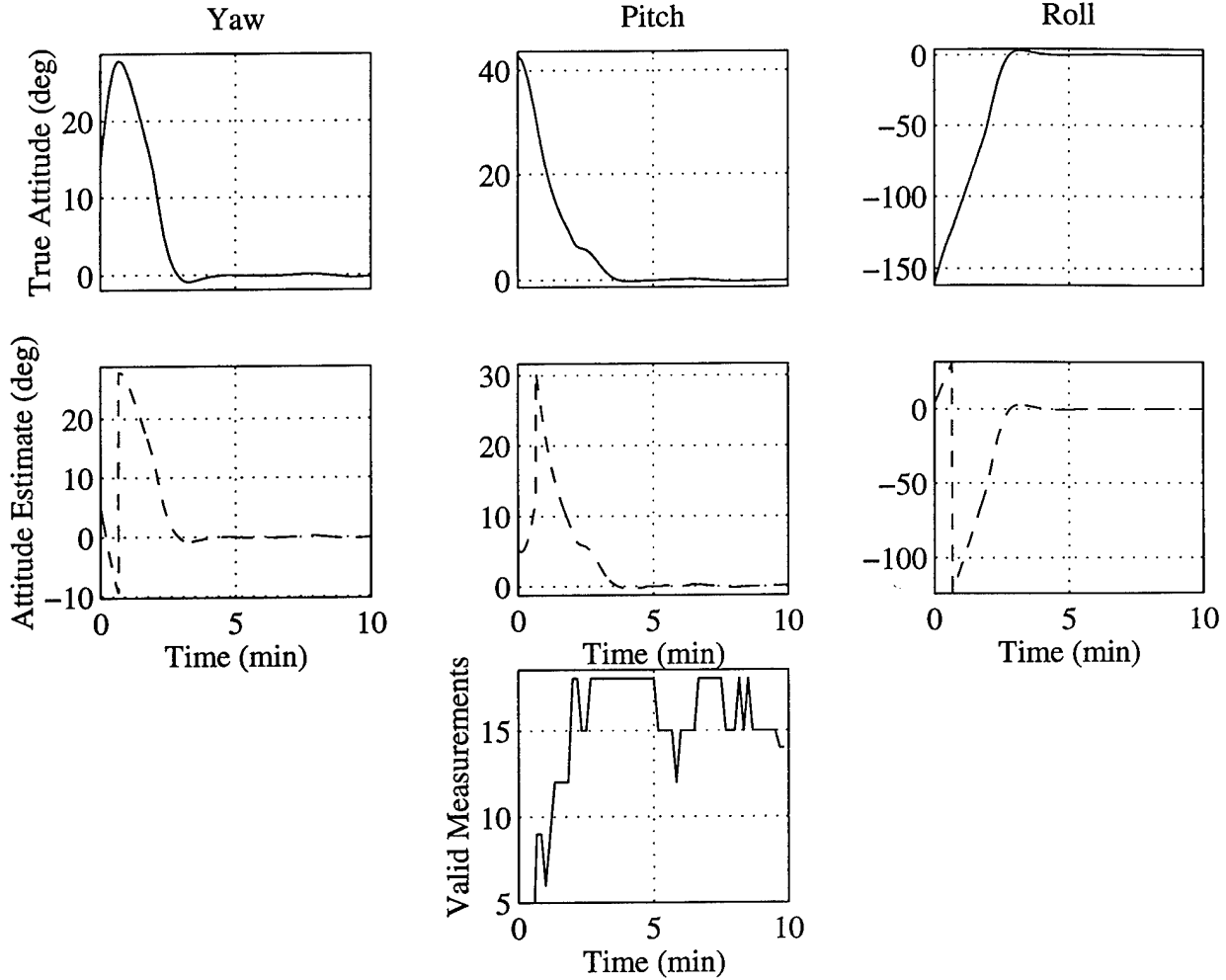


**Figure 6.26: Tumble Recovery Case 3**

Although the trial begins with no satellites visible, the angular drift brings additional satellites into view approximately one minute into the test. The filter initializes as soon as three satellites become visible, and the control system returns the vehicle to the nominal attitude. These results indicate that the filter should be able to initialize in low earth orbit even if the initial attitude is not close to the nominal. They also demonstrate operation of the filter integrity monitoring algorithm. When additional satellites become valid at  $t = 2$  min, the algorithm recognizes that the measurement residuals are excessive. A new integer solution is commanded and a filter reset occurs when a good solution is reported.

### 6.5.5 Free Drift Test Cases

The free drift test is more strenuous than the initial tumble test. In this scenario, no controls are

commanded. The attitude dynamics are generated solely by rigid body kinematics and external disturbance torques on the vehicle. Figure 6.27 shows true attitude Euler angles and body rates for test case 07E-FD, which is chosen as a good demonstration of filter behavior in free drift mode:

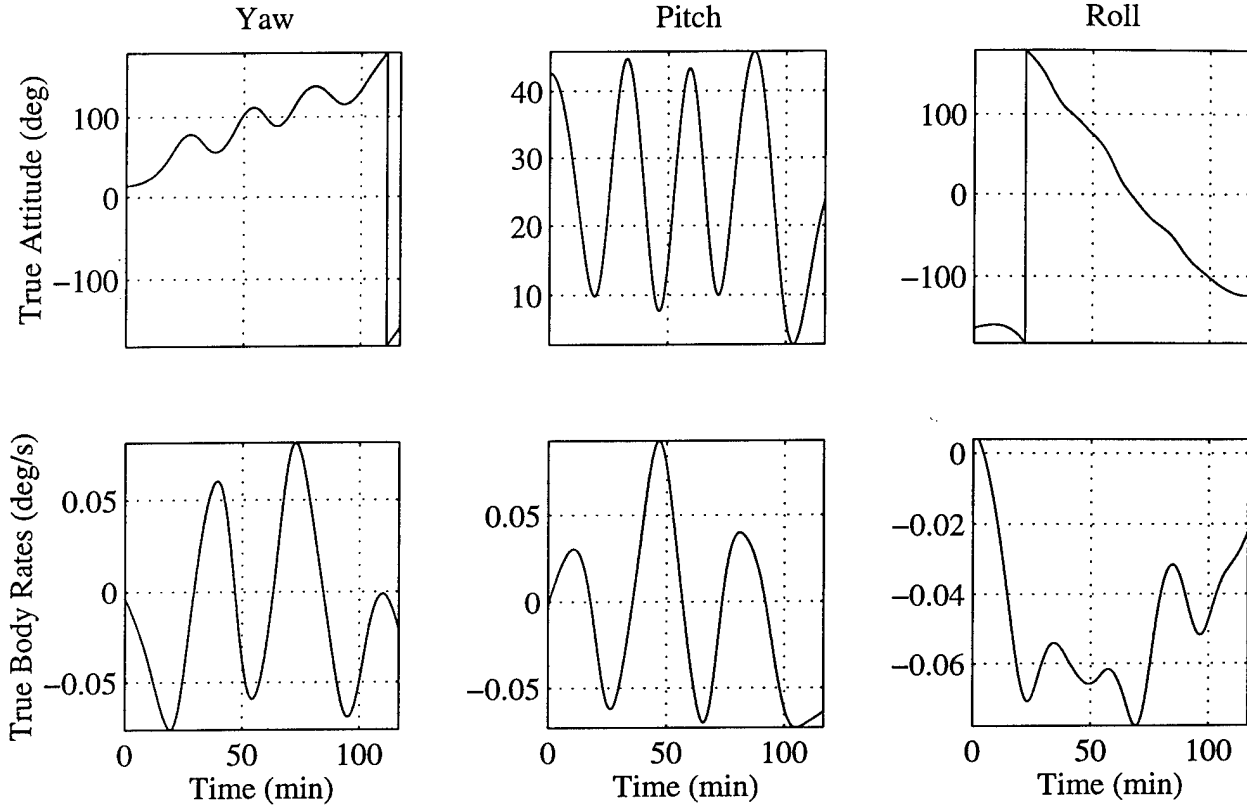


**Figure 6.27: True Attitude for Test 02E-FD**

In figure 6.28, filter performance is shown for the nominal free drift case, with all sensors operating. The key feature here is the loss of most of the satellites and increase in *ADOP* around  $t = 20$  min. The filter develops a large negative roll error during this period, but the error is quickly corrected when more satellites become available:

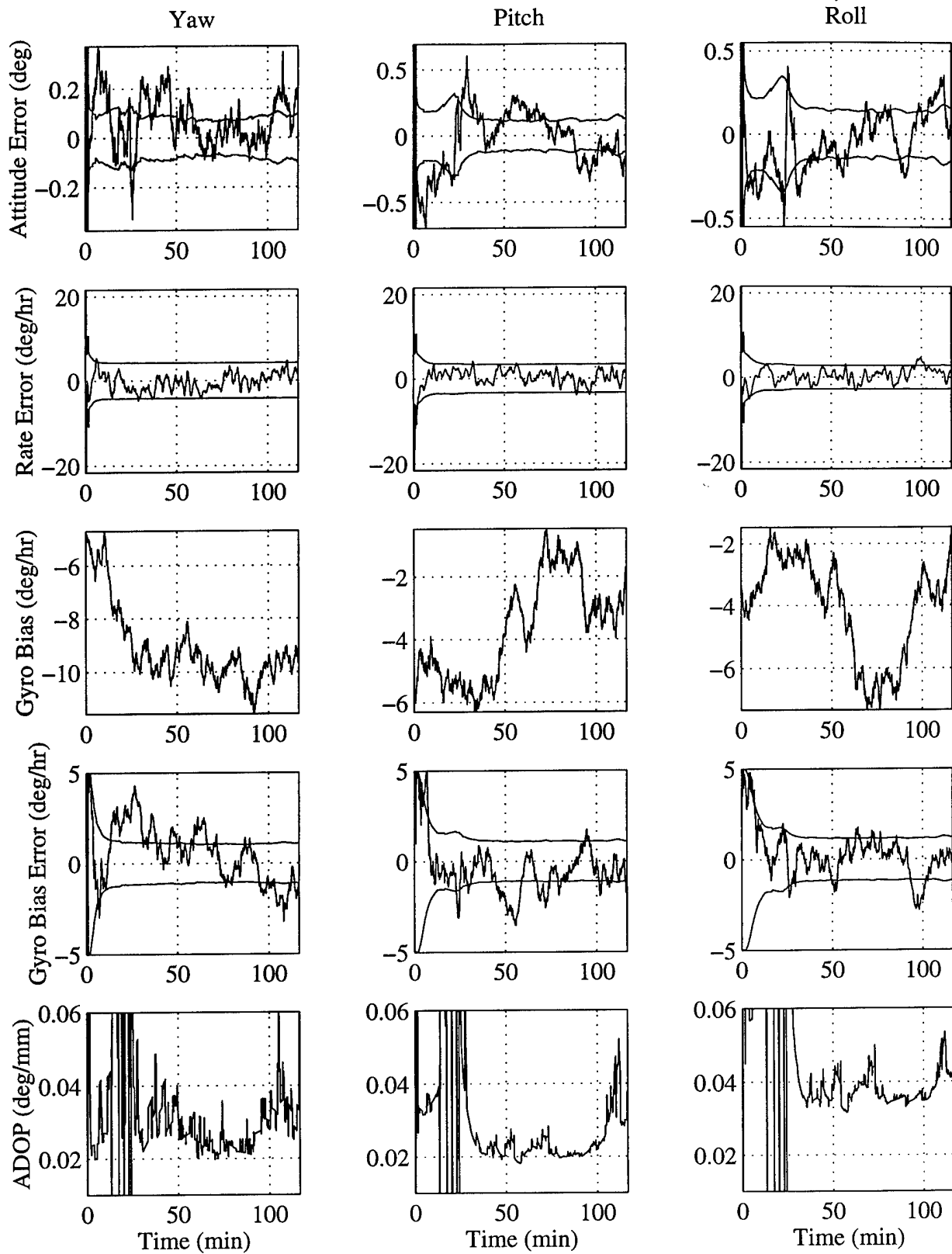


**Figure 6.28: Free Drift Test Case 02E-FD**

The chattering of  $ADOP$  from  $t = 10$  min to  $t = 20$  min is due to a lack of valid measurements. During most of this period, only one satellite is valid, providing three measurements to the filter. Attitude rotations about the LOS vector to the satellite are unobservable in the differential phase. The result is that the least squares small angle attitude error solution is ill-conditioned, and  $ADOP$  becomes very large or infinite. In the case of three measurements,  $ADOP$  cannot be calculated, and a value of  $ADOP = 0$  is stored in the simulation output.

Performance of the filter with and without gyros is compared in figure 6.29. The most significant characteristic of the no gyro attitude error is the spike in yaw, pitch and roll which occurs at  $t = 20$  min. These large errors result from the lack of angular velocity knowledge in the no gyro design. During periods of poor GPS visibility, angular rate knowledge is crucial to propagation of the attitude estimate. As shown in figure 6.29, errors in the angular velocity estimate can cause rapid

growth of the attitude estimate errors.

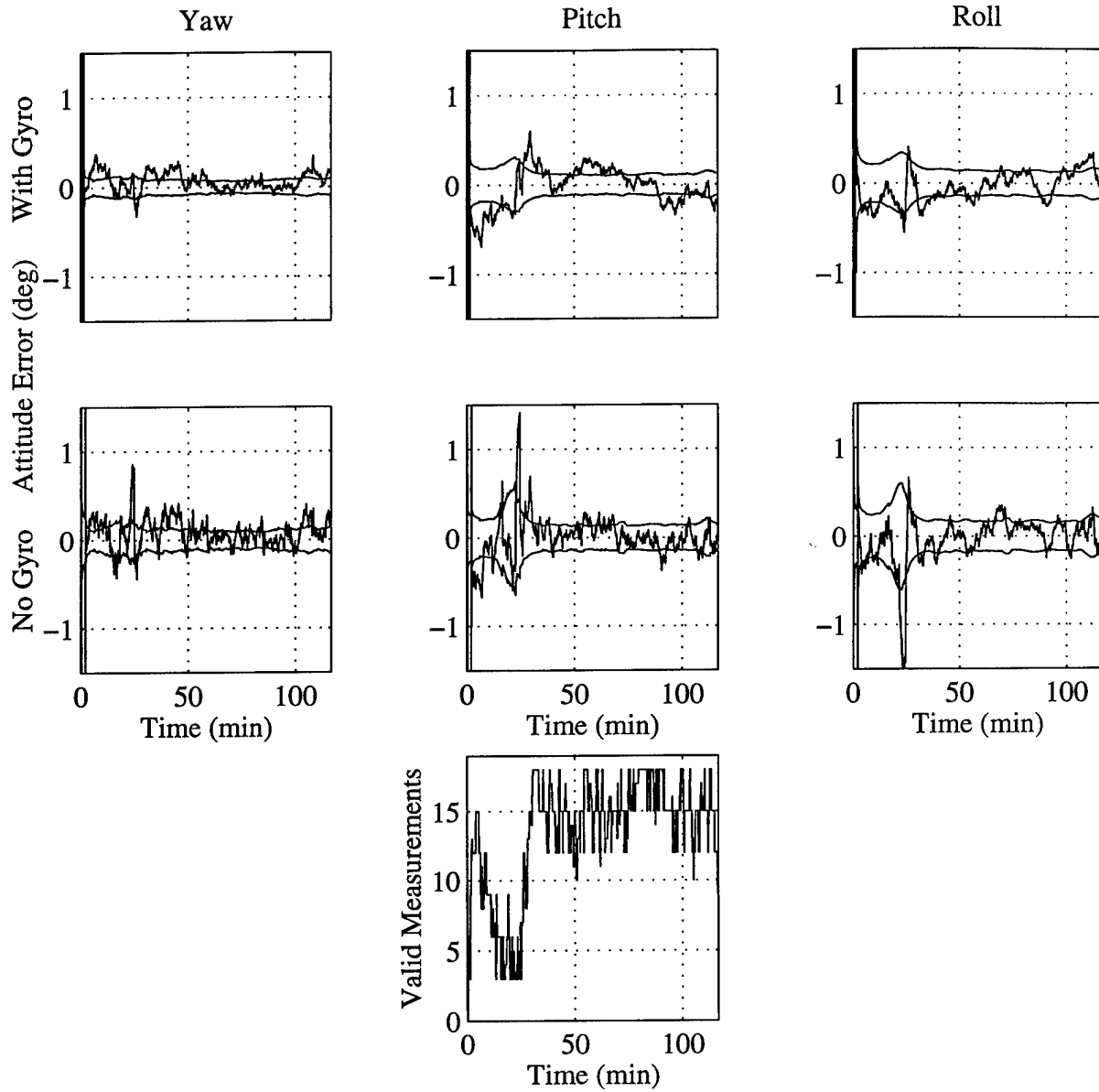


**Figure 6.29: Attitude Error for Tests 07E-FD and 07E-FDG**

The large error deviations for the no gyro case are evident in the attitude statistics, shown in table

6.10:

	RSS Attitude Error (deg)		
Case	Mean	3- $\sigma$	Max
02S	0.2021	0.5091	0.5285
02E-FD	0.3224	0.8021	0.8558
02E-FDG	0.4088	2.2524	2.4865

**Table 6.10: Free Drift RSS Attitude Error with and without Gyros**

Gyro augmentation provides a critical margin of safety in this free drift case. The results show that even a low cost TGA can improve performance of a GPS based attitude determination system. Any satellite platform which may operate in an uncontrolled mode should include inertial sensors in the attitude determination system design.

Both of these test cases demonstrate operation of the filter integrity monitoring system. At  $t = 20$  min, the attitude errors in each case become relatively large ( $>0.8^\circ$ ). Shortly thereafter, three new satellites become valid, as shown in figure 6.29. Large errors in the attitude estimate result in significant residuals when the new measurements are compared to the filter measurement prediction. The integrity monitoring algorithm recognizes this and calls the integer solution algorithm as a precaution in case the integers are in error. The ambiguity solution is good, and it agrees with the attitude estimate prior to the integrity check. As a result, all of the filter error estimates are preserved and only the attitude solution is re-initialized. The integrity monitoring algorithm quickly detects incorrect integers, but, as shown here, it also recognizes when a full filter reset is not needed.

### 6.5.6 Correlated Noise Test Cases

The correlated noise test cases presented here investigate two scenarios related to changes in the correlated noise environment. The bulk of the correlated noise energy in the nominal error model comes from mismodeling of the phase center error and body-fixed multipath states. A better bias calibration model or less body-fixed errors might reduce the magnitude of correlated noise errors. The first test case, 02S-NE, examines how filter performance changes in the nominal environment if the assumption of white GPS noise is made in the filter design (i.e. no correlated noise estima-

tion). The second test, 02S-NC considers an environment in which no correlated noise is present. That is, body fixed biases are modeled perfectly or are not present to begin with. Performance of the nominal filter in this situation is compared to that of an optimal filter designed for this environment.

### No Correlated Noise Estimation

If a white noise model is assumed for the measurement errors, 18 states can be removed from the filter. However, the filter can no longer track slowly varying biases caused by phase center variation and multipath errors, so the attitude error increases, as shown in figure 6.30:

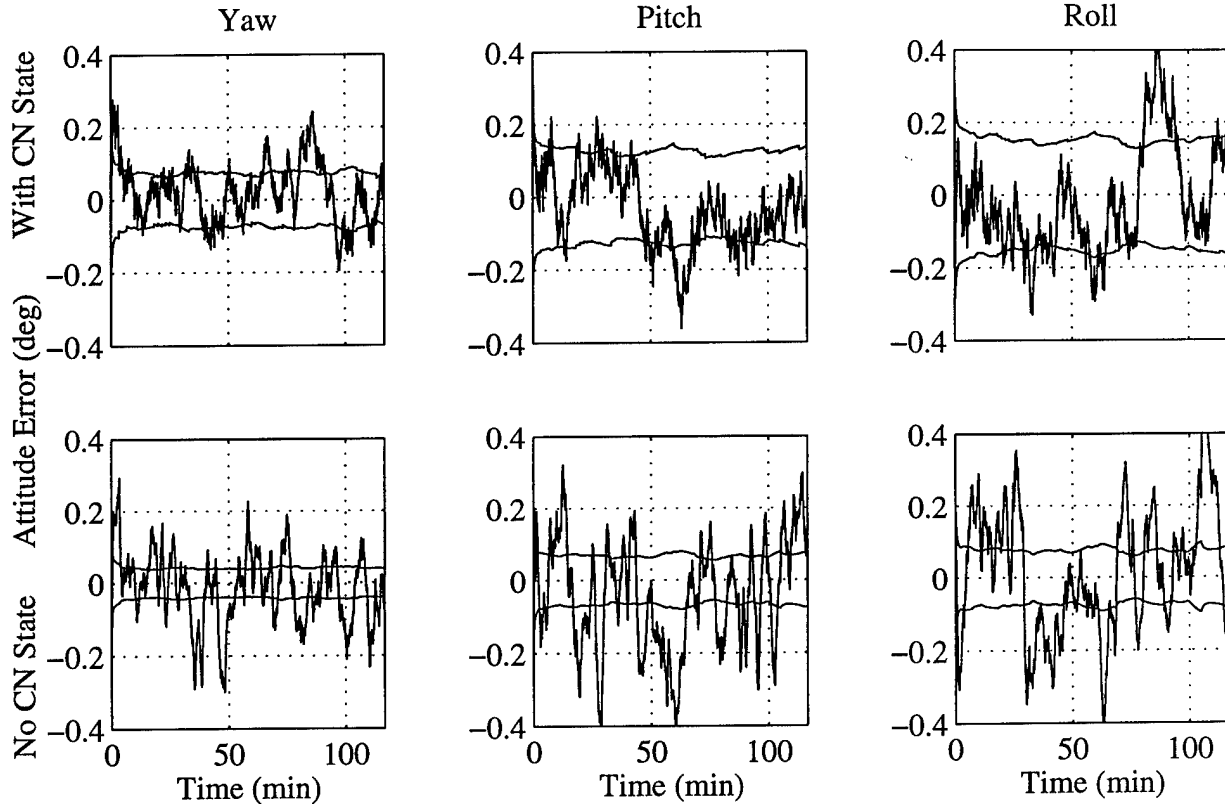


**Figure 6.30: Attitude Error with and without Correlated Noise Estimation**

Rather than simply eliminating the correlated error states, the white noise intensity estimate is increased by a factor of three in test case 02S-NE in an attempt to compensate for the absence of

the correlated error states. However, the effect on the attitude estimate is dramatic:

Case	RSS Attitude Error (deg)		
	Mean	3- $\sigma$	Max
02S	0.1997	0.4834	0.5123
02S-NE	0.2588	0.6457	0.6645

**Table 6.11: RSS Attitude Error with and without Correlated Noise Estimation**

Two important characteristics of the attitude solution for 02S-NE must be noted. Obviously, errors for the filter without correlated noise estimation are larger than for the nominal design. This was also shown through the linear covariance analysis of section 5. 2. Possibly more important is the drastic mismatch between the filter attitude error covariance estimate and the true error covariance for the white noise design. The filter estimate of RMS attitude error for test case 02S-NE is about  $0.1^\circ$  on each axis. This is denoted by the bounds in figure 6.30. True errors are closer to  $0.2^\circ$  RMS. The optimistic covariance estimate can lead to sluggish filter performance or even instability.

### No Correlated Noise

This test case examines theoretical filter performance in the absence of correlated noise both with and without correlated noise estimation states. Figure 6.31 shows the attitude error for the two cases. Performance of the optimal (no correlated noise states) design is shown on the second row.

Notice that much tighter covariance bounds are achievable if correlated noise is not present:

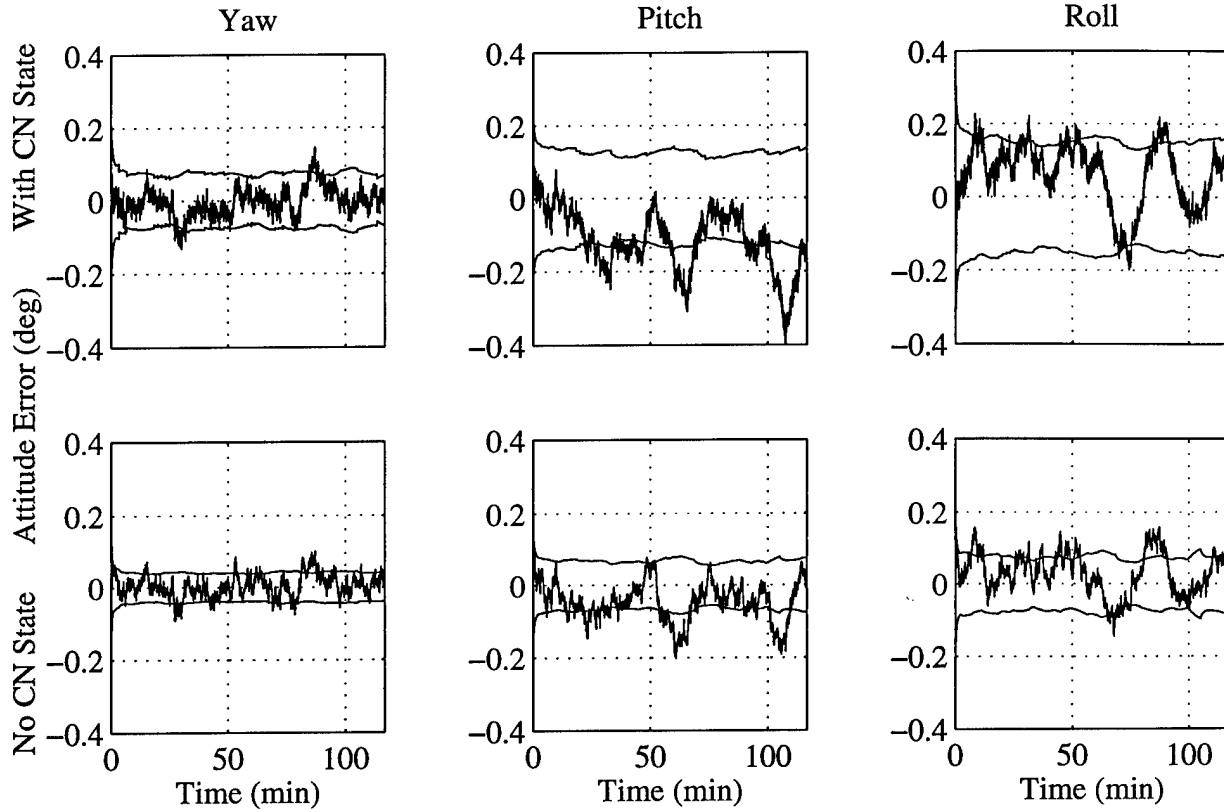


**Figure 6.31: Attitude Error With No Correlated Noise with and without Correlated Noise Estimation**

As table 6.12 shows, the optimal design reduces attitude error by almost one half. The challenge is really to eliminate correlated noise in the environment, because that is the only way to achieve this kind of performance.

Case	RSS Attitude Error (deg)		
	Mean	3- $\sigma$	Max
02S-NCNE	0.1826	0.3713	0.4033
02S-NC	0.1016	0.1916	0.2041

**Table 6.12: RSS Attitude Error with No Correlated Noise**

The correlated noise test cases have shown that elimination of correlated noise effects is the primary obstacle to improving filter performance. If the correlated noise environment is *uncertain*, meaning that the intensity of correlated noise is not known, incorporation of correlated noise estimation in the filter may cause sub-optimal performance. However, this is better than the alternative of designing for white noise and underestimating the attitude error covariance.



# Chapter 7

## Conclusion

The goal of this thesis has been to design an autonomous GPS based attitude determination system for spacecraft attitude determination. The attitude determination system includes an integer ambiguity solution algorithm and a Kalman filter incorporating measurements from multiple GPS antennas and a three-axis gyro assembly. An efficient ambiguity solution method was presented which integrates geometric integer constraints and decoupling of the three-axis attitude problem in order to reduce the number of required computations from order  $(2N)^6$  to order  $N^3$ . A model was developed for total GPS differential phase error using experimental GPS measurement data. The model was used to design an Extended Kalman Filter which incorporates tightly coupled GPS and gyro measurements. Performance of the complete system was tested using a non-linear orbital simulation, with nominal simulation parameters based on the Iridium GPCS constellation.

### 7. 1 Summary of Results

The key obstacle to the design of an autonomous GPS based attitude determination system is development of a fast and reliable system of initialization. The integer ambiguity solution presented here achieved an on-orbit first attempt success rate of 87.4% during tests with experimental measurement data, and solution success increased to 99.74% after 13 attempts. The ambiguity solution also proved successful at initializing the attitude solution with the spacecraft in a random tumble, which is an important practical consideration for satellite deployment. This level of speed and reliability should prove sufficient for most satellite applications.

Orbit simulations were conducted using experimental GPS measurements as well as measurements generated with the stochastic GPS error model. Comparison of the results indicates that the stochastic model accurately represents the nature of differential phase error. The largest uncertainty in the model involves phase center variation and multipath errors. Calibration of these errors eliminates a small percentage of the error energy, but the remainder must be modeled as a

first order correlated noise process. Although correlated noise estimation suppresses the effects of the mismodeling, they still make large contribution to the total attitude estimation error. Attitude errors are also very sensitive to line bias error and the size of the antenna array, while they show less sensitivity to baseline length variations and the performance level of the TGA.

Nominal performance in the computer simulation showed that a  $3\sigma$  total attitude estimation uncertainty of  $0.5^\circ$  can be achieved using a four antenna, 1-m square antenna array. The hardware configuration for the nominal tests used a zenith pointing GPS antenna array and a TGA composed of low cost MM gyros. ADS performance remained excellent up to an orbit altitude of about 10,000 km, where GPS visibility began to degrade. At these high altitudes, gyro measurements became increasingly important. However, the integrated design exhibited occasional attitude error biases which were not present in the GPS-only design. Another scenario in which gyro augmentation was critical was the free drift test. With the control system shut off and the space-craft in a free tumble, gyro measurements helped propagate the attitude solution through outages in the GPS signal.

The filter showed good suppression of multipath errors when a 20 mm peak-to-peak sinusoidal model for multipath was used to corrupt three GPS measurements. Gyro aiding and correlated noise estimation both limited the damage induced by this multipath model to less than  $0.1^\circ$  RMS.

The ADS requires a minimum of three GPS antennas and three low quality gyros. Given the rapid growth of commercial GPS technology and recent development of low cost gyro systems, this design could become a cheap, simple alternative to traditional methods of attitude determination.

## 7.2 Suggestions for Future Work

The most problematic errors in GPS differential phase are phase center variation and multipath. Further research into modeling of these errors could yield significant improvements to the performance of the EKF. Two possible approaches are better calibration of errors using experimental data and development of adaptive filter dynamics to achieve real time mitigation of multipath.

The calibration model used in this thesis was a least squares fit. A larger experimental measurement data base and use of a spherical harmonic error model would attenuate some of the unmodeled errors encountered with this design. Even the best calibration model cannot defeat environmental multipath. This requires adaptive filtering. An adaptive filtering technique involves real time identification of multipath corrupted signals and on line frequency and amplitude estimation. Advances in signal processing and computational speed are needed to make this kind of real time mitigation possible.

Another area which merits further study is the role of gyros in an integrated attitude determination system. The integrated design occasionally develops an attitude error bias, as displayed in the high altitude and multipath off-nominal test cases. Further research into the cause and possible remedies for this behavior are needed. Another topic for future research is incorporation of spacecraft dynamics in the EKF. In this research, the filter used spacecraft dynamics to propagate the attitude, and gyro outputs were treated as angular rate measurements. In contrast, a model-replacement approach uses gyro output to replace the angular rate estimate during propagation. A performance comparison of the two designs would provide insight into the benefits and costs of including a spacecraft dynamic model in the filter.

This thesis only investigated a small number of orbit scenarios for the ADS. System performance should be investigated for a wide range of missions, particularly highly elliptic orbits. Stand alone GPS attitude determination is not reliable for high apogee orbits due to degraded GPS visibility at altitudes approaching that of the GPS constellation. Gyro measurements may allow preservation of the attitude estimate through the high altitude portion of flight, with GPS measurements providing recalibration of the gyro biases and other error states at and around perigee.



## References

- [1] Anon, "GPS Interface Control Document," ICD-GPS-200, IRN-200B-RR-OOJ, Rev. B-PR, U. S. Air Force, Jul. 1992.
- [2] Axelrad, P., "GPS-Based Attitude Determination and an Overview of GPS Research at CCAR," University of Colorado at Boulder, Mar. 28, 1996.
- [3] Axelrad, P., C. Comp and P. MacDoran, "Use of Signal-to-Noise Ratio for Multipath Error Correction in GPS Differential Phase Measurements," *Proceedings of ION*, Vol. 1, 1994, pp. 655-666.
- [4] Buchler, R. J., C. A. Lee, and A. J. Brockstein, "Design and Test of a Synergistic Interferometric GPS-INS," *Proceedings of Position, Location and Navigation Symposium - PLANS '96*, Apr. 1996, pp. 612-619.
- [5] Caceres, M. A., "Satcoms Growth On Upswing," *Aviation Week and Space Technology*, Jan. 13, 1997, pp. 117-120.
- [6] Chesley, B. and P. Axelrad, "Integrated GPS Attitude Determination System for JAWSAT", *Proceedings of ION GPS*, Vol. 2, 1994, pp. 1251-1261.
- [7] Cohen, C. E., *Attitude Determination Using GPS*, Ph. D. Dissertations, Department of Aeronautics and Astronautics, Stanford University, Dec. 1992.
- [8] Cohen, C. E., and B. W. Parkinson, "Integer Ambiguity Resolution of the GPS Carrier for Spacecraft Attitude Determination," *Advances in the Astronautical Sciences*, Vol. 78, 1992, pp. 254.
- [9] Cohen, C.E. and B. Parkinson, "Mitigating Multipath Error in GPS Based Attitude Determination," *Advances in the Astronautical Sciences*, Vol. 74, 1991, pp. 53-68.
- [10] Erickson, C., "An Analysis of Ambiguity Resolution Techniques for Rapid Static GPS Surveys Using Single Frequency Data," *Proceedings of ION-GPS 92*, 1992, pp. 453-362.
- [11] Fujikawa, S. J. and D. F. Zimbelman, "Spacecraft Attitude Determination by Kalman Filtering of Global Positioning System Signals," *Journal of Guidance, Control and Dynamics*, Vol. 18, No. 6, Nov.-Dec. 1997, pp. 1365-1371.
- [12] Garrison, T., M. Ince, J. Pizzicaroli, and P. Swan, "IRIDIUM® Constellation Dynamics The Systems Engineering Trades," *46th International Astronautical Congress*, Oct. 1995.
- [13] Godart, D. F. and J. Peghaire, "The GLC8 - A Miniature Low Cost Ring Laser

Gyroscope," *Symposium Gyro Technology 1990, Proceedings*, 1990, pp. 12.0-12.12.

[14] Hardwick, C. D., and J. Liu, "Characterization of Phase and Multipath Errors for an Aircraft GPS Antenna," *Journal of the Institute of Navigation*, Vol. 48, No. 1, 1996, pp. 41-54.

[15] Howell, G. and W. Tang, "Tightly Coupled Attitude Determination Using GPS Carrier Phase Observable", *Proceedings of ION*, Sept. 12, 1995. p. 1759-1766.

[16] IRIDIUM® Web Page, <http://www.iridium.com>.

[17] Johnson, W., "Analysis of Initial GANE GPS Attitude Solutions," C. S. Draper Laboratory Memo #96-28, Aug 13, 1996.

[18] Koifman, M. and S. J. Merhav, "Autonomously Aided Strapdown Attitude Reference System," *Journal of Guidance*, Vol. 14, No. 6, 1990, pp. 1164-1172.

[19] Kourepinis, A., J. Borenstein, J. Connelly, P. Ward, and M. Weinberg, "Performance of Small, Low Cost Rate Sensors for Military and Commercial Applications," *23rd Joint Services Data Exchange for Guidance, Navigation and Control*, Nov., 1996.

[20] Larson, W. J., and J. R. Wertz (Ed.), *Space Mission Analysis and Design*, Microcosm, Inc., Torrance, California and Kluwer Academic Publishers, Dordrecht, The Netherlands, 1992.

[21] Lefferts, E. J., F. L. Markley, and M. D. Shuster, "Kalman Filtering for Spacecraft Attitude Estimation," *Journal of Guidance, Control and Dynamics*, Vol. 5, No. 5, Sept.-Oct. 1982, pp. 417-429.

[22] Montgomery, P. Y., *Carrier Phase Differential GPS as a Sensor for Automatic Control*, Ph. D. Dissertation, Department of Aeronautics and Astronautics, Stanford University, Jun. 1996.

[23] Mullen, F., and R. Greenspan, "Effect of Multipath on a GPS Interferometer," C. S. Draper Laboratory Memo #E33-96-116, Jun. 10, 1996.

[24] Parkinson, B. W., and J. J. Spilker, Jr. (Ed.), *GPS Theory and Applications*, American Institute of Aeronautics and Astronautics, Inc., Washington, D.C.

[25] Pavlath, G. A., "Fiber Optic Gyro Evolution Concept to Product," *AIAA Guidance and Control Conference, Technical Papers*, Pt. 2, 1992, pp. 575-586.

[26] Stohl, J. C., *Performance Analysis of a GPS Interferometric Attitude Determination System for a Gravity Gradient Stabilized Spacecraft*, S. M. Thesis,

Department of Aeronautics and Astronautics, MIT, May 1994.

- [27] Sullivan, W. I., *Performance Analysis of an Integrated Attitude Determination System*, S. M. Thesis, Department of Aeronautics and Astronautics, MIT, May 1994.
- [28] Tranquilla, J. M., and Colpitts, B. G., "GPS Antenna Design Characteristics for High Precision Applications," *Proceedings of the ASCE Specialty Conference on GPS-88 Engineering Applications of GPS Satellite Surveying Technology*, 1988, pp. 2-14.
- [29] Weill, L. R., "Optimal GPS Attitude Determination Without Ambiguity Resolution," *Proceedings of the 1994 Technical Meeting*, Institute of Navigation, 1994, pp. 433-439.
- [30] Wertz, J. R. (Ed.), *Spacecraft Attitude Determination and Control*, D. Reidel Publishing Company, Dordrecht, Holland, 1978.

